DTU Construct
Department of Civil and Mechanical Engineering

Phase field methods for fracture - With a special focus on hydrogen assisted fracture

Philip Kræn Kristensen

PhD Thesis

Phase field methods for fracture
-With a special focus on hydrogen assisted fracure

Philip Kræn Kristensen

Department of Civil and Mechanical Engineering
Technical University of Denmark 2022

Thesis title
Phase field methods for fracture
-With a special focus on hydrogen assisted fracure

Thesis author
Philip Kræn Kristensen

Main supervisor
Professor Christian Niordson
Technical University of Denmark

Co-supervisor
Associate professor, Emilio Martínez-Pañeda
Imperial College London

Co-supervisor
Professor, Rajan Ambat
Technical University of Denmark

PhD Thesis
November, 2022

Copyright: Reproduction of this publication in whole or in part must include the customary bibliographic citation, including author attribution, report title, etc.

Published by: DTU, Department of Civil and Mechanical Engineering,
Koppels Allé, Building 404,
2800 Kgs. Lyngby, Denmark
www.mek.dtu.dk
ISSN: 0903-1685
ISBN: 978-87-7475-711-5
DCAMM special report nr. S322
©2022 Philip Kræn Kristensen

Preface

This thesis is submitted to satisfy the requirements of a PhD degree at the Technical University of Denmark. This work was conducted at the Department of Civil and Mechanical Engineering, with funding from DTU Offshore under the Structural Integrity and Lifetime Evaluation research programme.

This thesis was completed under the primary supervision of Professor Christian Niordson and under the co-supervision of associate professor Emilio Martínez-Pañeda and Professor Rajan Ambat.

I would like to thank Christian for his immense understanding and support, which has played an important role in keeping me positive throughout my time at the department. I would like to thank Emilio for his drive and engagement in my work, which has been instrumental in bringing much of my work to fruition. Finally Rajan, thank you for making yourself and your expertise available, even if experimental work never became part of this thesis.

Most importantly, I would like to thank my beloved wife, Lilli Irene Ør Kristensen, who was a big part of my inspiration to pursue a PhD and who has supported me both emotionally and practically through all the years of my thesis.

Philip Kræn Kristensen
Kgs. Lyngby, November 2022

To Benjamin and Jonathan

Resumé (in Danish)

Denne afhandling omhandler udviklingen af numeriske modeller til forudsigelse af brud i stål under indflydelse af brint. Brint forekommer mange steder i naturen, ikke mindst omkring metaller der er udsat for aggressive miljøer som havvand eller syre. Derudover kan brint gå hen og blive en stor den af en bæredygtig energiinfrastruktur. Derfor er det en uheldig effekt at brint er i stand til at trænge ind i stål og ved sin tilstedeværelse gøre stålet sprødt. Denne brintskørhed kan medføre pludselige brud i højstyrkekomponenter ved langt laver belastninger end ellers ventet. Af denne grund er det vigtigt at udvikle effektive numeriske modeller til at forudse sådanne sprøde brud.

Som et grundelement i modellerne udviklet i denne afhandling benyttes den såkaldte phase field brudmodel, som har været umådeligt populær i de seneste år. Fordelen ved phase field modelen er at den er særligt fleksibel og kan anvendes både til komplekse brudformer og, som her, multifysik med interaktioner med brint.

Anvendeligheden af phase field modellen bliver i denne afhandling påvist gennem en række numeriske eksperimenter som viser at modellen giver pålidelige resultater i overensstemmelse med klassisk brudmekanik. Dernæst demonstreres det at modellen er i stand til at fange den forventede fysik bag brint-assisteret udmattelse. En række ingeniørfagligt relevante tilfælde bliver undersøgt for at påvise den foreslåede models anvendelighed i en praktisk sammenhæng hvor den både kan bidrage til virtuelle eksperimenter og vurdering af eksisterende komponenters tilbageværende styrke baseret på inspektionsdata.

Til sidst anvendes en avanceret udgave af modellen udvidet med tøjningsgradient plasticitet til at påvise at den anvendte model for brintskørhed og de forhøjede spændinger som tøjningsgradient plasticiteten forudser ved revnespidser tilsammen kan rationalisere et sprødt brud i et ellers duktilt materiale.

Herudover indeholder denne afhandling omfattende diskussion af relevante aspekter i phase field modelen, samt endnu upubliceret arbejde med at øge hastigheden af udmattelsesberegninger.

Abstract

This Thesis concerns the development of numerical models for the prediction of fractures in steel under the influence of hydrogen. Hydrogen is present many places in nature, not least around metals exposed to aggressive environments such as seawater or acid. Furthermore, hydrogen is poised to become a significant feature of a sustainable energy infrastructure. Therefore, it is an unfortunate effect that hydrogen is capable of diffusing into steel and, by its presence, make the steel brittle. This hydrogen embrittlement can cause sudden failure in high-strength components at loads far below what would otherwise be expected. For this reason, it is important to develop efficient numeric models for the prediction of such brittle fractures.

As a base element in the models developed in this thesis, the so-called *phase field* fracture model is used, which has been immensely popular in recent years. The advantage of the phase field model is that it is especially flexible and can be used for both complex fracture scenarios and, as here, multiphysics with hydrogen interaction.

The suitability of the phase field model is assessed in this Thesis through a succession of numerical experiments which reveal that the model yields reliable results in accordance with classic fracture mechanics. Afterwards, the capability of the model to capture the expected physics of hydrogen-assisted fatigue is demonstrated. A set of relevant engineering problems are studied to demonstrate the suitability of the proposed model in an applied context, where both virtual experiments and in-service strength assessments based on inspection data are shown to be possible.

Finally, an advanced version of the model is applied, which is enhanced with strain gradient plasticity, to show that the hydrogen embrittlement model utilized together with the increased crack tip stresses predicted by strain gradient plasticity are able to rationalize brittle fracture in an otherwise ductile material.

In addition, this thesis contains detailed discussion of relevant aspects of the phase field model and yet unpublished work on the acceleration of fatigue computations.

List of Publications

The following publications are part of this thesis:

[P1] Kristensen, Philip K., Martínez-Pañeda, Emilio. Phase field fracture modelling using quasi-Newton methods and a new adaptive step scheme. Theoretical and Applied Fracture Mechanics 2020. 107. 102446

[P2] Kristensen, Philip K., Niordson, Christian F., Martínez-Pañeda, Emilio. An assessment of phase field fracture: Crack initiation and growth. Philosophical Transactions of the Royal Society A: Mathematical, Physical and Engineering Sciences 2021, 379. 20210021

[P3] Golahmar, Alireza, Kristensen, Philip K., Niordson, Christian F., Martínez-Pañeda, Emilio. A phase field model for hydrogen-assisted fatigue. International Journal of Fatigue 2022. 154. 106521.

[P4] Kristensen, Philip K., Niordson, Christian F., Martínez-Pañeda, Emilio. Applications of phase field fracture in modelling hydrogen assisted failures. Theoretical and Applied Fracture Mechanics 2020. 110, 102837.

[P5] Kristensen, Philip K., Niordson, Christian F., Martínez-Pañeda, Emilio. A phase field model for elastic-gradient-plastic solids undergoing hydrogen embrittlement. Journal of the Mechanics and Physics of Solids 2020. 143. 104093.

Contents

1 Introduction

1.1 Background and motivation

Fracture mechanics has come a long way since its inception in 1921, marked by the publication of Griffith's field-defining work "On the rupture of solids" [1]. From the starting point of developing a criterion for the growth of long cracks in infinite elastic solids, modern fracture mechanics are now capable of delivering reliable solutions for most material types and fracture conditions, be it fast, branching, cracks in a brittle material or ductile tearing of metals. There are, however, still a number of areas that have not reached maturity yet. Two notable such fields are *fatigue* and *hydrogen embrittlement*, despite both fields being older than fracture Mechanics itself.

To many readers the latter field mentioned above may be unfamiliar, as it is a relatively niche field caught in the intersection of fracture mechanics, materials science and chemistry. It does, however, provide the original motivation for the entirety of this thesis: It has long been known that metal components subjected to aggressive environments, such as acid or seawater, are prone to unexpectedly fail at loads that would normally be considered entirely safe. It has also been long established that such premature failures are the result of a combined effect of mechanical load and environmental influence. There are multiple types of environmentally-assisted fractures (EAF), but among the most dangerous are those caused by hydrogen, which usually cause sudden *brittle* fracture in otherwise tough materials. As a result of this poorly understood and dangerous phenomenon known as hydrogen embrittlement, industries such as oil & gas and the energy sector have taken to using low strength steels in applications where materials are exposed to hostile environments as low strength steels are much less susceptible to hydrogen embrittlement than their high strength counterparts. Consequently, much more material is needed than what might otherwise have been necessary if modern high strength steel was employed at critical sections. Furthermore, as the field of material science marches on and develops increasingly stronger steels, the use of environmentally sensitive materials is becoming increasingly common across a wide range of industries that did not previously experience hydrogen embrittlement.

Consequently, there is great value in improving the predictive tools for hydrogen embrittlement in order to improve the safety of components exposed to hydrogenous or corrosive environments and to reduce material usage by enabling safe use of high strength steels where possible. This thesis is dedicated to the development and implementation of tools and models towards this goal.

1.2 Hydrogen embrittlement

Hydrogen embrittlement research predates the entire field of fracture mechanics, with the earliest known publication on the subject dating all the way back to 1885 [2]. While a lot has been discovered since that initial publication, the fundamental concept is unchanged: *When steel and some other metals are exposed to hydrogen, they suffer a significant reduction in strength, fracture toughness, and ductility.*

Hydrogen atoms are very small when compared to iron atoms. Most importantly, they are small enough to diffuse into the lattice of iron and other metals even at modest temperatures. Hydrogen may enter the metal either from high-pressure hydrogen gas, where the gas may be absorbed as atoms into the material or as a result of electrochemical reactions at the metal surface such as corrosion where Volmer reactions result in hydrogen atoms adsorbed to the metal surface of which some is subsequently absorbed into the

lattice [3].
Unfortunately, sheltering metals completely from corrosion is not feasible in a large number of applications and therefore the absorption, transport, and mechanical influence of hydrogen must be carefully understood. The absorption behaviour of hydrogen in metals is a matter of surface kinetics and thermodynamics which is outside of the scope of this thesis. The transport of hydrogen inside the metal lattice has been the subject of much work over the last century. It is by now well established that several key factors influence the distribution of hydrogen. First off, as is the case for most transport problems, concentration gradients act as a driving force for diffusion. Secondly, hydrostatic stress in the material has been shown to also significantly affect the transport of hydrogen, causing enhanced hydrogen concentrations in areas of high hydrostatic stress such as crack tips [4, 5]. Finally, microstructural effects play an important role, not only in how the lattice structure affects diffusion rates in general, but microstructural defects such as grain boundaries, martensite interfaces, voids and dislocations can all act as traps for hydrogen [6], slowing the diffusion of hydrogen throughout the material. A model describing the distribution of hydrogen between hydrogen stored in traps and diffusible hydrogen in normal intersticial lattice sites (NILS), based on a thermodynamic balance was proposed by Oriani in 1970 [7]. The role of dislocations in the transport of hydrogen and *vice versa* has been the topic of large amounts of research. Hydrogen was found in some cases to increase the mobility of dislocations [8, 9], although in other cases it has been shown to suppress dislocation motion [10, 11]. The complex interactions between hydrogen and microstructural features as well as the variety of hydrogen-metal systems studied has made the task of identifying the underlying mechanisms of hydrogen embrittlement difficult. For an overview of potential hydrogen embrittlement mechanisms, the reader is referred to reviews by Robertson *et al.* [12], Dadfarnia *et al.* [13] and Li *et al.* [6]. A few of the most important mechanisms will be repeated here.
In the Hydrogen-induced phase transition (HIPT) mechanism, hydrogen reacts with the metal to form a brittle hydride compound which provides a weak brittle fracture path. The stability of these hydrides depends greatly on the metal and the stress state. This mechanism is important for some metals where these hydrides form easily such as Ti, Zr, Nv, and V [14]. In the hydrogen-enhanced localized plasticity (HELP) mechanism, the increase in dislocation mobility associated with hydrogen leads to an increased buildup of hydrogen near the crack tip as dislocations drag the hydrogen along. The large crack tip concentration of hydrogen then locally brings the dislocation mobility to a critical point, causing a localized plastic collapse [15]. Finally, there is the hydrogen-enhanced decohesion (HEDE) mechanism where the presence of hydrogen either in a lattice plane or a grain-boundary reduces the cohesive energy of that plane causing it to fracture at sub-critical load [16]. All of these mechanisms have ample experimental and theoretical evidence supporting them, while also failing to describe other phenomena.
The approach in this thesis is primarily a phenomenological one, although the specific choice of embrittlement law can be characterized as reflecting the HEDE mechanism.
Regardless of the chosen mechanism for hydrogen embrittlement, another important element of developing numerical tools for predicting hydrogen-assisted fracture is the capability to model fracture. A promising model for providing this capability is the phase field fracture model, which has become a significant topic of this thesis.

1.3 Phase field fracture

The growth of a discrete discontinuous interface such as a crack, inside the computational domain of a continuous deformation problem is a difficult thing to track from a math-

ematical and computational standpoint. In spite of these difficulties, several numerical approaches for ongoing crack growth have been proposed over the years. These methods include discrete crack methods such as cohesive element and cohesive zone models [17], enriched element formulations such as X-FEM [18] and element deletion techniques based on local criteria [19]. For diffusive crack methods where the crack is approximated in a continuous manner, there are (gradient) damage models [20] and the thick level set method [21]. Each of these bring various advantages and disadvantages. For example, cohesive zone models are easy to implement and adapt to reflect well the strength and unloading behaviour of a given interface, but as a downside potential crack paths must be known *a priori*. Meanwhile, X-FEM methods can provide mesh-independent predictions of arbitrary crack paths, but is significantly more difficult to implement and difficult to apply to non-linear materials. Of special interest in this thesis is the class diffusive crack fracture models known as *phase field* models.

The phase field fracture model is still a relatively recent development. The first significant development was the reformulation of Griffith's original energy balance into a variational form by Francfort and Marigo in 1998 [22], which enabled implicit capture of crack path and nucleation. To implement Francfort and Marigo's variational approach, Bourdin proposed in the year 2000 to regularize the model using a broad class of functionals known as Ambrosio-Tortorelli functionals. This regularized approach later became know as phase field fracture models, most probably due to their similarity with Ginzburg-Landau models for phase transition [23]. The field did not really gain traction until almost a decade later where notable works such as those by Bourdin *et al.* [24], Amor *et al.* [25] and Miehe *et al.* [26, 27] helped push the model to broader adoption. Since then, phase field fracture models have gained immense popularity, for their capability to determine arbitrarily complex crack paths and nucleation without any additional criteria, although the latter capability remains a somewhat controversial topic [28–30].

The idea in phase field fracture is to have a scalar parameter which interpolates between an intact material phase and a broken one, that is governed by its own partial differential equation, coupled to the displacement problem for the solid. The gradient of this scalar parameter is penalized such that no infinitely thin bands are formed at effectively zero energy cost. While phase field models are arguably not significantly different from previous gradient damage models [31], they differ in a way that lends them a great deal of additional credibility: They are, at least nominally, variationally consistent and, as the inherent length scale found in phase field models tends to zero, the functional has been proven to Γ-converge towards the original Griffith solution. The fact that the model is mathematically well-founded, easy to implement and adapt, and applicable to a wide array of fracture problems has made the phase field fracture model extremely popular. The model has been extended and applied to a large number of special fracture problems, such as dynamic fracture [32–34], Herzian indentation fracture [35], mixed-mode fracture [36], fatigue damage [37, 38], interface fracture [39], and fracture in shells [40]. In addition, it has been modified for other materials and material behaviours including ductile fracture [41–44], quasi-brittle fracture [45, 46], elastomers [47], shape-memory alloys [48], functionally graded materials [49] and fiber composites [50]. Finally, it has also been applied to multiphysics problems such as Lithium ion batteries [51, 52], thermal shocks [53], moisture effects [54], and hydrogen embrittlement [55–57].

The phase field fracture model is a powerful framework on which to build a model for hydrogen-assisted fracture with broad applicability. As a results, large sections of this thesis will be dedicated to the development of the phase field model itself.

1.4 Thesis outline

The main body of the thesis consists of four chapters following this one. Chapter 2 contains the theoretical background for the phase field and hydrogen embrittlement models, as well as relevant discussion about these. In addition, an introduction to the strain gradient plasticity model of Gudmundson [58] is included as it is used in publication [P5]. Chapter 3 contains details regarding the numerical implementation of previously introduced models as well as discussion of solution strategies and details on ongoing work with acceleration strategies for fatigue. Chapter 4 summarizes the results from numerical experiments conducted throughout the publications and finally, chapter 5 describes the main findings and takeaways and provides an outlook to further work and opportunities.

1.5 A note on notation

Throughout this thesis, the following notation applies: Italic, non-bold Latin or Greek letters such as ψ or C denote scalars or scalar fields. Bold upright Latin or Greek letters denote vectors, for example $\mathbf{J}$ or $\mathbf{u}$. Finally, bold, italic Latin or Greek letters denote second-or-higher order tensors, such as $\boldsymbol{\sigma}$ or $\boldsymbol{\varepsilon}$. Additionally, vertically stacked dots denote an inner tensor product over a number of indices equal to the number of dots, i.e. $\boldsymbol{\sigma} : \boldsymbol{\varepsilon}$ is a double inner product. The gradient of a quantity $\mathbf{q}$ is denoted $\nabla \mathbf{q}$, the divergence is denoted $\nabla \cdot \mathbf{q}$ and the Laplacian is denoted $\Delta \mathbf{q}$. Domains such as the crack surface Γ are denoted by upright, lightface, capital Greek letters

2 | Theory

This chapter provides a detailed introduction to the underlying theory of the models used throughout this thesis. The first section, which concerns the phase field model, also includes detailed discussion on extensions and modifications of the standard phase field models. The second main section introduces hydrogen transport and embrittlement, which is relevant for the majority of the publications included in this thesis. The final section concerns strain gradient plasticity, which is only used for publication [P5].

2.1 The phase field fracture model

Consider an arbitrary volume of brittle material $\Omega \in \mathbb{R}^n$, with boundary $\delta\Omega \in \mathbb{R}^{n-1}$ and outwards unit normal n. The domain Ω may furthermore contain a crack surface $\Gamma \in \mathbb{R}^{n-1}$, as depicted in figure 2.1a. The strain energy density of the material is denoted ψ and the critical energy release rate for crack growth in the material G_c.

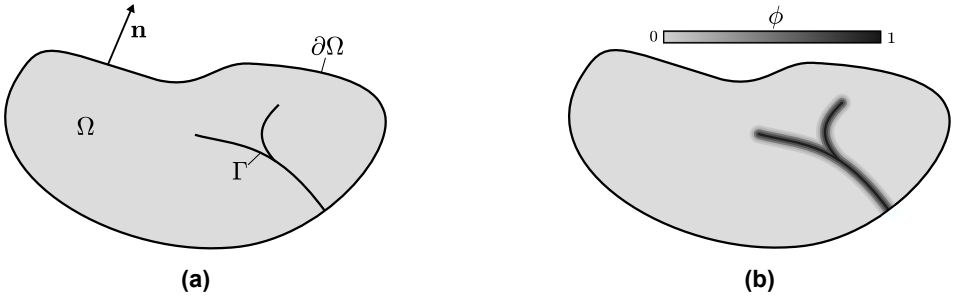

Figure 2.1: Sketch of the continuum domain with a) the actual crack surface Γ and b) the regularized crack surface represented by ϕ.

The internal free energy $\mathcal{E}$ may then be expressed as [22]

$$\mathcal{E} = \int_\Omega \psi \, \mathrm{d}V + \int_\Gamma G_c \, \mathrm{d}S, \tag{2.1}$$

where the first integral denotes the internal free energy and the latter the surface energy of the crack. Minimization of the internal free energy then yields the solution for the crack growth problem. In practice, however, finding such a minimum is difficult as it is dependent on the unknown path of Γ. To overcome this difficulty, the idea in phase field is to regularize the surface integral into a volume integral over the entire domain by the introduction of a scalar variable, which we shall refer to as the phase field variable ϕ. The phase field variable is bounded between 0 and 1, where 0 denotes intact material and 1 signifies the broken material phase, as shown in figure 2.1b. The physical meaning of intermediate values of ϕ is open to interpretation, but is often taken to signify damage. The phase field regularization is introduced by means of a surface density function γ, such that the regularized internal free energy $\mathcal{E}_\ell$ may be written as

$$\mathcal{E}_\ell = \int_\Omega \psi_\ell \, \mathrm{d}V + \int_\Omega G_c \gamma \, \mathrm{d}V. \tag{2.2}$$

Note that the first integral is also changed by the regularization, as the domain no longer includes an internal boundary and must therefore include a degradation function to introduce the (continuous approximation of the) discontinuity in strain energy across the crack

surface. The degraded strain energy ψ_ℓ is given by

$$\psi_\ell = g(\phi)\psi \tag{2.3}$$

Naturally, any choice of degradation function $g(\phi)$ and crack surface density function γ will not produce a good approximation of the crack growth problem. However, the restrictions on $g(\phi)$ are relatively simple: The function must be monotonic, continuous, differentiable and observe the boundary conditions

$$g(0) = 1, \qquad g(1) = 0. \tag{2.4}$$

A third condition, $g'(1) = 0$ is often imposed in practice, as it ensures automatic enforcement of the upper bound of ϕ, but it is not strictly necessary if the solution strategy is bounded. For the surface density function γ, a relatively broad class of functionals provide a suitable approximation of the fracture problem:

$$\gamma = \frac{1}{4c_w}\left(\frac{w(\phi)}{\ell} + \ell|\nabla\phi|^2\right) \tag{2.5}$$

Here, $w(\phi)$ is a continuous monotonic function fulfilling $w(0) = 0$ and $w(1) = 1$ which also determines the magnitude of the factor $c_w = \int_0^1 \sqrt{w(\varphi)}\,\mathrm{d}\varphi$. Finally, ℓ is a length scale which is necessary the regularization. Any phase field formulation of the form found in Eq. (2.2) which fulfills the above conditions will share an energy minimum with Eq. (2.1) in the limit $\ell \to 0$. In practice, the length scale cannot be chosen arbitrarily small, but good results can still be attained at finite values as shown in chapter 4.
In the context of this thesis, our attention is restricted to a single choice of the degradation function, namely

$$g(\phi) = (1-\phi)^2. \tag{2.6}$$

For the choice of $w(\phi)$, which defines the crack surface density function γ, two choices are considered. First, the choice $w(\phi) = \phi^2$, which, in combination with our choice of degradation function forms the original formulation from the by Bourdin and colleagues (2000) [59], which was in turn inspired from the use of the same formulation by Ambrosio and Tortorelli in 1991 [60] to solve the Mumford-Shah problem from image segmentation [61]. This formulation is now commonly referred to as the `AT2` phase field model,where AT stands for Ambrosio-Tortorelli. The internal free energy for this formulation becomes

$$\mathcal{E}_\ell = \int_\Omega \left[(1-\phi)^2\,\psi + \frac{G_c}{2}\left(\frac{\phi^2}{\ell} + \ell|\nabla\phi|^2\right)\right]\mathrm{d}V. \qquad (\texttt{AT2}) \tag{2.7}$$

While this formulation is the most common one, a second choice of formulation forms what is now known as the `AT1` phase field model. This model is defined by the choice $w(\phi) = \phi$, yielding the formulation:

$$\mathcal{E}_\ell = \int_\Omega \left[(1-\phi)^2\,\psi + \frac{3G_c}{8}\left(\frac{\phi}{\ell} + \ell|\nabla\phi|^2\right)\right]\mathrm{d}V. \qquad (\texttt{AT1}) \tag{2.8}$$

This formulation was first introduced by Bourdin and colleagues in 2014 [53]. It has the principal advantage of introducing a lower limit for damage initiation, such that infinitesimal strain does not introduce a corresponding infinitesimal increase in ϕ, as is the case for the `AT2` model. It does, however, come with the price that the lower bound of the phase field variable, $\phi \geq 0$, is not automatically enforced, which must be handled somehow in the numerical implementation, see section 3.2.1. More details on the differences between the `AT1` and `AT2` models and other available alternatives can be found in section 2.1.2.

2.1.1 Principle of virtual work

Throughout the entirety of the thesis, small strains are assumed, such that for a displacement field $\mathbf{u}$, the strain tensor $\boldsymbol{\varepsilon}$ is expressed as the symmetrized gradient of the displacement field

$$\boldsymbol{\varepsilon} = \frac{1}{2}\left[\nabla\mathbf{u} + (\nabla\mathbf{u})^T\right]. \tag{2.9}$$

We define for convenience the Cauchy stress tensor $\boldsymbol{\sigma}$ as

$$\boldsymbol{\sigma} = \frac{\partial\psi_\ell^e}{\partial\boldsymbol{\varepsilon}} = (1-\phi)^2\frac{\partial\psi^e}{\partial\boldsymbol{\varepsilon}}, \tag{2.10}$$

where ψ^e is the elastic portion of the strain energy. For now, and for the majority of this thesis, $\psi^e = \psi$. As derivations of the strong and weak form of the `AT2` phase field fracture model is included in the publications, it will here only be shown for the `AT1` model. We denote variations with respect to the strain field, the phase field and the gradient of the latter as $\delta\boldsymbol{\varepsilon}$, $\delta\phi$ and $\delta\nabla\phi$, respectively. The internal virtual work $\mathcal{W}$ is equal to the variation of the internal free energy

$$\begin{aligned}\mathcal{W} = \delta\mathcal{E}_\ell &= \frac{\partial\mathcal{E}_\ell}{\partial\boldsymbol{\varepsilon}} : \delta\boldsymbol{\varepsilon} + \frac{\partial\mathcal{E}_\ell}{\partial\phi}\delta\phi + \frac{\partial\mathcal{E}_\ell}{\partial\nabla\phi}\cdot\delta\nabla\phi \\ &= \int_\Omega \boldsymbol{\sigma} : \delta\boldsymbol{\varepsilon}\,\mathrm{d}V - \int_\Omega\left[2(1-\phi)\psi\delta\phi - \frac{3G_c}{8\ell}\left(1 + 2\ell^2\nabla\phi\cdot\delta\nabla\phi\right)\right]\mathrm{d}V.\end{aligned} \tag{2.11}$$

In the absence of body forces, external virtual work stems only from tractions $\mathbf{T}$ prescribed on the boundary $\partial\Omega_h \subseteq \partial\Omega$, as no external traction for the phase field is defined. The external virtual work $\mathcal{U}$ is thus given by:

$$\mathcal{U} = \int_{\partial\Omega_h}\mathbf{T}\cdot\delta\mathbf{u}\,\mathrm{d}S \tag{2.12}$$

Applying the Gauss divergence theorem to the balance of virtual work $\mathcal{W} - \mathcal{U} = 0$ yields:

$$\begin{aligned}&-\int_\Omega \nabla\cdot\boldsymbol{\sigma}\cdot\delta\mathbf{u}\,\mathrm{d}V + \int_{\Omega_h}\delta\mathbf{u}\cdot\boldsymbol{\sigma}\cdot\mathbf{n}\,\mathrm{d}S - \int_{\Omega_h}\mathbf{T}\cdot\delta\mathbf{u}\,\mathrm{d}S \\ &+\int_\Omega\left[-2(1-\phi)\psi\delta\phi + \frac{3G_c}{8\ell}\left(\delta\phi - 2\ell^2\Delta\phi\right)\delta\phi\right]\mathrm{d}V + \frac{3G_c}{4}\ell\int_{\partial\Omega}\nabla\phi\cdot\mathbf{n}\delta\phi\,\mathrm{d}S = 0\end{aligned} \tag{2.13}$$

By the standard arguments that the above must hold for any volume Ω and any set of kinematically admissible virtual quantities, we arrive at the strong form of the phase field displacement-damage problem:

$$\begin{aligned}\nabla\cdot\boldsymbol{\sigma} &= 0 \\ &\qquad\qquad\text{in } \Omega. \\ -2(1-\phi)\psi + \frac{3G_c}{8\ell}\left(1 - 2\ell^2\Delta\phi\right) &= 0\end{aligned} \tag{2.14}$$

With boundary conditions:

$$\begin{aligned}\boldsymbol{\sigma}\cdot\mathbf{n} &= \mathbf{T} && \text{on } \partial\Omega_h, \\ \nabla\phi\cdot\mathbf{n} &= \Phi && \text{on } \partial\Omega.\end{aligned} \tag{2.15}$$

The phase field traction Φ has little physical meaning, however, as non-homogenous Neumann boundary conditions on the phase field do not occur practice. in The corresponding

weak form of the phase field equations will be used to construct the finite element formulation in chapter 3, where further details on implementing and solving the above equation system will be provided. For completeness, the corresponding strong for equations for the AT2 formulation are

$$\begin{aligned} \nabla \cdot \boldsymbol{\sigma} &= 0 \\ & \qquad \text{in } \Omega, \\ -2(1-\phi)\psi + \frac{G_c}{\ell}\left(\phi - \ell^2 \Delta\phi\right) &= 0 \end{aligned} \tag{2.16}$$

and are also subject to the boundary conditions Eq. (2.15).

2.1.2 Alternative phase field formulations

In order to better understand the differences between available phase field models and why one might consider alternatives, we first consider the one-dimensional case of the phase field model, while leaving out the gradient term. For the AT2 model, the simplified form of the strong form phase field equation Eq. (2.16) becomes

$$\frac{G_c}{\ell}\phi - 2(1-\phi)\psi = 0. \tag{2.17}$$

In the 1D linear elastic case, the undegraded strain energy is

$$\psi = \frac{1}{2}E\varepsilon^2, \tag{2.18}$$

which leads to the following expression for the phase field,

$$\phi = \frac{E\ell\varepsilon^2}{G_c + E\ell\varepsilon^2}. \tag{2.19}$$

This expression is naturally bounded between 0 and 1, which is one of the primary features of the AT2 model, as no additional effort is required to enforce these bounds. In comparison, the 1D strong form phase field equation Eq. (2.14) for the AT1 model without the gradient term reads

$$\frac{3G_c}{8\ell} - 2(1-\phi)\psi = 0, \tag{2.20}$$

which gives rise to a relation

$$\phi = 1 - \frac{3G_c}{8\ell E\varepsilon^2}. \tag{2.21}$$

The unfortunate case in this expression is that for $\varepsilon \to 0$, the phase field tends towards negative infinity. In other words, the lower bound on the phase field must be enforced externally. In the 1D homogeneous case here, it is sufficient to write

$$\phi = \begin{cases} 0 & \text{if } \varepsilon \leq \sqrt{\dfrac{3G_c}{8\ell E}} \\ 1 - \dfrac{3G_c}{8\ell E\varepsilon^2} & \text{else} \end{cases}, \tag{2.22}$$

although this may become an issue when the gradient term is included. A stress-strain relation for the two phase field models may be obtained by inserting Eq. (2.22) and Eq. (2.19) respectively in the stress strain relation

$$\sigma = (1-\phi)^2 E\varepsilon. \tag{2.23}$$

A plot of these can be seen in figure 2.2. The exes are normalized by the critical stress σ_c and critical strain ε_c. The critical stress is defined as the maximum stress attained before the softening regime and is given by

$$\sigma_c^{\texttt{AT1}} = \sqrt{\frac{3EG_c}{8\ell}}, \qquad \sigma_c^{\texttt{AT2}} = \frac{3}{16}\sqrt{\frac{3EG_c}{\ell}}. \tag{2.24}$$

The critical strain is simply defined by $\varepsilon_c = \frac{1}{E}\sigma_c$.

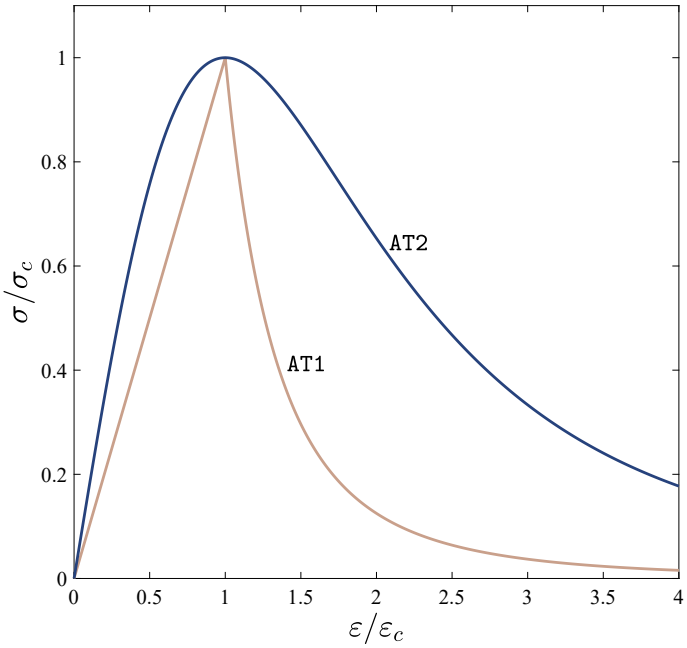

Figure 2.2: One-dimensional stress-strain response for the `AT1` and `AT2` phase field models in the absence of gradient terms. Adapted from [P2].

From figure 2.2, one of the advantages of the `AT1` model becomes clear; namely that it has a linear elastic regime, which many consider a necessity for accurately representing the physics of fracture. Furthermore, when gradient terms are included, the optimal crack profile of the `AT2` model tends asymptotically to zero, while the optimal crack profile of the `AT1` model has a finite width.

An important conclusion from this consideration is that the critical stress of these phase field models is effectively governed by the length scale ℓ, which is otherwise intended strictly as a numerical parameter with no physical meaning. Outside of the homogeneous 1D consideration the effect of the critical stress can be made apparent by considering crack initiation from crack of varying lengths as in figure 2.3. Here a crack of width W and height $6W$ is considered with an edge crack of length a. As can be seen, the phase field model transitions smoothly from the classic Griffith criterion to a strength criterion governed by the critical stress in (2.24) as the crack becomes short. This transition between criteria is usually considered a strength in the phase field model, but the fact that the critical stress is controlled by the length scale is often impractical as the necessary size of the length scale relative to the geometry problem may cause an unphysical critical stress or *vice versa* as remarked in [28].

Alternative phase field models usually retains the choice of $w(\phi)$ from either the `AT1` or `AT2` phase field model and instead seek to alter the formulation through the choice of degradation function. The use of either cubic or quartic degradation functions with $g'(0) = 0$, was explored in [62]. The advantage of such functions in what would otherwise be an `AT2`

model is the introduction of a linear elastic phase. The price to pay, however, is the numerical handling or these functions which requires the use of a perturbation at each load step.

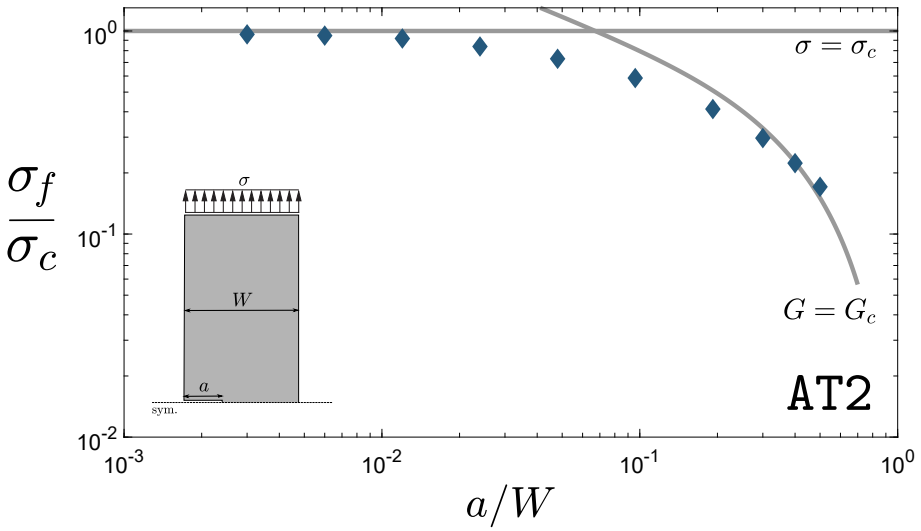

Figure 2.3: Transition of fracture criterion between a critical stress criterion and the classical Griffith criterion. Results are obtained with the `AT2` model. Adapted from [P2].

In order to decouple the critical stress from the phase field length scale, Sargado and colleagues proposed a parametric degradation function [63]. A more flexible approach was proposed in [28], which permitted the inclusion of a full critical stress envelope in 6D stress space as an additional term, however, at the cost that such a model is no longer variationally consistent. Even more recently a generalized approach for introducing arbitrary failure surfaces to the phase field odel while retaining variational consistency was introduced in [64]. Finally, there are even more exotic phase field models, such as the one by Karma *et al.* [23], which is based on the Ginzburg-landau equation and higher order phase field models [65]. The latter model reports excellent convergence properties, but requires a high order of continuity in the discretization, which has kept it from broad adoption.

2.1.3 Extensions of the phase field model and outstanding issues

As mentioned in the introductory chapter, the phase field model has been applied and extended to a large number of problems and phenomena. This section is not intended to provide an overview of such extensions, but rather to introduce some specific extensions used in this thesis and provide some context for their use and how they were chosen.

Crack behaviour in compression

In their basic form, the phase field equations Eq. (2.14) or (2.16) produce crack extension as a result of sufficient strain energy regardless of the stress state. A natural consequence of this is that cracks may grow in compression. Furthermore, as the cracked elements have no stiffness they do not prevent the interpenetration of crack surfaces in a compressive stress state. Early attempts to remedy both problems involved additively decomposing the strain energy into a passive or compressive part ψ^- and an active or tensile part ψ^+, such that:

$$\psi = \psi^+ + \psi^-, \tag{2.25}$$

where only the active part would contribute to crack growth and be degraded in turn by the phase phase field through the degradation function $g(\phi)$, such that the strong form equations would read

$$\begin{aligned} &(1-\phi)^2\nabla\cdot\boldsymbol{\sigma}^+ + \nabla\cdot\boldsymbol{\sigma}^- = 0 \\ &\qquad\qquad\qquad\qquad\qquad\qquad \text{in } \Omega, \\ &-2(1-\phi)\psi^+\frac{3G_c}{8\ell}\left(1-2\ell^2\Delta\phi\right) = 0 \end{aligned} \tag{2.26}$$

with $\boldsymbol{\sigma}^{\pm} = \frac{\partial\psi^{\pm}}{\partial\boldsymbol{\varepsilon}}$. Two such formulations became especially popular, the first being the so-called hydrostatic/deviatoric split by Amor *et al.* [25]. In the hydrostatic/deviatoric split, the hydrostatic strain energy belongs to the active strain energy only if the hydrostatic strain is positive. The deviatoric strain energy is meanwhile always included in the active part of the strain energy. This may be written as

$$\psi^+ = \frac{1}{2}K_b\langle\mathrm{tr}\,(\boldsymbol{\varepsilon})\rangle_+^2 + Q\left(\boldsymbol{\varepsilon}' : \boldsymbol{\varepsilon}'\right)\,, \tag{2.27}$$

$$\psi^- = \frac{1}{2}K_b\langle\mathrm{tr}\,(\boldsymbol{\varepsilon})\rangle_-^2\,, \tag{2.28}$$

where K_b is the bulk modulus, Q is the shear modulus, $\boldsymbol{\varepsilon}' = \boldsymbol{\varepsilon} - \frac{1}{3}\mathrm{tr}\boldsymbol{\varepsilon}$ is the deviatoric strain tensor and $\langle\cdot\rangle$ are Macaulay brackets.
The second very popular split is the spectral split proposed by Miehe *et al.* [26]. Here, positive principal strains contribute to the active strain energy and negative principal strains contribute to the passive strain energy.

$$\psi^{\pm} = \frac{1}{2}\lambda\langle\varepsilon_1+\varepsilon_2+\varepsilon_3\rangle_{\pm}^2 + Q\left(\langle\varepsilon_1\rangle_{\pm}^2 + \langle\varepsilon_2\rangle_{\pm}^2 + \langle\varepsilon_3\rangle_{\pm}^2\right) \tag{2.29}$$

These two decompositions, along with similar decompositions such as the one proposed by Freddi and Royer-Carfagni for masonry-like materials [66] have the excellent property that they do not compromise the variational consistency of the phase field model. They do, however, have some issues: First off, the stiffness of the material becomes nonlinear, which introduces significant computational cost in the construction of the material stiffness matrix. This drawback was, however, addressed quite effectively by Ambati and colleagues [67] with their so-called hybrid approach, where only the active part of the strain energy contributes to the crack evolution, while the elastic stiffness is isotropically degraded based on the relative size of the active and passive parts:

$$\boldsymbol{\sigma} = \begin{cases} \boldsymbol{\mathcal{L}}_0 : \varepsilon & , \text{if } \psi^+ < \psi^- \\ g(\phi)\boldsymbol{\mathcal{L}}_0 : \varepsilon & , \text{if } \psi^+ > \psi^- \end{cases}\,, \tag{2.30}$$

where $\boldsymbol{\mathcal{L}}_0$ is the fourth order linear elasticity tensor. The hybrid approach regains the linearity of the stiffness, while obtaining similar results to the full decompositions in the majority of cases. The second issue with decomposition of the strain energy is found in the objections raised by Strobl and Seelig. First, they found that the stress state in a compressed block of material with a complete crack perpendicular to the direction of compression was highly unphysical for both of the proposed strain decompositions [68]. Secondly, they showed that these decompositions introduce a significant influence of mesh orientation on the effective stiffness of a cracked element in tension [69].
Despite their issues, both the hydrostatic/deviatoric and the spectral strain decomposition have found widespread use in the literature and are also used in this thesis when strain

decomposition is relevant.

While they are not used in this thesis, a few promising techniques for addressing compression in the phase field have been proposed in the literature in recent years, which do now have the drawbacks discussed above. The first and most simple is a strain decomposition based on the direction of the crack. The idea was first proposed in [70], but was first implemented in a useful manner in [71]. A more exotic, but still variationally consistent, approach is found in [72], with the so-called representative crack element. Here, the idea is to define the desired behaviour of a block of material bisected by a crack and have the degradation function interpolate between this and the intact state. Functionally, the representative crack element is extremely similar to the crack direction-based strain decomposition, but offers significantly more flexibility. Finally, a variationally consistent technique for deriving phase field models presented by Feng and Li [45] makes it possible to impart a wide variety of behaviours in compression.

Phase field fatigue modeling

The extension of the phase field fracture model to capture fatigue has been the subject of significant attention as well. The models innate ability to handle nucleation and determine the path of cracks makes it an obvious candidate for virtual fatigue testing. Furthermore, with a relatively simple extension of the existing brittle fracture model, Carrara and colleagues [37] were able to demonstrate that a phase field fracture model could capture all three classical regimes of fatigue crack growth, including the Paris Law [73], through cycle-by-cycle simulation. A more pragmatic model was presented in [38], where the Paris-behaviour was taken as an input and the fatigue crack growth was computed by analogy between growth rate per cycle and growth rate in time. The work concerning phase field fatigue in publications [P3, P4] has taken has taken the model by Carrara *et al.* as a basis which effectively hinges on the following two additions to the phase field: i) A fatigue history variable $\bar{\alpha}$, which serves as a local measure of the load endured throughout the history of the material point and ii) a fatigue degradation function $f_\alpha(\bar{\alpha})$, which locally degrades the fracture toughness as a function of fatigue history in a similar manner to the hydrogen embrittlement model described in section 2.2. The strong form of the AT1 phase field equation becomes:

$$-2(1-\phi)\psi f_\alpha(\bar{\alpha})\frac{3G_c}{8\ell}\left(1-2\ell^2\Delta\phi\right)+\frac{3G_c\ell}{4}\nabla f_\alpha(\bar{\alpha})\cdot\nabla\phi=0 \tag{2.31}$$

which in the weak form reduces to a simple pre-multiplication of G_c by $f(\bar{\alpha})$. The exact choices of $f_\alpha(\bar{\alpha})$ and $\bar{\alpha}$ are of course critical to the physicality of the model, and some efforts have been devoted to improve the choices of these in [74, 75]. In its original conception, the evolution of the fatigue history variable was defined as

$$\dot{\bar{\alpha}}=H(\dot{\alpha})\dot{\alpha} \tag{2.32}$$

where H is the heaviside function and α is typically chosen as the active part of the elastic strain energy $\psi_\ell^+=g(\phi)\psi^+$. This formulation ensures that the fatigue only accumulates during loading and is unchanged during unloading. An alternative version introducing a mean load effect was also introduced in [37]. For the fatigue degradation function, two different suggestions were provided in the original paper. The work in this thesis has utilized the asymptotic one given by:

$$f(\bar{\alpha})=\begin{cases}1 & \text{if } \bar{\alpha}\leq\alpha_T\\ \left(\dfrac{2\alpha_T}{\bar{\alpha}+\alpha_T}\right)^2 & \text{if } \bar{\alpha}>\alpha_T\end{cases} \tag{2.33}$$

where $\alpha_T = \frac{G_c}{12\ell}$ defines a threshold below which fatigue does not affect the toughness of the material. Note that this formulation does not introduce an endurance limit as any load will, with sufficient cycles, accumulate sufficient fatigue to propagate a crack.

Know issues in phase field fracture modeling

While the phase field fracture model holds much promise and is almost certainly a tool that will see increasing use for the foreseeable future, it has also been met with healthy scientific scepticism, highlighting several issues in the phase field model. Some issues regarding compression have already been addressed above. A more fundamental issue is one of variational consistency. At its conception, the phase field method is a variational approach to fracture. The existence of a global energy minimum in accordance with the original Griffith criterion is guaranteed for $\ell \to 0$ in the sense of Γ-convergence. However, many modern phase field implementations violate the variational nature of the model by adding history variables or additional phenomenological terms. If variational consistency is violated, there is no longer any proof or guarantee that an energy minimum corresponding to the Griffith solution is preserved and the mathematical basis for the model is removed. Anecdotally, however, non-variational phase field models have produced promising results nonetheless throughout the literature, causing many to regard non-variational phase field models as a useful and reliable tool regardless of variational consistency. The models presented in this thesis are all non-variational as discussed in section 3.2.1.

Another important issue in phase field fracture modeling is the question of crack nucleation. In the case of nucleation from an existing, long, sharp defect, where linear elastic fracture mechanics is able to provide a solution, the phase field model should be able to provide an exact solution as well. AS discussed in [P2], however, small quantitative deviations can sometimes be observed. An energy correction has been proposed in [24] to minimize this effect, but it does not eliminate the problem entirely. It should, however, be noted that the deviation from an accurate solution is generally small and quite consistent. Further discussion of initiation in the phase field model both from sharp and non-sharp defects can be found in [28, 30, 76].

One final issue is the matter of computational performance. To minimmize errors, the phase field length scale ℓ should be small relative to relevant features of the geometry, such as holes or notches and the mesh should, in turn be smaller than ℓ, preferably by a factor of 8 or more [P2]. As a means to ease the requirements on the mesh, several efforts have been made, with the most common strategy being adaptive mesh refinement strategies [29, 32, 77]. As an alternative, specialized elements with exponential shape functions that mimic the optimal phase field crack profile were suggested in [78], A more recent but also promising approach has involved discretizing the phase field problem in an element-centered finite volume approach [79].
A much more significant issue, however, stems from the non-convexity of the phase field equations, which may cause traditional Newton solvers to become unstable and generally causes slow convergence. Efforts towards faster solution strategies is discussed in section 3.2.2.

2.2 Hydrogen transport and embrittlement

The transport of hydrogen is an important part of the hydrogen-assisted damage models in publications [P3-P5]. This section serves to provide a small overview of the utilized transport and embrittlement model as well as a brief overview of related topics and con-

siderations.

2.2.1 Hydrogen transport

We now consider again the arbitrary domain Ω depicted in figure 2.1a, with a new field C denoting the local hydrogen concentration. A basic mass balance dictates that in any point, the temporal change in hydrogen concentration $\dot{C}$ must be equal to the gradient of the flux of hydrogen $\mathbf{J}$, yielding what is generally known as the transport equation,

$$\dot{C} + \nabla \cdot \mathbf{J} = 0. \tag{2.34}$$

At low concentrations of hydrogen, the hydrogen flux $\mathbf{J}$ can be related to the chemical potential μ as

$$\mathbf{J} = -\frac{DC}{\mathcal{R}T}\nabla\mu, \tag{2.35}$$

where $\mathcal{R}$ is the gas constant, T the absolute temperature and D a diffusivity coefficient which is independent of the stress state by assumption. Under constant pressure and temperature, the chemical potential μ may be expressed as [80]

$$\mu = \mu_0 + \mathcal{R}T \ln C + \mu_\sigma. \tag{2.36}$$

In the previous equation, μ_0 denotes the chemical potential in the so-called "standard state" while μ_σ denotes the part of the chemical potential which is dependent on the stress field. If it is assumed that the hydrogen in normal interstitial lattice sites (NILS), which is to say hydrogen diffusing through the lattice, does not induce any shear in the lattice, but only a local dilation, the stress-dependent chemical potential is given by

$$\mu_\sigma = -\sigma_H \bar{V}_H, \tag{2.37}$$

where σ_H is the hydrostatic stress and $\bar{V}_H$ is the partial molar volume of dissolved hydrogen. Thus, the full stress-dependent hydrogen flux may be expressed as

$$\mathbf{J} = -D\nabla C + \frac{D\bar{V}_H C}{\mathcal{R}T}\nabla\sigma_H \tag{2.38}$$

The effect of the stress-dependent term is that hydrogen tends to diffuse towards regions of high hydrostatic stress. As a consequence, accurate predictions of crack tip stresses become exceedingly important in accurately capturing hydrogen-assisted cracking.

2.2.2 Accounting for microstructural traps

Microstructural traps do play a significant role in the transport of hydrogen in metals. Irregularities in the metal lattice such as grain boundaries, phase interfaces, voids, inclusions, and dislocations all act as "traps" for hydrogen; sites where hydrogen is stored and will only leave if there is a significant thermodynamic driving force for doing so. While none of the publications of this thesis account for these in an explicit manner, their influence is considered in the choice of D and in the binding energy in Eq (2.46). An adjacent work which does explicitly include trapping in the context of a phase field model of hydrogen embrittlement can be found in [81]. An small introduction to models for microstructural trapping is given here for completeness.

To account for microstructural trapping, a core idea is that the concentration of hydrogen is additively subdivided into hydrogen stored in normal interstitial lattice sites (NILS) and hydrogen stores in extraordinary sites or traps, often denoted C_L and C_T, respectively. The transport equation Eq. (2.34) for this system is then

$$\dot{C}_L + \dot{C}_T + \nabla \cdot \mathbf{J} = 0 \tag{2.39}$$

where the flux $\mathbf{J}$ is unaffected by the trapped hydrogen concentration and still follows Eq. (2.38) with only the lattice concentration, rather than the total one. How the hydrogen is divided between these two populations is dependent on the density of NILS and traps, denoted N_L and N_T. The local occupancy is thus defined as

$$\theta_L = \frac{C_L}{N_L}, \qquad \theta_T = \frac{C_T}{N_T}, \tag{2.40}$$

respectively. There are two main approaches to modeling hydrogen transport influenced by microstructural traps. First is the approach by Oriani [7] which is based on a balance law between hydrogen occupancy in traps and in NILS given by

$$\frac{1-\theta_L}{\theta_L}\frac{\theta_T}{1-\theta_T} = K_e, \tag{2.41}$$

where K_e is an equilibrium constant. Enforcing such a balance, along with enforcing the density of trapping sites as a function of plastic strain provides an easy-to-implement model.

The most prominent alternate approach is that of Mcnabb and Foster [82]. Instead of having balance law, the change in trapped hydrogen concentration $\dot{C}_T$ is given by an additional differential equation:

$$\dot{C}_T = k\frac{N_T}{N_L}C_L\left(1-\theta_L\right) - pC_T \tag{2.42}$$

where k and p are material constants. As a consequence of additional effort associated with this approach, it has not seen much use in modern coupled models for hydrogen assisted cracking. One recent example, however, may be found in [83].

2.2.3 Hydrogen-assisted fracture

As already presented in section 1.2, the underlying mechanism of hydrogen assisted fracture, even when narrowed down specifically to high-strength steel, is not a topic with an established consensus. The model utilized in publications [P3-P5] can be categorized as strictly relying on an hydrogen-enhanced decohesion (HEDE) model. As a phenomenological approach, the fracture toughness G_c from the phase field fracture law is introduced as a function of local hydrogen concentration;

$$G_c(C) = G_{c,0}f_c(C). \tag{2.43}$$

Here, $G_{c,0}$ is the nominal fracture toughness in an inert environment and $f_c(C)$ is some function of the local hydrogen concentration. This approach allows the introduction of a long line of phenomenological laws to mimic different observed behaviours. The idea of coupling fracture toughness and hydrogen concentration is not a new one and was used in the context of cohesive zone models, such as in the work of Serebrinsky and colleagues [84] in 2004. The approach by Serebrinsky was adapted for phase field in [56] and subsequently in publications [P3-P5]. The specific degradation law relies on numerical results obtained from density functional theory (DFT), performed by Jiang and Carter [16]. The DFT results show a correlation between the surface energy γ_s on a given lattice plane and the occupancy of hydrogen on that plane θ_p. In non-dissipative materials, the fracture toughness is exactly equal to two times the surface energy,

$$G_c = 2\gamma_s. \tag{2.44}$$

As a result, under the assumption that fracture happens along a given lattice plane, such as the [1,1,0] plane in the iron lattice, the fracture toughness can be directly related to the

hydrogen occupancy. In addition to the data by Jiang and Carter, which provides data for iron and aluminium, results for Nickel, which is usually presumed to display fracture mechanisms in the presence of hydrogen similar to those of iron, is available in [85]. In iron and aluminium, the relation between hydrogen occupancy θ_p and surface energy γ_s can be reasonably approximated by a simple linear relation on the form

$$\gamma_s(\theta_p) = (1 - \chi\theta_p)\,\gamma_{s,0}, \tag{2.45}$$

where $\gamma_{s,0}$ is the base surface energy in the absence of hydrogen. The original results by Jiang and Carter along with such linear fits can be seen in figure 2.4.

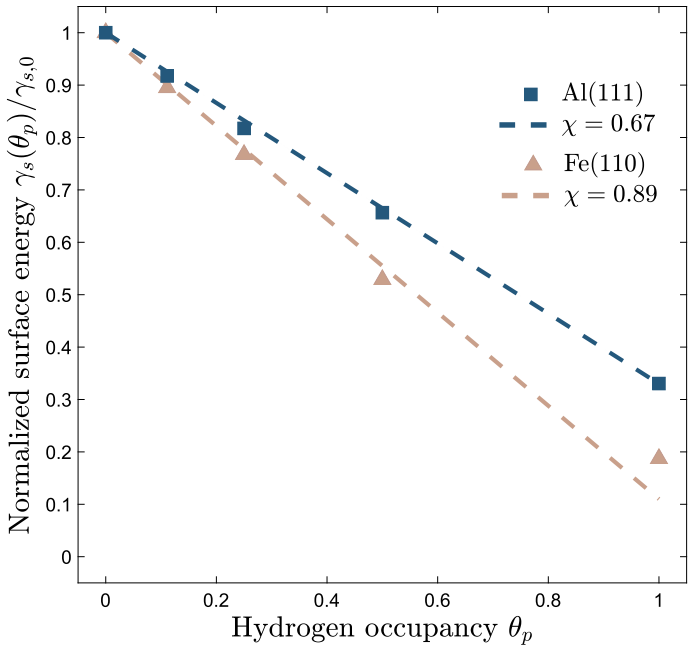

Figure 2.4: Surface energy in the (111) lattice plabe of aluminium and (110) plane of iron at different surface occupancies of hydrogen as computed using DFT methods in [16] and linear fits to the data as given by Eq. (2.45).

Consequently, the dependency of fracture toughness on hydrogen occupancy can, by introducing the linear fits Eq. (2.45) into Eq. (2.43). One final aspect not yet discussed is the relation between bulk hydrogen concentration C and hydrogen occupancy in a given lattice plane θ_p. This relation is accomplished using the Langmuir-McLean isotherm as proposed in [84].

$$\theta_p = \frac{C}{C + \exp\left(-\Delta g_b^0 / \mathcal{R}T\right)} \tag{2.46}$$

Here, Δg_b^0 is the difference in Gibbs free energy between the given lattice plane and the standard state in the lattice. As a default, a value of $\Delta g_b^0 = 30$kJ/mol is used based on a recommendation of this value for AISI 4340 high strength steel in [84].

The models presented in this thesis, which are based on [56], are not the only phase field models for hydrogen embrittlement found in the literature. At a similar time, a phase field model for elastic-plastic solids experiencing brittle fracture under the influence of hydrogen was implemented by Duda *et al.* [55], which also relied on the work of Serebrinsky [84] for the embrittlement law. In 2019, a phenomenological model was proposed by Anand and colleagues [57] for elastic-plastic materials where hydrogen causes an additional inelastic strain. A final work of note in the field of phase field models for hydrogen-assisted

fracture is recent the work of Cui *et al.* [86] which incorporates two interacting phase fields in an elastic-plastic material. One phase field handles hydrogen-assisted brittle fracture in a similar way to the current work, while the other field handles stress-assisted anodic dissolution. This model is the first to incorporate the effect and interplay of multiple environmental failure modes in a phase field setting.

2.3 Strain gradient plasticity

Specifically for [P5], strain gradient plasticity (SGP) is also a critical component of the model. Conventional plasticity theories fail to account for size effects such as those observed in the wire torsion experiment by Fleck *et al.* [87] and the bending experiments by Stölken and Evans [88]. Both experiments revealed that smaller specimens are stronger relative to their size than their larger counterparts, contrary to what would be expected from, for example, conventional J2 plasticity. These size effects have been found to stem from plastic strain gradients. Effectively, large gradients of plastic strain require a set of geometrically necessary dislocations (GND) in the lattice. These GNDs contribute to hardening alongside the ordinary statistically stored dislocations (SSD), which ultimately leads to increased stresses. The implementation in [P5] relies entirely on the higher order model by Gudmundson [58], for the purpose of determining accurate crack tip stresses in elastic-plastic materials, such that hydrogen concentrations can also be accurately predicted.

2.3.1 Principle of virtual work

We once again consider a solid occupying the volume Ω. The solid has a displacement field $\mathbf{u}$ and the symmetric gradient of this field is the strain tensor $\boldsymbol{\varepsilon}$, as in Eq. (2.9). The strain is additively decomposed into elastic strains $\boldsymbol{\varepsilon}^e$ and plastic strains $\boldsymbol{\varepsilon}^p$

$$\boldsymbol{\varepsilon} = \boldsymbol{\varepsilon}^e + \boldsymbol{\varepsilon}^p. \tag{2.47}$$

The plastic strain and its gradient $\nabla\boldsymbol{\varepsilon}^p$ are both considered primal variables with their own respective work conjugate stresses $\mathbf{q}$ and $\boldsymbol{\tau}$. The internal virtual work is then given by

$$\mathcal{W} = \int_\Omega \left[\boldsymbol{\sigma} : \delta\boldsymbol{\varepsilon}^e + \mathbf{q} : \delta\boldsymbol{\varepsilon}^p + \boldsymbol{\tau} \vdots \delta\nabla\boldsymbol{\varepsilon}^p\right] \mathrm{d}V, \tag{2.48}$$

where three stacked dots denote a triple inner product, i.e. a product over all indices of the two third order tensors $\boldsymbol{\tau} \vdots \nabla\boldsymbol{\varepsilon}^p = \tau_{ijk}\varepsilon^p_{ij,k}$.
A corresponding external virtual work is formulated with the traction $\mathbf{T}$, which was also present in the case of linear elasticity, and a higher order traction $\boldsymbol{t}$

$$\mathcal{U} = \int_{\partial\Omega} \left[\mathbf{T} \cdot \delta\mathbf{u} + \boldsymbol{t} : \delta\boldsymbol{\varepsilon}^p\right] \mathrm{d}S. \tag{2.49}$$

The strong form of the balance equations for the strain gradient plasticity problem can be derived from Eq. (2.48) as

$$\nabla \cdot \boldsymbol{\sigma} = 0, \tag{2.50}$$

$$\nabla \cdot \boldsymbol{\tau} + \boldsymbol{\sigma}' - \mathbf{q} = 0. \tag{2.51}$$

In the above, $\boldsymbol{\sigma}'$ denotes the deviatoric stress and in the absence of higher order stresses $\boldsymbol{\tau}$, the strong form is equal to that of conventional J2 plasticity. The accompanying boundary conditions are

$$\mathbf{T} = \boldsymbol{\sigma} \cdot \mathbf{n}, \tag{2.52}$$

$$\boldsymbol{t} = \boldsymbol{\tau} \cdot \mathbf{n}. \tag{2.53}$$

note that the higher order traction $\boldsymbol{t}$ is a second order tensor.

2.3.2 Constitutive equations

An important part of defining this higher order strain gradient plasticity model is the constitutive relations. This section is only here for completeness. A more comprehensive description of the constitutive derivation for this strain gradient plasticity model can be found in [89]. Here, a pivotal step is the additive partitioning of the microstress $\mathbf{q}$ and the higher order stress $\boldsymbol{\tau}$ into an energetic and a dissipative part:

$$\mathbf{q} = \mathbf{q}^E + \mathbf{q}^D \tag{2.54}$$

$$\boldsymbol{\tau} = \boldsymbol{\tau}^E + \boldsymbol{\tau}^D. \tag{2.55}$$

The microstress is here assumed purely dissipative, however, such that $\mathbf{q} = \mathbf{q}^D$. Here, we follow [58] and [89] in defining an effective plastic flow rate $\dot{E}^p$ and work conjugate effective stress Σ:

$$\dot{E}^p = \sqrt{\frac{2}{3}\dot{\boldsymbol{\varepsilon}} : \dot{\boldsymbol{\varepsilon}} + L_D^2 \nabla\dot{\boldsymbol{\varepsilon}}^p \vdots \nabla\dot{\boldsymbol{\varepsilon}}^p} \tag{2.56}$$

$$\Sigma = \sqrt{\frac{2}{3}\mathbf{q} : \mathbf{q} + L_D^{-2}\boldsymbol{\tau}^D \vdots \boldsymbol{\tau}^D} \tag{2.57}$$

where L_D is a dissipative length scale parameter. From these equivalent quantities, the dissipative stresses become

$$\mathbf{q} = \frac{2}{3}\frac{\Sigma}{\dot{E}^p}\dot{\boldsymbol{\varepsilon}}^p \tag{2.58}$$

$$\boldsymbol{\tau}^D = L_D^2 \frac{\Sigma}{\dot{E}^p}\nabla\dot{\boldsymbol{\varepsilon}}^p \tag{2.59}$$

and the energetic higher order stress is defined as

$$\boldsymbol{\tau}^E = QL_E^2 \nabla\boldsymbol{\varepsilon}^p. \tag{2.60}$$

Here, L_E is an energetic length scale and Q denotes the shear modulus. The flow stress σ_F of the material is assumed to follow a power law hardening of the form

$$\sigma_F = \sigma_y \left(1 + \frac{E^p}{\varepsilon_y}\right)^N, \tag{2.61}$$

where σ_y is the initial yield stress, N is the hardening exponent and $\varepsilon_y = \sigma_y/E$ is the initial yield strain. It is important to note that none of the plastic stresses contribute to the evolution of the phase field in [P5]. The model is therefore still strictly a model for brittle fracture.

3 | Numerical Implementation

This chapter details the implementation of the models from chapter 2 in a finite element framework. All of the models have been implemented in the commercial finite element software Abaqus, by means of so-called UEL subroutines, which allow the user to program custom finite elements using either FORTRAN or C. Additionally, an implementation has been made in Julia using the open source finite element package Ferrite.jl. This implementation has not seen published use yet, but it is a promising tool for the topics discussed in section 3.3. The majority of the codes have been made publicly available, such that other researchers may benefit from them and advance the field. Especially the code from [P1] has gathered particular interest and it was deemed one of the most efficient and reliable open source phase field codes for Abaqus in [90].
This chapter contains details regarding the discretization and couplings of the models from the previous chapter in section 3.1. Section 3.2 contains additional considerations for the phase field regarding the enforcement of irreversibility and solution strategies. Finally, section 3.3 contains details regarding ongoing work for accelerating fatigue computations.
Details regarding the implementation of the strain gradient plasticity modeling the framework of a viscoplastic law may be found in [89] and publication [P5].

3.1 Discretization

For completeness, the discretization of the full model including all the main components of chapter 2, as it is used in publication [P5] is presented. All other publications [P1-P4] do not include the plasticity field and in the case of [P1-P2], the hydrogen model is also not included. In the full model, the primal variables are the displacement field $\mathbf{u}$, the plastic strains ε^p, the phase field variable ϕ and the hydrogen concentration field C. The weak form of the full system may be obtained from equations (2.50), (2.51), (2.16) and (2.34) by the standard method of introducing trial functions and integrating with the use of the divergence theorem, after which the boundary condition of the strong form equations are applied.

$$\int_\Omega \left[\boldsymbol{\sigma} : \delta\boldsymbol{\varepsilon}^e + \mathbf{q} : \delta\boldsymbol{\varepsilon}^p + \boldsymbol{\tau} \vdots \delta\nabla\boldsymbol{\varepsilon}^p \right] \mathrm{d}V - \int_{\partial\Omega} \left[\mathbf{T} \cdot \delta\mathbf{u} + \boldsymbol{t} : \delta\boldsymbol{\varepsilon}^p \right] \mathrm{d}S = 0 \tag{3.1}$$

$$\int_\Omega \left[-2(1-\phi)\psi\delta\phi + G_c \left(\frac{\phi\delta\phi}{\ell} + \nabla\phi \cdot \delta\nabla\phi \right) \right] \mathrm{d}V - \int G_c \ell \Phi \delta\phi \, \mathrm{d}S = 0 \tag{3.2}$$

$$\int_\Omega \left[\frac{1}{D}\dot{C} + \nabla C \cdot \delta\nabla C - \frac{\bar{V}_H C}{\mathcal{R}T} \nabla\boldsymbol{\sigma}_H \cdot \delta\nabla C \right] \mathrm{d}V + \frac{1}{D} \int_{\partial\Omega} \rho\delta C \, \mathrm{d}S = 0 \tag{3.3}$$

The primal variables are discretized using standard Lagrange shape functions. Details can be found in publication [P5], along with explicit description of the residuals and stiffness matrices. The residuals for each field are restated here, with special attention to terms that have been dropped from the formulation. Note that stresses and strains are here given as matrices in Voigt notation. Matrices of shape functions are denoted $\boldsymbol{N}$ and their derivatives $\boldsymbol{B}$.

Displacement problem
The residual for the displacement problem is given by:

$$\mathbf{R}_\mathbf{u} = \int_\Omega \left[\boldsymbol{B}_u^T \boldsymbol{\sigma} \right] \mathrm{d}V - \int_{\partial\Omega} \boldsymbol{N}_u^T \mathbf{T} \, \mathrm{d}S \tag{3.4}$$

Here, the Cauchy stress σ is given by

$$\boldsymbol{\sigma} = (1-\phi)^2 \boldsymbol{\mathcal{L}}_0 : \boldsymbol{\varepsilon}^e \tag{3.5}$$

rather than the thermodynamically consistent

$$\boldsymbol{\sigma} = (1-\phi)^2 \boldsymbol{\mathcal{L}}_0 : \boldsymbol{\varepsilon}^e - K_b \bar{V}_H (C - C_0)\boldsymbol{I}, \tag{3.6}$$

where K_b is the bulk modulus and $\boldsymbol{I}$ is the identity tensor. The chemo-elastic term is omitted on the assumption that hydrogen atoms only induce negligible dilatant strains in the lattice.

Plasticity problem
The residual of the plasticity problem is given by

$$\mathbf{R}_{\boldsymbol{\varepsilon}^p} = \int_\Omega \left[\left(\boldsymbol{N}_{\boldsymbol{\varepsilon}^p}\right)^T (\boldsymbol{q} - \boldsymbol{\sigma}) + \left(\boldsymbol{B}_{\boldsymbol{\varepsilon}^p}\right)^T \boldsymbol{\tau} \right] \mathrm{d}V - \int_{\partial\Omega} \left[\left(\boldsymbol{N}_{\boldsymbol{\varepsilon}^p}\right)^T \boldsymbol{t} \right] \mathrm{d}S. \tag{3.7}$$

While this residual remains fully thermodynamically consistent with all of its terms preserved, it is worth noting that it is far less strongly coupled to the hydrogen problem than some literature would suggest. Along with the influence of plasticity on microstructural trapping as discussed in section 2.2.2, the influence of hydrogen on plastic flow is in some cases considered an important part of hydrogen-assisted fracture as for example in the HELP mechanism which was introduced in section 1.2.

Phase field fracture problem
The residual for the phase field fracture problem is given by:

$$R_\phi = \int_\Omega \left\{ -2\left(1-\phi\right) N\mathcal{H} + G_c(C) \left[\frac{\phi}{\ell} N + \ell \left(\mathbf{B}\right)^T \nabla\phi \right] \right\} \mathrm{d}V. \tag{3.8}$$

Where $\mathcal{H}$ is a history variable of the maximum strain energy in the loading history, see section 3.2.1. This residual also does not have any terms that have been removed from the formulation. It should however be noted that depending on the context, it may be the `AT1` formulation instead and/or the fatigue degradation function $f_\alpha(\bar{\alpha})$ might be included. In addition, the hydrogen dependence of the fracture toughness is omitted in contexts not specific to hydrogen-assisted fracture or fatigue. Finally, the plasticity problem is not coupled directly to the phase field problem, which remains a balance between elastic strain energy and surface energy. This effectively means that the full model is only applicable to brittle fracture in elastic-plastic materials.

Hydrogen transport model
The residual for the hydrogen transport problem is given by

$$R_C = \int_\Omega \left[N\left(\frac{1}{D}\dot{C}\right) + \mathbf{B}^T \nabla C - \mathbf{B}^T \left(\frac{\bar{V}_H C}{\mathcal{R}T} \nabla \sigma_H \right) \right] \mathrm{d}V + \frac{1}{D} \int_{\partial\Omega_\rho} N\rho \, \mathrm{d}S. \tag{3.9}$$

This residual omits a rather complicated term. From a thermodynamic perspective; the chemical potential should include the partial derivative of the crack surface density function γ, from Eq. (2.5), with respect to the hydrogen concentration C, which would be non-zero as the fracture toughness is dependent on the local hydrogen concentration. The term is complicated and introduces a coupling between the two fields, which may

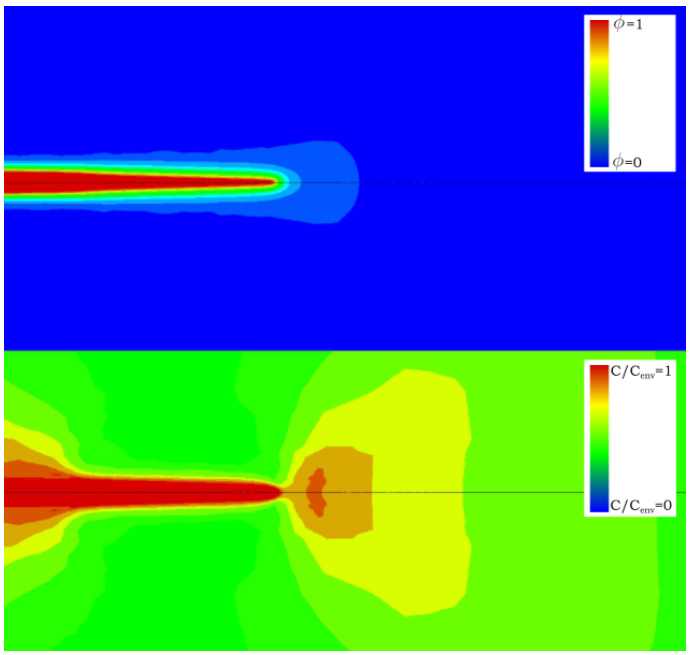

Figure 3.1: *Moving* chemical boundary conditions with a propagating crack, contours of phase field damage (top) and hydrogen concentration (bottom). From publication [P5].

not be desirable. The physics which should be captured near fracture surface has two main aspects. First, hydrogen tends to fully occupy surface sites, as the free energy in these sites is lower that in the lattice [91]. This effectively means that hydrogen should be present on the surface, either supplied by the environment or the lattice. Secondly, for cracks in the outer surface, the new crack surface may be expected to immediately contact the outside environment, which would then act as a hydrogen source if the environment is hydrogenous. To capture this phenomenon, a moving Dirichlet boundary condition implemented using the penalty method is introduced to the hydrogen transport problem. The following term is added to the residual

$$\int_{\Omega} k_p N (C - C_{env}) \langle 2\phi - 1 \rangle_+ \tag{3.10}$$

where k_p is the penalty factor, C_{env} is the hydrogen concentration of the environment and $\langle \bullet \rangle$ are Macaulay brackets. An example of the boundary condition acting near a crack in tension can be seen in figure 3.1. For numerical stability, the boundary condition is weakly enforced once the phase field exceeds $\phi = 0.5$ and the effective penalty factor increases up until the crack is fully formed.

Care should be taken with the above, as it contains no way of discerning contact to the outside environment, such that internal cracks may act as unphysical hydrogen sources as objected in currently unpublished work. A more advanced approach to hydrogen boundary conditions may be found in [83].

3.2 Considerations for phase field models

Implementation of the phase field equations has been the subject of much literature for a variety of reasons. At its core, the phase field fracture model presents a constrained non-convex optimization problem with a need for fine discretization. All of these factors contribute to make accurate, efficient and robust solution of the problem difficult and computationally demanding. This section aims to provide discussion on each of these issues and highlight the approaches used across the publications of this thesis.

3.2.1 Irreversibility of the phase field

The phase field is subject to a number of constraints. The most fundamental one is that ϕ is bounded between 0 and 1:

$$0 \leq \phi \leq 1. \tag{3.11}$$

In practice, however, some of these bounds can be handled implicitly. In the `AT2` phase field model, both the upper and lower bounds are naturally enforced, as no value of the elastic strain energy ψ can require the phase field to exit its bounds to obtain equilibrium. In the case of the `AT1` model, however, the lower bound is not enforced and the phase field will tend towards large negative values at small or zero loads, as seen in Eq. (2.22). The method of enforcing this is often closely related to the choice in enforcing the irreversibility of the phase field. Outside of specialized applications such as elastomers [47], cracks are rarely permitted to heal. In the phase field model, this can broadly be handled in two ways: The most common is strict irreversibility, such that

$$\dot{\phi} \geq 0, \tag{3.12}$$

which corresponds to the interpretation that intermediate values of the phase field imply damage, which does not heal. Alternatively, one might enforce that the phase field is only irreversible if it is (sufficiently close to) fully broken [24]. The latter implies that intermediate values of the phase field is a numerical tool or a measure of "cracking potential". It is an equally valid method for handling irreversibility from a mathematical standpoint and is variationally consistent. To handle the irreversibility of the phase field, it was suggested by Miehe and co-workers to introduce a history variable $\mathcal{H}$ to the phase field problem such that [26]

$$\mathcal{H}(t) = \max_{\tau \in [0,t]} \psi_0(\tau). \tag{3.13}$$

This approach has been immensely popular as it significantly simplifies the implementation and is easy to do in a wide range of commercial and open-source finite element packages. However, use of the history variable has also been criticised. The primary criticism lies in the fact that the use of this history variable breaks the variational consistency of the phase field model. The variational nature of the model is often considered one of the most attractive features of phase field. The use of non-variational phase field models is widespread, however, and generally seem to produce results in agreement with experimental findings and expectations. Another criticism of the history variable approach is an issue which occurs when phase field cracks initiate from non-sharp defects. In this case, the use of the history variable causes a widening of the crack in the initiation region which is not energetically optimal. Notable examples of this criticism may be found in [35] and [92]. An often used remedy for this latter issue is to only enforce the history variable when the crack is sufficiently well-developed [35], which circumvents this specific issue. In this case, the history variable is given as

$$\mathcal{H} = \begin{cases} \psi_0 & \text{if } \phi < \phi_t \\ \max\limits_{\tau \in [0,t]} \psi_0(\tau). & \text{else.} \end{cases} \tag{3.14}$$

where ϕ_t is a threshold value often chosen somewhere between 0.85 and 0.95. The original history variable formulation by Miehe and co-worders [26] is used throughout the publications of this thesis. However, with very few exceptions, the problems considered in these concern crack initiation from an initially sharp defects, where the issue is not as widespread.

As previously mentioned, the AT1 phase field model does not implicitly enforce the lower

bound on the phase field variable. A common strategy [93] for enforcing this lower bound is to introduce a minimum value for the history field $\mathcal{H}_{min}$, which corresponds exactly to the homogeneous 1D solution for $\phi = 0$ such that the history field is now given by

$$\mathcal{H}(t) = \max\left(\max_{\tau\in[0,t]} \psi_0(\tau),\, \mathcal{H}_{min}\right), \tag{3.15}$$

with

$$\mathcal{H}_{min} = \frac{1}{2}\sigma_c\varepsilon_c. \tag{3.16}$$

Here, σ_c is the critical stress given by (2.24) while $\varepsilon_c = \frac{1}{E}\sigma_c$ is the critical strain. Recently, however, Molnár and colleagues [76] showed that this minimum value may in some cases lead to an underestimation of the toughness of the specimen and proposed instead a scheme using Lagrange multipliers which was implemented in Abaqus to enforce boundedness and irreversibility on the phase field.
Other strategies for enforcing both irreversibility and boundedness may be found in [94], where a penalty method approach was introduced such that the following term was added to the weak form:

$$\int_\Omega \frac{\gamma_p}{2} \langle \phi - \phi_n \rangle_-^2 \, \mathrm{d}V. \tag{3.17}$$

where ϕ_n denoted the value of the phase field from the previous timestep and γ_p is a penalty factor recommended to be set as

$$\gamma_p = \begin{cases} \dfrac{27G_c}{64\ell \texttt{TOL}^2} & \text{if } \texttt{AT1} \\ \dfrac{G_c}{\ell}\left(\dfrac{1}{\texttt{TOL}^2} - 1\right) & \text{if } \texttt{AT2} \end{cases} \tag{3.18}$$

the enforcement tolerance, `TOL`, is recommended to be set at 0.01 [94]. The penalty method can be used both for strict irreversibility or for irreversibility of fully formed cracks with minor modification. The same is true for the active set method [95] and the interior point method, which are not discussed here. For irreversibility of a fully formed crack, the so-called crack set method [24] may also be used, where sufficiently damaged nodes are added to a set subject to a $\phi = 1$ Dirichlet condition.

3.2.2 Solution strategies

As already mentioned in section 2.1.3, computational performance is a very significant topic in the phase field literature. In the context of phase field fracture models, solution strategies are usually subdivided into *monolithic* and *staggered* schemes.

Monolithic strategies

Monolithic schemes refer to solution schemes where the fully coupled problem is solved for all solution variables simultaneously as is typically done in coupled problems. The issue these typically face is that as previously mentioned, the coupled displacement-damage problem is non-convex and for a *standard Newton-Raphson* solution scheme convergence is not guaranteed. Several remedies have been proposed in the literature, including specialized *line search methods* [96, 97], *local dissipation-based path following solvers* [98], and the *Schwarz preconditioned inexact Newton's method* [99]. A monolithic solution strategy of special interest in this thesis is the *quasi-Newton method* using the *Broyden-Fletcher-Goldfarb-Shannon* (BFGS) algorithm. Following the suggestion from [100], a study was performed in publication [P1] to determine the efficiency and robustness of the BFGS algorithm, relative to a staggered approach. Some of the results are

summarized in section 4.1.1. The BFGS algorithm was subsequently used in publication [P2] and parts of [P4]. To provide some brief context, the BFGS algorithm takes an initial guess for the tangent stiffness matrix and updates it on an as-needed basis within a given increment using an approximate method which conserves positive definiteness and symmetry. Furthermore, in the cases of a symmetric stiffness matrix, the approximate update can be applied directly to the inverted system matrix. In this thesis, the initial guess for the stiffness matrix is taken to be

$$\boldsymbol{K}_0 = \begin{bmatrix} \boldsymbol{K}_{uu} & 0 \\ 0 & \boldsymbol{K}_{\phi\phi} \end{bmatrix}, \tag{3.19}$$

neglecting the coupling terms $\boldsymbol{K}_{\phi u}$ and $\boldsymbol{K}_{u\phi}$. According to Wu *et al.* [36], including the coupling terms would introduce a better convergence rate for highly non-linear problems, but depending on the choice of strain decomposition and its implementation (see section 2.1.3) the positive definiteness of the initial stiffness matrix is not guaranteed and may cause the solution to diverge. A specialized numerical parameter for robustly ensuring positive definiteness when the coupling terms are included is introduced in [36], but an analysis is not performed to determine the increase in numerical performance. As a final note on the BFGS algorithm, the requirement that the initial guess for the tangent stiffness matrix is symmetric prohibits its use when the hydrogen problem is included, as this generally introduces an asymmetric stiffness matrix.

Staggered solution schemes

In the context of phase field fracture modeling, *staggered solution schemes* refer to solution strategies where the deformation and damage sub-problems are solved separately while keeping the other variable constant. The main advantage of these stems from the fact that while the coupled problem is non-convex, each of the subproblems are individually convex. In fact, in some cases each of the subpoblems can be expected to converge in a single iteration. The simplest staggered solution scheme is the so-called *single-pass scheme* introduced in [26]. Here, each sub-problem is solved once, with either the displacement field being solved using the phase field variable from the previous increment, followed by the phase field problem solved using the updated displacement or vice versa. This effectively means that a sensitivity to increment size is introduced and very small increments are necessary to approach the increment-insensitive limit. The advantage, however, is that the approach is extremely robust and will always yield a solution.
To circumvent this sensitivity to increment size, so-called *multi-pass algorithms* have been proposed, where values of the opposing field is taken from the previous iteration rather than increment. To highlight the difference between one-pass and multi-pass schemes, a flowchart is provided in figure 3.2. If an appropriate criterion is chosen for when to stop iterating between the two fields is chosen, the solution will be insensitive to increment size, although many iterations may be required for an increment which contains significant crack growth. Examples of such stopping criteria include the energy-based criterion by Ambati and co-workers found in [67] and the residual based approach implemented in Abaqus by Seleš and coworkers in [101]. The latter approach was used in publication [P3], as increment insensitivity was shown to be very influential in fatigue analyses in section 4.2.1 and the unsymmetrical stiffness matrix of the hydrogen transport problem prohibited the use of the BFGS algorithm. A one-pass staggered algorithm was used in [P5]. A special class of staggered schemes is the so-called *quasi-monolithic schemes* found for example in [77]. Here the idea is to solve the deformation sub-problem using an extrapolated value of the phase field and also including the coupling term $\mathbf{K}_{u\phi}$ in the stiffness matrix, while still neglecting the opposing coupling term. While these may in

some cases have excellent convergence, they have been shown to sometimes yield inaccurate results [102]. A correction to ensure the accuracy of the quasi-monolithic results was proposed in [97].

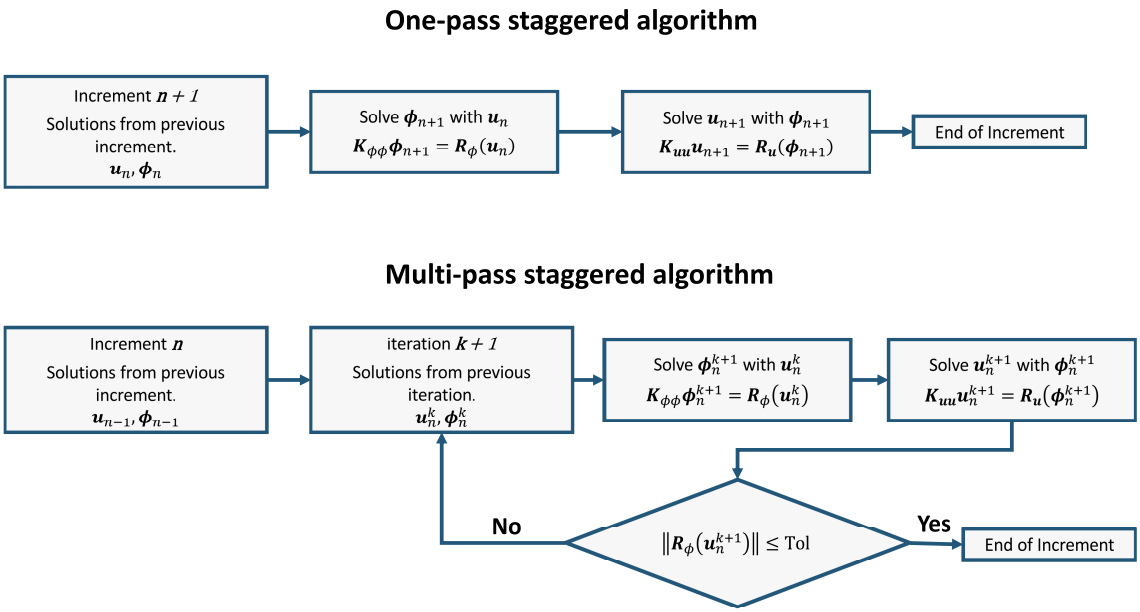

Figure 3.2: Flowchart of one-pass and multi-pass staggered algorithms. Note that these may also appear where the displacement problem is solved first.

3.3 Acceleration of fatigue calculations

Solution of the phase field problem is often computationally expensive, both due to the difficulties in solving the system, but also due to the requirements on the discretization imposed by the phase field. While improvements in computational performance is already of great interest in the phase field community, it is even more critical in the context of cycle-by-cycle phase field fatigue models. As one or more increments are required for each cycle and the number of cycles of interest in a fatigue context is often very large, the system must be solved a very large number of times. As a result, any improvement in computation speed is of great interest. Efforts in this area can generally be subdivided into three categories: i) Efforts to ease the need for fine discretization, as discussed in section 2.1.3. ii) Efforts towards faster solution strategies for the phase field, as discussed in section 3.2.2 and finally, iii) efforts to skip the calculation of some fatigue cycles using so-called cycle jump strategies. Here, only the latter is specific to fatigue, while the others are of general interest.

Efforts to speed of fatigue calculations, especially for high-cycle fatigue, have been the subject of much work behind this thesis, although none has reached a published stage. This section seeks to introduce some of that ongoing work.

3.3.1 Acceleration by specialization of the solution strategy

A distinct feature of high-cycle fatigue where extensive crack growth might take millions of cycles is the fact that very little happens during the individual cycle. The change in the accumulated fatigue history field is small and consequently the change in the phase field is small. One way to utilize this that is currently being investigated is to avoid updating the tangent stiffness matrix more often than needed. The strategy is implemented in the context of a multi-pass staggered algorithm based on [101]. The tangent stiffness

matrix is updated only if an increment is experiencing issues with convergence or if a large number of cycles have passed without such an update occurring. The tangent stiffness matrix is stored in a factorized version between increments, such that the solution of the sub-problems requires no factorization or matrix inversion which is normally the most time-consuming aspect of a finite element solution. A flowchart of the solution strategy as it is in the Julia implementation shown in figure 3.3. A similar strategy for Abaqus does unfortunately not appear to be an option, as the global solution strategy is not accessible from user subroutines.

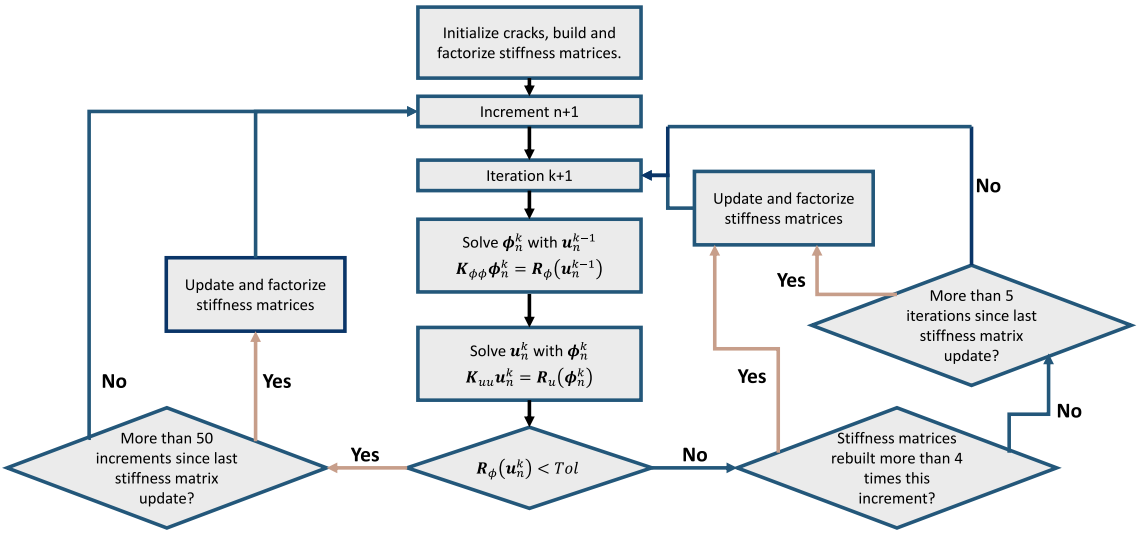

Figure 3.3: Flowchart of the specialized fatigue solution strategy. Stiffness matrices are only updated and factorized on an as-needed basis. The integer values shown in the decision boxes are examples for simplicity.

The load ratio R of a cyclic loading problem is typically defined as

$$R = \frac{K_{min}}{K_{max}}, \tag{3.20}$$

where K_{min} and K_{max} denote the minimum and maximum stress intensity factor experienced by the crack in a load cycle. If the problem is sufficiently simple, for example if $R \geq 0$ or if the loading stage from K_{min} to K_{max} is otherwise the only stage contributing to fatigue accumulation, the solution strategy can be simplified even further. If only the positive loading stage contributes to fatigue accumulation, a valid simplification is to keep the applied load constant at K_{max} and change the accumulation criterion from Eq. (2.32) to

$$\dot{\bar{\alpha}} = \alpha, \tag{3.21}$$

such that each time increment corresponds to a load cycle[1]. Not only does this lower the number of increments per cycle, it also reduces the effort of solving the displacement problem considerably, as only changes to the phase field are causing changes to the displacement field. This makes the solution scheme from figure 3.3 especially potent and the combination of these two approaches has the potential for very drastic reductions in computation times.

[1]Credit for this adjustment to the solution strategy should be attributed to Alireza Golahmar from the Technical University of Denmark

Furthermore, this latter simplification seems to eliminate an existing convergence issue that otherwise occurs in both the Julia and Abaqus implementations: At high cycles, often shortly after crack growth has begun, convergence seemingly becomes increasingly difficult in the standard formulation, ultimately leading to a complete loss of convergence. An as of yet untested alternative approach to tackle this issue is the use of the crack set method [24]. In the crack set method, nodes where the phase field exceed a threshold, for example $\phi \geq 0.95$, are added to a set of nodes which is subject to a $\phi = 1$ Dirichlet condition. If the phase field sub-problem is effectively no longer solved at the original crack tip, this may ease convergence issues in that area.

3.3.2 Cycle jumping

The idea of accelerating cycle-by-cycle fatigue calculations by extrapolating the solution to skip some cycles is neither new, nor unique to the phase field fracture model. Much effort has been dedicated to the development of accelerated high-cycle fatigue computations in the field of damage mechanics [103–105]. Early efforts within this thesis towards the acceleration of phase field fatigue focused on adapting the work of Cojocaru and Karlsson [106] for a phase field context. The simple scheme would be to locally extrapolate the accumulated fatigue variable $\bar{\alpha}$ based on its evolution over a number of cycles. However, a cycle jump scheme for phase field fatigue was first published by Loew *et al.* [75], which contained a scheme effectively identical to the ongoing efforts in this thesis, which were subsequently halted. As an alternative to acceleration schemes based on local extrapolation of internal variables, the option of extrapolation based on the macroscopic evolution of the crack was explored. The conceptual principle is illustrated in figure 3.4. Tracking the macroscopic crack evolution can be reduced to a relatively simple series of operations: i) An image of the crack must be constructed at different points in time. This could be a contour plot of the phase field or a simplified two-color image where the color of each point is determined by whether the phase field is above or below a given threshold. ii) Crack tips must be identified in each image. iii) Crack tips between subsequent images are paired to determine the growth direction and velocity of the crack. If several images are used, an acceleration can also be included.

Once the crack growth direction and velocity is known, this can be used as a basis for extrapolation. The two main challenges associated with this approach is the identification of an arbitrary number of crack tips and the extrapolation procedure.

Identifying an arbitrary number of crack tips is not trivial. However, the field of computational image analysis and computer vision does provide a number of potential options. Early efforts towards determining the direction and velocity of cracks relied on so-called optical flow as described by Horn and Schunck [107], which is an early technique for tracking movement in a series of images. The results obtained, did not, however, reliably yield useful results that accurately reflected the actual crack tip velocity. A simple but promising alternative was the Harris corner detection algorithm [108], which quite reliably identified crack tips on a simplified phase field image. The main disadvantage of the corner detection strategy is that it is restricted to identifying discrete points in the image corresponding to either nodes or Gauss points, depending on how the image is constructed. A more elegant approach to identifying crack tips without this restriction may be found in [21], where a combination of the ball-shrinking algorithm of Ma *et al.* [109] and the solution of a spanning tree problem is used to identify the center curves of a thick level set. This approach would allow the identification of center curves for a level set corresponding, for example, to the $\phi = 0.5$ contour, where the endpoints of said curves would designate crack tips.

The subsequent extrapolation of cracks is another pressing issue. The phase field crack

itself can relatively easily be extrapolated either using a Dirichlet condition or, less elegantly, prescribing a large value of the history value $\mathcal{H}$. However, if only the crack is extrapolated, the fatigue behavior is likely to revert to the initiation regime of the Paris curve, as the crack enters a region without the accumulation of fatigue experienced near a growing crack tip. To circumvent this issue, one option is to translate the crack tip fatigue field $\bar{\alpha}$ to the crack tip formed after extrapolation.

Cycle jumping based on macroscopic crack extension is an original approach to accelerating fatigue computations with potential for significant development. It does not conflict with other acceleration strategies as long as the response history that the extrapolation procedure is based on is representative of the future response, meaning that it could easily be used in conjunction with the acceleration scheme from Loew *et al.* [75] or the one described in section 3.3.1, which is especially suited for the initiation stage which this approach may not handle as well. Finally, an image-based approach to cycle jumping enables the use of many interesting techniques from computer vision and image analysis. Most prominently, predicting future crack extension from a series of images is a problem where machine learning techniques would be highly suitable.

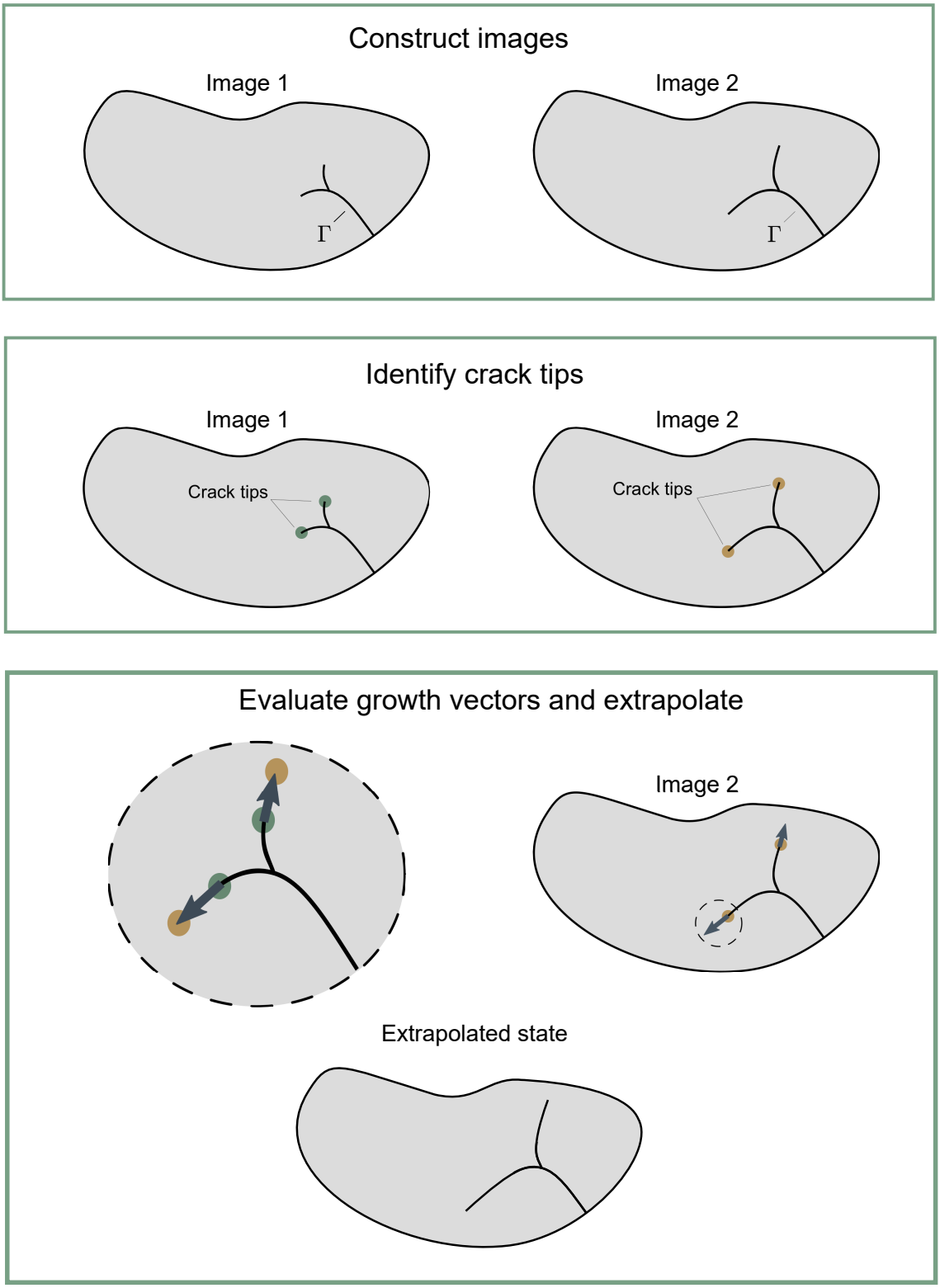

Figure 3.4: Sketch of the process of an image-based fatigue cycle jump strategy. Crack tips are identified in a series of images after which growth velocities and directions can be introduced and used to extrapolate the crack.

4 | Results

This chapter aims to summarize some the numerical experiments performed in connection with this thesis as well as the most important findings. Some unpublished work is included in section 4.1.3. The chapter is organised in four main sections. The first details fundamental investigations of the phase field fracture model. The second outlines results related to fatigue, especially in the presence of hydrogen. The third section demonstrates some applications of a phase field model for hydrogen assisted fracture on engineering components. The final section summarizes the results obtained with the full model including strain gradient plasticity.

4.1 Suitability of the phase field model

To assess the suitability of phase field models as a tool for predicting fracture in complex engineering structures, a number of behaviours is examined. First, the suitability of the quasi-Newton method as an efficient and robust solution strategy is examined in section 4.1.1, before it is subsequently used for examining crack initiation in section 4.1.2. Afterwards, the suitability of the phase field model for capturing stable crack growth is analysed in 4.1.3, including unpublished work which shows crack growth driven by external work. Finally, the ability to capture complex crack topologies is demonstrated using a dynamic crack branching problem in section 4.1.4.
All results in this section are computed for linear elastic materials in the absence of hydrogen, using the quasi-Newton method unless otherwise stated.

4.1.1 The quasi-Newton method

To demonstrate the efficiency and robustness of the quasi-Newton solution method, two simple fracture problems are examined and the performance is compared to the single-pass staggered algorithm (see section 3.2.2).

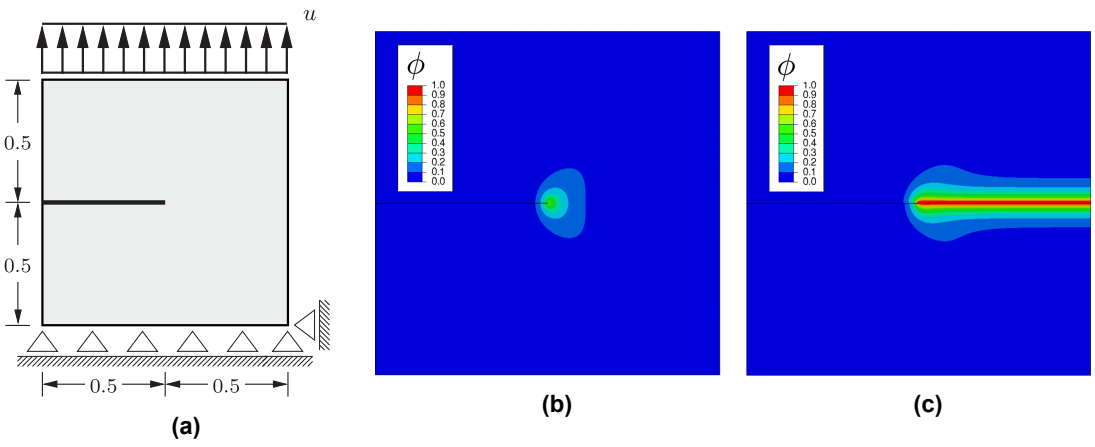

Figure 4.1: Single-edged notched tension specimen: (a) sketch of the problem with dimensions in mm. (b) and (c) contour plot of the phase field crack. the two figures are separated by a single very small load increment. From [P1].

The single-edge-notched tension problem

The first case study is the single-edge-notched tension (SENT) specimen. It is a standard benchmark problem in the phase field literature. The geometry is shown in figure 4.1a. One of the key features of this problem is the unstable nature of the crack growth, leading to a sudden drop in the force-displacement response, which may cause numerical difficulties in some cases. An example of the crack growth behavior can be found in figures 4.1b and 4.1c. It should be noted that a single very small time increment separates the two figures, demonstrating the robustness and implicit nature of the quasi-Newton scheme. The force-displacement response of the SENT specimen using the quasi-Newton scheme and the single-pass staggered algorithm can be found in figure 4.2a, where it is clear that a very high number of staggered increments is needed to closely capture the sudden drop in stiffness. In fact, 10^5 staggered increments are necessary to closely capture the monolithic response. Furthermore in figure 4.2b, the total cumulative number of iterations is shown, demonstrating that far less iterations are needed when a monolithic solution strategy is used. When comparing to the case of 10^5 staggered increments, roughly two orders of magnitude separate the required number of iterations.

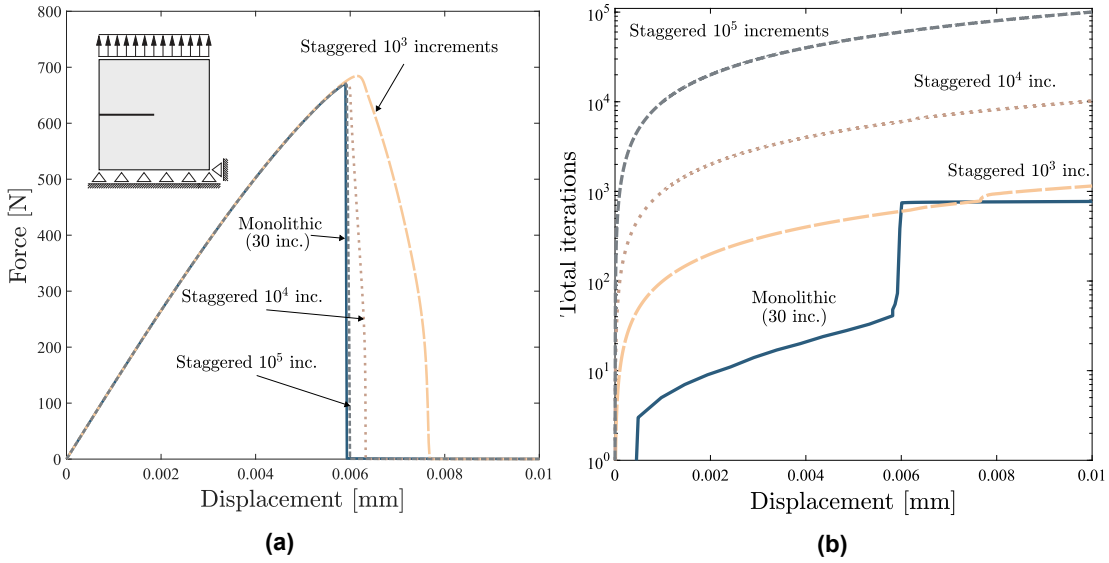

Figure 4.2: Comparison of the quasi-Newton and single-pass staggered solution strategy on the SENT specimen: (a) Force-displacement response. (b) cumulative number of iterations. Adapted from [P1].

	CPU hours			
Mesh size	$\ell/h_e = 6$ 25908 DOFs	$h_e/\ell = 9$ 47376 DOFs	$h_e/\ell = 12$ 74697 DOFs	$h_e/\ell = 18$ 152772 DOFs
Monolithic	0.31	0.80	1.79	3.41
Staggered	31.6	60.17	87.47	187.90

Table 4.1: Computation times for the SENT specimen at different problem sizes. results for the staggered algorithm are taken from the case with 10^5 staggered increments. From [P1].

The comparison is repeated across several mesh sizes to demonstrate that the computational gain is roughly independent of the problem size, at least when problems are large enough that the solution of the problem dominates the computation time. Computation times are given in table 4.1. When comparing to the case with 10^5 staggered increments,

which is needed to closely reproduce the monolithic response, a very large computational gain is observed, spanning a 50-100 times improvement.

Mixed-stability crack growth in a single-edge-notched shear specimen

The second case study involved a single-edge-notched shear (SENS) specimen. This problem involves two sections of unstable crack growth separated by a region of stable crack growth. This makes the problem more difficult from a numerical perspective and the region of stable crack growth might be expected to be less advantageous for the monolithic approach. The geometry and boundary conditions are sketched in figure 4.3a and the crack path is visualized in figure 4.3b.

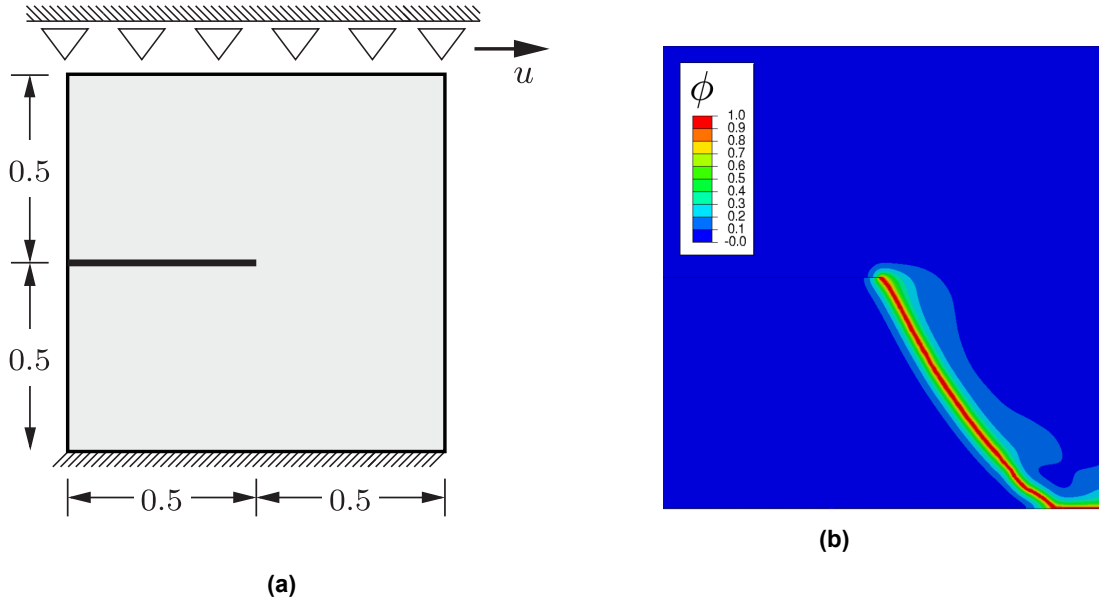

Figure 4.3: Single-edged notched shear specimen: (a) Sketch of the problem with dimensions in mm, and (b) contour plot of the phase field crack path. From [P1].

In order to produce a physical crack path, a strain split is needed as discussed in section 2.1.3. Here, the volumetric/deviatoric split from [25] is used with the hybrid implementation of [67]. The force-displacement response demonstrating the two sudden drops in stiffness can be found in figure 4.4a, computed using the quasi-Newton method and the single-pass staggered algorithm with differing numbers of staggered increments. Much like for the SENT specimen, a large number of staggered increments is needed to closely capture the monolithic response. If the final unstable stage of crack propagation must be captured accurately, the number of staggered increments must be on the order of 10^5. The total cumulative number of iterations is shown in figure 4.4b. Here we observe a difference in the total number of iterations between the monolithic and the most accurate staggered approach by a factor of roughly 30.
Computation times across varying problem times are shown in table 4.2. While the computational gain is not as dramatic as the ones reported for the SENT specimen, they still exceed a factor 10 in all cases and a factor 20 in all but one case.

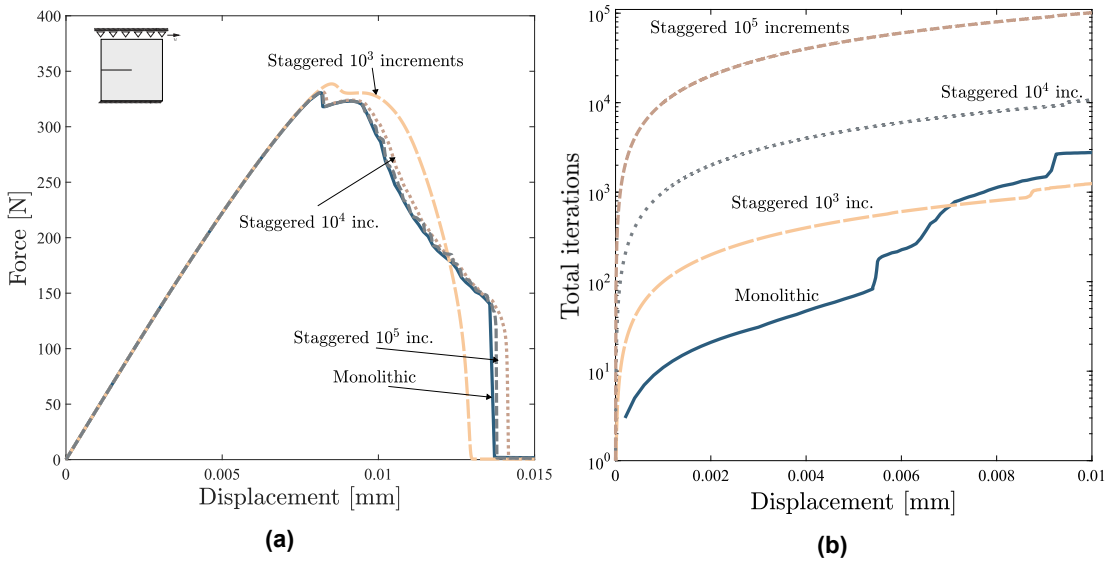

Figure 4.4: Comparison of the quasi-Newton and single-pass staggered solution strategy on the shear specimen: (a) Force-displacement response. (b) cumulative number of iterations. Adapted from [P1].

	CPU hours			
Mesh size	$\ell/h_e = 6$ 58518 DOFs	$h_e/\ell = 9$ 128451 DOFs	$h_e/\ell = 12$ 222111 DOFs	$h_e/\ell = 18$ 386112 DOFs
Monolithic	2.02	6.56	11.62	46.60
Staggered	74.85	159.50	272.25	469.48

Table 4.2: Computation times for the shear specimen at different problem sizes. results for the staggered algorithm are taken from the case with 10^5 staggered increments. From [P1].

In conclusion, the quasi-Newton method has been shown to yield robust and efficient solutions that significantly outperform the single-pass staggered algorithm if quantitative accuracy is desired.

4.1.2 Assessment of crack initiation using a modified boundary layer problem

As a next step, the agreement between the phase field model and classical linear elastic fracture mechanics for the initiation of crack growth is analysed. Both the `AT1` and `AT2` models are utilized, although the former has later been shown to suffer from a pathology related to the use of the history variable as a means to enforce the lower bound of the phase field, as was highlighted in [76]. The monolithic quasi-Newton method is used as the solution strategy and no strain split is introduced to differentiate between compression and tension (see section 2.1.3). The purpose of this analysis is to further examine the discrepancies in phase field results compared to linear elastic fracture mechanics which has been the subject of much previous work [29, 92, 110], especially in the context of crack nucleation from a sharp defect. The analysis here is performed using the so-called modified boundary layer problem, which is sketched in figure 4.5.

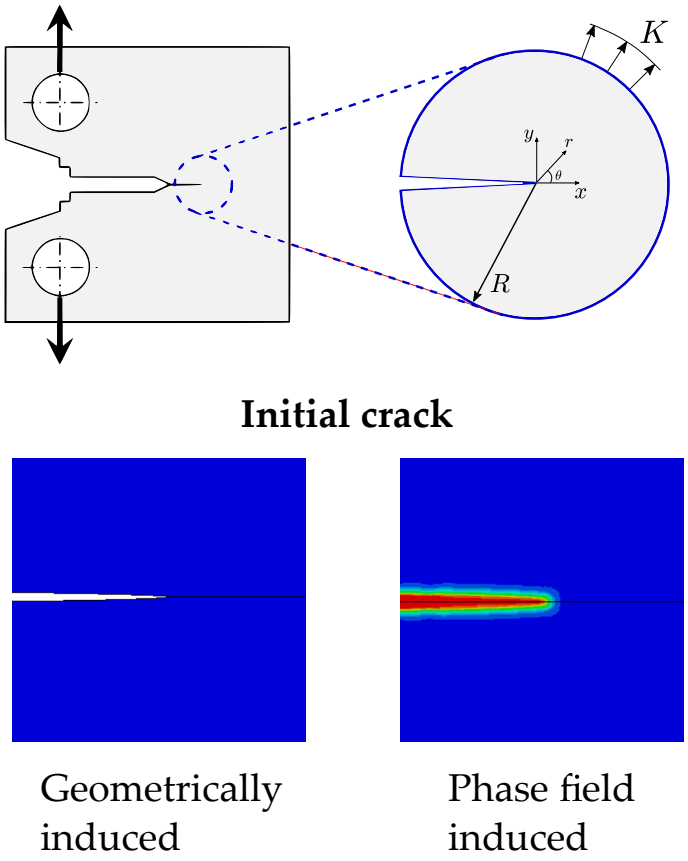

Figure 4.5: Sketch of the boundary layer problem. The circular area is the modeling domain, with only half of it being considered due to symmetry along the crack plane. Below are illustrations of the approaches used to initialize cracks. From [P2].

The modified boundary layer is a classic fracture mechanics problem. The main advantage is that the energy release rate G for a mode I fracture problem, can be prescribed directly as displacements on the boundary using the relation to the stress intensity factor K:

$$G = \left(1 - \nu^2\right) \frac{K_I^2}{E} \,. \tag{4.1}$$

The displacements around a mode I crack are known from the singular term of the Williams expansion:

$$u_i = \frac{K}{E} r^{1/2} f_i\left(\theta, \nu\right) \,, \tag{4.2}$$

where θ denotes the rotational coordinate in the polar coordinate system centered at the crack tip and f_i is given by:

$$f_x = \frac{1+\nu}{\sqrt{2\pi}} \left(3 - 4\nu - \cos\theta\right) \cos\left(\frac{\theta}{2}\right) \,, \tag{4.3}$$

$$f_y = \frac{1+\nu}{\sqrt{2\pi}} \left(3 - 4\nu - \cos\theta\right) \sin\left(\frac{\theta}{2}\right) \,. \tag{4.4}$$

As also illustrated in figure 4.5, we distinguish between initial cracks introduced as discontinuities in the mesh (geometric cracks) and cracks introduced through the phase field

(phase field cracks). The problem has several length scales including the phase field length scale ℓ, the characteristic element size h and the material length L_f,

$$L_f = \frac{G_c(1-\nu^2)}{E}\,. \tag{4.5}$$

In addition, the boundary layer radius R is also a length scale, but is irrelevant as long as it is sufficiently large relative to all other length scales. Furthermore the length scale L_f was also shown to have no discernible influence om crack initiation in the boundary layer problem in [P2]. The geometry is discretized using roughly 30.000 quadratic quadrilateral plane strain elements, with a refined region near the crack tip. We first consider the dimensionless group ℓ/h. The relative size of the phase field length scale and the elements in the crack path is know to significantly affect results if ℓ is not sufficiently resolved by the mesh. A comparison on crack initiation loads for all combinations of phase field formulation and crack prescription is shown in figure 4.6. A few conclusions can be drawn: First, geometrically induced cracks significantly overestimate the crack initiation energy. This effect is studied more in figure 4.7. Secondly a phase field length scale eight times the characteristic element size is sufficient to guarantee fully mesh-converged results. Additionally, a smaller ℓ/h appears sufficient in all other cases than the `AT2` phase field crack. It should be noted that the objection in [76] is exactly that when a Dirichlet condition is used on the `AT1` phase field while the lower bound is enforced by a minimum $\mathcal{H}$ Eq. (3.15). Thus, better agreement for the `AT1` phase field crack might be expected with better bounds enforcement.

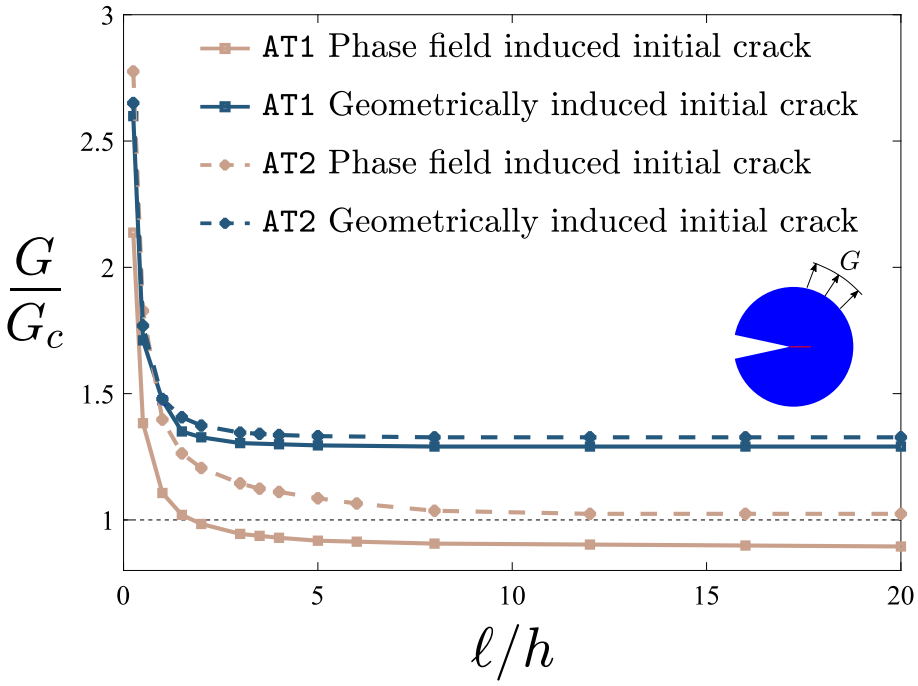

Figure 4.6: Boundary layer analysis: Influence of mesh size relative to the phase field length scale. The analysis is performed for both the `AT1` and `AT2` phase field models and with both geometric and phase field-induced initial cracks. Adapted from [P2].

To study the overestimation of fracture energy when using geometric cracks further, the phase field contours just prior to fracture for the `AT1` model are shown in figure 4.7a. As can be seen, the geometrically prescribed crack must develop the phase field in all directions prior to crack growth, while is is already well-formed for the crack prescribed

though the phase field. This effect introduces an energy barrier, which may rationalize the overestimation shown in figure 4.6.

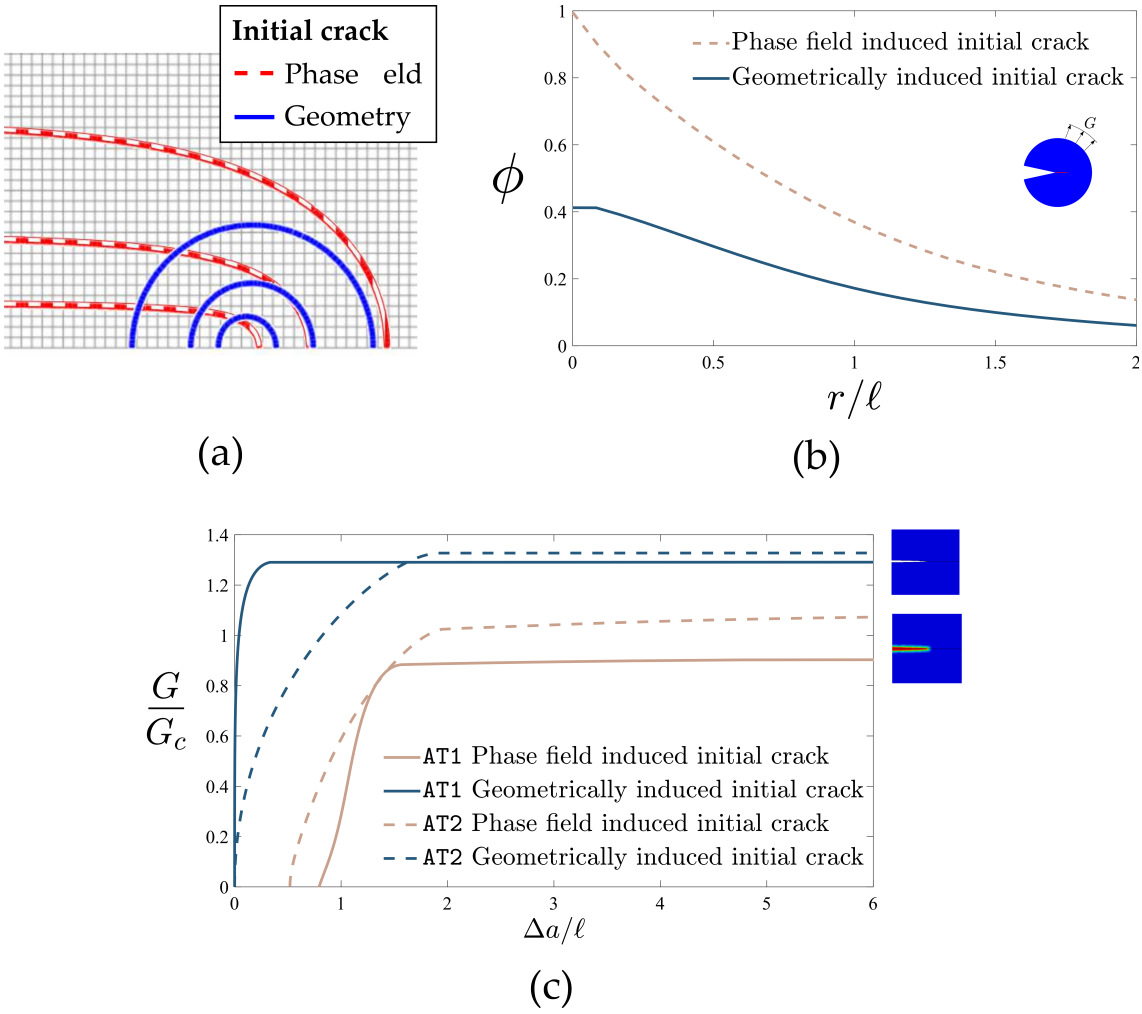

Figure 4.7: Boundary layer analysis of the crack initiation process. (a) Phase field contours for the `AT1` model just prior to crack growth; (b) crack tip phase field distribution for the `AT1` model along the crack plane just prior to crack growth; and (c) crack extension, as computed by integrating the crack surface density function - Eq. (2.5). Adapted from [P2].

The distribution of the phase field variable in the crack plane immediately in front of he crack just prior to crack growth is shown in figure 4.7b, where the natural $\nabla\phi\cdot\mathbf{n}=0$ boundary condition of the phase field is made evident. For the geometric crack, the boundary condition forces a plateau of the phase field. Finally, in figure 4.7c, the crack extension as measured by the integral of the crack surface density function γ from Eq. (2.5) is shown for all combinations of phase field formulation and crack prescription technique. Here it can be seen that the use of an initial crack prescribed through the phase field smooths the transition into active crack growth by displaying significantly more evolution of the phase field prior to the unstable cracking event.
An attempt to rationalize the overestimation of fracture energy was to suspect the history variable $\mathcal{H}$, as it may in some cases prevent the phase field from attaining its optimal crack profile [92]. As shown in figure 4.8, this effect is negligible for sharp cracks, but may be significant in non-sharp defects [35]. An example of this behavior with sub-optimal crack profile can be found in figure 4.1c, where a widened region appears at the original crack

tip.

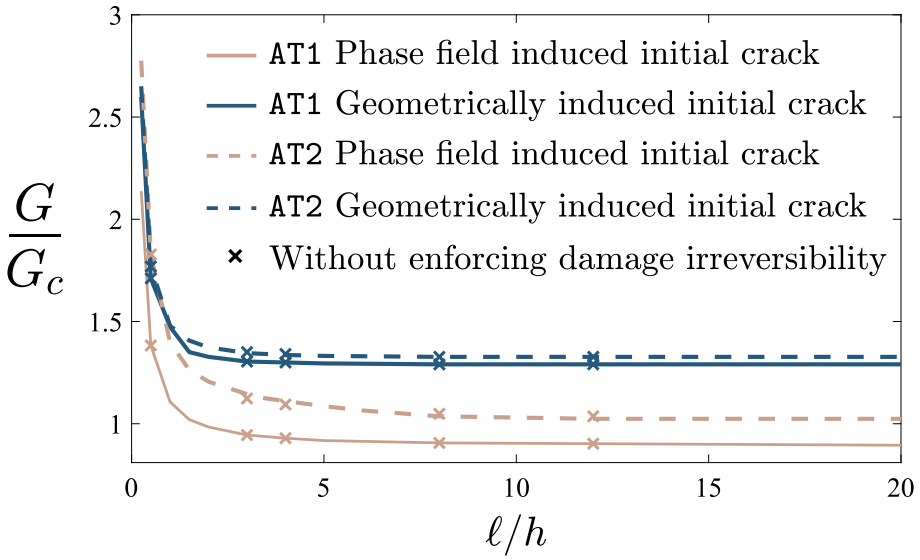

Figure 4.8: Boundary layer analysis: Influence on crack initiation when irreversibility is not enforced and the phase field is free to form its optimal profile. Note that the lower bound $\phi \geq 0$ is still enforced through the history variable $\mathcal{H}$. Adapted from [P2].

It is important to note that in figure 4.8, the history variable is still used to enforce the lower bound on the phase field, i. e. $\phi \geq 0$.

4.1.3 Stable crack growth in a double cantilever beam

To investigate the suitability of the phase field model in capturing stable crack growth in brittle materials, a double cantilever beam problem is analysed. The geometry is sketched in figure 4.9, note the double symmetry. The problem is modeled under plane strain conditions with an assumed out-of-plane thickness $B = 1\,\mathrm{mm}$, beam height $H = 0.9\,\mathrm{mm}$, initial crack half-length $a_0 = 10\,\mathrm{mm}$ and the total half-length of the computational domain is $L = 20\,\mathrm{mm}$, although identical results were obtained with $L = 30\,\mathrm{mm}$, demonstrating that edge effects do not dominate this problem. The problem is discretized using approximately 190.000 quadratic quadrilateral elements.

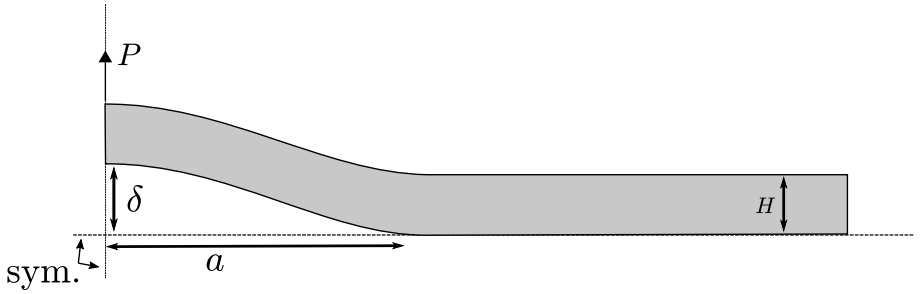

Figure 4.9: Sketch of the double cantilever beam analysis. Due to symmetry, only a quarter of the domain is modeled, as shown. From [P2].

The beam is loaded by a prescribed displacement δ, with an equivalent force P. Based on Timoshenko beam theory, an analytical solution for this problem can be derived. The

force P may be related to the displacement δ by,

$$\delta = \frac{Pa^3}{\bar{E}BH^3} + \frac{Pa}{\kappa QBH}\,. \tag{4.6}$$

In the above, the plane strain Young's modulus is denoted $\bar{E} = E/(1-\nu^2)$, the shear modulus is denoted Q and $\kappa \approx 5/6$ is the shear coefficient for a beam with a rectangular cross-section. The compliance of the beam may be expressed as $C = \delta/P$ and consequently, the energy release rate for the symmetric problem becomes:

$$G = 2 \cdot \frac{P^2}{2B}\frac{\mathrm{d}C}{\mathrm{d}a} = \frac{3P^2a^2}{\bar{E}B^2H^3} + \frac{P^2}{\kappa QB^2H}\,, \tag{4.7}$$

Which may be reformulated as a function of δ as follows:

$$G = \frac{3\bar{E}H^3}{a^4} \cdot \frac{1 + \dfrac{\bar{E}}{3\kappa Q}\left(\dfrac{H}{a}\right)^2}{\left(1 + \dfrac{\bar{E}}{\kappa Q}\left(\dfrac{H}{a}\right)^2\right)^2} \cdot \delta^2\,. \tag{4.8}$$

As a result, at $G = G_c$, the crack length a and prescribed displacement δ are uniquely related.
In the numerical solution of the problem, crack length is tracked in two ways; using the integral of the crack surface density function Eq. (2.5) to compute the amount of crack surface, and more simply by tracking the furthest point with $\phi \geq 0.95$. As in the previous boundary layer analysis, both `AT1` and `AT2` phase field models are used and both a geometric and a phase field initial crack is tested. Results using the crack density function can be seen in figure 4.10a and results using the furthest point method may be found in 4.10b.
The correspondence between analytical and computational results is decent, but not as good as one might have hoped. The `AT1` model appears to achieve the best correspondence with the analytic result, although whether crack length is over- or underestimated depends on how it is measured. It is worth noting that this problem was a difficult one, which displayed significant sensitivity to the relation ℓ/H. The mode I cracking is not particularly stable in the sense that the solution easily transitions into a mixed-mode crack. Correspondence to the analytical solution may have been improved if a strain decomposition split was utilized, such that the phase field remained zero on the top part of the beam and thus did not affect the bending stiffness. Other examples of stable crack growth may be found in [110] with the so-called "surfing crack problem" and in the tapered double cantilever beam in [111], which both indicate that the phase field fracture model yields accurate results for stable crack propagation in linear elastic solids.

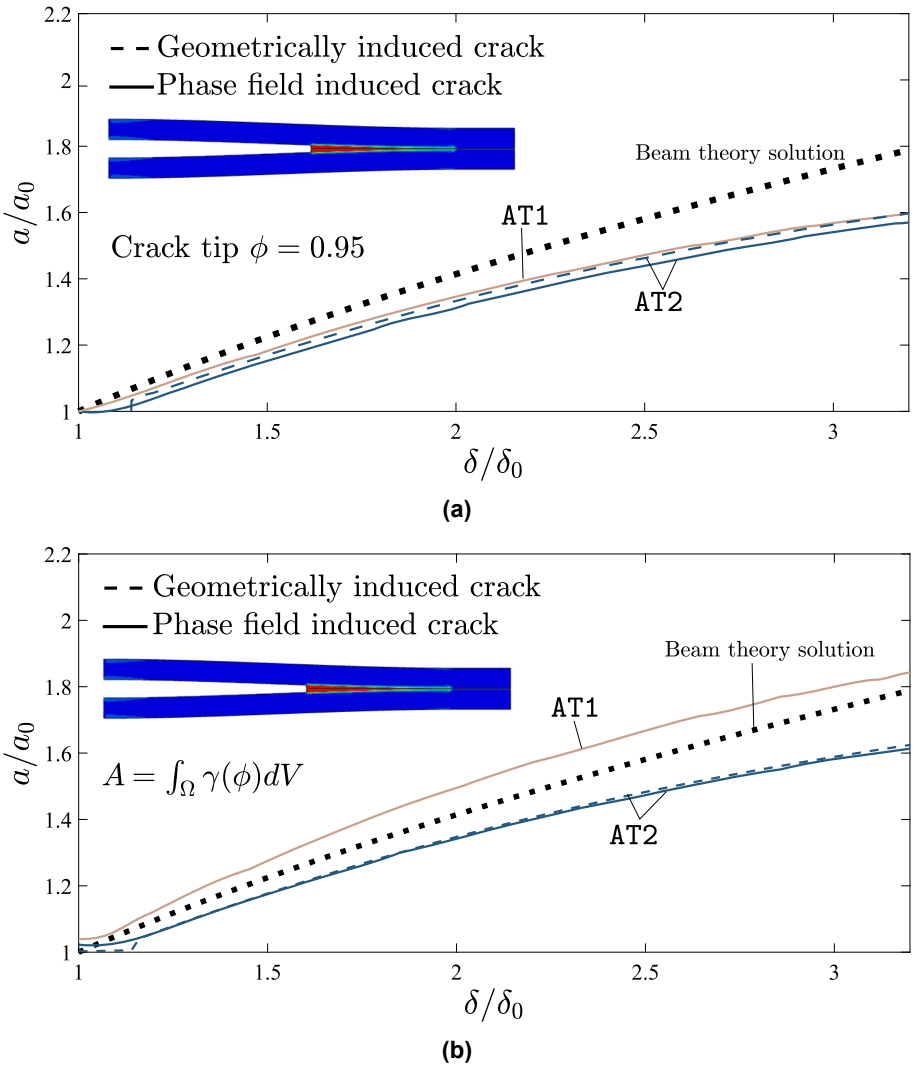

Figure 4.10: Double cantilever beam analysis: Stable crack growth as measured by a) the furthest point with $\phi = 0.95$ and b) by the integral of the crack surface density function Eq. (2.5). Adapted from [P2].

Crack growth driven by external work [unpublished]

To follow up on the cantilever beam results, a second study was performed on a single beam glued to a rigid substrate. One end of the beam of length a is free from the substrate. The free end is subjected to an applied moment M causing a rotation φ of the end surface. The problem is sketches in figure 4.11.

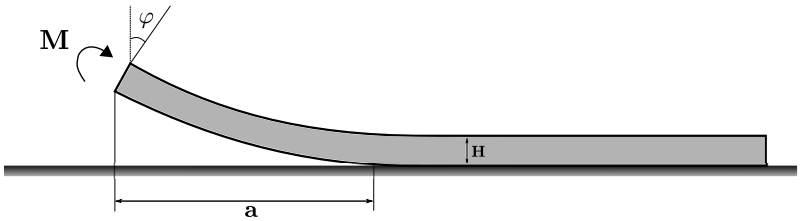

Figure 4.11: Sketch of the peel test. With the exception of the free end of length a, the beam is glued to a rigid substrate.

The purpose of this problem is to demonstrate that although internal strain energy is the driving force for crack growth in the phase field fracture model, crack growth driven by external work is still possible. The total potential energy Π for the problem is given by:

$$\Pi = U + W = \frac{1}{2}M\varphi - M\varphi \tag{4.9}$$

Where U is the stored elastic strain energy, subject to degradation by the phase field, and W is the potential energy of the external loading. Since the end-surface rotation φ is related to the applied moment by

$$\varphi = \frac{12Ma}{E'bH^3} \tag{4.10}$$

where b is the out-of-plane thickness and $E' = E/(1-\nu)$ is the plane strain equivalent stiffness. The energy release rate G for this problem is

$$G = -\frac{1}{b}\frac{\partial \Pi}{\partial a} = \frac{6M^2}{E'b^2h^3}. \tag{4.11}$$

Thus, this is a critically stable problem in the sense that the energy release rate neither increases nor decreases as the crack grows. Figure 4.12 shows the evolution of total potential energy, internal strain energy and external work as the load is increased. The key result here is that the phase field model is capable of predicting crack growth under monotonically increasing strain energy where the fracture energy is provided by the external work. It is once again emphasized that the strain energy shown is the degraded strain energy ψ_ℓ as given by equation (2.3). Furthermore, the internal strain energy calculated by integration of degraded strain energy density is shown to exactly match the analytical strain energy as given by the equations (4.9) and (4.10).

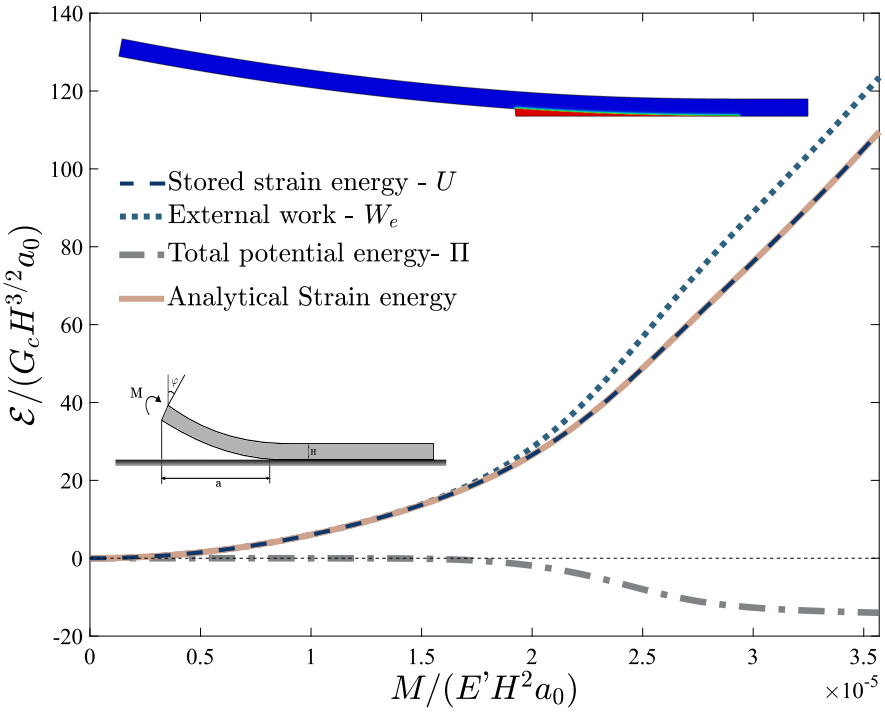

Figure 4.12: Evolution of energy quantities $\mathcal{E}$ under increasing applied moment M. Crack growth occurs when there is a drop in total potential energy.

4.1.4 Dynamic Crack branching

As a final benchmark, a dynamic fracture problem taking into account inertia effects is considered. This benchmark is widely used in the phase field community [32, 34, 112] as it demonstrates the innate ability of phase field models to capture complex crack topologies and crack branching. The geometry is a rectangular area of height $40\,\mathrm{mm}$ and width $100\,\mathrm{mm}$. A horizontal initial crack extends from the leftmost edge to the center of the plate and the plate is subjected to an instantaneously applied tensile load of $1\,\mathrm{MPa}$ on the horizontal edges. The geometry is sketched in figure 4.13.

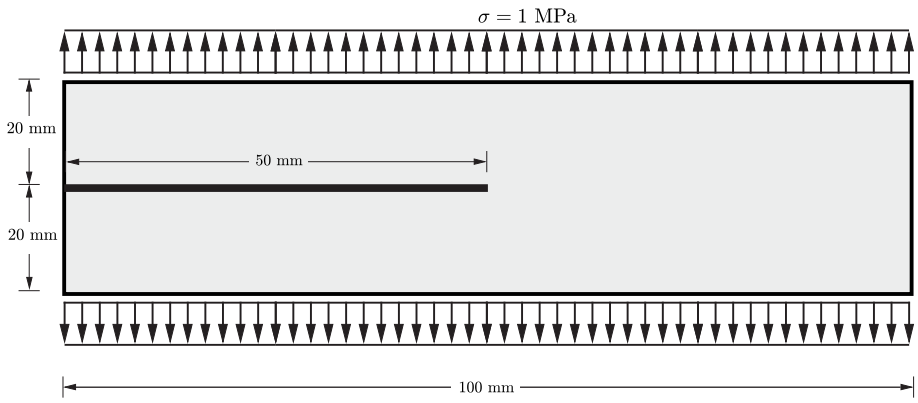

Figure 4.13: Sketch of the dynamic crack problem. The full tensile load is applied instantaneously. From [P1].

The resulting crack pattern for this problem is highly dependent on material parameters. We use $E = 32\,\mathrm{GPa}$, $\nu = 0.2$, $G_c = 0.5\,\mathrm{J/m^2}$, $\ell = 0.25\,\mathrm{mm}$ and a material density of $\rho = 2450\,\mathrm{kg/m^3}$. The rayleigh wave speed for this material is thus $v_r = 2125\,\mathrm{m/s^2}$. The domain is uniformly meshed using linear quadrilateral elements and the time integration is done using a backward Euler approach with time increments of $1\,\mu\mathrm{s}$.

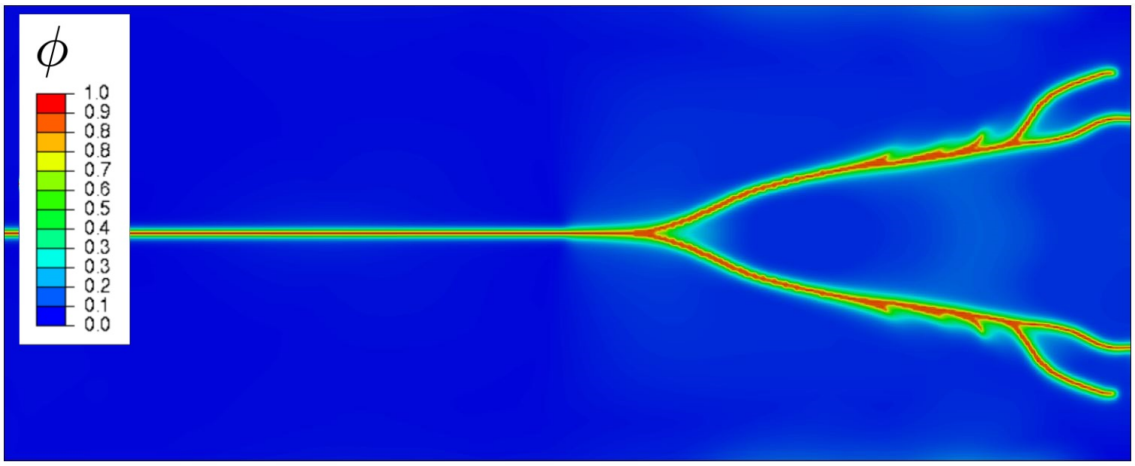

Figure 4.14: Crack trajectory for the dynamic crack branching problem. Adapted from [P1].

The crack pattern observed in figure 4.14 displays rather intricate features despite the fact than the mesh is relatively coarse. These examples demonstrate that the quasi-Newton method is able to capture highly complex fracture phenomena without diverging.

4.2 Phase field fatigue modeling in the presence of hydrogen.

We now consider a phase field model for hydrogen-assisted fatigue. We here restrict the consideration to linear elastic materials, making the model suitable only for medium to high-cycle fatigue where the influence of plasticity is often negligible. The phase field model used is the AT2 model enhanced with the fatigue extension from Carrara *et al.* [37] which was introduced in section 2.1.3. Irreversibility is enforced by the history variable approach. This section introduces the basic considerations of hydrogen fatigue and also demonstrates the interaction of alternating load and hydrogen transport.

4.2.1 Initial fatigue considerations for a single-edge-notched tension problem

We start by once again considering the SENT geometry which was first shown in figure 4.1a, although now with an alternating load. The load ratio (Eq. (3.20)) is $R = -1$, meaning that the plate is subjected to tension and compression of equal magnitude $\bar{u} = \pm 0.002\text{mm}$. No strain split is introduced for this problem, meaning that compressive loading contributed equally to fatigue and crack growth relative to tension. For an initial consideration, hydrogen is not included in the model. It takes a minimum of four increments to resolve a load cycle (tensile loading, unloading, compressive loading and unloading), this can be resolved using the monolithic method, while the one-pass staggered approach requires more increments to accurately capture the fatigue results. Crack extension as measured by the furthest point which exceeds $\phi = 0.95$ is shown as a function of cycle number for the monolithic and staggered scheme is shown in figure 4.15.

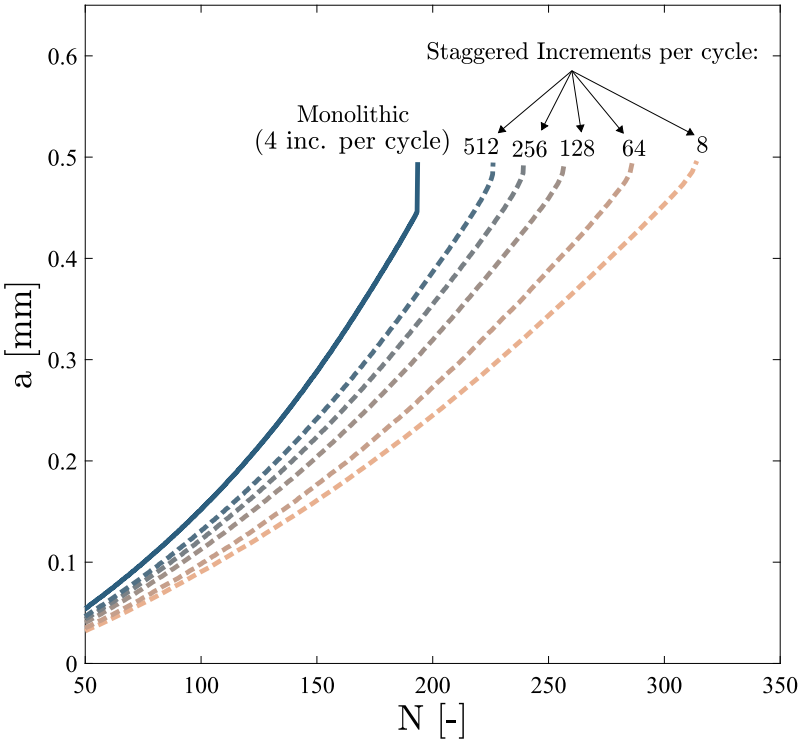

Figure 4.15: Fatigue crack extension a over a number of cycles N for the SENT specimen: A comparison between the quasi-Newton method and the single-pass staggered algorithm. Adapted from [P1].

The trend of the results seem to indicate that in order to predict the number of cycles to failure within a reasonable accuracy, well over 1000 staggered increments per cycle are

necessary. Such a large number of increments per cycle makes the one-pass staggered algorithm largely unsuitable for fatigue computations. It is not clear how sensitive these results are to the total number of cycles to failure, however, and a high-cycle problem may be less sensitive. Computation times for the results are compiled in table 4.3

Solutions strategy	Monolithic	Staggered				
Increments per cycle	4	8	32	64	128	256
CPU hours	14.85	3.24	16.52	20.29	34.30	73.98

Table 4.3: Computation time for complete fatigue failure of the SENT specimen. compariosn between the quasi-Newton method and the single-pass staggered algorithm with 256 increments pr. cycle. From [P1].

The quasi-Newton method requires computation times roughly five times smaller than those for 256 staggered increments per cycle, which seems to be a least four times less than required for accurate results. Unfortunately, as we move on to consider hydrogen, the use of the quasi-Newton model becomes impossible. As the single-pass staggered algorithm is clearly infeasible, we instead use the residual-controlled multi-pass staggered algorithm of Seleš [101]. A comparison of the results for the SENT fatigue problem using different strain decompositions using both the quasi-Newton method and the Seleš algorithm is shown in figure 4.16a. It should be noted that the Seleš algorithm here uses 20 increments per cycle, which causes a slight deviation in the results at very low cycle numbers as the change in the phase field during the loading portion of the cycle is taken into account. The results are also compared to the original results presented in [37], showing good agreement. Some deviation is present, especially in the spectral decomposition split, however, this may all be due to differences in mesh and problem setup. It is also noted that the number of cycles to complete failure with the spectral split is almost exactly twice that of the isotropic split, meaning that the contribution from the compressive part of the load cycle is almost completely eliminated.

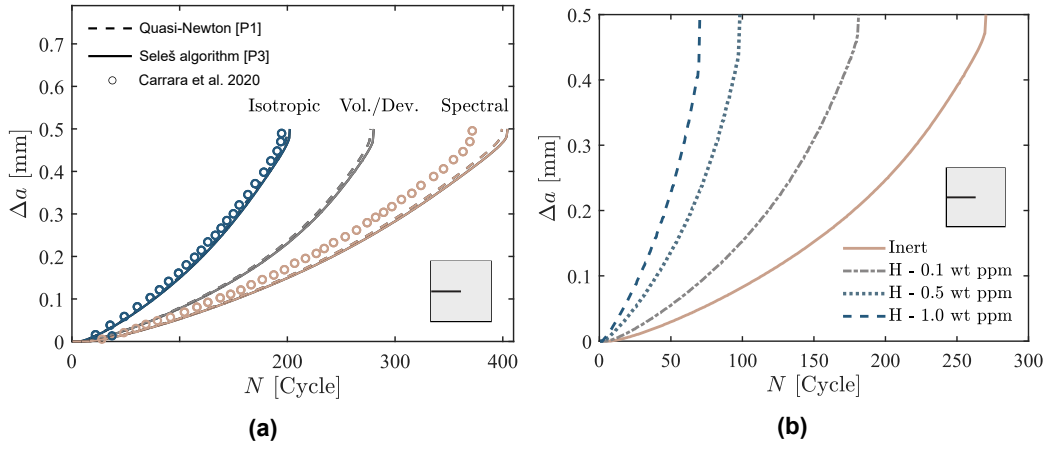

Figure 4.16: Fatigue crack growth of the SENT specimen: (a) verification of the implementation of the Seleš multi-pass staggered algorithm [101], (b) Influence of hydrogen on fatigue crack growth rate. Adapted from [P3].

The effect of hydrogen on the SENT problem is examined in figure 4.16b, where the sample is assumed to be pre-charged with a given hydrogen concentration and all boundaries of the domain, including the initial crack faces, has the same initial concentration

prescribed throughout the simulation. The analysis is performed using the volumetric/deviatoric strain decomposition and the results reveal the expected trend that the number of cycles to failure decreases with increasing hydrogen concentration. For the highest concentration prescribed, a very drastic reduction in cycles to failure by a factor of 4 is observed.

4.2.2 Modified boundary layer analysis

We now return to the modified boundary layer problem introduced in figure 4.5. The applied stress intensity factor is now cyclic and characterized as follows;

$$K_I(t) = K_m + \frac{\Delta K}{2}\sin(2\pi f \cdot t). \tag{4.12}$$

here, f denotes the load frequency, $\Delta K = K_{max} - K_{min}$ denotes the load amplitude and the mean load K_m is given by

$$K_m = \frac{\Delta K}{2} + \frac{R\Delta K}{1-R}. \tag{4.13}$$

Recall that R denotes the load ratio as given in Eq. (3.20). For the following analysis, we introduce the length scale $L_0 = (K_m/E)^2$. The temporal evolution of crack tip hydrogen concentration can be characterized using the following dimensionless groups:

$$\frac{C}{C_0} = \mathcal{F}\left(\frac{fL_0^2}{D}, \frac{tD}{L_0^2}, \frac{E\bar{V}_H}{\mathcal{R}T}\right) \tag{4.14}$$

The first group will be denoted as the normalized frequency $\bar{f} = fL_0^2/D$ and the second group the normalised time $\bar{t} = tD/L_0^2$. If the loading rate is slow, the hydrogen in the specimen is allowed to redistribute to its equilibrium distribution, which is governed by the hydrostatic stress σ_H. If the domain is pre-charged with a hydrogen concentration C_0 and hydrogen is not allowed to escape, the local hydrogen concentration is given by [113]

$$C = C_0 \exp\left(\frac{\bar{V}_H\sigma_H}{\mathcal{R}T}\right). \tag{4.15}$$

Close to the crack tip, the hydrostatic stress follows the well-known $1/\sqrt{r}$ singularity, meaning that extreme local hydrogen concentrations can be observed immediately in front of the crack tip. However, if the loading frequency is high relative to the diffusion rate D, unloading occurs before the equilibrium concentration is attained. The evolution of hydrogen concentration at some point ahead of the crack is examined for different normalized frequencies $\bar{f}$ in figure 4.17. The response can be seen to have a small initiation region which quickly converges towards a steady state with no overshoot. In the steady state, the response follows a sinusoidal wave for which the amplitude is inversely proportional to the normalized frequency. Regardless of the load frequency, the mean hydrogen concentration appears identical, although it may be expected that the hydrogen concentration when the load is near its peak is the most influential for fatigue crack growth.

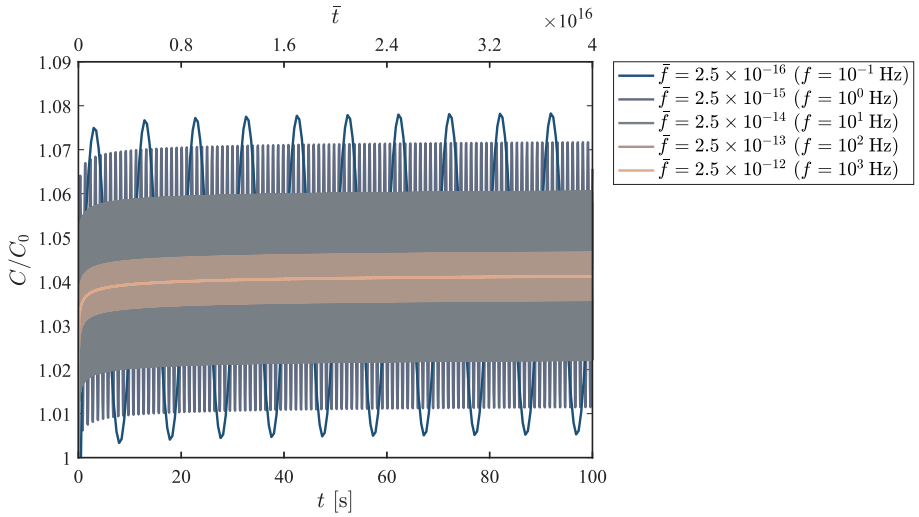

Figure 4.17: Normalized hydrogen concentration at a point ahead of the crack tip. Here, high loading frequencies are shown, with a load ratio of $R = 0$. Adapted from [P4].

As a next step, the influence of hydrogen and loading frequency on the crack growth rate is investigated. Crack extension Δa is normalized with respect to the material length scale L_f from Eq. (4.5) and the load amplitude ΔK is normalized with respect to the nominal critical stress intensity factor in an inert environment,

$$K_0 = \sqrt{\frac{G_c E}{(1-\nu)^2}}. \tag{4.16}$$

The influence of hydrogen concentration is investigated as a load ratio $R = 0.1$, a load amplitude $\Delta K = 0.08 K_0$ and a normalized frequency $\bar{f} = 2.5 \cdot 10^{-14}$. As can be seen from figure 4.18a, fatigue crack growth is faster at higher hydrogen concentrations. Each of the curves reach an approximately linear stage with differing slopes. These slopes are a measure of crack growth rate, which is recorded for a number of different load amplitudes ΔK and shown in figure 4.18b. The crack growth rates accurately follow a power law relation with the load amplitude, corresponding to the Paris law:

$$\frac{da}{dN} = C_p \Delta K^m \tag{4.17}$$

Furthermore, the exponent m can be seen to be practically insensitive to the hydrogen concentration, while the coefficient C_p increases for increasing hydrogen concentrations. As it has been established that hydrogen increases crack growth rate and that loading frequency affects the peak hydrogen concentration, attention is now devoted to examining directly the impact of loading frequency on crack growth rate. Results at a load rate of $R = 0$ with load amplitude $\Delta K / K_0 = 0.24$ at an initial hydrogen concentration of $C_0 = 0.1\,\mathrm{wt\ ppm}$ are shown in figure 4.19. Two distinct regimes are identified with a smooth transition in between. In the first regime, which features a high crack growth rate, loading frequency is slow relative to the diffusion rate of hydrogen. As a result, crack tip hydrogen is near its equilibrium value when crack growth occurs. In the second regime, where loading amplitude is fast relative to the diffusion rate, hydrogen does not attain its equilibrium value and crack growth is slower as a result. The crack growth rate can still, however, be expected to be faster than if hydrogen was kept constant at the initial concentration, as fast loading sees the crack tip hydrogen converge to an average value for the load cycle, as was seen in figure 4.17.

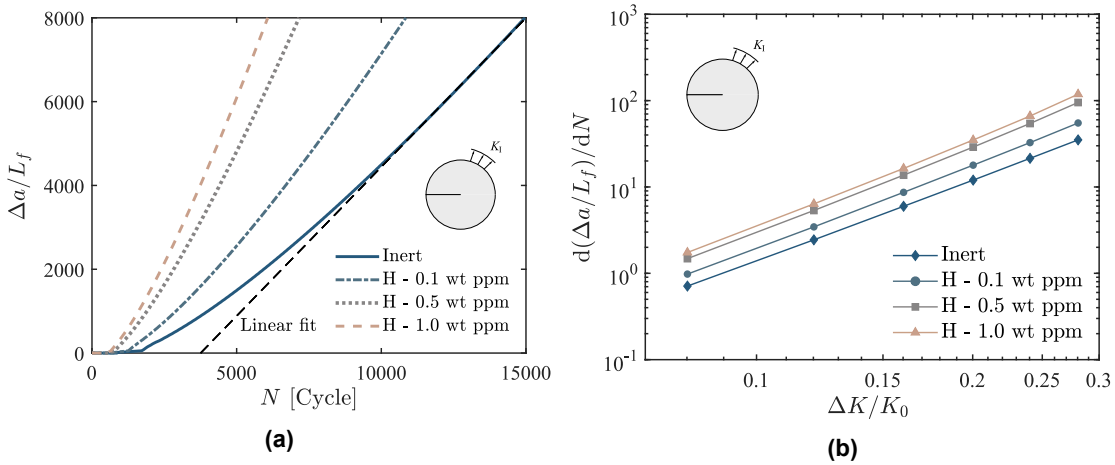

Figure 4.18: Boundary layer fatigue analysis: a) Crack growth by number of cycles, b) crack growth rate as a function of stress intensity factor amplitude, corresponding to a Paris Law relation. Adapted from [P3].

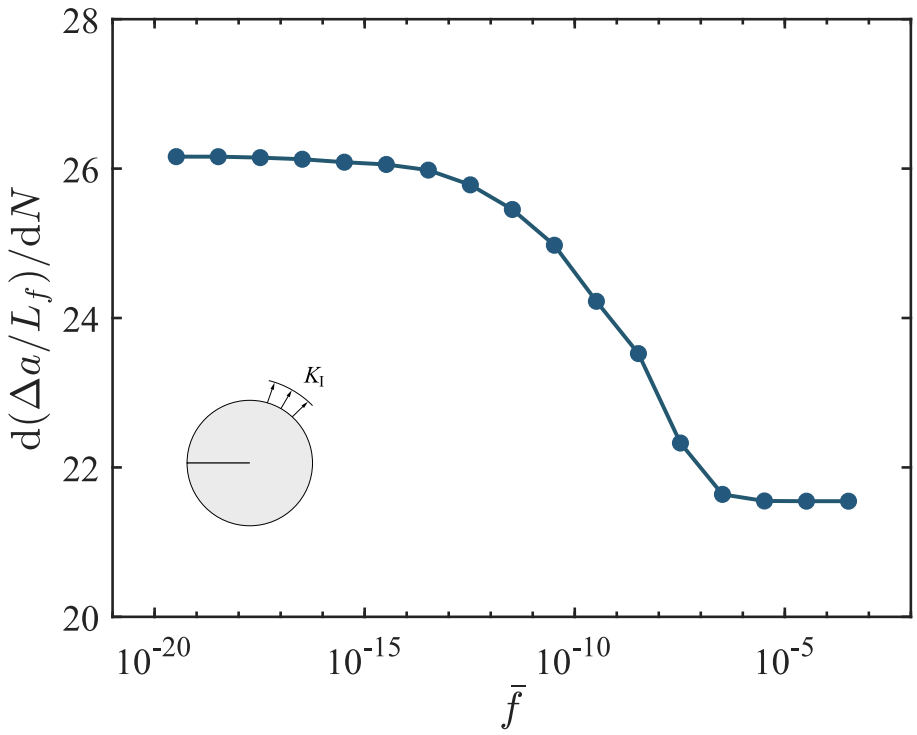

Figure 4.19: Influence of normalized loading frequency $\bar{f}$ on fatigue crack growth rate. Load ratio is $R = 0$, load amplitude $\Delta K/K_0 = 0.24$. The specimen is pre-charged with a hydrogen concentration $C_0 = 0.1\,\mathrm{wt\ ppm}$. Adapted from [P3].

In conclusion, the model is able to capture the expected physics of a smooth transition between two regimes of normalized loading frequency.

4.3 Applications of phase field models for hydrogen-assisted failure

In this section a series of potential applications for phase field fracture models, enhanced with hydrogen transport and embrittlement, are highlighted. The presented results are primarily qualitative in nature and intended to demonstrate promising use-cases that are feasible with a best-practice phase field implementation. All of the problems considered here use linear elastic phase field models enhanced with hydrogen transport and embrittlement.

4.3.1 Virtual fatigue assessment of a notched cylindrical bar

As a first problem, fatigue of a notched cylindrical bar is considered. The bar is considered as pre-charged with a hydrogen concentration C_0 and all outer surfaces are considered to be in contact with the same environment such that an identical concentration is enforced on all outer boundaries. This way, the number of cycles to failure can be recorded for numerous load amplitudes and at different hydrogen concentrations to generate virtual S-N curves for hydrogen-assisted fatigue. The notched cylindrical bar is considered as an axisymmetric planar problem, which is sketched in figure 4.20a.

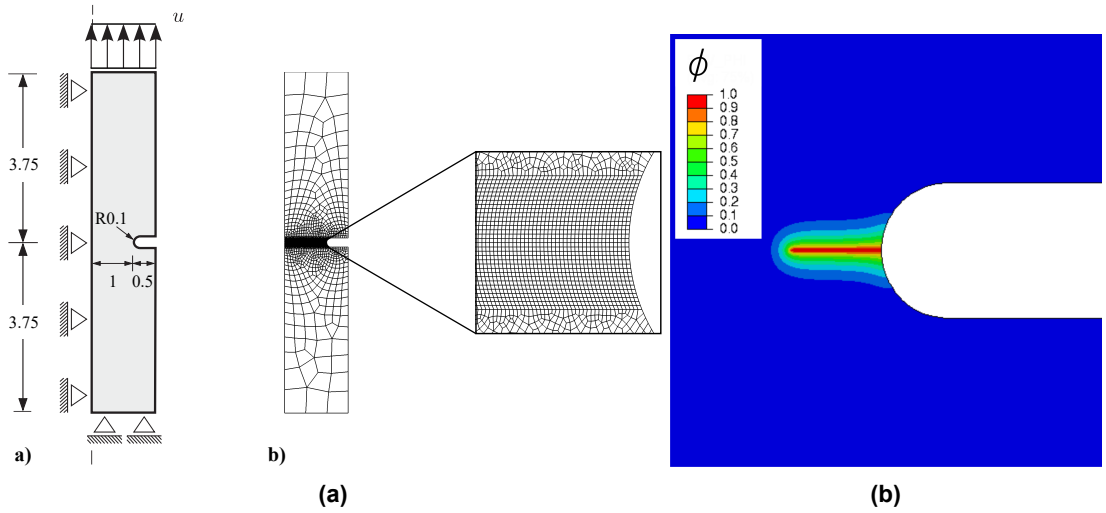

Figure 4.20: Axisymmetric cylindrical notched tension problem: a) Sketch of geometry and boundary conditions. b) Contour of the phase field crack in the axisymmetric tension problem during fatigue crack growth. From [P3].

The problem involves crack initiation from a non-sharp defect and as a result, it is dominated by the critical stress of the specimen, rather than the fracture toughness. The stress concentration factor for the geometry is $K_t = 3.354$. The loading is applied as an applied displacement, which induces a nominal remote stress σ_a^∞. To incorporate the effect of newly formed crack surface coming into contact with the hydrogenous environment, the moving chemical boundary from section 3.1 is included in the consideration. the results are computed at a load frequency of $f = 1\,\mathrm{Hz}$, which is relatively fast compared to the diffusion rate of $D = 0.00127\,\mathrm{mm}^2/\mathrm{s}$ in steel. The length scale L_0 is not a meaningful parameter in this problem, so a normalized load frequency comparable to figure 4.17 is not available. The virtual S-N curves are shown in figure 4.21 and reveal that hydrogen does not induce a change in slope for the S-N curves, but do offset the curve such that for a given applied remote stress amplitude, the number of cycles to failure is lower when hydrogen is present.

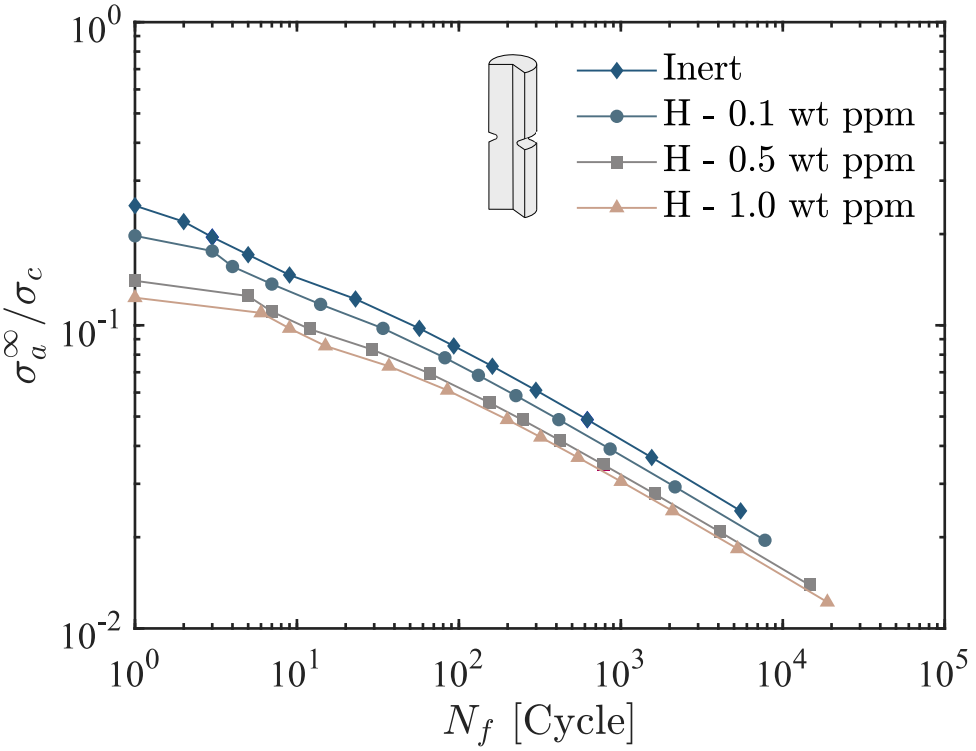

Figure 4.21: Cycles-to failures curves for the axisymmetric tension problem. The specimen is exposed to various concentrations of hydrogen on all exterior surfaces. Adapted from [P3].

4.3.2 Virtual experiment of a concrete screw anchor

We go on to study the case of failure in a concrete screw anchor. In order to showcase the potential for hydrogen-enhanced phase field models in assisting experimental campaigns and designing components for aggressive environments, we mimic the testing conditions described in the ASTM E488/E488M standard [114]. The standardized test is intended to test the strength of concrete screw anchors exposed to hydrogen. While the conditions in concrete are typically alkaline, hydrogen embrittlement is still a concern as the screw anchors are typically made from high-strength galvanized steel. If the zinc coating is damaged, a very low electrochemical potential occurs as a result of the galvanic coupling between zinc and steel. The steel will act as cathode in the electrochemical reaction and be protected from corrosion, but the electrochemical potential is low enough that hydrogen evolution is a likely cathode reaction, in spite of the alkaline conditions. As a result, a small crack or scratch in the zinc coating is likely to expose the steel to hydrogen. In the standardized test of the ASTM E488/E488M standard, the screw anchor is pre-charged with hydrogen by exposing it to an alkaline solution representative of the one found in concrete pores. The pre-charging is performed while the screw anchor is kept under tension and potentiostatic control is used to keep the electrochemical potential low enough to facilitate hydrogen evolution. After the pre-charging protocol, a tensile test up to ultimate failure is performed. During both the pre-charging and the tensile test, the thread of the anchor is embedded in a concrete slab, as would be the case in service, and tension is applied to the head of the anchor. The experimental setup is shown in figure 4.22.

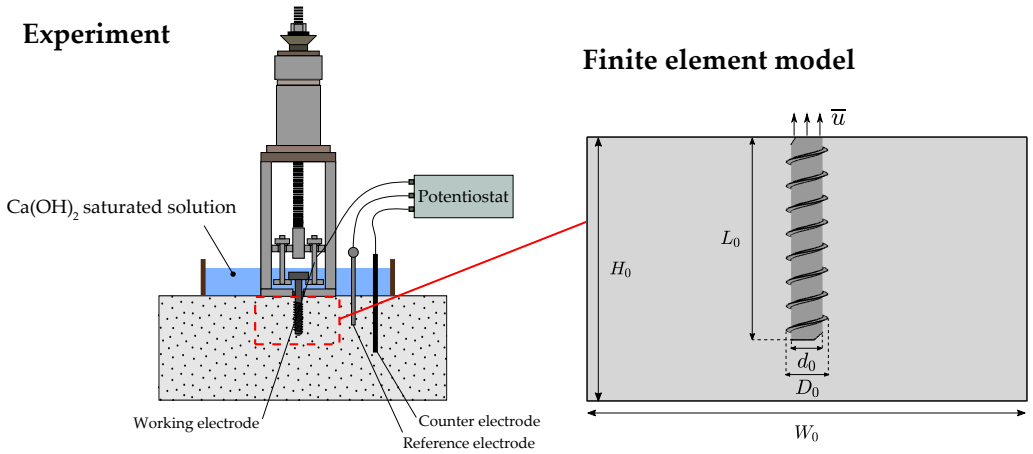

Figure 4.22: Setup of the concrete screw anchor test (left) and sketch of the finite element model (right). From [P4].

As our model does not include electrochemistry, there is no meaningful way to include the pre-charging phase as part of the modeling procedure here. The pre-charging protocol is, however, similar to the experimental work by Recio *et al.* [115]. Taking into accounts the differences between the standardised test and their experimental work, a conservative estimate of the initial hydrogen concentration is $C_0 = 2\,\mathrm{wppm}$.
The modeling domain is shown in figure 4.22. We model both the embedded portion of the screw anchor and a rectangular section of the surrounding concrete slab. The concrete slab has a height $H_0 = 76.2\,\mathrm{mm}$ a width $W_0 = 127\,\mathrm{mm}$ in the two other directions. The concrete is modeled as purely linear elastic with $E_c = 23.6\,\mathrm{GPa}$ and $\nu_c = 0.2$. The phase field and hydrogen transport models are not applied to the concrete domain. The screw anchor made from high-strength steel and has a modeled length of $L_0 = 58.4\,\mathrm{mm}$ and a core diameter of $d_0 = 9.1\,\mathrm{mm}$. The outer diameter of the thread is $D_0 = 11.9\,\mathrm{mm}$. The screw material is modeled as a linear elastic material with phase field damage and hydrogen transport. It has elastic parameters $E_s = 210\,\mathrm{GPa}$, $\nu_s = 0.3$ and a fracture toughness $G_c = 64\,\mathrm{N/mm^2}$ with a phase field length scale of $3.05\,\mathrm{mm}$. The phase field length scale is roughly 5 times the characteristic element length $h_e \approx 0.6\,\mathrm{mm}$. The assumed diffusivity of the steel is $D_s = 0.0127\,\mathrm{mm^2/s}$ and as previously mentioned the assumed initial concentration of hydrogen is $2\,\mathrm{wppm}$. The surface boundary condition for the screw is here set as the $\mathbf{J} = 0$ Neumann boundary condition. Contact across the bolt thread is handled by the built-in contact capabilities of Abaqus. Friction is taken into consideration with a coefficient of friction $\mu = 0.35$. As shown in figure 4.23, both the concrete slab and the screw are modeled using tetrahedral elements with quadratic shape functions. approximately 117.000 and 155.000 elements are used for the concrete and the steel, respectively.
As the problem here considers crack initiation from a non-sharp defect, we employ the `AT1` phase field model in accordance with the recommendations of [110]. Arguably a more detailed implementation of a stress criterion like the work of Kumar *et al.* [28] could also have been considered. The applied loading is displacement controlled. The fracture occurs after 0.53 seconds of loading, which is a relatively fast load. More computations at different load rates would most likely result in a lower peak load as hydrogen would have more time to concentrate at the crack tip. The test standard does not include details on the applied load rate. The force-displacement response of the screw is shown in figure 4.24. The material exhibits a very close to linear response up until a point very close to final fracture, which occurs at a peak value of $27.88\,\mathrm{kN}$, corresponding to a nominal core stress of the screw of $429\,\mathrm{MPa}$ which is well below the yield stress of a high strength steel.

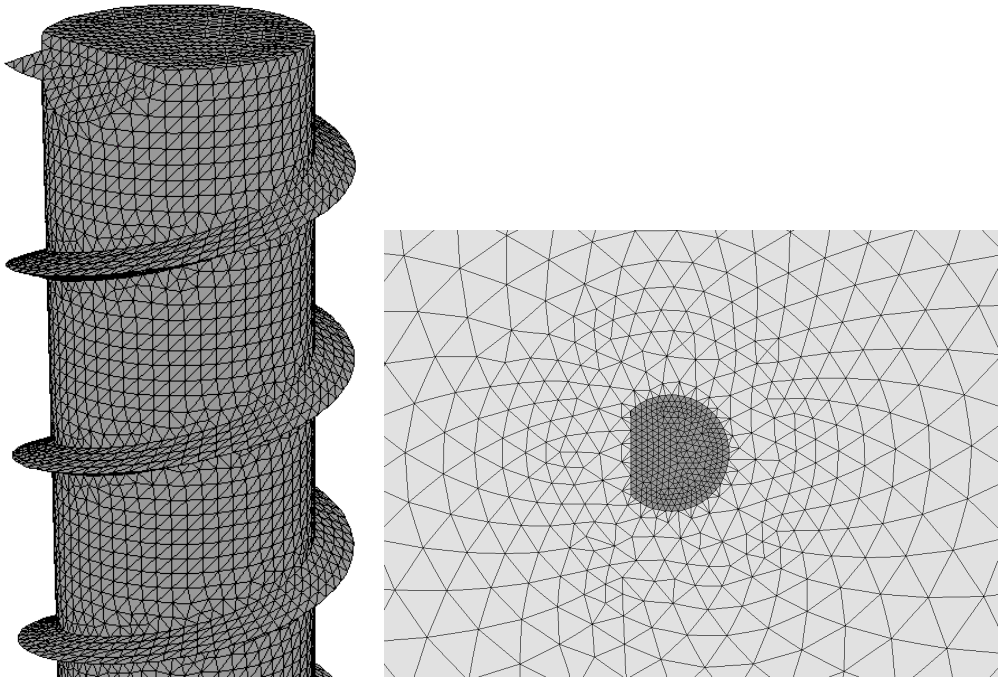

Figure 4.23: Finite element mesh for the concrete screw anchor. a) Mesh of the steel screw. b) mesh of the assembly as seen from above with the concrete slab in light grey and the screw n dark grey. From [P4].

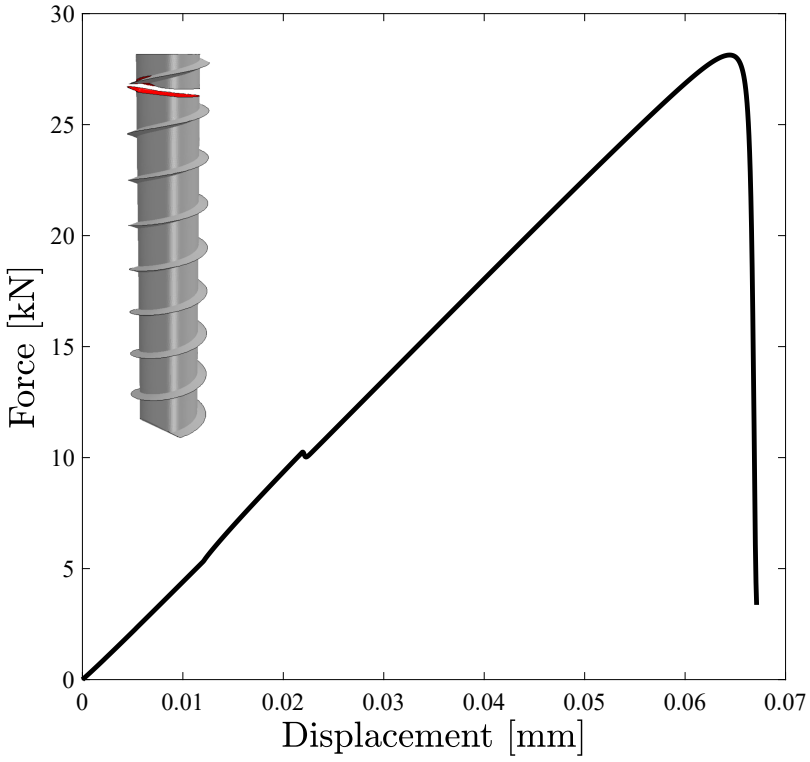

Figure 4.24: Force versus displacement curve for the virtually tested screw anchor. From [P4].

The fracture topology after the fracture of the bolt is illustrated in figure 4.25. Here elements are removed where $\phi > 0.98$ and $\phi > 0.96$ in figures a) and b), respectively. The $\phi = 0.98$ and $\phi = 0.96$ isosurfaces are shown in red in the two figures and all other material is shown in grey. The concrete slab is hidden for visualization purposes. As can be seen in figure 4.25b), the fracture extends through the entire cross-section at a height roughly half a winding of the thread from the top. This agrees well with the general observation that the first winding of thread carries the most load in any bolted connection. As revealed by figure 4.25a), the highest values of the phase field is found near the stress concentration at the root of the thread, which is a likely point of initiation.

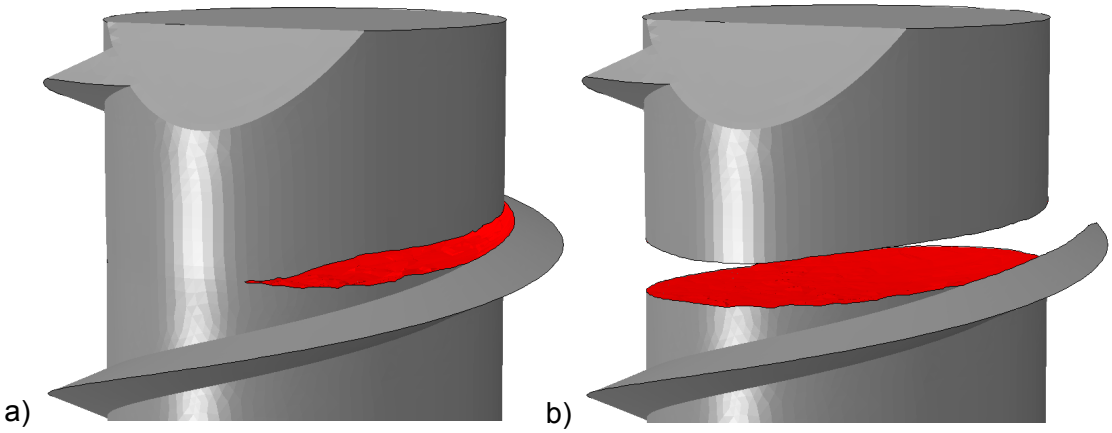

Figure 4.25: Cracking of the screw anchor visualized by removing areas above a phase field threshold ϕ_t and coloring the surfaces at $\phi = \phi_t$ red. a) $\phi_t = 0.98$, b) $\phi_t = 0.96$. From [P4].

4.3.3 Strength assessment of a pipeline based on inspection data

A significant advantage of the phase field model is it's capability to capture complex crack topologies. In this final example, we take advantage of this capability to evaluate the remaining strength in a pipeline that has developed corrosion pits during its lifetime. Non-destructive in-line inspection of corrosion damage was performed on a riser pipeline in [116]. A very large number of corrosion pit defects was detected and a statistical analysis was performed on their shape, orientation and depth. The data is visualized in figure 4.26

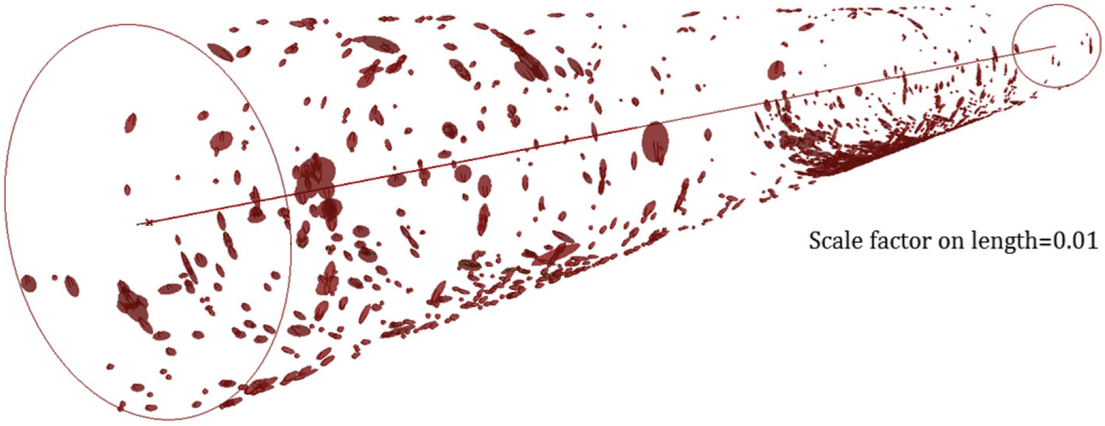

Figure 4.26: Distribution of corrosion pit defects in a riser pipeline as determined by non-destructive in-line inspection. From [P4], where it was adapted from [116].

From the data directly, a (section of) the pipe could hypothetically be directly modeled

and analysed. Here, we model a hypothetical critical section of the pipeline with a large number of pseudo-random defects based on the statistics of the measured data. The full pipeline is 11 kilometers long, has an outer diameter of $162\,\mathrm{mm}$ and a wall thickness of $40\,\mathrm{mm}$. We model a $2\,\mathrm{m}$ long critical section with the same cross-sectional dimensions as the original pipeline. In order to minimize the computational costs of this problem, we here consider only a quarter of the cross-section, using symmetry, although the distribution of defects is not in reality rotationally symmetric. The considered quarter section has 28 defects, meaning that the full cross-section contains 112 defects in the considered $2\,\mathrm{m}$ segment. The defects are introduced by a small script which introduces a number of ellipsoids representing the defects and adds all nodes within these ellipsoids to a node set which is prescribed a $\phi = 1$ Dirichlet condition. This makes the task of introducing a large number of three dimensional pseudo-random ellipsoidal defects relatively efficient and easy. The initial defects can be seen in figure 4.28a). The pipeline is subjected to a mix of axial tension and internal pressure. The axial tension is kept constant, while the internal pressure increases in time. Loading is slow to allow hydrogen to redistribute around the defects. In figure 4.28b), a critical defect located close to the symmetry condition starts growing. figure 4.28c) shows the critical defect coalescing and penetrating the thickness of the pipe. For an in-service strength assessment, this would constitute the end of the simulation, as the pipe is now leaking and has failed. More extensive damage can, however, be see in figures 4.28d-f) and in figure 4.27.

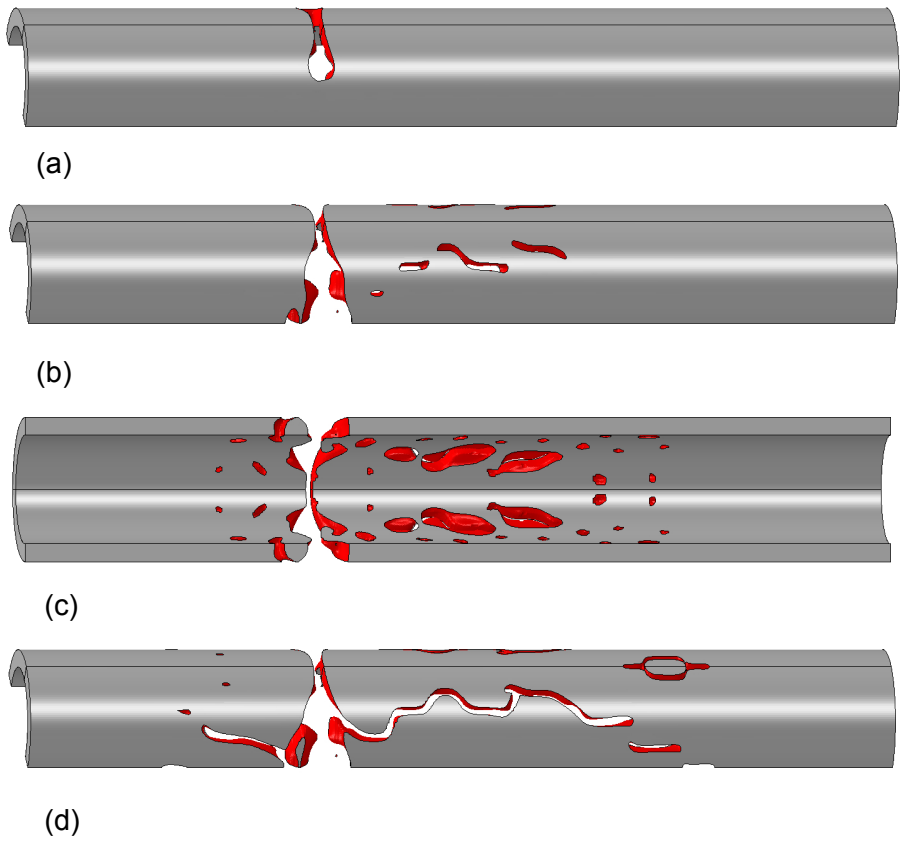

Figure 4.27: Alternative view of crack initiation and growth in the corrosion-damaged pipeline. Here areas with $\phi > 0.8$ are removed. From [P4].

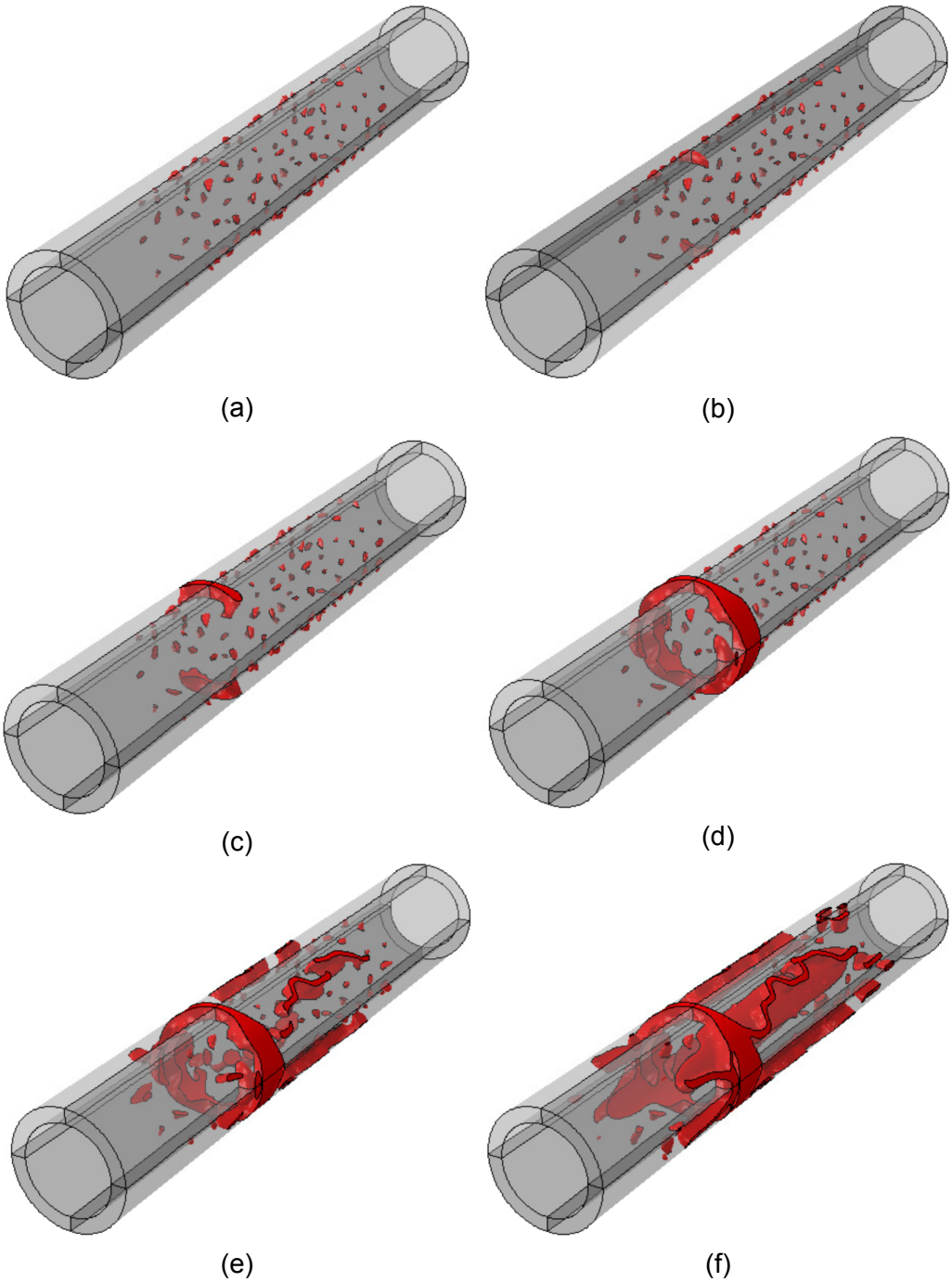

Figure 4.28: Crack growth for the corrosion-damaged pipeline. Red contours signify $\phi \geq 0.8$. The pipe is subjected to constant tension and increasing internal pressure. (a) Initial state. (b) Growth of a single critical defect. (c) The crack penetrates the pipe thickness. (d) Full cross-sectional failure. (e) Axial crack growth by coalescence of multiple defects. (f) Advanced axial crack growth. From [P4].

4.4 The influence of plastic strain gradients

Finally, the full model presented in chapter 2 is considered to account for the influence of plastic strain gradients on hydrogen-assisted crack growth. The phase field model used is strictly the `AT2` model and the solution strategy is the single-pass staggered algorithm. A high number of staggered increments, 10.000 increments per K_0 of load, is used to ensure an accurate solution. Every analysis in this section is performed on the modified boundary layer model which was shown in figure 4.5. A quick sketch of the problem with the boundary conditions considered here is shown in figure 4.29a. The boundary condition $\varepsilon^p_{12} = 0$ is the appropriate symmetry condition in strain gradient plasticity as shown in [P5].

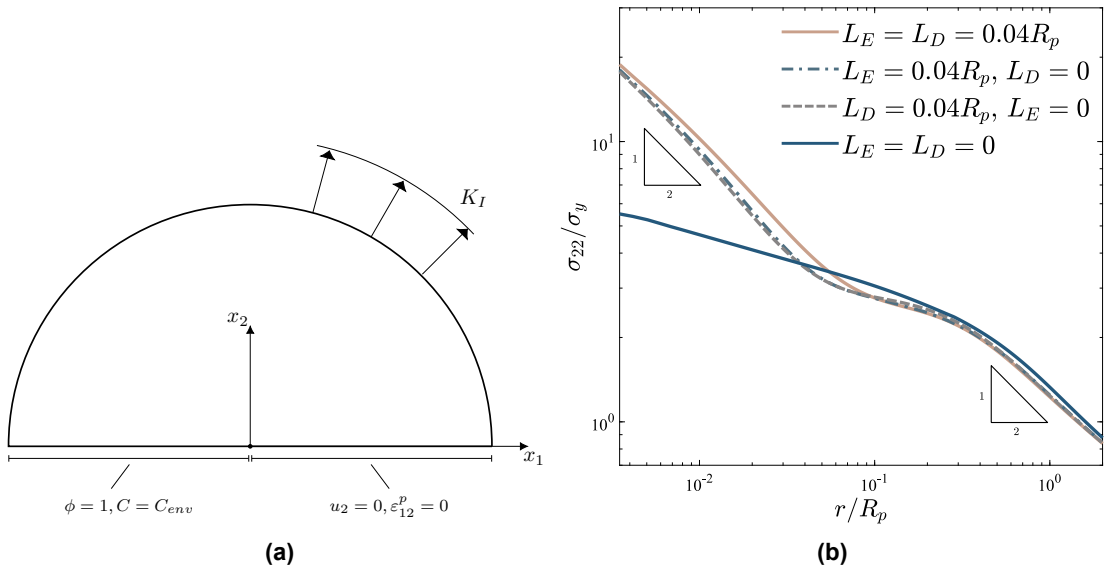

Figure 4.29: Modified boundary layer problem: a) Sketch of the boundary conditions. b) Distribution of crack opening stress in front of the crack tip. Adapted from [P5].

The computations are all performed under small scale yielding conditions. First, a stationary crack is considered in the absence of hydrogen and the plastic zone size can be approximated as

$$R_p = \frac{1}{3\pi}\left(\frac{K_I}{\sigma_y}\right)^2, \tag{4.18}$$

where K_I is the applied mode I stress intensity factor and σ_y is the initial yield stress. The crack tip opening stress σ_{22} is shown for different values of the plastic length scales in figure 4.29b. The cases considered are $L_E = 0.04R_p$ with $L_D = 0$, corresponding to purely energetic hardening, the opposite case, $L_D = 0.04R_p$ with $L_E = 0$, where the hardening is purely dissipative. In addition, a mixed case $L_E = L_D = L_p = 0.04R_p$ is considered where L_p denotes the plastic length scale in cases where the two are equal, which will be the case in later problems. Finally, a conventional J2 plasticity case with $L_p = 0$, corresponding to no gradient effects. The results reveal that almost independently of the distribution of the length scales, the gradient plastic cases recover the elastic $1/\sqrt{r}$ singularity very close the the crack tip inside the plastic zone. The result corresponds to an elastic core as presented in [117]. In conclusion, very close to the crack tip, plastic gradients play an immense role for the opening stress and also the hydrostatic stress, at least when plastic length scales are on the order $L_p \approx 0.04R_p$.

4.4.1 Influence of strain gradients on crack growth resistance.

Attention is now moved to initiation and growth of cracks. The influence of hydrogen is omitted here, but is investigated from section 4.4.2 onward. Rather than the current plastic zone size, we now introduce a reference fracture process zone size R_0 [17],

$$R_0 = \frac{1}{3\pi\left(1-\nu^2\right)}\frac{EG_c}{\sigma_y^2}. \tag{4.19}$$

Through the inherent critical stress of the phase field model σ_c , which is given in equation (2.24) and depends on the phase field length scale ℓ, a relation can be defined between the dimensionless groups R_0/ℓ and σ_c/σ_y;

$$\frac{R_0}{\ell} = \frac{256}{81\pi\left(1-\nu^2\right)}\left(\frac{\sigma_c}{\sigma_y}\right)^2. \tag{4.20}$$

Thus, the size of the phase field length scale relative to the fracture process zone is effectively a measure indicative of the necessary stress for brittle fracture to occur in the plastic solid. In addition, we introduce the references stress intensity factor K_0, which denotes the critical stress intensity factor for an identical linear elastic material under the same loading conditions as the problem considered and in the absence of hydrogen:

$$K_0 = \left(\frac{EG_c}{1-\nu^2}\right)^{1/2}. \tag{4.21}$$

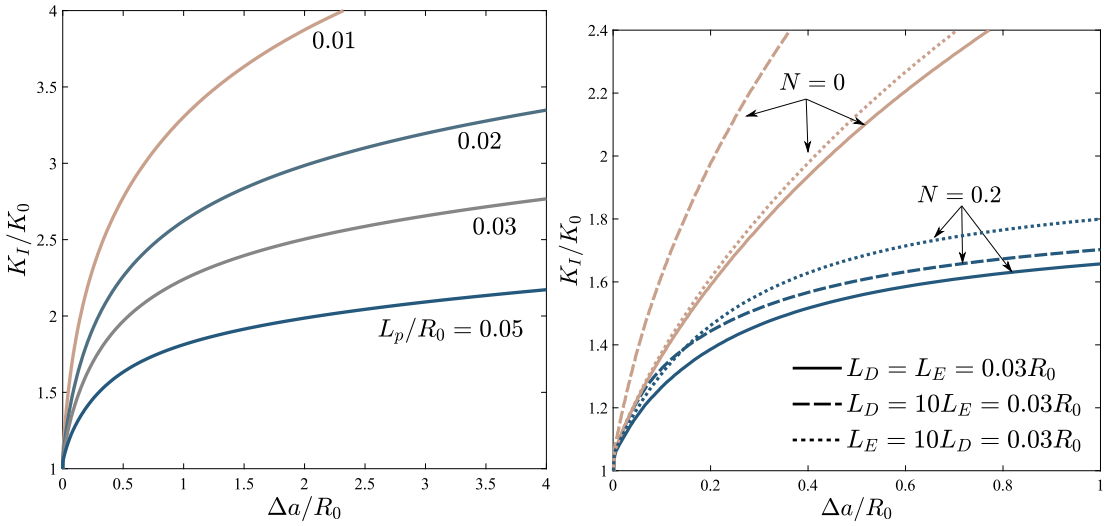

Figure 4.30: Fracture resistance in the modified boundary layer problem: a) Influence of varying plastic length scale. b) Influence of individual plastic length scales for two values of the hardening exponent N. Adapted from [P5].

As a first step in investigating the influence of plastic properties on crack growth resistance, plastic parameters are tested to verify the they yield the expected trends. Figure 4.30a shows that for smaller plastic length scales L_p, fracture resistance increases. This matches the expectation that the contribution of gradient hardening to crack tip stresses lead to crack growth at lower loads. Next, the plastic length scales are once again differentiated from one another to produce a mostly energetic, mostly dissipative and a mixed

hardening scenario. The analysis is repeated for two hardening exponents $N = 0$ and $N = 0.2$, as shown in figure 4.30b. Unsurprisingly, a larger hardening exponent leads to lower fracture resistance. More interestingly, in the $N = 0$ case, the contribution to hardening is dominated by the energetic length scale, while the dissipative contribution dominates in the $N = 0.2$ case. The difference arises from the constitutive equations (2.59) and (2.60), where the latter is linearly dependent on the gradient of plastic strain while the former is ultimately dictated by the power law (2.61).
Now, the influence of the critical stress, as given by the dimensionless group R_0/ℓ, is examined. Recall that in order for quasi-cleavage to occur, the stress level should be on the order of the lattice strength $\sigma_c \approx 10\sigma_y$, as discussed in section 2.2.3. The results are shown in figure 4.31 and reveal a very significant influence of the critical stress on fracture resistance. However, the result that crack growth occurs at all in contrary to existing result for conventional plasticity where crack growth does not occur if the critical stress exceeds $\approx 3 - 4\sigma_y$ [17].

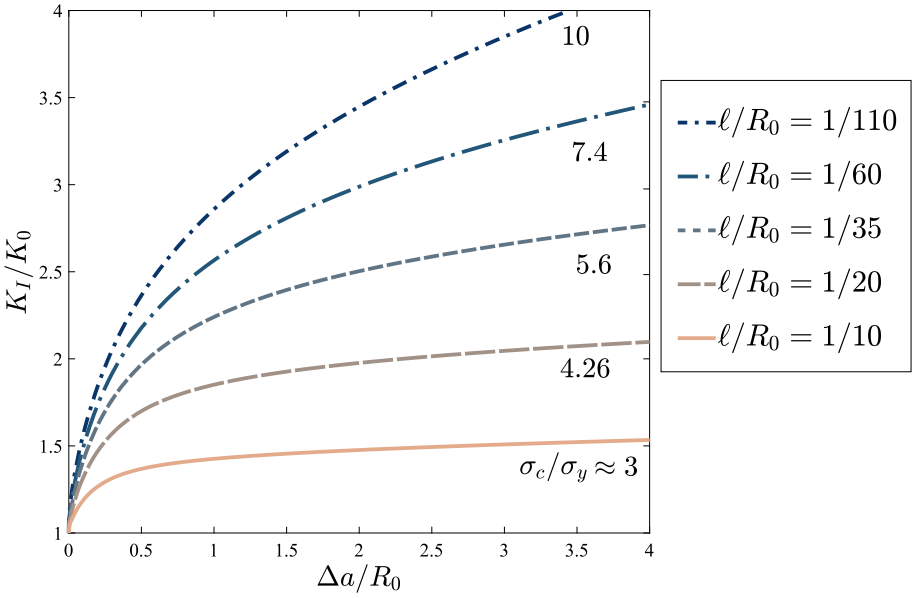

Figure 4.31: Influence of the dimensionless group ℓ/R_0, which effectively governs σ_c/σ_y, on the fracture resistance of the modified boundary layer. Adapted from [P5].

It should be noted, however, that although crack growth occurs at high levels of critical stress, it requires very high load levels and in this case a plastic length scale of $L_p = 0.03R_0$, which exceeds realistic values of $L_p \approx 0.001 - 0.01R_0$ for ductile steels [118]. In conclusion, strain gradient plasticity is sufficient to rationalize the quasi-cleavage fracture mode, but in the case of ductile steels, not at realistic material parameters.

4.4.2 Influence of hydrogen

Hydrogen is now considered in the model. In no cases are the specimens pre-charged with hydrogen. Instead, the crack surface is prescribed a hydrogen concentration $C = C_{env}$. Furthermore, the moving hydrogen boundary condition from section 3.1 is included in all results, except figure 4.32b. First, the influence of hydrogen is examined at a realistic plastic length scale $L_p = 0.01R_0$ in figure 4.32a. The results are obtained at a very slow load rate $\dot{K}_I/K_0 = 4 \cdot 10^{-s}\,\mathrm{s}^{-1}$, which is shown in figure 4.32b to be well within the rate-independent limit. Results in figure 4.32a reveal that for a realistic plastic length scale, the fracture resistance tends to infinity as the hydrogen concentration tends to zero. Mean-

while, for a high hydrogen concentration, fracture initiates well below the nominal fracture toughness and the fracture resistance appears to reach a horizontal just above K_0. Note that the results shown in figure 4.32b are not directly comparable to figure 4.32a, as the phase field length scale is here $\ell = R_0/60$, roughly corresponding to $\sigma_c = 7.4\sigma_y$. Note also the very large jump in load rate between the final two curves.

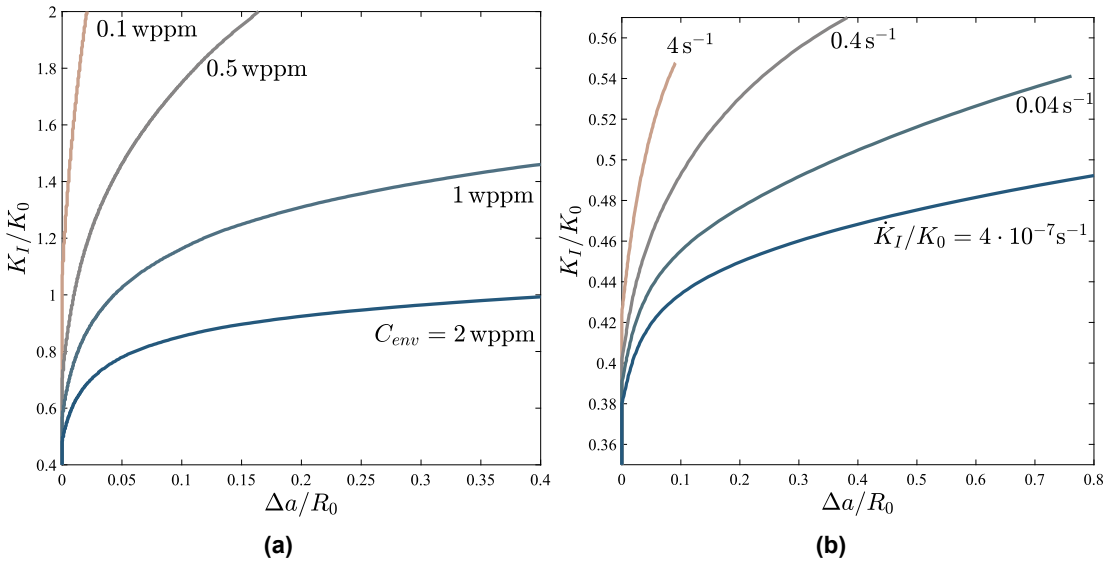

Figure 4.32: Fracture resistance in the modified boundary layer problem: a) Influence of hydrogen at a critical stress corresponding to quasi-cleavage in the load rate independent limit. b) Influence of load rate in the presence of hydrogen. Diffusion rate is $D = 0.0127\,\mathrm{mm}^2/\mathrm{s}$. Adapted from [P5].

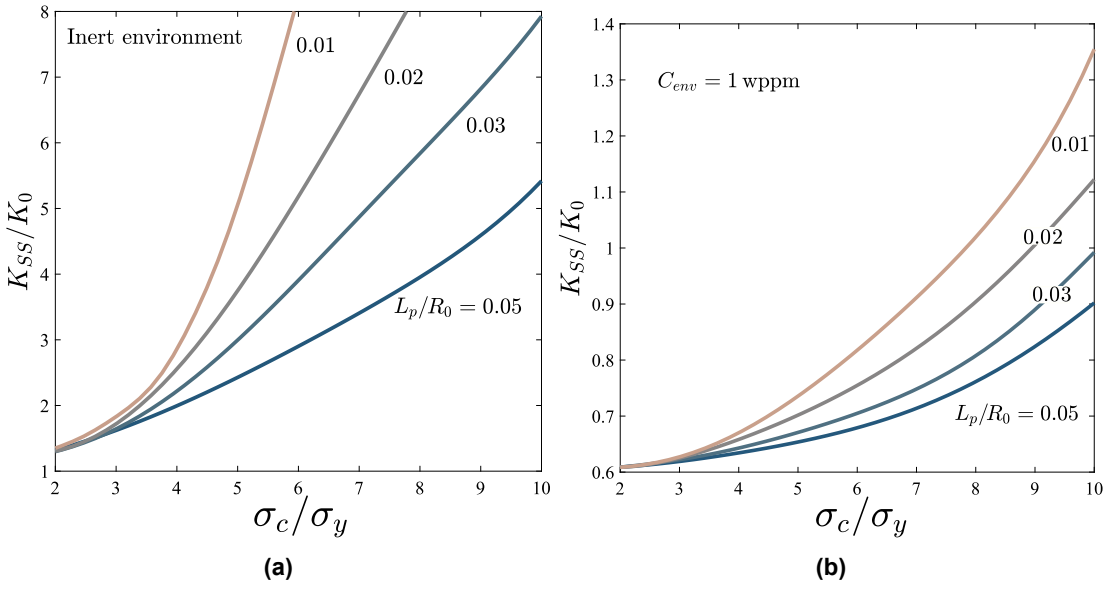

Figure 4.33: Steady state fracture toughness for increasing critical stress: a) Inert environment without hydrogen. b) Environmental hydrogen concentration prescribed on the crack surface. Adapted from [P5].

The horizontal asymptotes of fracture resistance curves are now termed the steady-state fracture toughness K_{SS} and denotes the load where the crack reaches a steady state of unstable brittle crack growth. The existence of a finite value of reasonable magnitude for the steady-state fracture toughness for a given material with $\sigma_c \approx 10\sigma_y$ implies that quasi-cleavage is feasible, under the assumption that the numerical model presented here is valid. We present in figures 4.33a and 4.33b steady state fracture toughness curves in the absence and presence of an environment hydrogen concentration of $C_{env} = 1\,\mathrm{wt.\ ppm}$, respectively.
It is noted that in the absence of hydrogen, very high steady state fracture toughnesses are observed when the critical stress approaches the lattice strength, even for very large values of the plastic lengths scales. Near realistic values of the plastic length scale of $L_p = 0.01R_0$, the steady state fracture toughness appears to rapidly tend towards infinity. Meanwhile, very modest values of steady state fracture toughness is observed in the presence of hydrogen across all examined values of L_p and σ_c. Thus, it can be concluded that within the presented model, plastic strain gradient hardening and hydrogen embrittlement by hydrogen-enhanced decohesion (HEDE) is sufficient in unison to rationalize the quasi-cleavage fracture mode.

4.4.3 Quantitative agreement with experimental results

As a final result, the quantitative agreement of the full model with strain gradient effects with the experimental crack initiation results of ultra-high-strength steels AerMet100 and a similar alloy Ferrium M54 from [119] and [120]. Specifically, the aim is to replicate the results for AerMet100, with the Ferrium results shown for context. The material properties for AerMet100 as reported in [119] are used directly. The phase field length scale is chosen to yield a critical stress 10 times the initial yield stress of $\sigma_y = 1725\,\mathrm{MPa}$. The effective critical stress intensity factor is approximated as the maximum crack initiation value observed where the fracture modes is reported as brittle, $K_0 = 30\,\mathrm{Mpa}\sqrt{\mathrm{m}}$. The experiments are reported to be carried out with pre-cracked fracture mechanics specimens submerged in a saltwater solution of $0.6\,\mathrm{M}$ NaCl under potentiostatic control. The experiments are repeated for various imposed elecrochemical potentials in the range $E_p = -1.1\,\mathrm{V_{SCE}}$ to $E_p = -0.5\,\mathrm{V_{SCE}}$. The applied loading rate is slow and the effective available hydrogen concentrations can be approximated from empirical formulae as was done in [121], where a similar comparison to experiments was carried out. The only case of tuning of material parameters utillized to obtain the best possible agreement with experiments is an adjustment of the embrittlement parameter from Eq. (2.6) from $\chi = 0.89$ to $\chi = 0.97$. The results in figure 4.34 show an excellent agreement between the model presented here and the experimental results in the regime where experimental scatter is small. In the domain where the imposed electrochemical potential is larger than the equilibrium potential, experimental scatter is large and the agreement seems poorer, even when the partially ductile fractures are not considered.

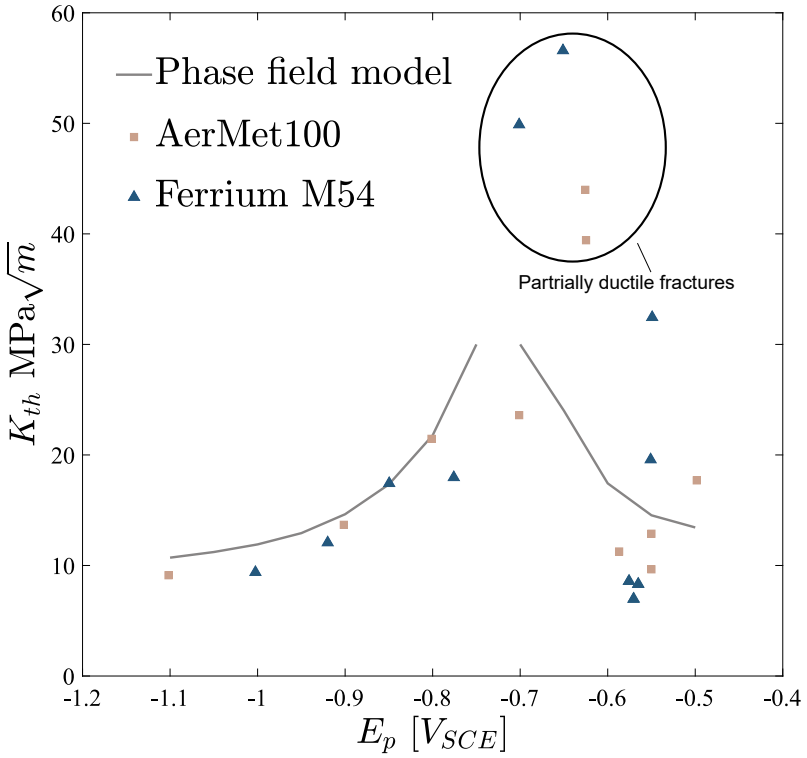

Figure 4.34: Comparison of model predictions with experiemntal results from [119] and [120]. Adapted from [P5].

5 | Conclusions

This thesis presents an advanced model for hydrogen-assisted brittle fracture in a phase field framework. A large number of numerical tests have been performed to asses the suitability of the model and its components. The phase field has received special attention as it has shown great potential and is an active and thriving research field. We have shown that the phase field fracture model is a robust tool, capable of capturing advanced crack paths such as dynamic branching and interaction of several defects. Furthermore crack initiation results are very close to established linear elastic fracture mechanics predictions. The extension of the phase field fracture model to hydrogen embrittlement is a flexible one, which can be adapted for future experimental findings. By including strain gradient hardening effects, much larger crack tip stresses are observed, which translates to higher crack tip hydrogen concentrations and fracture at lower loads. These crack tip effects play a key role in understanding how brittle fracture occurs in an otherwise ductile material.
One main conclusion from each publication in order:

- The BFGS algorithm provides robust solutions for the phase field fracture model very efficiently relative to the single-pass staggered algorithm.
- The phase field fracture model provides accurate solutions for crack initiation for cracks of all lengths that are prescribed through the phase field itself.
- When fatigue loading is considered the interaction of diffusion rate and loading frequency plays an important role in the response, which is accurately portrayed in the model.
- With the capability to predict hydrogen-assisted failure, the phase field model is very promising for a number of industrial applications, such as virtual experiments and in-service strength assessments.
- Plastic strain gradient effects play and important role in the underlying physics of hydrogen embrittlement. Hydrogen embrittlement and strain gradient effects together are able to rationalize the quasi-cleavage failure mode.

5.1 Directions for further work

There are many directions in which future work based in the work presented here could be taken. Currently the focus is on the ongoing work of accelerating phase field fatigue calculations, which currently require a very large amount of computational effort.
Another very interesting direction would be to explore the interactions between hydrogen and plasticity further, taking into account microstructural trapping as described in section 2.2.2. This could potentially lead to the ability to also capture completely or partially ductile fractures and a ductile-to-brittle transition. However, this would most likely be associated with some significant computational difficulties.
Some efforts have already been expended towards developing a phase field model for the hydrogen-induced fast fracture mechanism presented in [91], using a rate-dependent phase field model.
Another interesting subject would be to use an interfacial phase field model such as the one in [54] for grain boundaries to make a microstructural model capable of handling cracking both through grains and grain boundaries, which may not be affected identically by hydrogen. Such a direction of work would be inspired by [122].

Bibliography

[1] A . A . Griffith. “The Phenomena of Rupture and Flow in Solids”. In: *Philosophical transactions of the royal society of london. Series A, containing papers of a mathematical or physical character* 221.1921 (1920), pp. 163–198.

[2] W H Johnson. “On Some Remarkable Changes Produced in Iron and Steel by the Action of Hydrogen and Acids”. In: *Proceedings of the Royal Society of London* 23 (1875), pp. 168–179.

[3] Tim Hageman and Emilio Martínez-Pañeda. “An electro-chemo-mechanical framework for predicting hydrogen uptake in metals due to aqueous electrolytes”. In: *Corrosion Science* 208 (2022), p. 110681. DOI: https://doi.org/10.1016/j.corsci.2022.110681.

[4] Alexander Troiano. “Embrittlement by Hydrogen and Other Interstitials”. In: *Metal progress* (1960), pp. 112–117.

[5] W Beck et al. “Hydrogen Permeation in Metals as a Function of Stress, Temperature and Dissolved Hydrogen Concentration”. In: *Proceedings of the Royal Society of London. Series A, Mathematical and Physical Sciences* 290.1421 (1966), pp. 220–235.

[6] Xinfeng Li et al. “Review of Hydrogen Embrittlement in Metals: Hydrogen Diffusion, Hydrogen Characterization, Hydrogen Embrittlement Mechanism and Prevention”. In: *Acta Metallurgica Sinica (English Letters)* 33.6 (2020), pp. 759–773. DOI: 10.1007/s40195-020-01039-7.

[7] R. A. Oriani. “The diffusion and trapping of hydrogen in steel”. In: *Acta Metallurgica* 18.1 (1970), pp. 147–157. DOI: 10.1016/0001-6160(70)90078-7.

[8] I. M. Robertson and H. K. Birnbaum. *Effect of Hydrogen on the Dislocation Structure of Deformed Nickel.* 9. Pergamon Books Ltd, 1986, pp. 585–590. DOI: 10.1016/b978-0-08-034813-1.50081-4.

[9] John P. Hirth. “Effects of hydrogen on the properties of iron and steel”. In: *Metallurgical Transactions A* 11.6 (1980), pp. 861–890. DOI: 10.1007/BF02654700.

[10] Jun Song and W. A. Curtin. “Atomic mechanism and prediction of hydrogen embrittlement in iron”. In: *Nature Materials* 12.2 (2013), pp. 145–151. DOI: 10.1038/nmat3479.

[11] Degang Xie et al. “Hydrogenated vacancies lock dislocations in aluminium”. In: *Nature Communications* 7.1 (2016), p. 13341. DOI: 10.1038/ncomms13341.

[12] Ian M. Robertson et al. “Hydrogen Embrittlement Understood”. In: *Metallurgical and Materials Transactions A: Physical Metallurgy and Materials Science* 46.6 (2015), pp. 2323–2341. DOI: 10.1007/s11661-015-2836-1.

[13] Mohsen Dadfarnia et al. “Recent advances on hydrogen embrittlement of structural materials”. In: *International Journal of Fracture* 196.1 (2015), pp. 223–243. DOI: 10.1007/s10704-015-0068-4.

[14] R Dutton et al. “Mechanisms of hydrogen induced delayed cracking in hydride forming materials”. In: *Metallurgical Transactions A* 8.10 (1977), pp. 1553–1562. DOI: 10.1007/BF02644858.

[15] H. K. Birnbaum and P. Sofronis. “Hydrogen-enhanced localized plasticity - a mechanism for hydrogen-related fracture”. In: *Materials Science and Engineering A* 176 (1994), pp. 191–202. DOI: 10.1016/0921-5093(94)90975-X.

[16] D. E. Jiang and Emily A. Carter. “First principles assessment of ideal fracture energies of materials with mobile impurities: Implications for hydrogen embrittlement of metals”. In: *Acta Materialia* 52.16 (2004), pp. 4801–4807. DOI: 10.1016/j.actamat.2004.06.037.

[17] J. W. Hutchinson and Viggo Tvergaard. “The relation between crack growth resistance and fracture process parameters elastic-plastic solids”. In: *Journal of the Mechanics and Physics of Solids* 40.6 (1992), pp. 1377–1397. DOI: 10.1016/0022-5096(92)90020-3.

[18] N. Moës, A. Gravouil, and T. Belytschko. “Non-planar 3D crack growth by the extended finite element and level sets-Part I: Mechanical model”. In: *International Journal for Numerical Methods in Engineering* 53.11 (2002), pp. 2549–2568. DOI: 10.1002/nme.429.

[19] Xiao Tian Zhang et al. “Element fracture technique for hypervelocity impact simulation”. In: *Advances in Space Research* 55.9 (May 2015), pp. 2293–2304. DOI: 10.1016/J.ASR.2015.01.040.

[20] Ellen Kuhl, Ekkehard Ramm, and René De Borst. “An anisotropic gradient damage model for quasi-brittle materials”. In: *Computer Methods in Applied Mechanics and Engineering* 183.1-2 (Mar. 2000), pp. 87–103. DOI: 10.1016/S0045-7825(99)00213-3.

[21] L. A.T. Mororó, A. Poot, and F. P. van der Meer. “Skeleton curve and phantom node method for the Thick Level Set approach to fracture”. In: *Engineering Fracture Mechanics* 268.April (2022), p. 108443. DOI: 10.1016/j.engfracmech.2022.108443.

[22] G. A. Francfort and J. -J. Marigo. “Revisiting Brittle Fracture As an Energy Minimization Problem”. In: *Journal of the Mechanics and Physics of Solids* 46.8 (1998), pp. 1319–1342.

[23] Alain Karma, David A Kessler, and Herbert Levine. “Phase-Field Model of Mode III Dynamic Fracture”. In: (2001), pp. 3–6. DOI: 10.1103/PhysRevLett.87.045501.

[24] Blaise Bourdin, Gilles A. Francfort, and Jean Jacques Marigo. *The variational approach to fracture*. 2008, pp. 1–164. DOI: 10.1007/978-1-4020-6395-4.

[25] Hanen Amor, Jean Jacques Marigo, and Corrado Maurini. “Regularized formulation of the variational brittle fracture with unilateral contact: Numerical experiments”. In: *Journal of the Mechanics and Physics of Solids* 57.8 (2009), pp. 1209–1229. DOI: 10.1016/j.jmps.2009.04.011.

[26] Christian Miehe, Martina Hofacker, and Fabian Welschinger. “A phase field model for rate-independent crack propagation: Robust algorithmic implementation based on operator splits”. In: *Computer Methods in Applied Mechanics and Engineering* 199.45-48 (2010), pp. 2765–2778. DOI: 10.1016/j.cma.2010.04.011.

[27] C. Miehe, Fabian Welschinger, and M. Hofacker. “Thermodynamically consistent phase-field models of fracture: Variational principles and multi-field FE implementations”. In: *International Journal for Numerical Methods in Engineering* 83 (2010), pp. 1273–1311. DOI: 10.1002/nme.

[28] Aditya Kumar et al. “Revisiting nucleation in the phase-Field approach to brittle fracture”. In: *Journal of the Mechanics and Physics of Solids* 142 (2020), p. 104027. DOI: 10.1016/j.jmps.2020.104027.

[29] Markus Klinsmann et al. “An assessment of the phase field formulation for crack growth”. In: *Computer Methods in Applied Mechanics and Engineering* 294 (2015), pp. 313–330. DOI: 10.1016/j.cma.2015.06.009.

[30] E. Tanné et al. “Crack nucleation in variational phase-field models of brittle fracture”. In: *Journal of the Mechanics and Physics of Solids* 110 (2018), pp. 80–99. DOI: 10.1016/j.jmps.2017.09.006.

[31] Jean Jacques Marigo, Corrado Maurini, and Kim Pham. “An overview of the modelling of fracture by gradient damage models”. In: *Meccanica* 51.12 (2016), pp. 3107–3128. DOI: 10.1007/s11012-016-0538-4.

[32] Michael J. Borden et al. “A phase-field description of dynamic brittle fracture”. In: *Computer Methods in Applied Mechanics and Engineering* 217-220 (2012), pp. 77–95. DOI: 10.1016/j.cma.2012.01.008.

[33] Alexander Schlüter et al. “Phase field approximation of dynamic brittle fracture”. In: *Computational Mechanics* 54.5 (2014), pp. 1141–1161. DOI: 10.1007/s00466-014-1045-x.

[34] Shuwei Zhou, Timon Rabczuk, and Xiaoying Zhuang. “Phase field modeling of quasi-static and dynamic crack propagation: COMSOL implementation and case studies”. In: *Advances in Engineering Software* 122.April (2018), pp. 31–49. DOI: 10.1016/j.advengsoft.2018.03.012.

[35] M. Strobl and Th Seelig. “Phase field modeling of Hertzian indentation fracture”. In: *Journal of the Mechanics and Physics of Solids* 143 (2020). DOI: 10.1016/j.jmps.2020.104026.

[36] Jian Ying Wu et al. “Three-dimensional phase-field modeling of mode I + II/III failure in solids”. In: *Computer Methods in Applied Mechanics and Engineering* 373 (2021), p. 113537. DOI: 10.1016/j.cma.2020.113537.

[37] P. Carrara et al. “A framework to model the fatigue behavior of brittle materials based on a variational phase-field approach”. In: *Computer Methods in Applied Mechanics and Engineering* 361 (2020), p. 112731. DOI: 10.1016/j.cma.2019.112731. arXiv: 1811.02244.

[38] Yu Sheng Lo et al. “A phase-field model for fatigue crack growth”. In: *Journal of the Mechanics and Physics of Solids* 132 (2019), p. 103684. DOI: 10.1016/j.jmps.2019.103684.

[39] T. T. Nguyen et al. “A phase-field method for computational modeling of interfacial damage interacting with crack propagation in realistic microstructures obtained by microtomography”. In: *Computer Methods in Applied Mechanics and Engineering* 312 (2016), pp. 567–595. DOI: 10.1016/j.cma.2015.10.007.

[40] J. Reinoso, M. Paggi, and C. Linder. “Phase field modeling of brittle fracture for enhanced assumed strain shells at large deformations: formulation and finite element implementation”. In: *Computational Mechanics* 59.6 (2017), pp. 981–1001. DOI: 10.1007/s00466-017-1386-3.

[41] Charlotte Kuhn, Timo Noll, and Ralf Müller. “On phase field modeling of ductile fracture”. In: *GAMM Mitteilungen* 39.1 (2016), pp. 35–54. DOI: 10.1002/gamm.201610003.

[42] C. Miehe, S. Teichtmeister, and F. Aldakheel. “Phase-field modelling of ductile fracture: a variational gradient-extended plasticity-damage theory and its micromorphic regularization”. In: *Philosophical Transactions of the Royal Society A: Mathematical, Physical and Engineering Sciences* 374.20150170 (2016). DOI: 10.1016/S0140-6736(02)10308-4.

[43] Marreddy Ambati, Tymofiy Gerasimov, and Laura De Lorenzis. “Phase field modeling of ductile fracture”. In: *Computational Mechanics* 55.1 (2015), pp. 1017–1040.

[44] R Alessi et al. “Comparison of Phase-Field Models of Fracture Coupled with Plasticity”. In: *Computational Methods in Applied Sciences* 46 (2018), pp. 1–21. DOI: 10.1007/978-3-319-60885-3.

[45] Ye Feng and Jie Li. “Phase-Field cohesive fracture theory: A unified framework for dissipative systems based on variational inequality of virtual works”. In: *Journal of the Mechanics and Physics of Solids* 159 (2022), p. 104737.

[46] Jian-ying Wu. “A unified phase-field theory for the mechanics of damage and quasi-brittle failure”. In: *Journal of the Mechanics and Physics of Solids* 103 (2017), pp. 72–99. DOI: 10.1016/j.jmps.2017.03.015.

[47] Aditya Kumar, Gilles A. Francfort, and Oscar Lopez-Pamies. “Fracture and healing of elastomers: A phase-transition theory and numerical implementation”. In: *Journal of the Mechanics and Physics of Solids* 112 (2018), pp. 523–551. DOI: 10.1016/j.jmps.2018.01.003.

[48] Marlini Simoes and Emilio Martínez-Pañeda. “Phase field modelling of fracture and fatigue in Shape Memory Alloys”. In: *Computer Methods in Applied Mechanics and Engineering* 373 (2021), p. 113504. DOI: https://doi.org/10.1016/j.cma.2020.113504.

[49] Hirshikesh et al. “Phase field modelling of crack propagation in functionally graded materials”. In: *Composites Part B: Engineering* 169 (2019), pp. 239–248. DOI: https://doi.org/10.1016/j.compositesb.2019.04.003.

[50] B B Yin and L W Zhang. “Phase field method for simulating the brittle fracture of fiber reinforced composites”. In: *Engineering Fracture Mechanics* 211 (2019), pp. 321–340. DOI: https://doi.org/10.1016/j.engfracmech.2019.02.033.

[51] Markus Klinsmann et al. “Modeling crack growth during Li insertion in storage particles using a fracture phase field approach”. In: *Journal of the Mechanics and Physics of Solids* 92 (2016), pp. 313–344. DOI: 10.1016/j.jmps.2016.04.004.

[52] Xiaoxuan Zhang, Andreas Krischok, and Christian Linder. “A variational framework to model diffusion induced large plastic deformation and phase field fracture during initial two-phase lithiation of silicon electrodes”. In: *Computer Methods in Applied*

Mechanics and Engineering 312 (2016), pp. 51–77. DOI: 10.1016/j.cma.2016.05.007.

[53] Blaise Bourdin et al. “Morphogenesis and Propagation of Complex Cracks Induced by Thermal Shocks”. In: *Phys. Rev. Lett.* 112.1 (Jan. 2014), p. 14301. DOI: 10.1103/PhysRevLett.112.014301.

[54] Jia Yu Ye and Lu Wen Zhang. “Damage evolution of polymer-matrix multiphase composites under coupled moisture effects”. In: *Computer Methods in Applied Mechanics and Engineering* 388 (2022), p. 114213. DOI: 10.1016/j.cma.2021.114213.

[55] F. P. Duda et al. “A phase-field model for solute-assisted brittle fracture in elastic-plastic solids”. In: *International Journal of Plasticity* 102.November 2017 (2018), pp. 16–40. DOI: 10.1016/j.ijplas.2017.11.004.

[56] Emilio Martínez-Pañeda, Alireza Golahmar, and Christian F. Niordson. “A phase field formulation for hydrogen assisted cracking”. In: *Computer Methods in Applied Mechanics and Engineering* 342 (2018), pp. 742–761. DOI: 10.1016/j.cma.2018.07.021.

[57] Lallit Anand, Yunwei Mao, and Brandon Talamini. “On modeling fracture of ferritic steels due to hydrogen embrittlement”. In: *Journal of the Mechanics and Physics of Solids* 122 (2019), pp. 280–314. DOI: 10.1016/j.jmps.2018.09.012.

[58] Peter Gudmundson. “A unified treatment of strain gradient plasticity”. In: *Journal of the Mechanics and Physics of Solids* 52.6 (2004), pp. 1379–1406. DOI: 10.1016/j.jmps.2003.11.002.

[59] B. Bourdin, G. A. Francfort, and J. J. Marigo. “NUMERICAL EXPERIMENTS IN REVISITED BRITTLE FRACTURE”. In: *Journal of the Mechanics and Physics of Solids* 48.4 (2000), pp. 1–23. DOI: //dx.doi.org/10.1016/S0022-5096(99)00028-9.

[60] L Ambrosio and V M Tortorelli. “Approximation of functionals depending on jumps by elliptic functionals via gamma-convergence”. In: *Communications on Pure and Applied Mathematics* 43 (1991), pp. 999–1036.

[61] David Mumford and Jayant Shah. “Optimal approximations by piecewise smooth functions and associated variational problems”. In: *Communications on Pure and Applied Mathematics* 42.5 (1989), pp. 577–685.

[62] Charlotte Kuhn, Alexander Schlüter, and Ralf Müller. “On degradation functions in phase field fracture models”. In: *Computational Materials Science* 108 (2015), pp. 374–384. DOI: https://doi.org/10.1016/j.commatsci.2015.05.034.

[63] Juan Michael Sargado et al. “High-accuracy phase-field models for brittle fracture based on a new family of degradation functions”. In: *Journal of the Mechanics and Physics of Solids* 111 (2018), pp. 458–489. DOI: 10.1016/j.jmps.2017.10.015.

[64] Yousef Navidtehrani, Covadonga Betegón, and Emilio Martínez-Pañeda. “A general framework for decomposing the phase field fracture driving force, particularised to a Drucker–Prager failure surface”. In: *Theoretical and Applied Fracture Mechanics* 121 (Oct. 2022), p. 103555. DOI: 10.1016/J.TAFMEC.2022.103555.

[65] Michael J Borden et al. “A higher-order phase-field model for brittle fracture: Formulation and analysis within the isogeometric analysis framework”. In: *Computer Methods in Applied Mechanics and Engineering* 273 (2014), pp. 100–118. DOI: https://doi.org/10.1016/j.cma.2014.01.016.

[66] Francesco Freddi and Gianni Royer-Carfagni. “Regularized variational theories of fracture: A unified approach”. In: *Journal of the Mechanics and Physics of Solids* 58.8 (2010), pp. 1154–1174. DOI: 10.1016/j.jmps.2010.02.010.

[67] Marreddy Ambati, Tymofiy Gerasimov, and Laura De Lorenzis. “A review on phase-field models of brittle fracture and a new fast hybrid formulation”. In: *Computational Mechanics* 55.2 (2014), pp. 383–405. DOI: 10.1007/s00466-014-1109-y.

[68] Michael Strobl and Thomas Seelig. “A novel treatment of crack boundary conditions in phase field models of fracture”. In: *Pamm* 15.1 (2015), pp. 155–156. DOI: 10.1002/pamm.201510068.

[69] Michael Strobl and Thomas Seelig. “Restrictions in phase field modeling of brittle fracture”. In: *Pamm* 18.1 (2018), e201800157. DOI: 10.1002/pamm.201800157.

[70] Michael Strobl and Thomas Seelig. “On constitutive assumptions in phase field approaches to brittle fracture”. In: *Procedia Structural Integrity* 2 (2016), pp. 3705–3712. DOI: 10.1016/j.prostr.2016.06.460.

[71] Christian Steinke and Michael Kaliske. “A phase-field crack model based on directional stress decomposition”. In: *Computational Mechanics* 63.5 (2019), pp. 1019–1046. DOI: 10.1007/s00466-018-1635-0.

[72] J. Storm, D. Supriatna, and M. Kaliske. “The concept of representative crack elements for phase-field fracture: Anisotropic elasticity and thermo-elasticity”. In: *International Journal for Numerical Methods in Engineering* 121.5 (2020), pp. 779–805. DOI: 10.1002/nme.6244.

[73] P Paris and F Erdogan. “A Critical Analysis of Crack Propagation Laws”. In: *Journal of Basic Engineering* 85.4 (Dec. 1963), pp. 528–533. DOI: 10.1115/1.3656900.

[74] Karlo Seleš et al. “A general phase-field model for fatigue failure in brittle and ductile solids”. In: *Computational Mechanics* 67.5 (2021), pp. 1431–1452. DOI: 10.1007/s00466-021-01996-5.

[75] Pascal J. Loew et al. “Accelerating fatigue simulations of a phase-field damage model for rubber”. In: *Computer Methods in Applied Mechanics and Engineering* 370 (2020), p. 113247. DOI: 10.1016/j.cma.2020.113247.

[76] Gergely Molnár et al. “Thermodynamically consistent linear-gradient damage model in Abaqus”. In: *Engineering Fracture Mechanics* 266 (2022), p. 108390.

[77] Timo Heister, Mary F. Wheeler, and Thomas Wick. “A primal-dual active set method and predictor-corrector mesh adaptivity for computing fracture propagation using a phase-field approach”. In: *Computer Methods in Applied Mechanics and Engineering* 290 (June 2015), pp. 466–495. DOI: 10.1016/J.CMA.2015.03.009.

[78] Charlotte Kuhn and Ralf Mueller. “A NEW FINITE ELEMENT TECHNIQUE FOR A PHASE FIELD MODEL OF BRITTLE FRACTURE”. In: *JOURNAL OF THEORETICAL AND APPLIED MECHANICS* 49.4 (2011), pp. 1115–1133.

[79] Juan Michael Sargado et al. “A combined finite element–finite volume framework for phase-field fracture”. In: *Computer Methods in Applied Mechanics and Engineering* 373 (2021), p. 113474. DOI: 10.1016/j.cma.2020.113474. arXiv: 1904.12395.

[80] P. Sofronis and R. M. McMeeking. “Numerical analysis of hydrogen transport near a blunting crack tip”. In: *Journal of the Mechanics and Physics of Solids* 37.3 (1989), pp. 317–350. DOI: 10.1016/0022-5096(89)90002-1.

[81] Mehrdad Isfandbod and Emilio Martínez-Pañeda. “A mechanism-based multi-trap phase field model for hydrogen assisted fracture”. In: *International Journal of Plasticity* 144 (2021), p. 103044. DOI: https://doi.org/10.1016/j.ijplas.2021.103044.

[82] A Mc Nabb and P R Foster. “A new analysis of the diffusion of hydrogen in iron and ferritic steels”. In: *TMS AIME* 227 (1963), p. 618.

[83] Emilio Martínez-Pañeda et al. “Generalised boundary conditions for hydrogen transport at crack tips”. In: *Corrosion Science* 173.March (2020), p. 108698. DOI: 10.1016/j.corsci.2020.108698. arXiv: 2004.05611.

[84] S. Serebrinsky, E. A. Carter, and M. Ortiz. “A quantum-mechanically informed continuum model of hydrogen embrittlement”. In: *Journal of the Mechanics and Physics of Solids* 52.10 (2004), pp. 2403–2430. DOI: 10.1016/j.jmps.2004.02.010.

[85] A. Alvaro et al. “Hydrogen embrittlement in nickel, visited by first principles modeling, cohesive zone simulation and nanomechanical testing”. In: *International Journal of Hydrogen Energy* 40.47 (2015), pp. 16892–16900. DOI: 10.1016/j.ijhydene.2015.06.069.

[86] Chuanjie Cui, Rujin Ma, and Emilio Martínez-Pañeda. “A generalised, multi-phase-field theory for dissolution-driven stress corrosion cracking and hydrogen embrittlement”. In: *Journal of the Mechanics and Physics of Solids* 166 (2022), p. 104951. DOI: https://doi.org/10.1016/j.jmps.2022.104951.

[87] N. A. Fleck et al. “Strain gradient plasticity: Theory and experiment”. In: *Acta Metallurgica Et Materialia* 42.2 (1994), pp. 475–487. DOI: 10.1016/0956-7151(94)90502-9.

[88] J. S. Stölken and A. G. Evans. “A microbend test method for measuring the plasticity length scale”. In: *Acta Materialia* 46.14 (1998), pp. 5109–5115. DOI: 10.1016/S1359-6454(98)00153-0.

[89] Emilio Martínez-Pañeda et al. “The role of plastic strain gradients in the crack growth resistance of metals”. In: *Journal of the Mechanics and Physics of Solids* 126 (2019), pp. 136–150. DOI: 10.1016/j.jmps.2019.02.011.

[90] Anna Gustafsson and Hanna Isaksson. “Phase field models of interface failure for bone application - evaluation of open-source implementations”. In: *Theoretical and Applied Fracture Mechanics* 121 (2022), p. 103432. DOI: https://doi.org/10.1016/j.tafmec.2022.103432.

[91] Siamak S. Shishvan, Gábor Csányi, and Vikram S. Deshpande. “Hydrogen induced fast-fracture”. In: *Journal of the Mechanics and Physics of Solids* 134 (2020), p. 103740. DOI: 10.1016/j.jmps.2019.103740.

[92] Thomas Linse et al. “A convergence study of phase-field models for brittle fracture”. In: *Engineering Fracture Mechanics* 184 (2017), pp. 307–318. DOI: 10.1016/j.engfracmech.2017.09.013.

[93] Jian-ying Wu and Yuli Huang. “Comprehensive implementations of phase-field damage models in Abaqus”. In: *Theoretical and Applied Fracture Mechanics* 106.December 2019 (2020), p. 102440. DOI: 10.1016/j.tafmec.2019.102440.

[94] Tymofiy Gerasimov and Laura De Lorenzis. “On penalization in variational phase-field models of brittle fracture”. In: *Computer Methods in Applied Mechanics and Engineering* 354 (2019), pp. 990–1026. arXiv: arXiv:1811.05334v1.

[95] Pascal J. Loew, Bernhard Peters, and Lars A.A. Beex. “Rate-dependent phase-field damage modeling of rubber and its experimental parameter identification”. In: *Journal of the Mechanics and Physics of Solids* 127 (2019), pp. 266–294. DOI: 10.1016/j.jmps.2019.03.022.

[96] T. Gerasimov and L. De Lorenzis. “A line search assisted monolithic approach for phase-field computing of brittle fracture”. In: *Computer Methods in Applied Mechanics and Engineering* 312 (2016), pp. 276–303. DOI: 10.1016/j.cma.2015.12.017.

[97] Olivier Lampron, Daniel Therriault, and Martin Lévesque. “An efficient and robust monolithic approach to phase-field brittle fracture using a modified Newton method”. In: *Computer Methods in Applied Mechanics and Engineering* 306 (2021).

[98] Elias Börjesson, Joris J.C. Remmers, and Martin Fagerström. “A generalised path-following solver for robust analysis of material failure”. In: *Computational Mechanics* (2022). DOI: 10.1007/s00466-022-02175-w.

[99] Alena Kopaničáková, Hardik Kothari, and Rolf Krause. *Nonlinear Field-split Preconditioners for Solving Monolithic Phase-field Models of Brittle Fracture*. 2022. DOI: 10.48550/ARXIV.2203.13738.

[100] Jian Ying Wu, Yuli Huang, and Vinh Phu Nguyen. “On the BFGS monolithic algorithm for the unified phase field damage theory”. In: *Computer Methods in Applied Mechanics and Engineering* 360 (2020), p. 112704. DOI: 10.1016/j.cma.2019.112704.

[101] Karlo Seleš et al. “A residual control staggered solution scheme for the phase-field modeling of brittle fracture”. In: *Engineering Fracture Mechanics* 205.September 2018 (2019), pp. 370–386. DOI: 10.1016/j.engfracmech.2018.09.027.

[102] Thomas Wick. “An Error-Oriented Newton/Inexact Augmented Lagrangian Approach for Fully Monolithic Phase-Field Fracture Propagation”. In: *SIAM Journal on Scientific Computing* 39.4 (2017), B589–B617. DOI: 10.1137/16M1063873.

[103] R H J Peerlings et al. “Gradient-enhanced damage modelling of high-cycle fatigue”. In: *International Journal for Numerical Methods in Engineering* 49.12 (2000), pp. 1547–1569. DOI: 10.1002/1097-0207(20001230)49:12<1547::AID-NME16>3.0.CO;2-D.

[104] Thomas Titscher and Jörg F. Unger. “Efficient higher-order cycle jump integration of a continuum fatigue damage model”. In: *International Journal of Fatigue* 141.April (2020), p. 105863. DOI: 10.1016/j.ijfatigue.2020.105863.

[105] Jacob Fish and Qing Yu. “Computational mechanics of fatigue and life predictions for composite materials and structures”. In: *Computer Methods in Applied Mechanics and Engineering* 191.43 (2002), pp. 4827–4849. DOI: https://doi.org/10.1016/S0045-7825(02)00401-2.

[106] D. Cojocaru and A. M. Karlsson. “A simple numerical method of cycle jumps for cyclically loaded structures”. In: *International Journal of Fatigue* 28.12 (2006), pp. 1677–1689. DOI: 10.1016/j.ijfatigue.2006.01.010.

[107] Berthold K. Horn and Brian G. Schunck. *Determining Optical Flow*. 1981. DOI: 10.1117/12.965761.

[108] Christopher G Harris and M J Stephens. “A Combined Corner and Edge Detector”. In: *Alvey Vision Conference*. 1988.

[109] Jaehwan Ma, Sang Won Bae, and Sunghee Choi. “3D medial axis point approximation using nearest neighbors and the normal field”. In: *The Visual Computer* 28.1 (2012), pp. 7–19. DOI: 10.1007/s00371-011-0594-7.

[110] E. Tanné et al. “Crack nucleation in variational phase-field models of brittle fracture”. In: *Journal of the Mechanics and Physics of Solids* 110 (2018), pp. 80–99. DOI: 10.1016/j.jmps.2017.09.006.

[111] Gergely Molnár et al. “Toughness or strength? Regularization in phase-field fracture explained by the coupled criterion”. In: *Theoretical and Applied Fracture Mechanics* 109.August (2020), p. 102736. DOI: 10.1016/j.tafmec.2020.102736.

[112] Guowei Liu et al. “Abaqus implementation of monolithic and staggered schemes for quasi-static and dynamic fracture phase-field model”. In: *Computational Materials Science* 121 (2016), pp. 35–47. DOI: 10.1016/j.commatsci.2016.04.009.

[113] H. W. Liu. “Stress-Corrosion Cracking and the Interaction Between Crack-Tip Stress Field and Solute Atoms”. In: *Journal of Basic Engineering* (1970), pp. 633–638.

[114] ASTM International. *Standard Test Methods for Strength of Anchors in Concrete Elements (E488/E488M)*. Vol. i. 2013, pp. 1–21. DOI: 10.1520/E0488.

[115] F. J. Recio et al. “Hydrogen embrittlement risk of high strength galvanized steel in contact with alkaline media”. In: *Corrosion Science* 53.9 (2011), pp. 2853–2860. DOI: 10.1016/j.corsci.2011.05.023.

[116] N. O. Larrosa, P. Lopez-Crespo, and R. A. Ainsworth. “An efficient procedure for reducing in-line-inspection datasets for structural integrity assessments”. In: *Theoretical and Applied Fracture Mechanics* 93 (2018), pp. 79–87. DOI: 10.1016/j.tafmec.2017.07.005.

[117] Emilio Martínez-Pañeda and Norman A Fleck. “Mode I crack tip fields: Strain gradient plasticity theory versus J2 flow theory”. In: *European Journal of Mechanics - A/Solids* 75 (2019), pp. 381–388. DOI: https://doi.org/10.1016/j.euromechsol.2019.02.009.

[118] Yueguang Wei and John W. Hutchinson. “Steady-state crack growth and work of fracture for solids characterized by strain gradient plasticity”. In: *Journal of the Mechanics and Physics of Solids* 45.8 (1997), pp. 1253–1273. DOI: 10.1016/S0022-5096(97)00018-5.

[119] Yongwon Lee and R P Gangloff. “Measurement and modeling of hydrogen environment-assisted cracking of ultra-high-strength steel”. In: *Metallurgical and Materials Transactions A: Physical Metallurgy and Materials Science* 38 A.13 (2007), pp. 2174–2190.

[120] Greger L Pioszak and Richard P Gangloff. “Hydrogen Environment Assisted Cracking of Modern Ultra-High Strength Martensitic Steels”. In: *Metallurgical and Materials Transactions A* 48.9 (2017), pp. 4025–4045. DOI: 10.1007/s11661-017-4156-0.

[121] Emilio Martínez-pañeda, Christian F Niordson, and Richard P Gangloff. “Strain gradient plasticity-based modeling of hydrogen environment assisted cracking”. In: *Acta Materialia* 117 (2016), pp. 321–332. DOI: 10.1016/j.actamat.2016.07.022.

[122] Kim Louisa Auth, Jim Brouzoulis, and Magnus Ekh. “A fully coupled chemo-mechanical cohesive zone model for oxygen embrittlement of nickel-based superalloys”. In: *Journal of the Mechanics and Physics of Solids* 164 (July 2022), p. 104880. DOI: 10.1016/J.JMPS.2022.104880.

Publications

[P1]

Kristensen, Philip K., Martínez-Pañeda, Emilio. Phase field fracture modelling using quasi-Newton methods and a new adaptive step scheme. Theoretical and Applied Fracture Mechanics 2020. 107. 102446

Theoretical and Applied Fracture Mechanics 107 (2020) 102446

Contents lists available at ScienceDirect

Theoretical and Applied Fracture Mechanics

journal homepage: www.elsevier.com/locate/tafmec

Phase field fracture modelling using quasi-Newton methods and a new adaptive step scheme

Philip K. Kristensen[a], Emilio Martínez-Pañeda[b,*]

[a] Department of Mechanical Engineering, Technical University of Denmark, DK-2800 Kgs. Lyngby, Denmark
[b] Department of Civil and Environmental Engineering, Imperial College London, London SW7 2AZ, UK

ARTICLE INFO

Keywords:
Phase field fracture
Quasi-Newton
BFGS
Fracture
Finite element analysis

ABSTRACT

We investigate the potential of quasi-Newton methods in facilitating convergence of monolithic solution schemes for phase field fracture modelling. Several paradigmatic boundary value problems are addressed, spanning the fields of quasi-static fracture, fatigue damage and dynamic cracking. The finite element results obtained reveal the robustness of quasi-Newton monolithic schemes, with convergence readily attained under both stable and unstable cracking conditions. Moreover, since the solution method is unconditionally stable, very significant computational gains are observed relative to the widely used staggered solution schemes. In addition, a new adaptive time increment scheme is presented to further reduce the computational cost while allowing to accurately resolve sudden changes in material behavior, such as unstable crack growth. Computation times can be reduced by several orders of magnitude, with the number of load increments required by the corresponding staggered solution being up to 3000 times higher. Quasi-Newton monolithic solution schemes can be a key enabler for large scale phase field fracture simulations. Implications are particularly relevant for the emerging field of phase field fatigue, as results show that staggered cycle-by-cycle calculations are prohibitive in mid or high cycle fatigue. The finite element codes are available to download from www.empaneda.com/codes.

1. Introduction

The phase field fracture method has emerged as a promising variational framework for modelling advanced cracking problems. Fracture can be revisited as an energy minimisation problem by solving for an auxiliary variable, the phase field parameter ϕ [1,2]. Consequently, complex fracture features, such as crack branching, crack initiation from arbitrary sites or coalescence of multiple cracks, are naturally captured in the original finite element mesh (see, e.g., [3–5]). Not surprisingly, the method is becoming increasingly popular and the number of applications has soared. Recent examples include hydrogen embrittlement [6,7], fatigue damage [8,9], cracking of lithium-ion batteries [10,11], rock fracture [12], composites delamination [13,14], and fracture of functionally graded materials [15], among other; see [16] for a review.

A great deal of attention has been devoted to the development of efficient schemes for solving the coupled deformation-fracture problem. The total potential energy functional, including the contributions from the bulk and fracture energies, is non-convex with respect to the primary kinematic variables, the displacement field $\boldsymbol{u}$ and the phase field ϕ. Due to this non-convexity, the Jacobian matrix in Newton's method becomes indefinite, hindering convergence and robustness in monolithic solution schemes, where $\boldsymbol{u}$ and ϕ are solved simultaneously. Different numerical strategies have been adopted to overcome these drawbacks: error-oriented Newton methods [17], *ad hoc* line search algorithms [18–20] and modified Newton methods [21]. While promising results have been obtained, performance is very problem-dependent and the monolithic minimisation of the energy functional "remains extremely challenging" [21]. Staggered solution schemes, based on alternating minimisation, enjoy a greater popularity [22–26]. By fixing one primal kinematic variable, the total potential energy becomes convex with respect to the other primal kinematic variable. The method has proven to be very robust but computationally demanding. First, convergence of critical loading steps requires a significant amount of iterations [18]. In addition, the method is no longer unconditionally stable, requiring the use of very small load steps to effectively track the equilibrium solution [19] or recursive iteration schemes [2].

In this work, we demonstrate that a robust and efficient numerical framework for phase field fracture analyses can be obtained by combining quasi-Newton methods and a monolithic solution scheme. There is a large literature devoted to the analysis of the robustness of quasi-Newton methods when dealing with non-convex minimization

* Corresponding author.
E-mail address: e.martinez-paneda@imperial.ac.uk (E. Martínez-Pañeda).

https://doi.org/10.1016/j.tafmec.2019.102446

Available online 26 December 2019
0167-8442/ © 2019 Elsevier Ltd. All rights reserved.

problems - see, e.g., [27–29] and references therein. Very recently, Wu et al. [30] showed the potential of quasi-Newton monolithic approaches in the context of the so-called unified phase field damage theory, a phase field regularisation of cohesive zone models (PF-CZM) [31,32]. We extend their analysis to the standard phase field fracture formulation and showcase the potential of the method in three problems of different nature: quasi-static fracture, phase field fatigue and dynamic fracture. In addition, we introduce a new adaptive time stepping criterion for phase field cracking. The results obtained reveal computation times that are up to 100 times smaller than those required to obtain the same result with the widely used staggered solution. These results back the earlier findings by Wu et al. [30] in the context of quasi-static fracture and the PF-CZM model, emphasising the promise of monolithic quasi-Newton implementations for phase field fracture and fatigue modelling.

The remainder of this manuscript is organized as follows. The theoretical phase field formulation employed to model (quasi-static and dynamic) fracture is shown in Section 2. Details of the numerical implementation are given in Section 3, including a comprehensive description of the Broyden-Fletcher-Goldfarb-Shanno (BFGS) algorithm employed. Representative numerical results are shown in Section 4. First, paradigmatic examples in quasi-static phase field fracture are revisited with the new solution scheme. The analysis is then extended to the case of fatigue cracking. And finally, the potential of the method is showcased in dynamic fracture, where off-diagonal matrices have a larger relative weight. Concluding remarks are given in Section 5.

2. The phase field fracture method

2.1. Phase field approximation of the fracture energy

Alan Arnold Griffith's energy-based analysis of cracks in 1920 is considered to be the birth of the field of fracture mechanics [33]. Consider a cracked solid with strain energy density $\psi(\boldsymbol{\varepsilon})$, which is a function of the strain tensor $\boldsymbol{\varepsilon}$. In the absence of external forces, the variation of the total energy Π due to an incremental increase in the crack area $\mathrm{d}A$ is given by

$$\frac{\mathrm{d}\Pi}{\mathrm{d}A} = \frac{\mathrm{d}\psi(\boldsymbol{\varepsilon})}{\mathrm{d}A} + \frac{\mathrm{d}W_c}{\mathrm{d}A} = 0, \tag{1}$$

where W_c is the work required to create new surfaces. The last term is the so-called critical energy release rate $G_c = \mathrm{d}W_c/\mathrm{d}A$, a material property that characterises the fracture resistance. Griffith's energy balance can be formulated in a variational form as:

$$\Pi = \int_\Omega \psi(\boldsymbol{\varepsilon})\mathrm{d}V + \int_\Gamma G_c\,\mathrm{d}\Gamma, \tag{2}$$

with Γ being the crack surface and V denoting the volume of the solid, occupying an arbitrary domain Ω. The crack surface is unknown, hindering minimization of (2). However, an auxiliary variable, the phase field ϕ, can be used to track the crack interface, see Fig. 1. The phase field ϕ is a damage-like variable that takes the values of 0 in an intact material point, and of 1 in a fully cracked material point.

Following continuum damage mechanics arguments, a degradation function $g(\phi) = (1-\phi)^2$ is defined that diminishes the stiffness of the material with evolving damage [2]. Accordingly, the total potential energy functional can be formulated as

$$\Pi_\ell = \int_\Omega \left\{(1-\phi)^2\psi_0(\boldsymbol{\varepsilon}) + G_c\left(\frac{1}{2\ell}\phi^2 + \frac{\ell}{2}\left|\nabla\phi\right|^2\right)\right\}\mathrm{d}V \tag{3}$$

where ℓ is a length scale parameter that governs the size of the fracture process zone and ψ_0 denotes the elastic strain energy of the undamaged solid. The work required to create a cracked surface, is now expressed as a volume integral, making the problem computationally tractable. As shown by Γ-convergence, the regularized functional Π_ℓ approaches the functional of the discrete crack problem Π for $\ell \to 0$ [34,35]. The choice (3) is based on the work by Bourdin et al. [2] and the earlier regularization by Ambrosio and Tortorelli of the Mumford-Shah problem in image processing [36]. This surface regularization is commonly referred to as the AT2 model. See Ref. [37] for other choices and a detailed numerical comparison in the context of phase field fracture. Considering the earlier work by Wu et al. [30], the superior performance of monolithic quasi-Newton solution strategies is therefore demonstrated for both the PF-CZM and AT2 regularizations; the analysis of the so-called AT1 model [38] remains to be addressed.

2.2. Governing balance equations of the coupled problem

2.2.1. Basic fields and boundary conditions

We proceed now to formulate the governing equations for the displacement field $\boldsymbol{u}$ and the phase field ϕ. With respect to $\boldsymbol{u}$, the outer surface of the body is decomposed into a part $\partial\Omega_u$, where the displacement is prescribed by Dirichlet-type boundary conditions

$$\boldsymbol{u}(\boldsymbol{x}, t) = \boldsymbol{u}_\mathrm{D}(\boldsymbol{x}, t) \quad \text{at} \quad \boldsymbol{x} \in \partial\Omega_u \tag{4}$$

and into a part $\partial\Omega_h$, where the traction $\boldsymbol{h}$ is prescribed by Neumann-type boundary conditions (see Fig. 2a). With respect to the fracture phase field, a cracked region can be prescribed through the initial condition

$$\phi(\boldsymbol{x}, t) = 1 \quad \text{at} \quad \boldsymbol{x} \in \Gamma_\mathrm{D} \tag{5}$$

where Γ_D is a possible given sharp crack surface inside the solid Ω (see Fig. 2b). The crack phase field ϕ is considered to be driven by the displacement field $\boldsymbol{u}$ of the solid. Consequently, no prescribed external

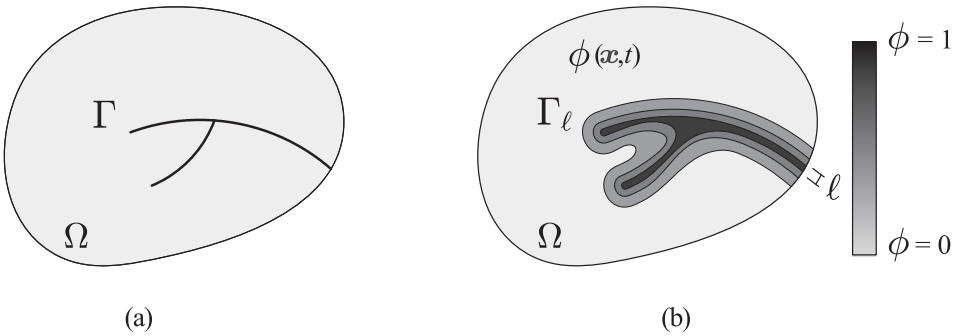

Fig. 1. Schematic representation of a solid body with (a) internal discontinuity boundaries, and (b) a phase field approximation of the discrete discontinuities.

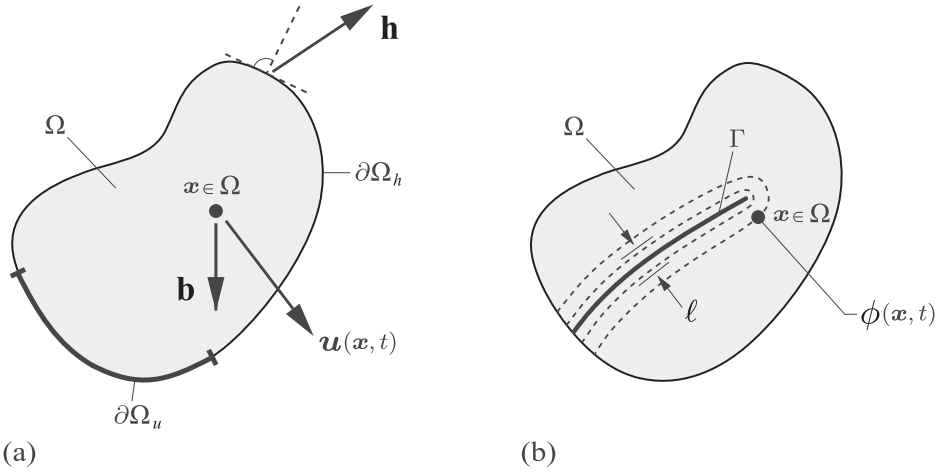

Fig. 2. Two-field model of phase field fracture in deformable solids. The displacement field $\boldsymbol{u}$ is constrained by the Dirichlet- and Neumann-type boundary conditions $\boldsymbol{u} = \boldsymbol{u}_{\mathrm{D}}$, on $\partial\Omega_u$ and $\boldsymbol{\sigma}\cdot\boldsymbol{n} = \boldsymbol{h}$, on $\partial\Omega_h$. (b) The crack phase field ϕ is constrained by the Dirichlet- and Neumann-type boundary conditions $\phi = 1$, on Γ and $\nabla\phi\cdot\boldsymbol{n} = 0$ *on* $\partial\Omega$.

loading is considered corresponding to the crack phase field ϕ.

As both quasi-static and dynamic fracture will be considered in this work, we define the kinetic energy of the solid as:

$$\Psi^k(\dot{\boldsymbol{u}}) = \frac{1}{2}\int_\Omega \rho\, \dot{\boldsymbol{u}}\cdot\dot{\boldsymbol{u}}\, \mathrm{d}V, \tag{6}$$

where ρ is the material density and $\dot{\boldsymbol{u}} = \partial\boldsymbol{u}/\partial t$.

2.2.2. Coupled balances

With the kinetic and potential energies defined, along with the boundary conditions of the system, the Lagrangian for the regularised fracture problem is given by

$$L(\boldsymbol{u}, \dot{\boldsymbol{u}}, \phi) = \Psi^k(\dot{\boldsymbol{u}}) - \Pi_\ell(\boldsymbol{u}, \phi). \tag{7}$$

By insertion of (3) and (6) into (7), the Lagrangian can be formulated as:

$$L(\boldsymbol{u}, \dot{\boldsymbol{u}}, \phi) = \int_\Omega \left\{\frac{1}{2}\rho\dot{\boldsymbol{u}}\cdot\dot{\boldsymbol{u}} - (1-\phi)^2\psi_0(\boldsymbol{\varepsilon}) - G_c\left(\frac{1}{2\ell}\phi^2 + \frac{\ell}{2}\left|\nabla\phi\right|^2\right)\right\}\mathrm{d}V. \tag{8}$$

The weak form can be readily obtained by taking the stationary of the Lagrangian functional $\delta L(\boldsymbol{u}, \dot{\boldsymbol{u}}, \phi) = 0$, such that:

$$\int_\Omega \left\{\rho\ddot{\boldsymbol{u}}\cdot\delta\boldsymbol{u} + \boldsymbol{\sigma}\colon\delta\boldsymbol{\varepsilon} - 2(1-\phi)\delta\phi\psi_0(\boldsymbol{\varepsilon}) + G_c\left(\frac{\phi}{\ell}\delta\phi + \ell\nabla\phi\cdot\nabla\delta\phi\right)\right\}\mathrm{d}V - \int_\Omega \boldsymbol{b}\cdot\delta\boldsymbol{u}\,\mathrm{d}V - \int_{\partial\Omega_h}\boldsymbol{h}\cdot\delta\boldsymbol{u}\,\mathrm{d}S = 0. \tag{9}$$

Here, $\boldsymbol{b}$ is a prescribed body force field per unit volume and the Cauchy stress tensor $\boldsymbol{\sigma}$ is given in terms of the stress tensor of the undamaged solid $\boldsymbol{\sigma}_0$ and the degradation function $g(\phi)$ as:

$$\boldsymbol{\sigma} = g(\phi)\boldsymbol{\sigma_0} = (1-\phi)^2\boldsymbol{\sigma_0} = (1-\phi)^2\boldsymbol{C_0}\colon\boldsymbol{\varepsilon}, \tag{10}$$

with $\boldsymbol{C_0}$ being the linear elastic stiffness matrix. By application of the Gauss divergence theorem and considering that (9) must hold for any arbitrary permissible variations $\delta\boldsymbol{u}$, $\delta\dot{\boldsymbol{u}}$ and $\delta\phi$, we arrive at the balance equations:

$$\begin{aligned}&\nabla\boldsymbol{\sigma} + \boldsymbol{b} = \rho\ddot{\boldsymbol{u}}\\ &G_c\left(\frac{1}{\ell}\phi - \ell\Delta\phi\right) - 2\left(1-\phi\right)\psi_0(\boldsymbol{\varepsilon}) = 0\end{aligned} \tag{11}$$

where $\Delta\phi$ refers to the Laplacian of the phase field. The strong form balance equations are subject to the Neumann-type boundary conditions

$$\boldsymbol{\sigma}\cdot\boldsymbol{n} = \boldsymbol{h} \quad \text{on} \quad \partial\Omega_h \quad \text{and} \quad \nabla\phi\cdot\boldsymbol{n} = 0 \quad \text{on} \quad \partial\Omega. \tag{12}$$

where $\boldsymbol{n}$ denotes the outward unit vector normal to the surface $\partial\Omega$.

3. Finite element implementation

This section contains the details of the numerical implementation in a finite element setting. First, some numerical considerations are presented for the phase field in Section 3.1, to prevent crack healing and crack growth from compressive stresses. Afterwards, the discretisation of the problem and the formulation of residuals and stiffness matrices is addressed in Section 3.2. The solution strategies considered in this paper are presented in Section 3.3 and details of the Broyden-Fletcher-Goldfarb-Shanno (BFGS) algorithm for the quasi-Newton solution technique are provided in Section 3.4. Finally, a scheme for selectively reducing the increment size within a monolithic approach is presented in Section 3.6. The implementation is carried out in the commercial finite element package Abaqus by means of a user element (UEL) subroutine. Abaqus2Matlab is employed to pre-process the input files [39].

3.1. Addressing irreversibility and crack growth in compression

First, a history variable field H is introduced to ensure damage irreversibility,

$$\phi_{t+\Delta t} \geqslant \phi_t \tag{13}$$

where $\phi_{t+\Delta t}$ is the phase field variable in the current time increment while ϕ_t denotes the value of the phase field on the previous increment. To ensure irreversible growth of the phase field variable, the history field must satisfy the Kuhn-Tucker conditions

$$\psi_0 - H \leqslant 0, \quad \dot{H} \geqslant 0, \quad \dot{H}(\psi_0 - H) = 0 \tag{14}$$

for both loading and unloading scenarios. Accordingly, the history field may for a current time t be written as:

$$H = \max_{\tau\in[0,t]}\psi_0(\tau). \tag{15}$$

Other approaches such as crack-sets [38,40] or penalty-based methods [41,42] have been proposed, and the treatment of the irreversibility constraint is receiving increasing attention. See the recent work by Gerasimov and De Lorenzis [42] for a detailed discussion and comparative studies.

Second, we introduce a strain energy decomposition to prevent cracking in compression. A few options have been proposed in the literature, of which the most popular ones are: the spectral tension-compression decomposition by Miehe et al. [23] and the volumetric-deviatoric split by Amor et al. [43]. Both are considered here but the latter will be generally adopted, unless otherwise stated. Both models have a similar intent: to maintain resistance in compression and during crack closure. In the volumetric-deviatoric split by Amor et al. [43], the idea is that the volumetric and deviatoric strain energies can be subjected to damage but not the compressive volumetric strain energy. Thus, the strain energy can be decomposed as $\psi = g(\phi)\psi_0^+ + \psi_0^-$, where

$$\psi_0^+ = \frac{1}{2}K_n \langle tr(\boldsymbol{\varepsilon})\rangle_+^2 + \mu(\boldsymbol{\varepsilon}^{dev}\colon \boldsymbol{\varepsilon}^{dev}) \tag{16}$$

$$\psi_0^- = \frac{1}{2}K_n \langle tr(\boldsymbol{\varepsilon})\rangle_-^2 \tag{17}$$

where $K_n = \lambda + 2\mu/n$ is bulk modulus (with n being the number of dimensions of the problem), $\langle a\rangle_\pm = (a \pm |a|)/2$ and $\boldsymbol{\varepsilon}^{dev} = \boldsymbol{\varepsilon} - tr(\boldsymbol{\varepsilon})\boldsymbol{I}/3$. We follow the hybrid implementation of Ambati et al. [44] in considering ψ_0^+ in the evaluation of the history variable field H, therefore referring to it as H^+ henceforth, while considering ψ_0 in the displacement problem. In this regard, we emphasize that our findings relate to the incrementally linear problem resulting from the hybrid approach by Ambati et al. [44]; the performance of monolithic quasi-Newton methods in other models remains unaddressed.

3.2. Finite element discretisation of variational principles

Consider (9), in the absence of body forces, the two-field weak form can be formulated as

$$\begin{aligned}&\int_\Omega (\rho\ddot{\mathbf{u}}\cdot\delta\mathbf{u} + \boldsymbol{\sigma}\colon\delta\boldsymbol{\varepsilon} - \mathbf{b}\cdot\delta\mathbf{u})\,\mathrm{d}V - \int_{\partial\Omega_h}\mathbf{h}\cdot\delta\mathbf{u}\,\mathrm{d}S = 0\\ &\int_\Omega \left\{-2(1-\phi)\delta\phi\,H^+ + G_c\left(\tfrac{1}{\ell}\phi\delta\phi + \ell\nabla\phi\cdot\nabla\delta\phi\right)\right\}\mathrm{d}V = 0\end{aligned} \tag{18}$$

Now make use of Voigt notation and consider a plane strain solid. The displacement field $\mathbf{u}$ and the phase field ϕ can be discretised as

$$\mathbf{u} = \sum_{i=1}^{m}\mathbf{N}_i^{\mathbf{u}}\mathbf{u}_i \quad\text{and}\quad \phi = \sum_{i=1}^{m}N_i\phi_i \tag{19}$$

where the shape function matrix is expressed as

$$\mathbf{N}_i^{\mathbf{u}} = \begin{bmatrix} N_i & 0\\ 0 & N_i\end{bmatrix} \tag{20}$$

Here, N_i denotes the shape function associated with node i, m is the total number of nodes per element, and $\mathbf{u}_i = \{u_x, u_y\}^T$ and ϕ_i are the displacement and phase field values at node i, respectively. Consequently, the corresponding derivatives can be discretised as

$$\boldsymbol{\varepsilon} = \sum_{i=1}^{m}\mathbf{B}_i^{\mathbf{u}}\mathbf{u}_i \quad\text{and}\quad \nabla\phi = \sum_{i=1}^{m}\mathbf{B}_i^{\phi}\phi_i \tag{21}$$

where $\boldsymbol{\varepsilon} = \{\varepsilon_{xx}, \varepsilon_{yy}, \gamma_{xy}\}^T$. Here, γ denotes the engineering strain, such that $\gamma_{xy} = 2\varepsilon_{xy}$. Accordingly, the strain-displacement matrices associated with a given node i are expressed as

$$\mathbf{B}_i^{\mathbf{u}} = \begin{bmatrix}\partial N_i/\partial x & 0\\ 0 & \partial N_i/\partial y\\ \partial N_i/\partial y & \partial N_i/\partial x\end{bmatrix} \quad\text{and}\quad \mathbf{B}_i^{\phi} = \begin{bmatrix}\partial N_i/\partial x\\ \partial N_i/\partial y\end{bmatrix} \tag{22}$$

Considering this finite element discretisation and the fact that (18) must hold for arbitrary values of $\delta\mathbf{u}$ and $\delta\phi$, the discrete equation corresponding to the equilibrium condition can be expressed as the following residual with respect to the displacement field

$$\mathbf{r}_i^{\mathbf{u}} = \int_\Omega [(1-\phi)^2 + k](\mathbf{B}_i^{\mathbf{u}})^T\boldsymbol{\sigma}_{\mathbf{0}}\,\mathrm{d}V + \int_\Omega \rho(\mathbf{N}_i^{\mathbf{u}})^T\ddot{\boldsymbol{u}}\,\mathrm{d}V - \int_{\partial\Omega_h}(\mathbf{N}_i^{\mathbf{u}})^T\mathbf{h}\,\mathrm{d}S \tag{23}$$

where k is a numerical parameter introduced to keep the system of equations well-conditioned. Similarly, the residual with respect to the evolution of the crack phase field can be expressed as

$$r_i^{\phi} = \int_\Omega \left\{-2(1-\phi)N_i\,H^+ + G_c\left[\frac{1}{\ell}N_i\,\phi + \ell(\mathbf{B}_i^{\phi})^T\nabla\phi\right]\right\}\mathrm{d}V \tag{24}$$

3.3. Solution schemes

The Newton-Raphson method is employed to obtain the solutions for which $\mathbf{r}^{\mathbf{u}} = \boldsymbol{0}$ and $\mathbf{r}^{\phi} = \boldsymbol{0}$, given the nonlinearity of the residuals. An iterative scheme is adopted to solve for the displacement $\boldsymbol{u}$ and the phase field $\boldsymbol{\phi}$. The tangent stiffness matrices and the mass matrix can be readily computed by taking the first derivative of the residual vectors, and read

$$\begin{aligned}&\mathbf{K}_{ij}^{\mathbf{uu}} = \frac{\partial\mathbf{r}_i^{\mathbf{u}}}{\partial\mathbf{u}_j} = \int_\Omega [(1-\phi)^2 + k](\mathbf{B}_i^{\mathbf{u}})^T\mathbf{C}_{\mathbf{0}}\,\mathbf{B}_j^{\mathbf{u}}\,\mathrm{d}V\\ &\mathbf{K}_{ij}^{\phi\phi} = \frac{\partial r_i^{\phi}}{\partial\phi_j} = \int_\Omega \left\{\left[2H^+ + \tfrac{G_c}{\ell}\right]N_iN_j + G_c\ell(\mathbf{B}_i^{\phi})^T(\mathbf{B}_j^{\phi})\right\}\mathrm{d}V\\ &\mathbf{M} = \int_\Omega \rho(\mathbf{N}_i^{\boldsymbol{u}})^T\mathbf{N}_i^{\boldsymbol{u}}\,\mathrm{d}V.\end{aligned} \tag{25}$$

Two solution approaches are generally used to solve the phase field - displacement system: (1) solving for $\boldsymbol{u}$ and $\boldsymbol{\phi}$ simultaneously (*monolithic*) or (2) solving for $\boldsymbol{u}$ and $\boldsymbol{\phi}$ separately as sequentially coupled *staggered* fields. Staggered solution schemes are very robust and can overcome snap-back instabilities. However, they are not unconditionally stable and the time increment must be sufficiently small to prevent deviating from the equilibrium solution. On the other hand, monolithic implementations retain unconditional stability, enabling to use much larger time increments. Notwithstanding, the use of the more efficient monolithic schemes has been hindered by their poor performance in attaining a converged solution. We show that this Achilles' heel of monolithic solution schemes can be overcome by using quasi-Newton methods, such as the Broyden-Fletcher-Goldfarb-Shanno (BFGS) algorithm. The performance of the BFGS algorithm will be compared to that of a staggered solution scheme where convergence is assessed independently for the displacement and phase fields at the end of each increment. This widely used approach is typically referred to as one-pass or single-iteration alternating minimisation solver. The reader is referred to the recent work by Wu et al. [30] for a comparison between the BFGS algorithm and the staggered approach employed by Bourdin et al. [2], which iterates on the current phase field and displacement solutions.

3.4. The Broyden-Fletcher-Goldfarb-Shanno (BFGS) algorithm

Consider the following linearized system, with initial stiffness matrix $\mathbf{K}$, to be solved in an iterative manner,

$$\begin{Bmatrix}\mathbf{u}\\ \boldsymbol{\phi}\end{Bmatrix}_{t+\Delta t} = \begin{Bmatrix}\mathbf{u}\\ \boldsymbol{\phi}\end{Bmatrix}_{t} - \begin{Bmatrix}\mathbf{K^{uu}}+\mathbf{M} & 0\\ 0 & \mathbf{K^{\phi\phi}}\end{Bmatrix}_{t}^{-1}\begin{Bmatrix}\mathbf{r^{u}}\\ \mathbf{r^{\phi}}\end{Bmatrix}_{t} \tag{26}$$

In quasi-Newton methods, in contrast to standard Newton, the stiffness matrix $\mathbf{K}$ is not updated after each iteration. Instead, after a set number of iterations without convergence, an approximation of the stiffness $\widetilde{\mathbf{K}}$ is introduced. This approximated stiffness matrix $\widetilde{\mathbf{K}}$ satisfies the following:

$$\widetilde{\mathbf{K}}\Delta\mathbf{z} = \Delta\mathbf{r} \tag{27}$$

where

$$\mathbf{z} = \begin{Bmatrix}\mathbf{u}\\ \boldsymbol{\phi}\end{Bmatrix}$$

and $\Delta\mathbf{z} = \mathbf{z}_{t+\Delta t} - \mathbf{z}_t$. Likewise, $\Delta\mathbf{r} = \mathbf{r}_{t+\Delta t} - \mathbf{r}$. In the BFGS algorithm, the approximated stiffness matrix is updated in the following way:

$$\widetilde{\mathbf{K}} = \widetilde{\mathbf{K}}_t - \frac{(\widetilde{\mathbf{K}}_t\Delta\mathbf{z})(\widetilde{\mathbf{K}}_t\Delta\mathbf{z})^T}{\Delta\mathbf{z}^T\widetilde{\mathbf{K}}_t\Delta\mathbf{z}} + \frac{\Delta\mathbf{r}\Delta\mathbf{r}^T}{\Delta\mathbf{z}^T\Delta\mathbf{r}} \tag{28}$$

Note that, although the non-diagonal coupling terms of the initial stiffness matrix have been dropped, see (26), the approximation (28) couples the displacement and phase fields. Also, if the stiffness matrix is symmetric, the update to the approximate stiffness matrix can instead be written in terms of its inverse [45]:

$$\widetilde{\mathbf{K}}^{-1} = \left(\mathbf{I} - \frac{\Delta\mathbf{z}\Delta\mathbf{r}^T}{\Delta\mathbf{z}^T\Delta\mathbf{r}}\right)\widetilde{\mathbf{K}}_t^{-1}\left(\mathbf{I} - \frac{\Delta\mathbf{z}\Delta\mathbf{r}^T}{\Delta\mathbf{z}^T\Delta\mathbf{r}}\right)^{-1} + \frac{\Delta\mathbf{z}\Delta\mathbf{z}^T}{\Delta\mathbf{z}^T\Delta\mathbf{r}}, \tag{29}$$

which offers significant computational savings and retains symmetry and positive definiteness, if such was already present. The BFGS algorithm has been implemented in most commercial finite element packages (such as Abaqus), often in conjunction with a line search algorithm.

3.5. Convergence criteria

The standard convergence criteria available in Abaqus are used for both the monolithic and staggered solution schemes without any modification. Hence, both a residual control and a solution correction control have to be met to achieve convergence. Regarding the former, the largest residual in the balance equations r^{α}_{max} must be equal or smaller than the product of a tolerance constant R^{α}_{n} with an overall time-averaged flux norm for the solution $\widetilde{q}^{\alpha}$:

$$r^{\alpha}_{max} \leqslant R^{\alpha}_{n}\widetilde{q}^{\alpha} \tag{30}$$

We do not deviate from Abaqus default recommendations and consider a magnitude for the tolerance of $R^{\alpha}_{n} = 0.005$. If the inequality (30) is satisfied, convergence is accepted if the largest correction to the solution, c^{α}_{max}, is also small compared to the largest incremental change in the corresponding solution variable, Δa^{α}_{max},

$$c^{\alpha}_{max} \leqslant C^{\alpha}_{n}\Delta a^{\alpha}_{max} \tag{31}$$

Here, C^{α}_{n} denotes the magnitude of the convergence tolerance; as by default in Abaqus, we consider $C^{\alpha}_{n} = 0.01$. The residual-based and solution-based criteria are equally employed for the displacement field ($\alpha = u$) and the phase field ($\alpha = \phi$).

3.6. Incrementation control scheme

As it will be shown below, phase field fracture problems can be solved employing very large load increments when combining quasi-Newton algorithms with monolithic solution schemes. However, a sudden change in the material response (such as a large force drop due to unstable fracture) may be best captured by using small time increments. To benefit from the use of large time increments while resolving sudden changes in material behaviour we suggest the use of the following adaptive step scheme:

For any integration point i:
  If $\phi_i < 0.7$ & $\Delta\phi_i \geqslant 0.5$
    Re-start load increment reducing its size by 90%: $\Delta t_1 = 0.1\Delta t_0$.
  End if

Accordingly, smaller increments are used when there is a significant increase in damage in a material point that was not already highly damaged. This allows us to generalise the present time stepping scheme to case studies where the crack is initially introduced by prescribing $\phi = 1$. Obviously, the above criterion must be restrained such that it does not happen continuously. For simplicity, it has been restricted to happen only once during a given simulation. This criterion is particularly useful for unstable cracking problems, where large increments can be adopted until the onset of cracking and the load increment decreases to adequately resolve the fracture event.

4. Results

We proceed to showcase, via numerical experiments, the potential of the method in attaining convergence and reducing computation times in a wide range of problems. First, quasi-static fracture is considered in Section 4.1, including both stable and unstable cracking. Secondly, in Section 4.2, we show that the quasi-Newton method can enable cycle-by-cycle phase field fatigue calculations that are computationally prohibitive for staggered schemes. Finally, the capabilities of the method are also demonstrated for the case of dynamic crack branching in Section 4.3.

4.1. Quasi-static fracture

Two paradigmatic benchmarks will be addressed under quasi-static loading conditions, the fracture of a cracked square plate under: (1) uniaxial tension, and (2) shear.

4.1.1. Cracked square plate subjected to uniaxial tension

We consider first the case of unstable crack growth in a linear elastic specimen under monotonic loading, as exemplified by the mode I fracture of the single-edge notched tension (SENT) specimen sketched in Fig. 3a. This paradigmatic example has been widely used since the early works by Miehe and co-workers [23]. Loading conditions and specimen dimensions (in mm) are shown in Fig. 3a. Material properties are $E = 210$ GPa, $\nu = 0.3$, $\ell = 0.024$ mm, and $G_c = 2.7$ J/mm^2. We discretise the model with linear quadrilateral elements, with the characteristic element size along the extended crack path, h_e, being at least 6 times smaller than the phase field length scale ℓ. Cracking is unstable, with damage extending through the crack ligament instantaneously. With the quasi-Newton monolithic scheme, the unstable growth is captured within a single increment without convergence problems. This is illustrated by means of phase field contours in Fig. 3b and c.

The force versus displacement curve obtained is shown in Fig. 4. The results computed with a staggered solution scheme are also shown for selected values of the total number of load increments employed. It can be clearly seen that the staggered solution is sensitive to the increment size, and recovering the monolithic solution requires at least 10^5 increments. This is in clear contrast with the 30 increments

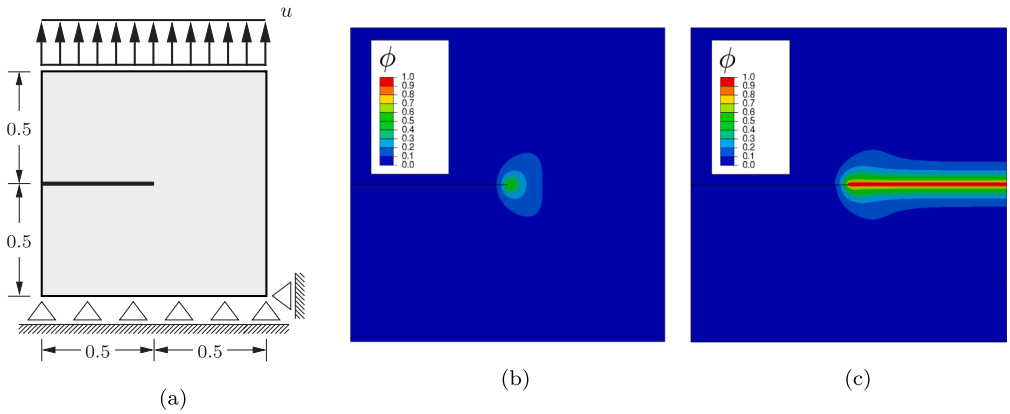

Fig. 3. Single-edged notched tension specimen: (a) Dimensions (in mm) and loading configuration. Crack patterns for a remote displacement of (b) $u = 5.90 \times 10^{-3}$ mm and (c) $u = 5.93 \times 10^{-3}$ mm. The complete extent of crack growth is captured within a single increment.

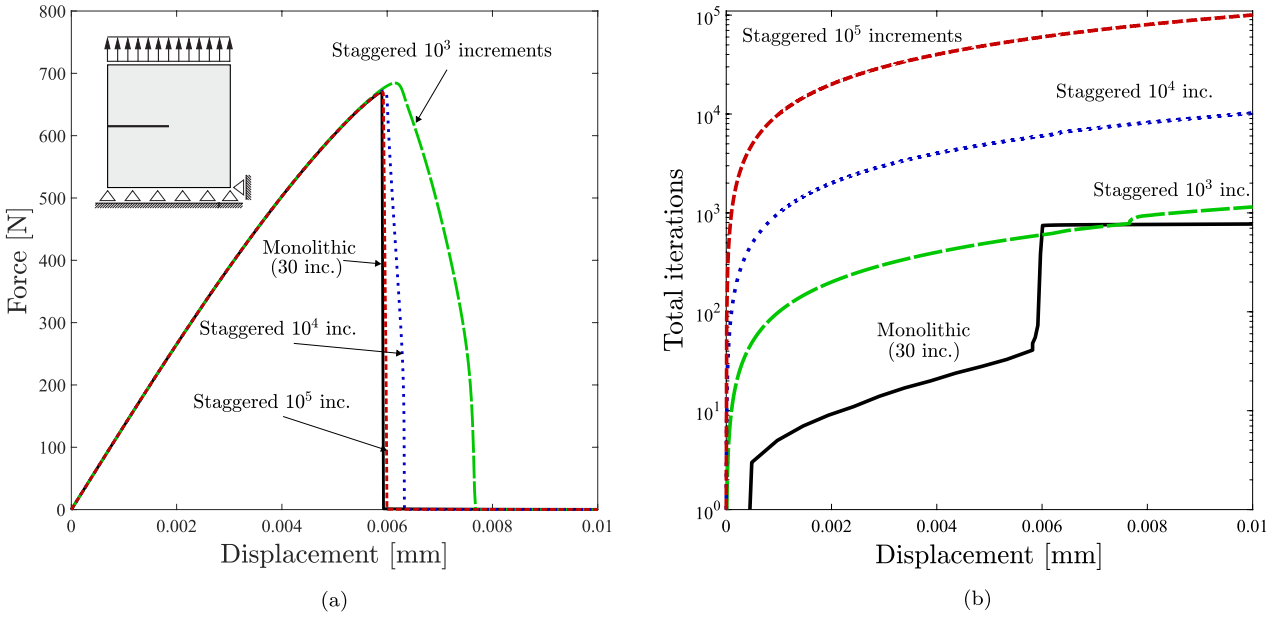

Fig. 4. Single-edged notched tension specimen: (a) force versus displacement curves, and (b) cumulative number of iterations.

employed to obtain the monolithic result. Both the staggered and monolithic computations require a large number of iterations to achieve convergence during the critical increments. The cumulative number of iterations is shown as a function of the applied displacement in Fig. 4b. Results reveal that reproducing the accurate monolithic result within a staggered scheme requires using a number of iterations that is two orders of magnitude larger. The quasi-Newton monolithic calculation is faster than the coarsest staggered time-stepping, which leads to ~20% errors in the computation of the critical displacement.

Computation times for different discretisations are reported in Table 1. Selected mesh densities are considered, as illustrated by the size of the characteristic element length along the crack path, h_e and the number of degrees-of-freedom (DOFs). It can be seen that the trends persist across mesh densities; the quasi-Newton monolithic implementation presented is roughly 100 times faster than the widely used staggered scheme. These massive differences in computation times are mainly due the reduced number of increments employed in the monolithic case.

The adaptive time stepping scheme presented in Section 3.6 allows to accurately capture the unstable response while resolving with large time increments outside of the cracking time frame. This is illustrated in Fig. 5, where the increment size and their required iterations are given, along with the development of the force-displacement curve. Large load increments are initially used, which require only a few iterations to converge. When cracking takes place, the algorithm drastically reduces the increment size to accurately capture unstable crack growth. As by default in Abaqus, the increment size increases when few iterations are needed to achieve convergence, enabling to recover large loading steps towards the end of the computation.

Table 1
Single-edged notched tension specimen. Computation times as a function of the mesh size. The staggered computations correspond to the 10^5 increments case, which is one that exhibits a comparable accuracy to the monolithic result.

	CPU hours			
Mesh size	$\ell/h_e = 6$ 25908 DOFs	$\ell/h_e = 9$ 47376 DOFs	$\ell/h_e = 12$ 74697 DOFs	$\ell/h_e = 18$ 152772 DOFs
Monolithic	0.31	0.80	1.79	3.41
Staggered	31.6	60.17	87.47	187.90

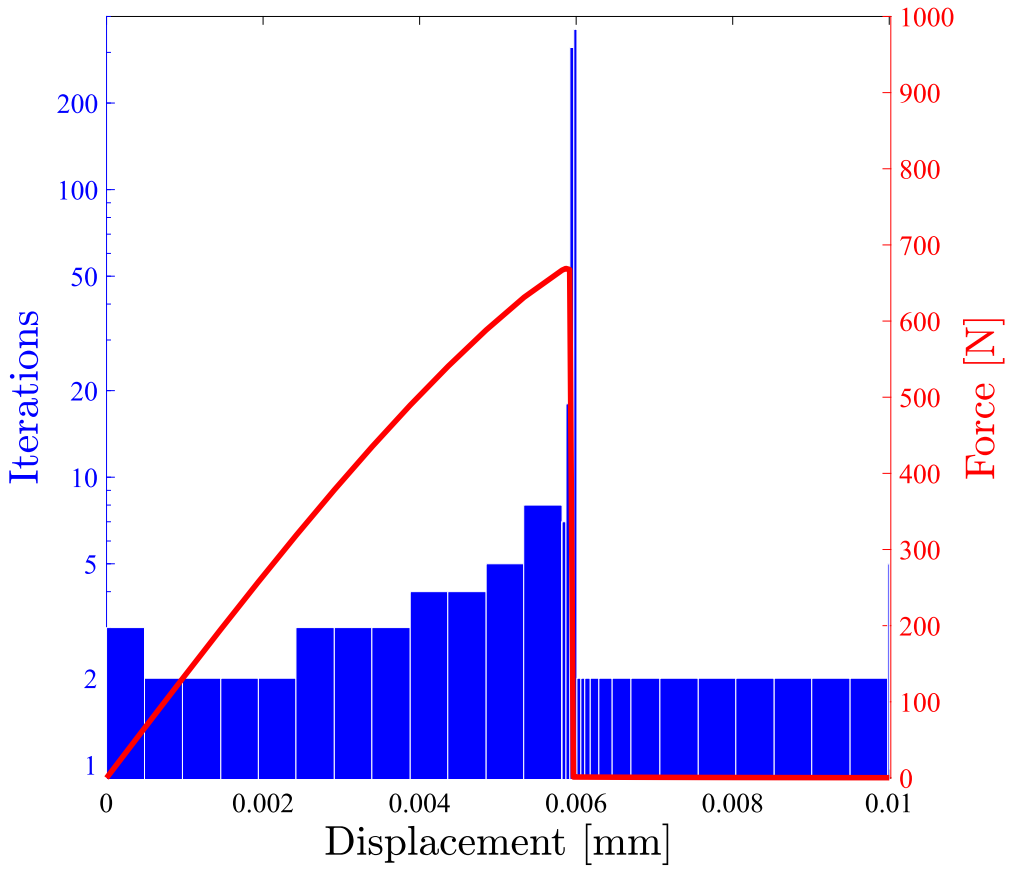

Fig. 5. Single-edged notched tension specimen. Number of iterations per increment, with the force versus displacement curve superimposed. When the critical point in the simulation is reached, the increment size is drastically reduced, such that the response of the system is accurately captured with only 30 load increments.

In the context of monolithic quasi-Newton, the same force versus displacement response can be achieved without the new adaptive time stepping scheme by using a reference load increment that is approximately 85% smaller than the one employed in Fig. 5. I.e., even without adaptive time stepping, quasi-Newton calculations are 20–40 times faster than staggered ones.

4.1.2. Single edge notched shear test

The performance of the monolithic quasi-Newton scheme presented is now assessed in the context of stable crack growth. The same specimen dimensions and material properties as in the previous case study are employed but the sample is now subjected to remote shear loading; see Fig. 6a. The mixed-mode crack tip conditions lead to crack

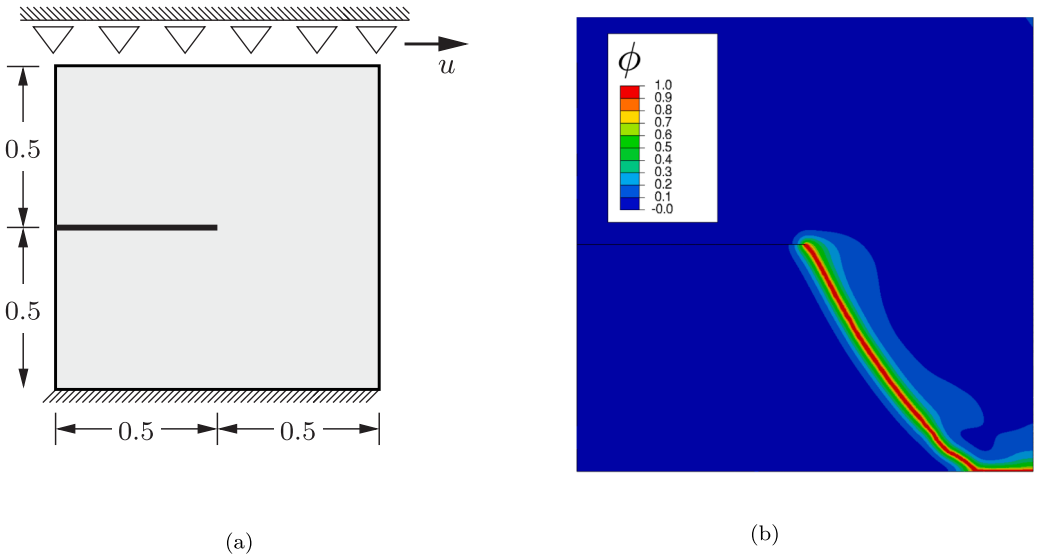

Fig. 6. Single-edged notched shear specimen: (a) Dimensions (in mm) and loading configuration, and (b) crack trajectory.

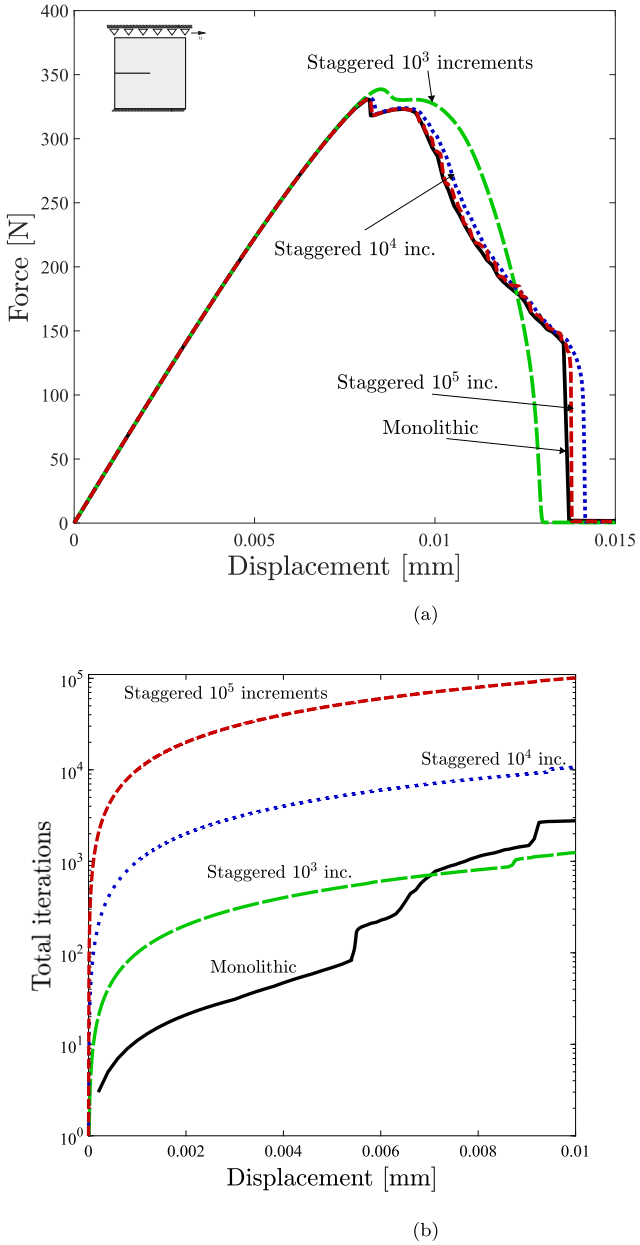

Fig. 7. Single-edged notched shear specimen: (a) force versus displacement curves, and (b) cumulative number of iterations.

deflection towards the lower part of the sample. The resulting crack trajectory, shown in Fig. 6b, agrees with results shown in the literature using the volumetric-deviatoric split - see, e.g. Ref. [25].

The force versus displacement curves obtained with both monolithic and staggered schemes are shown in Fig. 7a. As with the tension case, reproducing the accurate monolithic result with the staggered implementation requires using a very large number of increments, 10^5 or more. When using a smaller number, such as with the case of 10^3 increments, the force versus displacement result deviates substantially from the monolithic one and a different crack path is predicted. Differences in the total number of iterations between the staggered and monolithic results are smaller than in the unstable mode I crack growth example but remain very significant. As shown in Fig. 7b, the total number of iterations needed to obtain an accurate result with the staggered approach is roughly two orders of magnitude larger than in the quasi-Newton monolithic analysis.

Table 2
Single-edged notched shear specimen. Computation times as a function of the mesh size. The staggered computations correspond to the 10^5 increments case, which is one that exhibits a comparable accuracy to the monolithic result.

	CPU hours			
Mesh size	$\ell/h_e = 6$ 58518 DOFs	$\ell/h_e = 9$ 128451 DOFs	$\ell/h_e = 12$ 222111 DOFs	$\ell/h_e = 18$ 386112 DOFs
Monolithic	2.02	6.56	11.62	46.60
Staggered	74.85	159.50	272.25	469.48

Computation times for an increasingly refined mesh are compiled in Table 2. As in the previous example, only the accurate staggered solution with 10^5 increments is considered. In general, the computational cost is 10 times smaller in the monolithic quasi-Newton case.

Fig. 8 shows the performance of the present monolithic quasi-Newton scheme, with the adaptive time stepping defined in Section 3.6. The bar plot shows the number of iterations as a function of the remote displacement, together with the force versus displacement response. The performance is not as impressive as for the mode I unstable crack growth example but it still leads to substantial computational gains and remains useful for providing a well-timed transition from large to small increments.

Lastly, it should be noted that the method is very robust. Convergence is attained in all cases without the need for any viscous dissipation parameters. In both the tension and shear boundary value problems, the monolithic implementation based on the conventional Newton method fails to converge, even for 10^5 increments. This also holds true when combining the conventional Newton method with a line search algorithm.

4.2. Phase field fatigue

We proceed to investigate the effectiveness of the monolithic quasi-Newton solution approach within the emerging field of phase field fatigue modelling. We base our investigation on the framework that Carrara et al. [9] have very recently presented. First, a brief overview of the fatigue model is presented. Our implementation is then validated with the results by Carrara and co-workers [9]. Finally, we show that the present quasi-Newton monolithic implementation drastically outperforms staggered approaches, which are too computationally expensive for cycle-by-cycle fatigue analyses.

4.2.1. Theoretical framework

Consider the framework presented in Section 2 under quasi-static conditions. A fatigue degradation function $f(\overline{\alpha}(t))$ can be introduced, which depends upon a cumulative history variable $\overline{\alpha}$ [8,9]. Accordingly, the variation of the internal work reads:

$$\delta W_{int} = \int_\Omega \left\{ \boldsymbol{\sigma}: \delta\boldsymbol{\varepsilon} - 2(1-\phi)\delta\phi\ \psi_0(\boldsymbol{\varepsilon}) + f(\overline{\alpha}(t)) G_c \left(\frac{1}{\ell}\phi\delta\phi + \ell \nabla\phi \cdot \nabla\delta\phi \right) \right\} \mathrm{d}V \tag{32}$$

The choices of f and $\overline{\alpha}$ are of utmost importance in capturing the physics of fatigue damage. Since our aim is to investigate the performance of a new solution methodology, we restrict attention to one of the simplest choices proposed by Carrara et al. [9]. The cumulative history variable $\overline{\alpha}$ is assumed to be independent of the mean load and takes the form:

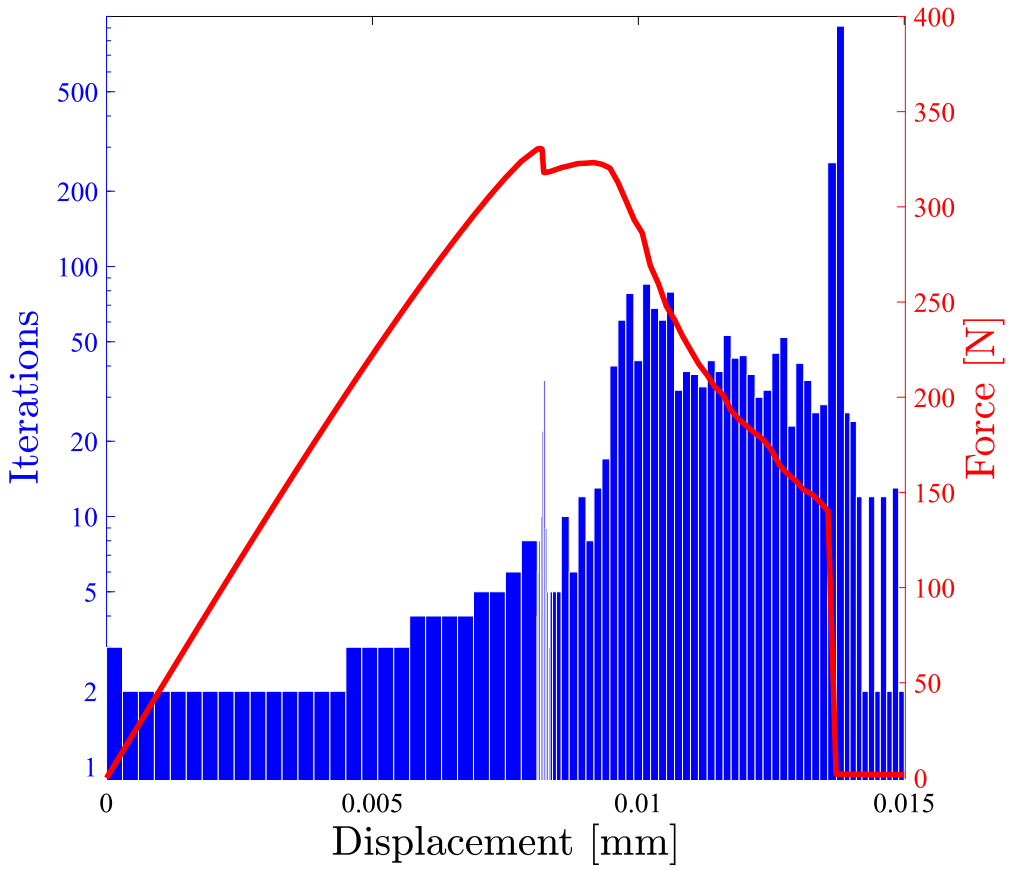

Fig. 8. Single-edged notched shear specimen. Number of iterations per increment, with the force versus displacement curve superimposed.

$$\overline{\alpha}(t) = \int_0^t \theta(\alpha\dot{\alpha})|\dot{\alpha}|\, \mathrm{d}\tau, \tag{33}$$

where τ is the pseudo-time and $\theta(\alpha\dot{\alpha})$ is the Heaviside function. Thus, $\overline{\alpha}$ only grows during loading. The fatigue history variable α must represent the loading condition in the solid. For simplicity, the choice of $\alpha = g(\phi)\psi_0$ is made. Finally, the fatigue degradation function characterises the sensitivity of the fracture energy to the number of cycles. Here, we adopt a function that vanishes asymptotically:

$$f(\overline{\alpha}(t)) = \begin{cases} 1 & \text{if } \overline{\alpha}(t) \leq \alpha_T \\ \left(\frac{2\alpha_T}{\overline{\alpha}(t)+\alpha_T}\right) & \text{if } \overline{\alpha}(t) \geq \alpha_T \end{cases} \tag{34}$$

where α_T represents a threshold value, below which the fracture energy remains unaffected. The extension of the finite element implementation described in Section 3 to incorporate $f(\overline{\alpha}(t))$ is straightforward and will not be detailed here.

4.2.2. Verification

We mimic the first benchmark study by Carrara et al. [9]. A single-edge notched tension specimen like the one described in Fig. 3a is subjected to cyclic loading with a load ratio of $R = -1$ (equal compression and tension loads). As in the original study, material parameters are chosen as $E = 210$ GPa, $\nu = 0.3$, $Gc = 2.7$ N/mm, $\alpha_T = 56.25$ N/mm^2 and $\ell = 0.004$ mm. The loading amplitude is of 0.002 mm and the characteristic element size in the fracture zone is $h_e = \ell/5$. The crack extension a is computed as a function of the number of cycles N for three different decompositions of the strain energy density, see Fig. 9. Namely, the standard isotropic one, the volumetric-deviatoric split [43], and the spectral tension-compression decomposition [22]. The results obtained in Ref. [9] are shown superimposed using symbols. It should be noted that Carrara and co-workers [9] employ a staggered solution scheme that iterates until convergence to the monolithic solution using the energy-based convergence criterion presented in [25].

A relatively good agreement is observed for the predictions with the isotropic and spectral decomposition models. As discussed by Carrara et al. [9], the spectral split requires roughly twice as many cycles to trigger complete fracture, as compressive loading cycles do not contribute to damage. Interestingly, we note that our quasi-Newton monolithic implementation of the volumetric-deviatoric split convergences without problems until final fracture.

4.2.3. Performance of quasi-Newton in phase field fatigue

We proceed to evaluate the performance of the quasi-Newton approach. As in the other cases, we compare against the single iteration staggered approach presented in Section 3.3. For the sake of simplicity, we restrict our attention to the isotropic case, not considering any decomposition of the strain energy density. The results obtained with both staggered and monolithic approaches are shown in Fig. 10. It can be clearly seen that a very large number of increments per cycle is needed in the staggered case, as convergence towards the monolithic solution is slow.

The very large number of increments needed has an immediate impact on the computation times, as listed in Table 3. The most precise staggered calculation, which is far from the equilibrium result, requires computation times that are 5 times larger than the monolithic case.

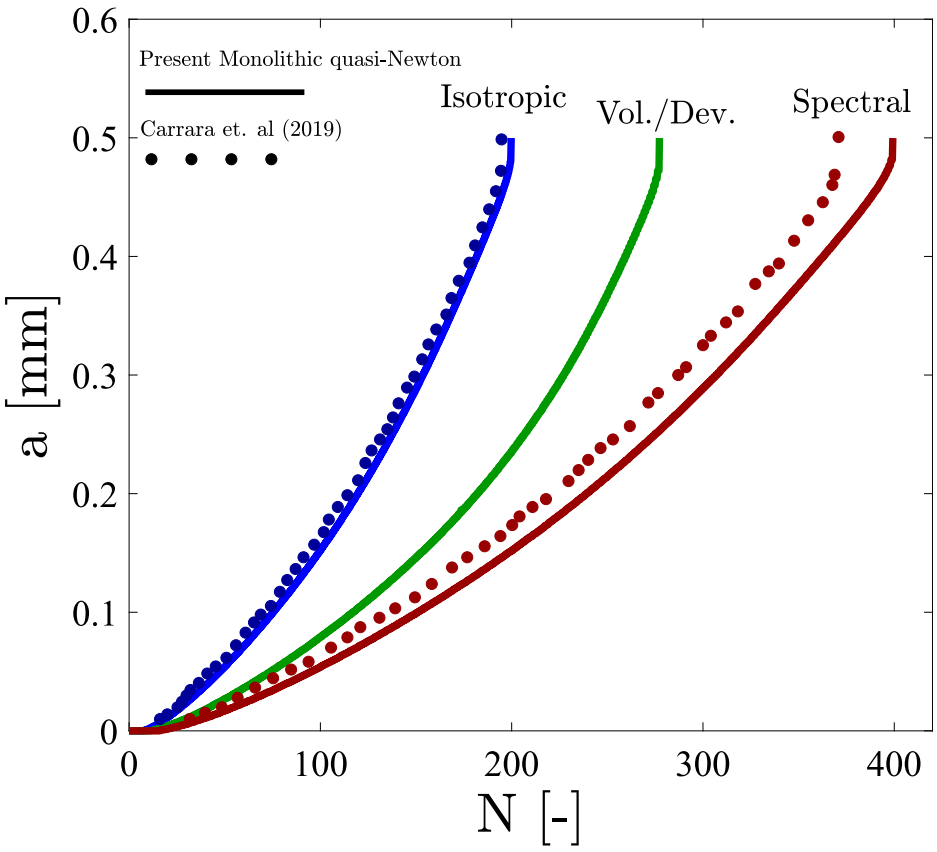

Fig. 9. Fatigue cracking of a single-edge notched tension specimen. Crack length a versus number of cycles N for different strain energy density splits. Solid lines are the results obtained with our quasi-Newton solution while symbols denote the results reported in Ref. [9].

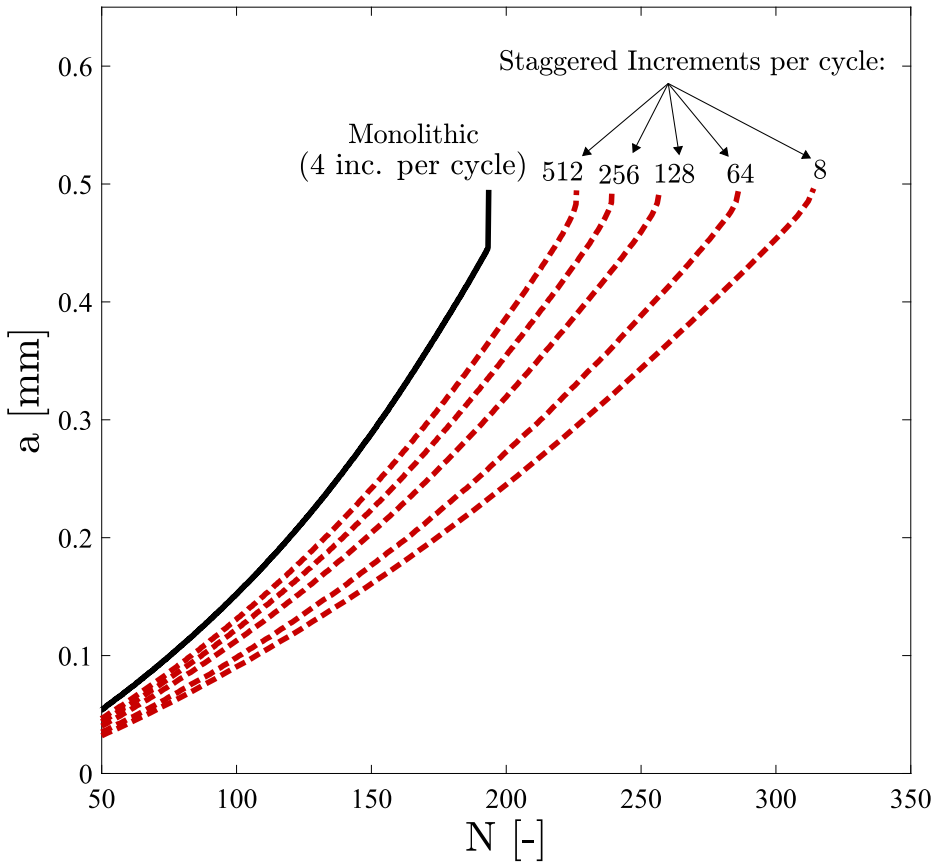

Fig. 10. Fatigue cracking of a single-edge notched tension specimen. Crack length a versus number of cycles N for quasi-Newton monolithic and staggered implementations. A very large number of increments is needed in the staggered scheme to reproduce the quasi-Newton monolithic prediction.

Table 3
Fatigue cracking of a single-edge notched tension specimen. Computation times for quasi-Newton monolithic and staggered approaches.

Solutions strategy	Monolithic	Staggered				
Increments per cycle	4	8	32	64	128	256
CPU hours	14.85	3.24	16.52	20.29	34.30	73.98

From Fig. 10, it seems likely that more than 1000 increments per cycle will be needed to approximate the monolithic result. This implies that mid, high and very high cycle fatigue problems cannot be addressed with staggered schemes; the use of quasi-Newton methods could open new horizons in phase field fatigue analyses.

4.3. Dynamic results

Finally, we conclude our study by examining the case of dynamic fracture, where inertia terms are present and off-diagonal matrices have a larger relative weight. The paradigmatic example of a rectangular specimen containing a sharp crack and subjected to a vertical tensile traction is considered, see Fig. 11 [3]. The vertical traction is of magnitude $\sigma = 1$ MPa and is instantaneously applied to the upper and lower boundaries. The dimensions of the specimen and the loading configuration are shown in Fig. 11. The material parameters for the solid are set to $\rho = 2450$ kg/m^3, $E = 32$ GPa, $\nu = 0.2$, $\ell = 0.25$ mm and $G_c = 3$ J/m^2, implying a Rayleigh wave speed of $v_r = 2125$ m/s. The domain is uniformly discretised using linear quadrilateral elements with side length $h_e = 0.25$ mm.

The increment size for both the staggered and the monolithic calculations is set according to $\Delta t \approx h_e/v_r \approx 0.1\,\mu$s. Thus, differences in computation times are caused only by the computational cost of updating the Jacobian and from the number of iterations required for each increment to converge. The dynamic system is solved using a Backward Euler approach, without the need for using other algorithms such as HHT or Newmark's β-method to achieve convergence. The staggered and monolithic approaches show the same qualitative result, crack growth followed by branching - see Fig. 12. However once the crack widening phase initiates, the staggered approach on average requires 4–6 times more iterations per increment, leading to a total computation time almost 3 times longer than the monolithic approach.

The result showcases how the monolithic quasi-Newton approach converges significantly faster than staggered solution schemes in highly non-linear problems. Moreover, it proves the capabilities of the quasi-Newton monolithic implementation in solving highly complex fracture problems. We further illustrate this aspect and the versatility of the method by obtaining results with $G_c = 0.5$ J/m^2, quadratic elements and an initial crack defined by prescribing ϕ. As shown in Fig. 13, complex crack patterns can be obtained with the present monolithic quasi-Newton implementation.

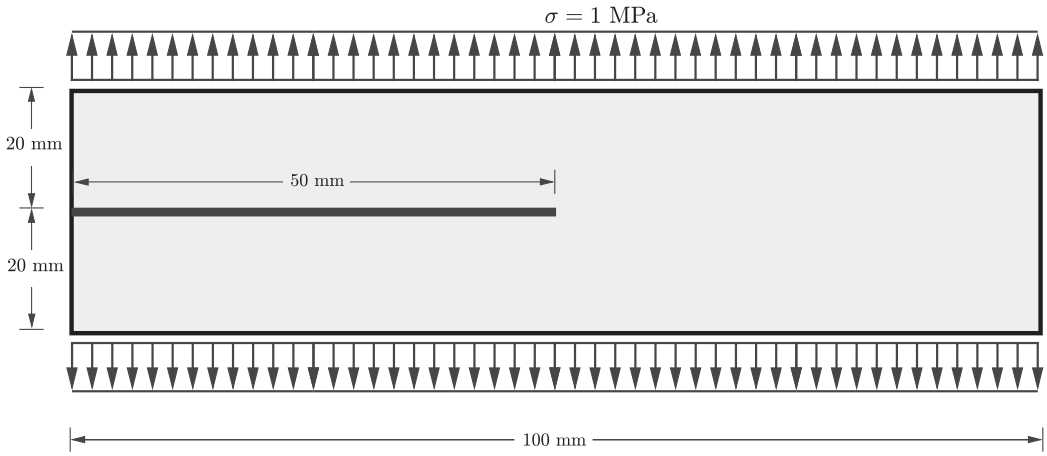

Fig. 11. Dynamic crack branching. Dimensions and loading conditions.

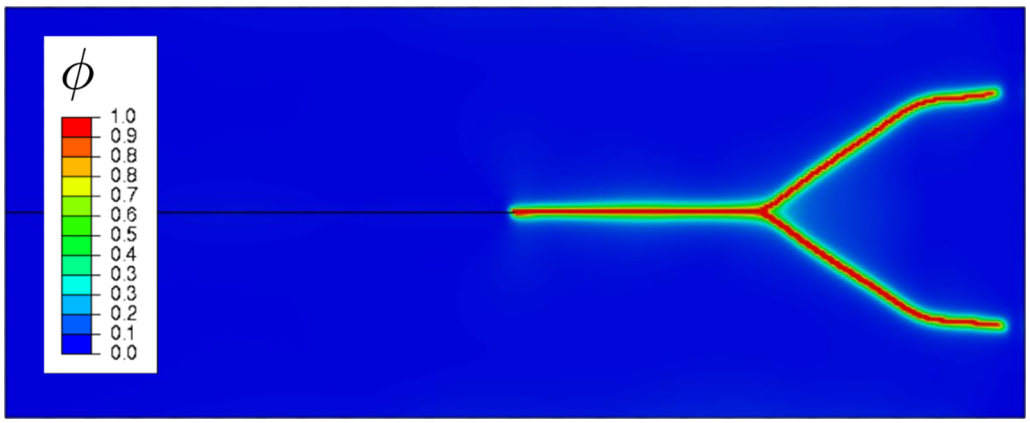

Fig. 12. Dynamic crack branching. Crack trajectory predicted with the monolithic quasi-Newton implementation.

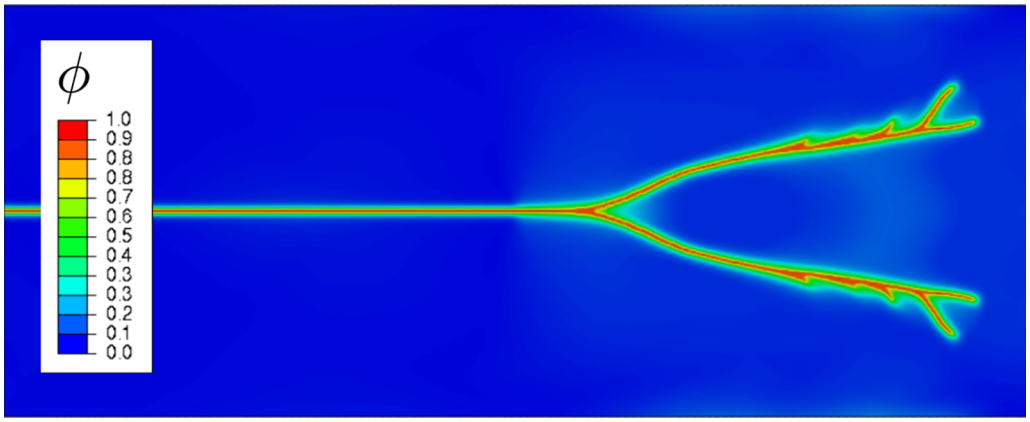

Fig. 13. Dynamic crack branching. Crack trajectory predicted with the monolithic quasi-Newton implementation for $G_c = 0.5$ J/m^2.

5. Conclusions

We present a quasi-Newton monolithic solution scheme for phase field fracture. The modelling framework makes use of the Broyden-Fletcher-Goldfarb-Shanno (BFGS) algorithm and is enhanced with a new adaptive time stepping algorithm. Several paradigmatic boundary value problems are solved, spanning stable and unstable quasi-static fracture, phase field fatigue and dynamic crack branching applications. Our main findings are:

(i) Monolithic quasi-Newton solution schemes are robust. Capable of solving various benchmark problems of varying complexity without convergence problems, unlike standard Newton monolithic frameworks.
(ii) By retaining unconditional stability, computation times are drastically reduced relative to widely used staggered solution schemes. Monolithic quasi-Newton computations are 10 to 100 times faster in all the problems considered.
(iii) Accurate phase field fatigue predictions can be obtained with only 4 increments per cycle, several orders of magnitude below the requirements of staggered approaches.

It is therefore expected that the use of monolithic quasi-Newton solution schemes will open new possibilities in phase field fracture modelling; for example, by enabling physically-based cycle-by-cycle fatigue calculations and tackling large scale problems. Of interest for future work is the study of the performance of the method in other challenging applications, including those involving large strains [46,47] and nearly incompressible materials [48].

Declaration of Competing Interest

The authors declare that they have no known competing financial interests or personal relationships that could have appeared to influence the work reported in this paper.

Acknowledgments

The authors gratefully acknowledge financial support from the Danish Hydrocarbon Research and Technology Centre (DHRTC) under the “Reliable in-service assessment in aggressive environments” project, publication number DHRTC-PRP-108. E. Martínez-Pañeda additionally acknowledges financial support from Wolfson College Cambridge (Junior Research Fellowship) and from the Royal Commission for the 1851 Exhibition through their Research Fellowship programme (RF496/2018).

References

[1] G. Francfort, J.-J. Marigo, Revisiting brittle fracture as an energy minimization problem, J. Mech. Phys. Solids 46 (8) (1998) 1319–1342.
[2] B. Bourdin, G.A. Francfort, J.J. Marigo, Numerical experiments in revisited brittle fracture, J. Mech. Phys. Solids 48 (4) (2000) 797–826.
[3] M.J. Borden, C.V. Verhoosel, M.A. Scott, T.J.R. Hughes, C.M. Landis, A phase-field description of dynamic brittle fracture, Comput. Methods Appl. Mech. Eng. 217–220 (2012) 77–95.
[4] M.J. Borden, T.J.R. Hughes, C.M. Landis, A. Anvari, I.J. Lee, A phase-field formulation for fracture in ductile materials: Finite deformation balance law derivation, plastic degradation, and stress triaxiality effects, Comput. Methods Appl. Mech. Eng. 312 (2016) 130–166.
[5] C. McAuliffe, H. Waisman, A coupled phase field shear band model for ductile-brittle transition in notched plate impacts, Comput. Methods Appl. Mech. Eng. 305 (2016) 173–195.
[6] E. Martínez-Pañeda, A. Golahmar, C.F. Niordson, A phase field formulation for hydrogen assisted cracking, Comput. Methods Appl. Mech. Eng. 342 (2018) 742–761.
[7] F.P. Duda, A. Ciarbonetti, S. Toro, A.E. Huespe, A phase-field model for solute-assisted brittle fracture in elastic-plastic solids, Int. J. Plast. 102 (2018) 16–40.
[8] R. Alessi, S. Vidoli, L. De Lorenzis, A phenomenological approach to fatigue with a variational phase-field model: the one-dimensional case, Eng. Fract. Mech. 190 (2018) 53–73.
[9] P. Carrara, M. Ambati, R. Alessi, L. De Lorenzis, A framework to model the fatigue behavior of brittle materials based on a variational phase-field approach, Comput. Methods Appl. Mech. Eng. (2020) 112731. (in press).
[10] C. Miehe, H. Dal, L.-M. Schanzel, A. Raina, A phase-field model for chemo-mechanical induced fracture in lithium-ion battery electrode particles, Int. J. Numer. Meth. Eng. 106 (2016) 683–711.
[11] Y. Zhao, B.X. Xu, P. Stein, D. Gross, Phase-field study of electrochemical reactions at exterior and interior interfaces in Li-ion battery electrode particles, Comput. Methods Appl. Mech. Eng. 312 (2016) 428–446.
[12] S. Zhou, X. Zhuang, H. Zhu, T. Rabczuk, Phase field modelling of crack propagation, branching and coalescence in rocks, Theoret. Appl. Fract. Mech. 96 (2018) 174–192.
[13] A. Quintanas-Corominas, J. Reinoso, E. Casoni, A. Turon, J.A. Mayugo, A phase field approach to simulate intralaminar and translaminar fracture in long fiber composite materials, Compos. Struct. 220 (2019) 899–911.
[14] A. Quintanas-Corominas, A. Turon, J. Reinoso, E. Casoni, M. Paggi, J.A. Mayugo, A phase field approach enhanced with a cohesive zone model for modeling delamination induced by matrix cracking, Comput. Methods Appl. Mech. Eng. 358 (2020) 112618.
[15] Hirshikesh, S. Natarajan, R.K. Annabattula, E. Martínez-Pañeda, Phase field modelling of crack propagation in functionally graded materials, Compos. Part B: Eng. 169 (2019) 239–248.
[16] J.-Y. Wu, V.P. Nguyen, C.T. Nguyen, D. Sutula, S. Sinaie, S. Bordas, Phase-field modelling of fracture, Adv. Appl. Mech. 53 (2020).
[17] T. Wick, An error-oriented newton/inexact augmented Lagrangian approach for fully monolithic phase-field fracture propagation, SIAM J. Sci. Comput. 39 (4) (2017) B589–B617.
[18] T. Gerasimov, L. De Lorenzis, A line search assisted monolithic approach for phase-field computing of brittle fracture, Comput. Methods Appl. Mech. Eng. 312 (2016) 276–303.
[19] N. Singh, C.V. Verhoosel, R. De Borst, E.H. Van Brummelen, A fracture-controlled path-following technique for phase-field modeling of brittle fracture, Finite Elem. Anal. Des. 113 (2016) 14–29.
[20] R. de Borst, S. May, J. Vignollet, A numerical assessment of phase-field models for fracture, in: P. Trovalusci (Ed.), Materials with Internal Structure, Springer, Cham, Switzerland, 2016, pp. 17–28.

[21] T. Wick, Modified Newton methods for solving fully monolithic phase-field quasi-static brittle fracture propagation, Comput. Methods Appl. Mech. Eng. 325 (2017) 577–611.
[22] C. Miehe, F. Welshinger, M. Hofacker, Thermodynamically consistent phase-field models of fracture: variational principles and multi-field FE implementations, Int. J. Numer. Meth. Eng. 83 (2010) 1273–1311.
[23] C. Miehe, M. Hofacker, F. Welschinger, A phase field model for rate-independent crack propagation: robust algorithmic implementation based on operator splits, Comput. Methods Appl. Mech. Eng. 199 (45–48) (2010) 2765–2778.
[24] M. Hofacker, C. Miehe, Continuum phase field modeling of dynamic fracture: variational principles and staggered FE implementation, Int. J. Fract. 178 (1–2) (2012) 113–129.
[25] M. Ambati, T. Gerasimov, L. De Lorenzis, A review on phase-field models of brittle fracture and a new fast hybrid formulation, Comput. Mech. 55 (2015) 383–405.
[26] P.K. Kristensen, C.F. Niordson, E. Martínez-Pañeda, A phase field model for elastic-gradient-plastic solids undergoing hydrogen embrittlement (2020) (submitted for publication).
[27] D.H. Li, M. Fukushima, A modified BFGS method and its global convergence in nonconvex minimization, J. Comput. Appl. Math. 129 (1–2) (2001) 15–35.
[28] D.-H. Li, M. Fukushima, On the global convergence of the BFGS method for non-convex unconstrained optimization problems, SIAM J. Optim. 11 (4) (2001) 1054–1064.
[29] A.S. Lewis, M.L. Overton, Nonsmooth optimization via quasi-Newton methods, Math. Program. 141 (1–2) (2013) 135–163.
[30] J.-Y. Wu, Y. Huang, V.P. Nguyen, On the BFGS monolithic algorithm for the unified phase field damage theory, Comput. Methods Appl. Mech. Eng. (2020) (in press).
[31] J.-Y. Wu, A unified phase-field theory for the mechanics of damage and quasi-brittle failure, J. Mech. Phys. Solids 103 (2017) 72–99.
[32] J.-Y. Wu, V.P. Nguyen, A length scale insensitive phase-field damage model for brittle fracture, J. Mech. Phys. Solids 119 (2018) 20–42.
[33] A. Griffith, The phenomena of rupture and flow in solids, Philos. Trans. A 221 (1920) 163–198.
[34] G. Bellettini, A. Coscia, Discrete approximation of a free discontinuity problem, Numer. Funct. Anal. Optimiz. 15 (3–4) (1994) 201–224.
[35] A. Chambolle, An approximation result for special functions with bounded deformation, J. Math. Pures Appl. 83 (7) (2004) 929–954.
[36] L. Ambrosio, V.M. Tortorelli, Approximation of functionals depending on jumps by elliptic functionals via gamma-convergence, Commun. Pure Appl. Math. 43 (1990) (1991) 999–1036.
[37] T.K. Mandal, V.P. Nguyen, J.Y. Wu, Length scale and mesh bias sensitivity of phase-field models for brittle and cohesive fracture, Eng. Fract. Mech. 217 (2019) 106532.
[38] K. Pham, H. Amor, J.J. Marigo, C. Maurini, Gradient damage models and their use to approximate brittle fracture, Int. J. Damage Mech 20 (4) (2011) 618–652.
[39] G. Papazafeiropoulos, M. Muñiz-Calvente, E. Martínez-Pañeda, Abaqus2Matlab: a suitable tool for finite element post-processing, Adv. Eng. Softw. 105 (2017) 9–16.
[40] E. Tanné, T. Li, B. Bourdin, J.J. Marigo, C. Maurini, Crack nucleation in variational phase-field models of brittle fracture, J. Mech. Phys. Solids 110 (2018) 80–99.
[41] M.F. Wheeler, T. Wick, W. Wollner, An augmented-Lagrangian method for the phase-field approach for pressurized fractures, Comput. Methods Appl. Mech. Eng. 271 (2014) 69–85.
[42] T. Gerasimov, L. De Lorenzis, On penalization in variational phase-field models of brittle fracture, Comput. Methods Appl. Mech. Eng. 354 (2019) 990–1026.
[43] H. Amor, J.J. Marigo, C. Maurini, Regularized formulation of the variational brittle fracture with unilateral contact: numerical experiments, J. Mech. Phys. Solids 57 (8) (2009) 1209–1229.
[44] M. Ambati, T. Gerasimov, L. De Lorenzis, Phase-field modeling of ductile fracture, Comput. Mech. 55 (5) (2015) 1017–1040.
[45] H. Matthies, G. Strang, The solution of nonlinear finite element equations, Int. J. Numer. Meth. Eng. 14 (1979) 1613–1626.
[46] J. Reinoso, M. Paggi, C. Linder, Phase field modeling of brittle fracture for enhanced assumed strain shells at large deformations: formulation and finite element implementation, Comput. Mech. 59 (6) (2017) 981–1001.
[47] C. Bilgen, K. Weinberg, On the crack-driving force of phase-field models in linearized and finite elasticity, Comput. Methods Appl. Mech. Eng. 353 (2019) 348–372.
[48] A. Kumar, G.A. Francfort, O. Lopez-Pamies, Fracture and healing of elastomers: a phase-transition theory and numerical implementation, J. Mech. Phys. Solids 112 (2018) 523–551.

[P2]

Kristensen, Philip K., Niordson, Christian F., Martínez-Pañeda, Emilio. An assessment of phase field fracture: Crack initiation and growth. Philosophical Transactions of the Royal Society A: Mathematical, Physical and Engineering Sciences 2021, 379. 20210021

PHILOSOPHICAL TRANSACTIONS A

royalsocietypublishing.org/journal/rsta

Research

Cite this article: Kristensen PK, Niordson CF, Martínez-Pañeda E. 2021 An assessment of phase field fracture: crack initiation and growth. *Phil. Trans. R. Soc. A* **379**: 20210021. https://doi.org/10.1098/rsta.2021.0021

Accepted: 8 March 2021

One contribution of 15 to a discussion meeting issue 'A cracking approach to inventing new tough materials: fracture stranger than friction'.

Subject Areas:
computational mechanics, mechanical engineering, mechanics, materials science

Keywords:
Griffith, phase field fracture, fracture mechanics, finite element analysis

Author for correspondence:
Emilio Martínez-Pañeda
e-mail: e.martinez-paneda@imperial.ac.uk

Downloaded from https://royalsocietypublishing.org/ on 21 June 2021

An assessment of phase field fracture: crack initiation and growth

Philip K. Kristensen[1], Christian F. Niordson[1] and Emilio Martínez-Pañeda[2]

[1]Department of Mechanical Engineering, Technical University of Denmark, DK-2800 Kgs. Lyngby, Denmark
[2]Department of Civil and Environmental Engineering, Imperial College London, London SW7 2AZ, UK

PKK, 0000-0002-0178-9985; EM-P, 0000-0002-1562-097X

The phase field paradigm, in combination with a suitable variational structure, has opened a path for using Griffith's energy balance to predict the fracture of solids. These so-called phase field fracture methods have gained significant popularity over the past decade, and are now part of commercial finite element packages and engineering fitness-for-service assessments. Crack paths can be predicted, in arbitrary geometries and dimensions, based on a global energy minimization—without the need for ad hoc criteria. In this work, we review the fundamentals of phase field fracture methods and examine their capabilities in delivering predictions in agreement with the classical fracture mechanics theory pioneered by Griffith. The two most widely used phase field fracture models are implemented in the context of the finite element method, and several paradigmatic boundary value problems are addressed to gain insight into their predictive abilities across all cracking stages; both the initiation of growth and stable crack propagation are investigated. In addition, we examine the effectiveness of phase field models with an internal material length scale in capturing size effects and the transition flaw size concept. Our results show that phase field fracture methods satisfactorily approximate classical fracture mechanics predictions and can also reconcile stress and toughness criteria for fracture. The accuracy of the approximation is however dependent on modelling and constitutive choices; we provide a rationale for these differences and identify suitable approaches for delivering

THE ROYAL SOCIETY PUBLISHING

© 2021 The Author(s) Published by the Royal Society. All rights reserved.

phase field fracture predictions that are in good agreement with well-established fracture mechanics paradigms.

This article is part of a discussion meeting issue 'A cracking approach to inventing new tough materials: fracture stranger than friction'.

Downloaded from https://royalsocietypublishing.org/ on 21 June 2021

1. Introduction

It has been 100 years since Alan Arnold Griffith [1] presented the energy balance that gave birth to the discipline of fracture mechanics. Cracks were postulated to propagate when the energy released due to crack growth is greater than or equal to the work required to create new free surfaces. Although this criterion for fracture is attractive, as it is based on simple thermodynamic principles, the fracture mechanics community soon moved in other directions to embrace local stress concepts such as stress intensity factors—a path opened by the work of Irwin [2]. More amenable to analytical and numerical solutions, these stress-intensity approaches came at the cost of imposing arbitrary criteria for determining the direction and extension of crack growth [3,4]; as discussed below, the spatial and temporal evolution of crack paths are a natural by-product of Griffith's energy balance. However, on the centenary of Griffith's seminal contribution, one can argue that the tables have been turned. The development of a variational stance for Griffith's theory and the subsequent pioneering use of the phase field paradigm to computationally track evolving cracks have again brought the view of fracture mechanics as an energetic problem in focus [5]. Originating in the early 2000s but mainly developed over the past decade [6–10], the field of phase field fracture mechanics has enjoyed ever-increasing popularity up to its current 'quasi-hegemonic status' [11].

The phase field fracture method has provided a suitable mathematical and computational framework for Griffith's energy balance. Phase field fracture analyses have proven capable of predicting—without ad hoc criteria—the nucleation, growth, merging, branching and arrest of cracks, in arbitrary dimensions and geometries (e.g. [12–15] and references therein). These capabilities are of increasing importance in advanced structural integrity assessment and the applications of phase field fracture have soared; examples include composite materials [16,17], shape memory alloys [18], rock-like materials [19], hydrogen embrittlement [20,21], functionally graded materials [22,23], dynamic fracture [9,24], fatigue damage [25,26], ductile damage [27,28] and Li-ion batteries [29,30]. On the occasion of the fracture mechanics meeting organized at the Royal Society, and the associated Special Issue, we review the fundamentals of phase field fracture and gain new insight into its ability to deliver predictions in agreement with the classical fracture mechanics theory laid out by Griffith and his contemporaries.

The remainder of this paper is organized as follows. In §2, we introduce the phase field fracture theory, starting from Griffith's energy balance. The formulation is presented in a generalized fashion, accommodating any constitutive choice for the crack density function. The details of the numerical implementation are given in §3, in the context of the finite element method. The main results and findings are presented in §4. First, we prescribe a remote K-field using a boundary layer model to quantify the energy released during crack initiation. Secondly, to investigate the capabilities of phase field fracture in accurately capturing stable crack growth, we use a double-cantilever beam with a known analytical solution for the crack extension as a function of the critical energy release rate and the applied load. Thirdly, using a plate of finite size with an edge crack, we investigate how phase field fracture models can capture size effects associated with the crack length. The present findings are discussed in the context of the literature in §5. Finally, concluding remarks end the manuscript in §6.

2. A variational framework for Griffith's energy balance

We shall describe the underlying mathematical formulation of phase field fracture models, focusing first on their construction as an approximation of Griffith's energy balance, and then

Downloaded from https://royalsocietypublishing.org/ on 21 June 2021

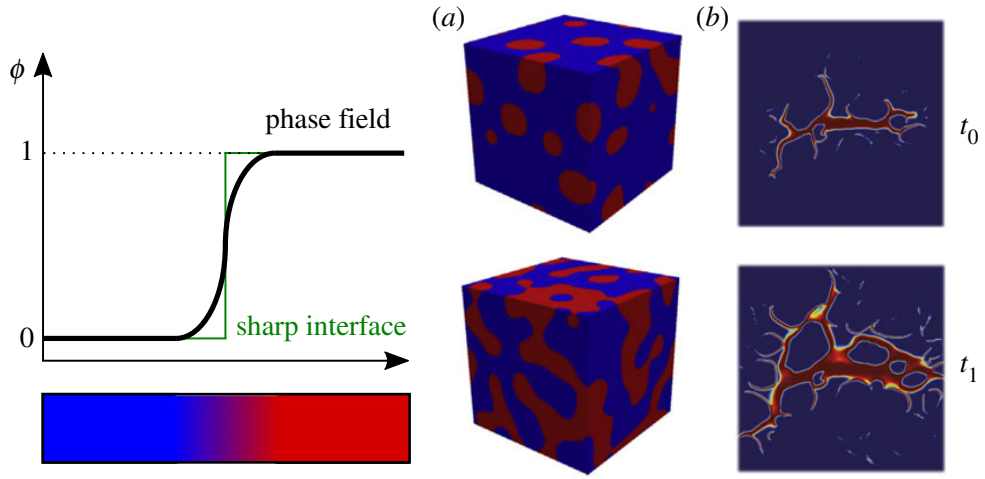

Figure 1. Tracking interfaces *implicitly* using an auxiliary phase field ϕ. Examples capturing (*a*) microstructural evolution [32], and (*b*) the propagation of cracks [33], for two instants in time (t_0, t_1). (Online version in colour.)

present a generalized virtual work formulation in which the phase field is introduced as an additional independent kinematical descriptor. The theory refers to the response of a solid with volume V occupying an arbitrary domain $\Omega \subset \mathbb{R}^n$ $(n \in [1,2,3])$, with external boundary $\partial\Omega \subset \mathbb{R}^{n-1}$, on which the outwards unit normal is denoted as $\mathbf{n}$.

(a) The phase field regularization

From a continuum viewpoint, the first law of thermodynamics provides a detailed balance describing the interplay between the work done on the system, the internal energy, the kinetic energy and the thermal power. Thus, thermodynamic equilibrium requires the total potential energy supplied by the internal strain energy density and external forces, Π, to remain constant. As noted by Griffith [1], in the context of a fracture process under quasi-static and isothermal conditions, this entails balancing the reduction of potential energy that occurs during crack growth with the increase in surface energy resulting from the creation of new free surfaces. Mathematically, this can be formulated as follows. Consider a cracked solid with elastic strain energy density $\psi^e(\boldsymbol{\varepsilon})$, which is a function of the strain tensor $\boldsymbol{\varepsilon}$. Under prescribed displacements, the variation of the total energy Π due to an incremental increase in the crack area $\mathrm{d}A$ is given by

$$\frac{\mathrm{d}\Pi}{\mathrm{d}A} = \frac{\mathrm{d}\psi^e(\boldsymbol{\varepsilon})}{\mathrm{d}A} + \frac{\mathrm{d}W_c}{\mathrm{d}A} = 0, \tag{2.1}$$

where W_c is the work required to create new surfaces. The last term is the so-called critical energy release rate $G_c = \mathrm{d}W_c/\mathrm{d}A$, a material property that characterizes the fracture resistance of the solid. Therefore, a pre-existing crack will grow as soon as the elastic energy stored in the material ψ^e is sufficiently large to overcome the material toughness G_c. Griffith's energy balance can be formulated in a variational form as [31]:

$$\Pi = \int_\Omega \psi^e(\boldsymbol{\varepsilon})\,\mathrm{d}V + \int_\Gamma G_c\,\mathrm{d}\Gamma, \tag{2.2}$$

where Γ is the crack surface. Griffith's minimality principle is now global and cracking phenomena can be captured by minimizing (2.2), with crack behaviour (nucleation, trajectory, etc.) being dictated *only* by the exchange between elastic and fracture energies. However, minimization of (2.2) is hindered by the unknown nature of Γ, making the problem computationally intractable. This obstacle can be addressed by exploiting the phase field paradigm—an auxiliary (phase) field variable ϕ can be defined to describe discrete discontinuous phenomena, such as cracks, with a smooth function. As illustrated in figure 1, the key idea is to smear a sharp interface into a *diffuse* region using this phase field order parameter ϕ, which takes

Downloaded from https://royalsocietypublishing.org/ on 21 June 2021

a distinct value for each of the two phases (e.g. 0 and 1) and exhibits a smooth change between these values near the interface. The use of phase field variables to *implicitly* track interfaces has gained significant traction in the condensed matter and materials science communities, becoming the most widely used technique for modelling microstructural evolution [34]. Also, the success has been recently extended to the phenomenon of corrosion, where the phase field is used to describe the solid metal–aqueous electrolyte interface [35].

In the context of fracture mechanics, the phase field can be used to track the solid-crack interface, enabling the handling of cracks with arbitrary topological complexity, as well as their potential interactions. Thus, the phase field resembles a damage variable, taking (e.g.) the value of $\phi = 0$ in intact regions and of $\phi = 1$ in fully cracked material points. Equally important, the evolution law for the phase field variable is grounded on Griffith's energy balance. Accordingly, the Griffith functional (2.2) can be approximated using the following phase field-regularized functional:

$$\Pi_\ell = \int_\Omega \left[g(\phi)\, \psi_0^e(\boldsymbol{\varepsilon}) + G_c \gamma(\phi, \ell) \right] \mathrm{d}V, \tag{2.3}$$

where ℓ is a length-scale parameter that governs the size of the fracture process zone, ψ_0^e denotes the elastic strain energy density of the undamaged solid, and γ is the so-called crack surface density function [7]. The work required to create a cracked surface is now expressed as a volume integral, making the problem computationally tractable. Also, a degradation function $g(\phi)$ is defined following continuum damage mechanics arguments, such that the stiffness of the solid is degraded as the phase field approaches the value corresponding to the crack phase (e.g. $\psi^e = 0$ for $\phi = 1$). Choices for crack surface density function γ have been mostly inspired in the Ambrosio & Tortorelli [36] approximation of the Mumford–Shah potential [37]—a well-known functional in image segmentation that closely resembles the variational fracture formulation described here. Upon these constitutive choices for γ, it can be proven using Γ-convergence that the regularized functional Π_ℓ (2.3) converges to the Griffith functional Π (2.2) when $\ell \to 0^+$ [38,39]. Thus, ℓ can be interpreted as a regularizing parameter in its vanishing limit. However, for $\ell > 0^+$ a finite material strength is introduced and thus ℓ becomes a material property governing the strength [10]; e.g. for plane stress

$$\sigma_c \propto \sqrt{\frac{G_c E}{\ell}} = \frac{K_{Ic}}{\sqrt{\ell}}, \tag{2.4}$$

where K_{Ic} is the material fracture toughness and E denotes Young's modulus. From a numerical perspective, the presence of a length scale ℓ regularizes the problem, ensuring mesh-objectivity as the model is non-local. We conclude this part by emphasizing that equation (2.3) provides a rigorous approximation to Griffith's energy balance that is amenable to numerical computations. Fracture can be predicted with no other consideration than the minimization of a free energy functional composed of the stored elastic bulk energy plus the fracture energy.

(b) Principle of virtual work: balance of forces

The primal kinematic variables of the model are the displacement field $\mathbf{u}$ and the damage phase field ϕ. We restrict our attention to small strains and isothermal conditions. Accordingly, the strain tensor $\boldsymbol{\varepsilon}$ is given by

$$\boldsymbol{\varepsilon} = \frac{1}{2}\left(\nabla \mathbf{u}^T + \nabla \mathbf{u} \right). \tag{2.5}$$

The balance equations for the coupled deformation-fracture system are now derived using the principle of virtual work. We use δ to denote virtual quantities and introduce the Cauchy stress $\boldsymbol{\sigma}$, which is work conjugate to the strains $\boldsymbol{\varepsilon}$. Accordingly, a traction $\mathbf{T}$ is defined, which is work conjugate to the displacements $\mathbf{u}$. Regarding damage, we introduce a scalar stress-like quantity ω, which is work conjugate to the phase field ϕ, and a phase field micro-stress vector $\boldsymbol{\xi}$, that is work conjugate to the gradient of the phase field $\nabla\phi$. The phase field is assumed to be driven by the

Downloaded from https://royalsocietypublishing.org/ on 21 June 2021

displacement problem alone. As a result, no external traction is associated with ϕ. Accordingly, in the absence of body forces, the principle of virtual work reads

$$\int_{\Omega} \left\{ \boldsymbol{\sigma} : \delta\boldsymbol{\varepsilon} + \omega\delta\phi + \boldsymbol{\xi} \cdot \delta\nabla\phi \right\} \mathrm{d}V = \int_{\partial\Omega} (\mathbf{T} \cdot \delta\mathbf{u}) \ \mathrm{d}S. \tag{2.6}$$

This equation must hold for an arbitrary domain Ω and for any kinematically admissible variations of the virtual quantities. Thus, by making use of the fundamental lemma of the calculus of variations, the local force balances are given by

$$\begin{aligned} \nabla \cdot \boldsymbol{\sigma} &= 0 \\ \nabla \cdot \boldsymbol{\xi} - \omega &= 0 \end{aligned} \quad \text{in } \Omega, \tag{2.7}$$

with natural boundary conditions

$$\begin{aligned} \boldsymbol{\sigma} \cdot \mathbf{n} &= \mathbf{T} \\ \boldsymbol{\xi} \cdot \mathbf{n} &= 0 \end{aligned} \quad \text{on } \partial\Omega. \tag{2.8}$$

(c) Constitutive theory

The potential energy density of the solid is defined as

$$\psi\left(\boldsymbol{\varepsilon}, \phi, \nabla\phi\right) = \psi^e + \psi^f = g\left(\phi\right) \frac{1}{2} \boldsymbol{\varepsilon} : \boldsymbol{C}_0 : \boldsymbol{\varepsilon} + G_c \gamma(\phi, \nabla\phi). \tag{2.9}$$

Here, ψ^f is the fracture energy and $\boldsymbol{C}_0$ is the linear elastic stiffness matrix. Accordingly, the Cauchy stress tensor is derived as

$$\boldsymbol{\sigma} = \frac{\partial\psi}{\partial\boldsymbol{\varepsilon}} = g\left(\phi\right)\left(\boldsymbol{C}_0 : \boldsymbol{\varepsilon}\right). \tag{2.10}$$

We shall now proceed to make constitutive choices for the phase field fracture formulation. The two models that are arguably most widely used will be considered and the implications of these constitutive choices investigated. First, we note that the degradation function $g(\phi)$ should be continuous and monotonic, and take the values $g(0) = 1$ and $g(1) = 0$; the following quadratic form is adopted:

$$g\left(\phi\right) = \left(1 - \phi\right)^2. \tag{2.11}$$

Secondly, restricting our attention to phase field formulations derived from the family of Ambrosio-Tortorelli functionals, we proceed to define the crack surface density function $\gamma(\phi)$ and the crack surface A as follows:

$$A = \int_{\Omega} \gamma\left(\phi\right) \ \mathrm{d}V = \int_{\Omega} \frac{1}{4c_w\ell} \left(w(\phi) + \ell^2 |\nabla\phi|^2 \right) \mathrm{d}V. \tag{2.12}$$

Here, the function $w(\phi)$ must fulfil $w(0) = 0$ and $w(1) = 1$, and

$$c_w = \int_0^1 \sqrt{w(\varphi)} \, \mathrm{d}\varphi. \tag{2.13}$$

The choice of $w(\phi) = \phi^2$ ($c_w = 1/2$) renders the so-called *standard* or AT2 phase field model [36], while the choice $w(\phi) = \phi$ ($c_w = 2/3$) introduces an elastic regime prior to the onset of damage, and is often referred to as the AT1 model [40]. The stress–strain response resulting from the solution to the homogeneous 1D problem ($\nabla\phi = 0$) is shown in figure 2 for both models. It can be readily seen how the AT1 model exhibits a linear response until reaching the critical stress, while the AT2 results deviate earlier from the undamaged stress–strain response. Also, the AT1 model exhibits a sharper drop of the stress upon reaching the material strength. The critical failure stress attained for each model is given by [20]

$$\sigma_c^{\mathtt{AT1}} = \sqrt{\frac{3EG_c}{8\ell}}, \quad \sigma_c^{\mathtt{AT2}} = \frac{3}{16}\sqrt{\frac{3EG_c}{\ell}}. \tag{2.14}$$

Thus, as $\ell \to 0$, the material strength goes to infinity; this is consistent with linear elastic fracture mechanics and Γ-convergence arguments. At this point, it should be noted that many other

Downloaded from https://royalsocietypublishing.org/ on 21 June 2021

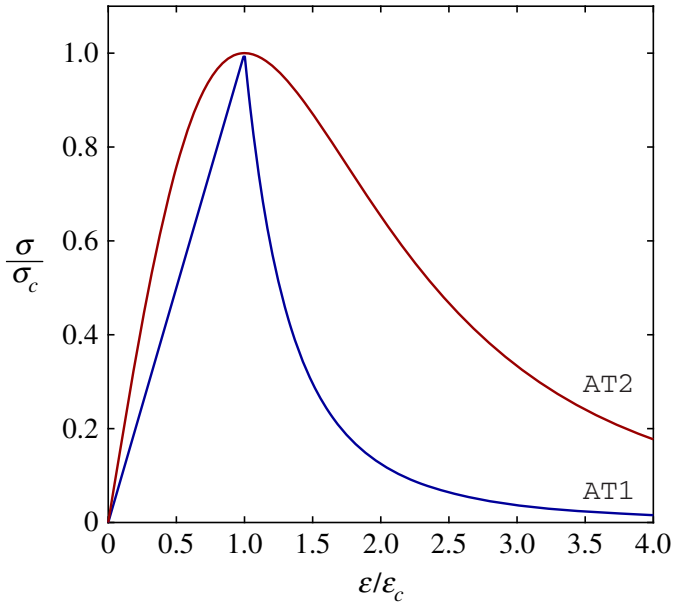

Figure 2. Uniaxial stress–strain responses predicted by the AT1 and AT2 constitutive choices of the crack density function. (Online version in colour.)

constitutive choices have been proposed in the literature. For example, some models are based on the Ginzburg–Landau formulations used in phase transition studies [41], while others, closer to the formulation presented here, aim at coupling phase field with cohesive zone concepts [42–44].

The fracture micro-stress variables ω and $\boldsymbol{\xi}$, which can have energetic and dissipative parts, are defined as follows. Independently of the constitutive choices outlined above (AT1 versus AT2), we derive the scalar micro-stress as

$$\omega = \frac{\partial \psi}{\partial \phi} = g'(\phi)\psi^e + \frac{1}{4c_w \ell} G_c w'(\phi). \tag{2.15}$$

Similarly, the phase field micro-stress vector $\boldsymbol{\xi}$ reads

$$\boldsymbol{\xi} = \frac{\partial \psi}{\partial \nabla \phi} = \frac{\ell}{2c_w} G_c \nabla \phi. \tag{2.16}$$

The phase field evolution law (2.7)b can then be reformulated accordingly

$$\frac{G_c}{2c_w \ell}\left(\frac{w'(\phi)}{2} - \ell^2 \nabla^2 \phi\right) + g'(\phi)\psi^e(\boldsymbol{\varepsilon}) = 0 \tag{2.17}$$

showcasing the competition between the stored elastic energy and the fracture energy.

3. Numerical implementation

We proceed to describe the numerical implementation, in the context of the finite element method, of the variational fracture framework described in §2. First, we introduce a history field variable to ensure damage irreversibility. Secondly, we address the discretization of the weak formulation, formulate the residuals and the stiffness matrices, and discuss solution schemes for the two-field problem. The implementation is conducted within an Abaqus user-element (UEL) subroutine, with the pre-processing of the input files carried out using Abaqus2Matlab [45].

(a) Damage irreversibility

Following Miehe *et al.* [7], a history variable field $\mathcal{H}$ is introduced to prevent crack healing, ensuring that the following condition is always met

$$\phi_{t+\Delta t} \geq \phi_t, \tag{3.1}$$

Downloaded from https://royalsocietypublishing.org/ on 21 June 2021

where $\phi_{t+\Delta t}$ is the phase field variable in the current time step while ϕ_t denotes the value of the phase field on the previous time step. For both loading and unloading scenarios, the history field must satisfy the Kuhn–Tucker conditions

$$\psi_0^e - \mathcal{H} \leq 0, \quad \dot{\mathcal{H}} \geq 0, \quad \dot{\mathcal{H}}(\psi_0^e - \mathcal{H}) = 0. \tag{3.2}$$

Accordingly, the history field for a current time t over a total time τ can be written as

$$\mathcal{H} = \max_{\tau \in [0,t]} \psi_0^e(\tau). \tag{3.3}$$

(b) Finite element discretization

We shall now describe the finite element discretization. Our numerical implementation uses as nodal unknowns the displacement vector $\hat{\mathbf{u}}$ and the phase field $\hat{\phi}$ fields. Considering the history field $\mathcal{H}$ described above and the constitutive choices outlined in §2, one can formulate the weak form of the two-field problem as

$$\int_\Omega \left\{ \left[g(\phi) + \kappa \right] \boldsymbol{\sigma}_0 : \delta\boldsymbol{\varepsilon} - g'(\phi)\mathcal{H}\delta\phi + \frac{G_c}{2c_w\ell} \left(\frac{w'(\phi)}{2}\delta\phi - \ell^2 \nabla\phi \nabla\delta\phi \right) \right\} \mathrm{d}V = 0. \tag{3.4}$$

Here, $\boldsymbol{\sigma}_0$ is the undamaged Cauchy stress tensor and κ is a small positive-valued constant that is introduced to prevent ill-conditioning when $\phi = 1$; a value of $\kappa = 1 \times 10^{-7}$ is here adopted.

Making use of Voigt notation, the nodal quantities are interpolated as

$$\mathbf{u} = \sum_{i=1}^{m} \boldsymbol{N}_i \hat{\mathbf{u}}_i, \quad \phi = \sum_{i=1}^{m} N_i \hat{\phi}_i, \tag{3.5}$$

where m is the total number of nodes per element, N_i denotes the shape function associated with node i and $\boldsymbol{N}_i$ is the shape function matrix, a diagonal matrix with N_i in the diagonal terms. Similarly, the associated gradient quantities can be discretized using the corresponding $\boldsymbol{B}$-matrices, containing the derivative of the shape functions, such that

$$\boldsymbol{\varepsilon} = \sum_{i=1}^{m} \boldsymbol{B}_i^{\boldsymbol{u}} \hat{\mathbf{u}}_i, \quad \nabla\phi = \sum_{i=1}^{m} \mathbf{B}_i \hat{\phi}_i. \tag{3.6}$$

Considering the weak form (3.4) and the discretization (3.5)–(3.6), we derive the residuals for each primal kinematic variable as

$$\mathbf{R}_i^{\mathbf{u}} = \int_\Omega \left\{ \left[g(\phi) + \kappa \right] \left(\boldsymbol{B}_i^{\mathbf{u}} \right)^T \boldsymbol{\sigma}_0 \right\} \mathrm{d}V \tag{3.7}$$

and

$$R_i^{\phi} = \int_\Omega \left\{ g'(\phi) N_i \mathcal{H} + \frac{G_c}{2c_w\ell} \left[\frac{w'(\phi)}{2} N_i + \ell^2 \left(\mathbf{B}_i \right)^T \nabla\phi \right] \right\} \mathrm{d}V. \tag{3.8}$$

And finally, the consistent tangent stiffness matrices $\boldsymbol{K}$ are then obtained as follows:

$$\boldsymbol{K}_{ij}^{\mathbf{u}} = \frac{\partial \boldsymbol{R}_i^{\boldsymbol{u}}}{\partial \boldsymbol{u}_j} = \int_\Omega \left\{ \left[g(\phi) + \kappa \right] (\boldsymbol{B}_i^{\boldsymbol{u}})^T \boldsymbol{C}_0 \boldsymbol{B}_j^{\boldsymbol{u}} \right\} \mathrm{d}V \tag{3.9}$$

and

$$\boldsymbol{K}_{ij}^{\phi} = \frac{\partial R_i^{\phi}}{\partial \phi_j} = \int_\Omega \left\{ \left(g''(\phi)\mathcal{H} + \frac{G_c}{4c_w\ell} w''(\phi) \right) N_i N_j + \frac{G_c \ell}{2c_w} \mathbf{B}_i^T \mathbf{B}_j \right\} \mathrm{d}V. \tag{3.10}$$

Therefore, the global system of equations reads

$$\begin{Bmatrix} \mathbf{u} \\ \boldsymbol{\phi} \end{Bmatrix}_{t+\Delta t} = \begin{Bmatrix} \mathbf{u} \\ \boldsymbol{\phi} \end{Bmatrix}_t - \begin{bmatrix} \mathbf{K}^{\mathbf{u}} & 0 \\ 0 & \mathbf{K}^{\phi} \end{bmatrix}_t^{-1} \begin{Bmatrix} \mathbf{R}^{\mathbf{u}} \\ \mathbf{R}^{\phi} \end{Bmatrix}_t. \tag{3.11}$$

Several schemes have been proposed to obtain the solutions for which $\mathbf{R}^{\mathbf{u}} = \mathbf{0}$ and $\mathbf{R}^{\phi} = \mathbf{0}$. In so-called *monolithic* solution schemes, the displacement and phase field sub-systems are

Downloaded from https://royalsocietypublishing.org/ on 21 June 2021

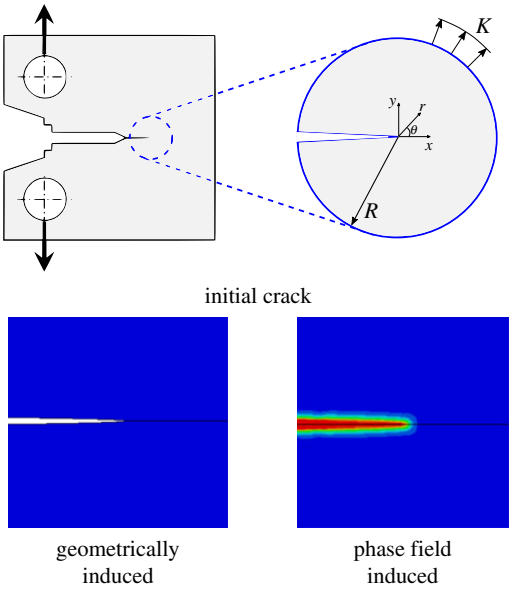

Figure 3. Boundary layer analysis: illustration of the boundary value problem and of the approaches adopted to introduce the initial crack in the solid. (Online version in colour.)

solved simultaneously; while *staggered* (or alternate minimization) approaches solve each sub-system sequentially. Monolithic solution strategies are unconditionally stable and, therefore, more efficient. However, the total potential energy functional (2.3) is non-convex with respect to $\mathbf{u}$ and ϕ, hindering convergence. Contrarily, for a fixed $\mathbf{u}$, equation (2.3) is convex with respect to ϕ (and vice versa) and the associated robustness has made staggered solution schemes more popular. Notwithstanding, it has been recently demonstrated that the use of quasi-Newton methods such as the Broyden–Fletcher–Goldfarb–Shanno (BFGS) algorithm enables the implementation of robust monolithic schemes that are very efficient and do not exhibit convergence issues [46,47]. Accordingly, the BFGS algorithm is employed here, in conjunction with a monolithic approach.

4. Results

We shall now model three paradigmatic boundary value problems to investigate the capabilities of phase field fracture models in predicting crack initiation and growth in agreement with the fracture energy balance. First, in §4a, the onset of crack growth is investigated by applying a remote energy release rate through a boundary layer model. Secondly, we model crack propagation in a double cantilever beam to compare phase field predictions with analytical results derived from beam theory from a known applied displacement and material toughness (§4b). Finally, in §4c, we show how size effects and the transition flaw size concept are a natural by-product of phase field fracture models.

(a) Initiation of crack growth: prescribing a remote *G*

The initiation of crack growth is investigated under plane strain conditions using a so-called boundary layer model. As illustrated in figure 3, the crack tip fields can be characterized as a function of the remote elastic K-field. Thus, considering a polar coordinate system (r, θ) and a Cartesian coordinate system (x, y) centred at the crack tip, with the crack plane along the negative x-axis, the displacement is given by the first term in Williams expansion [48]:

$$u_i = \frac{K}{E} r^{1/2} f_i(\theta, \nu), \tag{4.1}$$

Downloaded from https://royalsocietypublishing.org/ on 21 June 2021

where the subscript i denotes the Cartesian components, and the functions $f_i(\theta, \nu)$ are given by

$$f_x = \frac{1+\nu}{\sqrt{2\pi}} (3 - 4\nu - \cos\theta) \cos\left(\frac{\theta}{2}\right) \tag{4.2}$$

and

$$f_y = \frac{1+\nu}{\sqrt{2\pi}} (3 - 4\nu - \cos\theta) \sin\left(\frac{\theta}{2}\right). \tag{4.3}$$

Here, ν is Poisson's ratio. The relationship between the stress intensity factor K and the energy release rate G is given by Irwin's relation [2]

$$G = \left(1 - \nu^2\right) \frac{K^2}{E}. \tag{4.4}$$

Consequently, the crack tip mechanics for a given remote G (or K) can be evaluated by prescribing the displacements of the nodes located in the outer boundary of the finite element model following (4.1)–(4.4). Only one half of the boundary layer geometry is modelled due to symmetry. The model is discretized using approximately 30 000 quadratic quadrilateral elements with reduced integration. The mesh is refined in the crack propagation region, where the element aspect ratio is kept equal to 1. Throughout this manuscript, Poisson's ratio is given by $\nu = 0.3$.

The initiation of crack growth is investigated considering both the AT1 and AT2 constitutive choices for the crack density function. Also, we assess the influence of the two approaches that can potentially be used to define the initial crack: (1) *via* the phase field, by defining $\phi = 1$ as the initial condition (or enforcing $\mathcal{H} \to \infty$), and (2) geometrically, by duplicating the nodes along the crack faces; see figure 3. The aim is to assess whether phase field fracture models predict the initiation of cracking at $G = G_c$, as it would be expected based on the classical fracture mechanics theory. Fracture is unstable, exhibiting a flat crack growth resistance response and therefore the remote load at initiation (as characterized by G or K) can be easily identified. By dimensional analysis, the length scales governing the problem are the phase field length scale ℓ, the element size h and a fracture or characteristic material length (e.g. [49]):

$$L_f = \frac{G_c(1-\nu^2)}{E}. \tag{4.5}$$

Note that the initial crack length a and the outer radius of the boundary layer R (chosen such that $R, a >> \ell, L_f$) are not relevant in the present boundary value problem. Thus, we investigate the role that the two remaining non-dimensional groups (ℓ/h, L_f/ℓ) play on our fracture mechanics assessment.

The results obtained for the non-dimensional group ℓ/h are shown in figure 4. Note first that, in all cases, the solution appears to converge when the mesh sufficiently resolves the phase field and fracture length scales. The results are essentially identical if eight elements or more are used to resolve ℓ. This is not unexpected given the mesh objectivity of non-local models but element length-dependent corrections for the surface energy have been proposed [5].[1]

Secondly, we observe that the predictions of the AT2 model lead to higher G values than those of the AT1 crack density function. This could be due to the larger unloading region exhibited in the AT2 model after the critical stress has been reached, see figure 2. Thirdly, and arguably most importantly, while all mesh-converged values of G at crack initiation approach G_c, the approximation is notably better when the initial crack has been introduced by prescribing the nodal values of the phase field. Values of G/G_c very close to unity are attained with both AT1 and AT2 models when the initial crack has been defined using the phase field, showcasing the agreement between phase field models and classical fracture mechanics theory. However, when the crack is introduced geometrically (e.g. by duplicating the nodes along the crack faces), the magnitude of the energy release rate at the initiation of crack growth is noticeably larger than the fracture energy ($G/G_c \approx 1.3$). We further investigate this by plotting the phase field contours in

[1]No mesh anisotropy effects are investigated in this work.

Downloaded from https://royalsocietypublishing.org/ on 21 June 2021

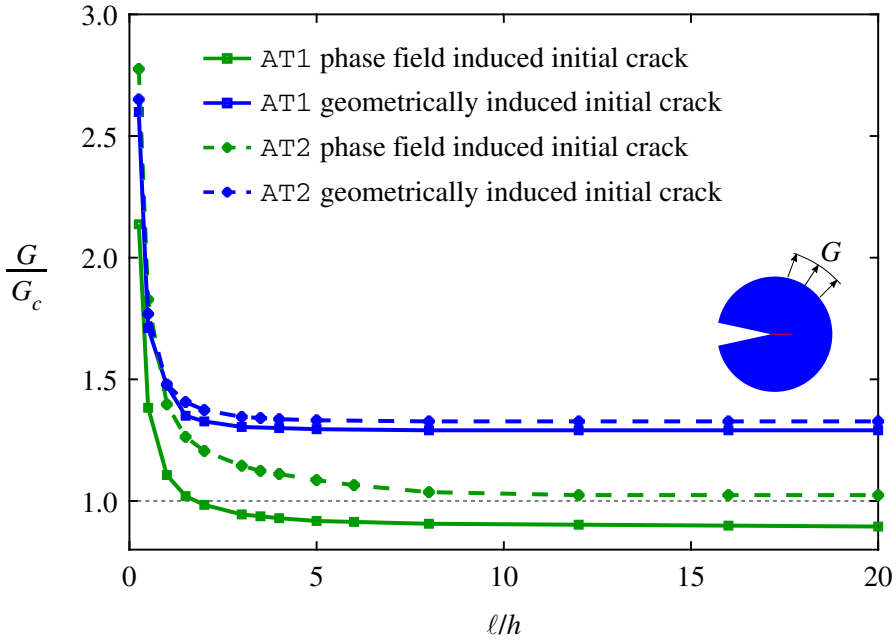

Figure 4. Boundary layer analysis: Mesh sensitivity of the energy release rate at initiation of crack growth for different constitutive choices and approaches for implementing the initial crack. The value of the characteristic fracture length scale to the phase field length scale is $L_f/\ell = 10$. (Online version in colour.)

the vicinity of the crack tip, the distribution of ϕ along the extended crack plane ($r, \theta = 0^\circ$), and the crack extension as a function of the remote G—see figure 5.

We shall first discuss the phase field contours, figure 5a. The qualitative results presented emphasize the additional energy cost associated with prescribing the crack geometrically; the phase field has to increase upon loading in all directions surrounding the crack tip. On the other hand, the phase field is already fully developed at the existing crack faces when the crack is prescribed through the phase field region. This energy barrier can rationalize the differences observed in figure 4. Another related and relevant effect is the role that the phase field natural boundary condition plays. Upon making use of the constitutive choices, equation (2.8)*b* can be re-formulated as

$$\nabla\phi \cdot \mathbf{n} = 0, \tag{4.6}$$

implying that the phase field variable ϕ must approximate the free surface with a zero slope. This is shown in figure 5*b*, which depicts the distribution of ϕ along the extended crack plane ($\theta = 0^\circ$), with r being the distance ahead of the crack tip. Results are shown as computed with the AT1 model and for both the cases of the initial crack being induced by the phase field and geometrically. The distribution of ϕ shown corresponds to an instant close to the fracture event; due to the sudden crack extension observed in the case of the geometric initial crack, the phase field variable takes significantly lower values. More importantly, when the crack is induced geometrically a plateau can be observed close to the crack tip, while the result obtained for the phase field induced initial crack (where there is no free crack surface) reveals a monotonically increasing ϕ as $r \to 0$. Finally, let us turn our attention to figure 5*c*. The crack extension has been computed using the crack surface expression given in equation (2.12). Thus, the cases where the initial crack has been introduced prescribing the phase field variable $\phi = 1$ exhibit a non-zero crack surface even before applying the load, as ϕ drops away from the crack tip in a smooth manner, with the smearing of the crack controlled by the magnitude of ℓ. This additional contribution to the crack surface, not present in the case of the geometrically induced cracks, is likely to contribute to the different values of G measured at crack initiation. The figure also highlights a key difference between the AT1 and AT2 formulations. Owing to the lack of a purely elastic phase in AT2 models, the magnitude of the crack surface formed prior to brittle fracture is larger.

Downloaded from https://royalsocietypublishing.org/ on 21 June 2021

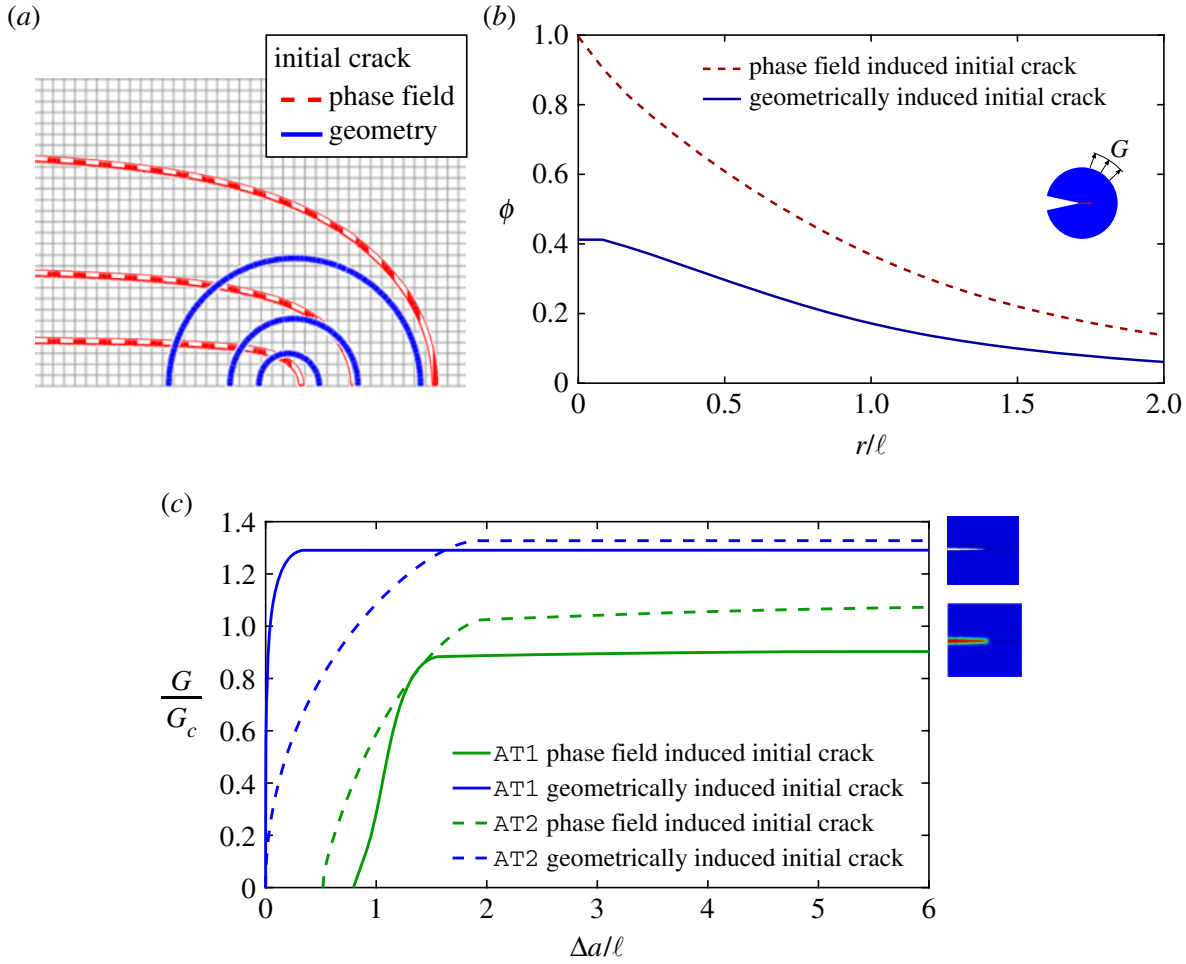

Figure 5. Boundary layer analysis. (*a*) Phase field contours for the AT1 model and both geometrically (red, dashed) and phase field (blue, solid) induced initial cracks; (*b*) crack tip phase field distribution for the AT1 model ($r, \theta = 0^\circ$), shortly before the onset of crack growth; and (*c*) crack extension, as computed from the crack surface density function—equation (2.12). The value of the characteristic fracture length scale to the phase field length scale is $L_f/\ell = 10$. (Online version in colour.)

There could be other factors influencing the precision of the phase field fracture model in predicting the initiation of crack growth. One aspect that has been discussed in the literature [50,51] is the influence of the damage irreversibility condition (§3a). In particular, it has been argued that the irreversibility condition (3.3) prevents the phase field from attaining its optimal crack profile, providing a source of inaccuracy. Thus, we re-calculate figure 4 enforcing the irreversibility condition (3.3) only when $\phi \geq 0.95$, ensuring damage irreversibility in fully cracked material points but leaving the gradients free to form their optimal profile. As shown in figure 6, no noticeable effect is observed in the present boundary value problem (a long, infinitesimally sharp crack). Differences are in all cases below 0.2%.

Finally, we explore the role of the value of the characteristic fracture length scale to the phase field length scale, L_f/ℓ, as the Γ-convergence properties of the approximation of the Griffith functional by the phase field functional hold for $\ell \to 0$. The results, shown in figure 7, reveal a negligible influence of the L_f/ℓ over a range spanning six orders of magnitude. Thus, the results and conclusions from figure 4 hold; phase field fracture predictions for the initiation of crack growth are close to those of classical fracture mechanics but the approximation improves if the initial crack is defined using the phase field variable.

(b) Stable crack growth: double cantilever beam analysis

We shall now investigate the effectiveness of phase field fracture methods in approximating stable crack growth. For this purpose, we will model crack propagation in a double cantilever beam; a

Downloaded from https://royalsocietypublishing.org/ on 21 June 2021

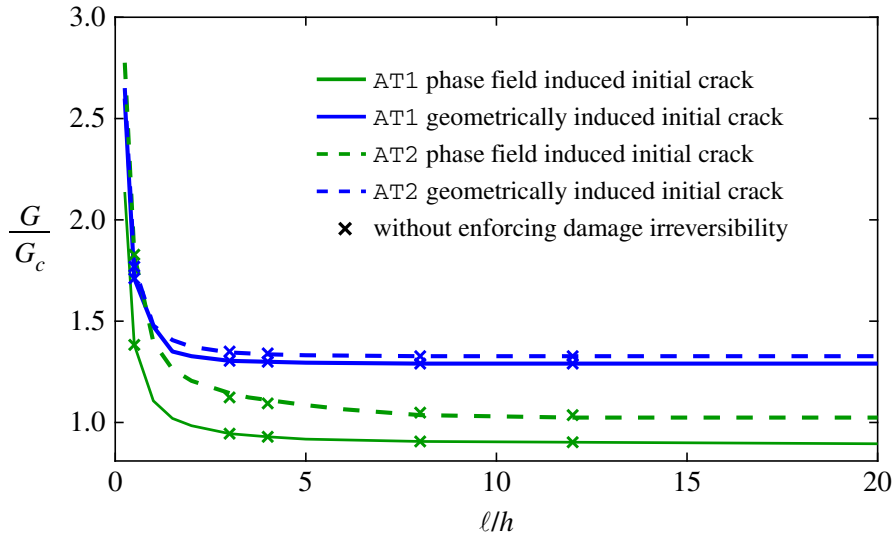

Figure 6. Boundary layer analysis: influence of enforcing damage irreversibility on the initiation of crack growth. Symbols denote the results without the irreversibility condition, equation (3.3). The value of the characteristic fracture length scale to the phase field length scale is $L_f/\ell = 10$. (Online version in colour.)

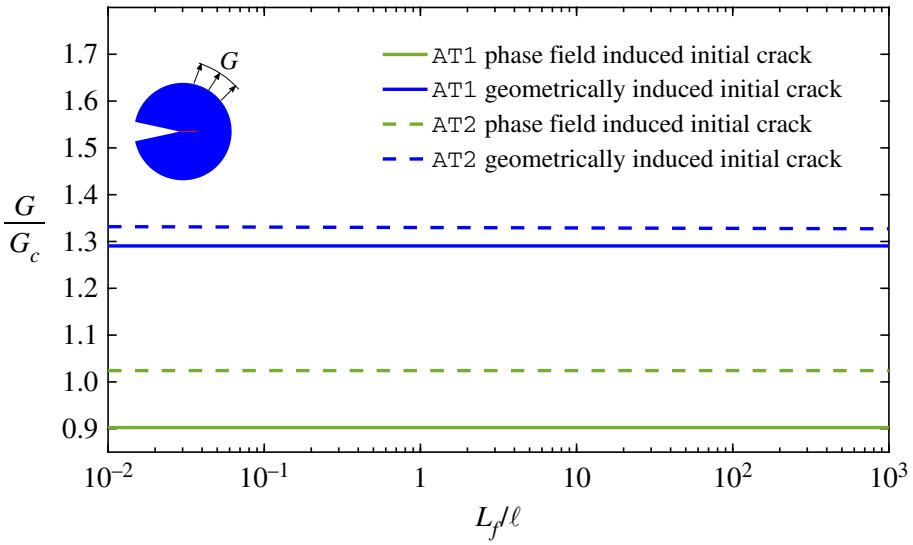

Figure 7. Boundary layer analysis: influence of varying the fracture length scale $L_f = G_c(1 - \nu^2)/E$, with $\ell/h = 12$. (Online version in colour.)

boundary value problem with a known analytical solution, based on beam theory, for relating the energy release rate, the applied displacement and the crack length. To the best of our knowledge, this analysis has not been conducted before.

The geometry of the model is shown in figure 8. Only a quarter of the boundary value problem is modelled, taking advantage of symmetry. Plane strain conditions are assumed, with a thickness of $B = 1$ mm. The height is also taken to be equal to $H = 0.9$ mm. The initial crack length is given by $a = a_0 = 10$ mm and a vertical crack mouth opening displacement δ is prescribed along the symmetry axis. Here, Poisson's ratio is also taken to be $\nu = 0.3$. The model is discretized using a total of 190 140 quadratic quadrilateral elements with reduced integration, with the characteristic length of the element along the crack propagation region being ten times smaller than the phase field length scale (in agreement with the mesh sensitivity analysis conducted above; figure 4). The phase field length scale is chosen to be $\ell = 0.03$ mm and $L_f/\ell \approx 0.003$. A representative result of crack propagation is shown in figure 9, where the red colour is employed to denote fully cracked material points ($\phi > 0.95$) while blue colour is used to denote intact material points ($\phi \approx 0$).

Downloaded from https://royalsocietypublishing.org/ on 21 June 2021

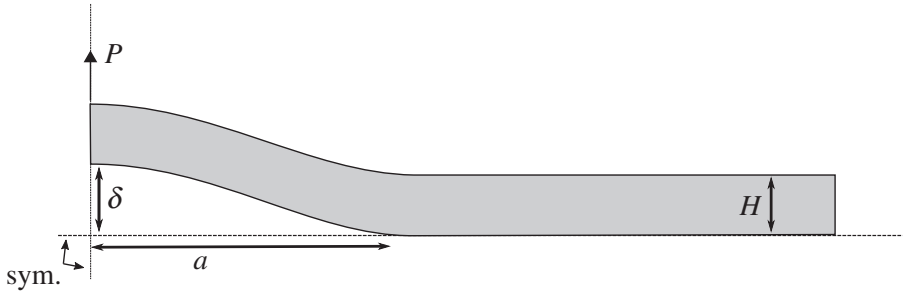

Figure 8. Double cantilever beam analysis: sketch of the boundary value problem. Only one quarter of the problem is modelled taking advantage of symmetry.

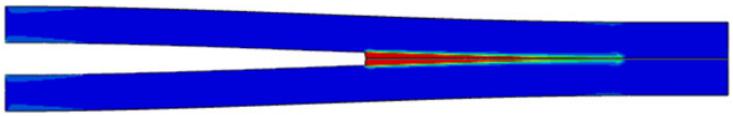

Figure 9. Double cantilever beam analysis: snapshot of the crack propagation process, with red colour denoting fully cracked material points ($\phi > 0.95$) and blue colour used to denote intact material points ($\phi \approx 0$). (Online version in colour.)

An analytical relation between the energy release rate and the applied displacement for a given crack size, a, can be readily derived using Timoshenko beam theory. The relationship between the transverse force P acting on the quarter model (figure 8) and the displacement δ is given by

$$\delta = \frac{Pa^3}{\bar{E}BH^3} + \frac{Pa}{\kappa \mu BH}. \tag{4.7}$$

Here, $\bar{E} = E/(1-\nu^2)$ is the plane strain Young's modulus, $\mu = E/(2(1+\nu))$ is the shear modulus, and $\kappa \approx 5/6$ is the shear coefficient for the rectangular beam cross section. Exploiting symmetry around the horizontal axis, the energy release rate may be calculated from the compliance $C = \delta/P$ by

$$G = 2 \cdot \frac{P^2}{2B}\frac{\mathrm{d}C}{\mathrm{d}a} = \frac{3P^2a^2}{\bar{E}B^2H^3} + \frac{P^2}{\kappa \mu B^2 H}. \tag{4.8}$$

Accordingly, the energy release rate can be formulated as a function of displacement, δ, and crack length, a, as follows:

$$G = \frac{3\bar{E}H^3}{a^4} \cdot \frac{1 + (\bar{E}/3\kappa\mu)\,(H/a)^2}{\left(1 + (\bar{E}/\kappa\mu)\,(H/a)^2\right)^2} \cdot \delta^2, \tag{4.9}$$

and thus, for a given material toughness G_c, equation (4.9) provides a unique relation between the beam displacement δ and the crack length a.

As in the previous case study, we employ both the AT1 and AT2 models and assess as well the influence of either defining the initial crack geometrically or using the phase field. In addition, unlike the previous analysis, results are now sensitive to the methodology employed to measure crack extension; we choose to compare two options: (1) using the crack surface integral (2.12), and (2) assuming that the crack front is given by the $\phi = 0.95$ contour. The results for each approach are shown in figure 10*a* and 10*b*, respectively.

A satisfactory agreement is observed. All finite element results provide a stable cracking response that qualitatively mimics that of the analytical solution. However, quantitative differences can be observed, and these are particularly noticeable for specific modelling and constitutive choices. Namely, a better agreement is attained when the crack extension is measured using the crack density function (2.12), as opposed to assuming the crack front to be the furthest point with $\phi = 0.95$. Also, the AT1 model appears to deliver predictions that are closer to the beam theory solution, relative to the AT2 model. Nevertheless, all results appear to display a

Downloaded from https://royalsocietypublishing.org/ on 21 June 2021

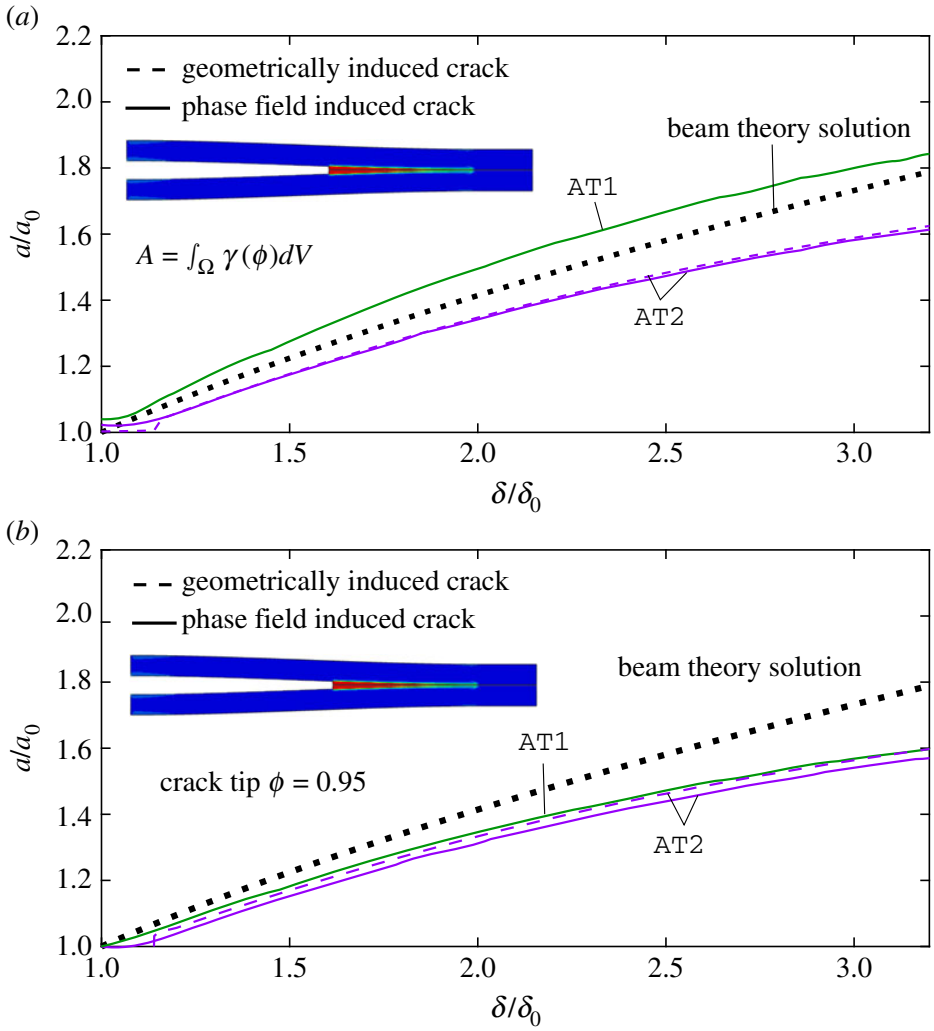

Figure 10. Double cantilever beam analysis. Crack extension as measured by: (*a*) the crack surface density function, equation (2.12), and (*b*) the furthest point with $\phi = 0.95$. (Online version in colour.)

similar shape and the differences are mainly related to the onset of crack initiation and the length of the initial crack. Thus, all phase field results require a larger applied displacement to initiate the fracture process. Also, as in the previous case study, the AT1 model with a phase field-induced crack overpredicts the initial crack length, as there is a contribution from the gradients of ϕ to the crack density function. Some general trends to take note of are that the problem exhibits some sensitivity to the size of ℓ/H and that all constitutive choices exhibit a slowing of the crack growth relative to the analytical solution. This is seemingly not caused by edge effects, as identical results have been obtained for a beam of length $L = 30$ mm. The correspondence between the analytical and predicted curves may be improved by accounting for the slight loss of bending stiffness caused by the degradation from the phase field in the gradient region. Furthermore, the phase field attains non-zero values along the top edge which further reduces the bending stiffness of the beam. The latter may be remedied by introducing a strain split scheme for preventing damage evolution from compression [7,52].

(c) Size effects and the transition flaw size

So far, we have focused on the original phase field fracture formalism, with the aim of providing a regularization that accurately approximates Griffith's energy balance in the $\ell \to 0^+$ limit. Thus, the length scale has been considered *exclusively* a regularizing parameter. However, there is an increasing interest in investigating the implications of considering a finite phase field length scale and the resulting analogies with gradient damage models [10,53,54]. As discussed in §1, the

Downloaded from https://royalsocietypublishing.org/ on 21 June 2021

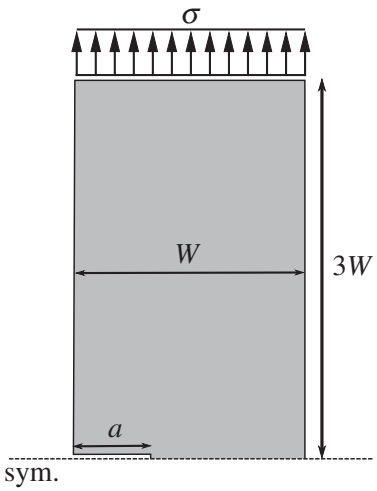

Figure 11. Transition flaw size analysis: geometry and loading configuration of the numerical model.

consideration of a finite $\ell > 0^+$ introduces a critical stress proportional to $1/\sqrt{\ell}$, which is absent in Griffith's formulation and linear elastic fracture mechanics. Thus, ℓ becomes a material property. The motivation for adopting a positive, constant ℓ stems from the fact that Griffith's theory is unable to capture some well-characterized size effects. One of these important size effects is the transition flaw size concept, which is the cornerstone of many engineering standards and fracture mechanics-based engineering design; if a crack is smaller than the transition flaw size, then the crack will not grow and the specimen will fail at the material strength (or at the yield stress σ_y, if plastic design is considered). We shall show here that the transition flaw size paradigm is a natural by-product of variational phase field fracture models that consider ℓ to be an internal material length.

We model fracture in a single-edge notched specimen of width W and height $6W$. The plate is subjected to a remote tensile stress σ. As shown in figure 11, only the upper half of the sample is considered for the finite element analysis, taking advantage of symmetry. The specimen contains a crack of length a, which will be varied throughout the analysis. In all cases, the crack is introduced into the model by defining the initial condition $\phi = 1$ on the phase field, in agreement with our findings above for best practice. Both the `AT1` and `AT2` models are considered, to assess the implications of different constitutive choices for the crack density function. The phase field length scale is chosen to be small relative to the sample dimensions, $\ell/W = 0.03$, and the mesh is refined along the crack ligament, where the characteristic element length equals $h/\ell = 0.1$. The model is discretized using a total of 11 251 quadratic quadrilateral elements with reduced integration.

The results obtained are shown in figure 12, where we have superimposed the strength failure criterion (also referred to as *plastic collapse* if $\sigma_c = \sigma_y$) and the Griffith (linear elastic fracture mechanics) prediction:

$$\sigma = \sqrt{\frac{EG_c}{\pi a\left(1-\nu^2\right)}}\frac{1}{f\left(a/W\right)}, \tag{4.10}$$

with the following geometry factor $f(a/W)$ for a plate of finite size with an edge crack:

$$f\left(\frac{a}{W}\right) = \left(\frac{2W}{\pi a}\tan\frac{\pi a}{2W}\right)^{1/2}\left(\cos\frac{\pi a}{2W}\right)^{-1}\left[0.752 + 2.02\frac{a}{W} + 0.37\left(1-\sin\frac{\pi a}{2W}\right)^3\right]. \tag{4.11}$$

The results shown in figure 12 are given in terms of the failure stress σ_f as a function of the crack size a, for both `AT1` and `AT2` models. Note that the material strength takes different values for each of these constitutive choices—see (2.14). It can be observed that phase field fracture models are capable of reconciliating stress and toughness criteria for fracture; a good agreement with the Griffith criterion is observed for large cracks and predictions transition smoothly to a strength-driven failure as the crack size decreases below the transition flaw size.

Downloaded from https://royalsocietypublishing.org/ on 21 June 2021

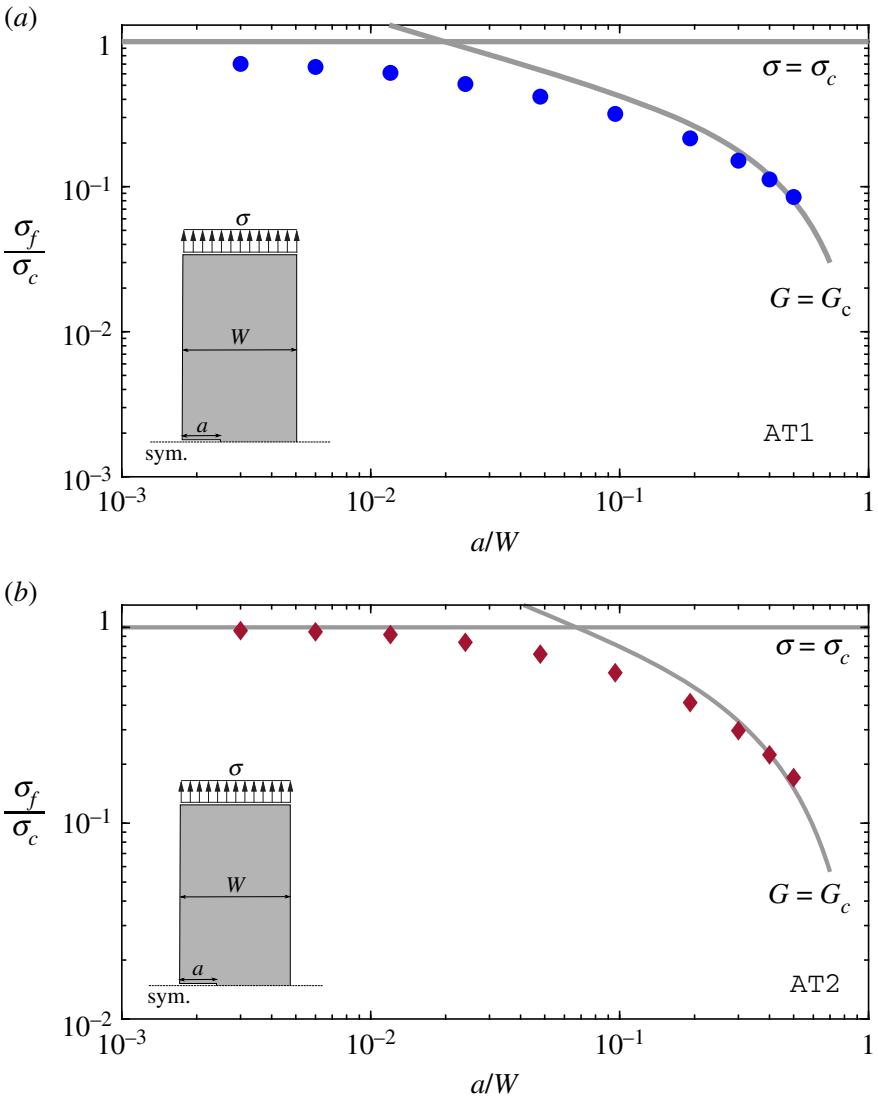

Figure 12. Transition flaw size analysis: failure strength as a function of the crack size for (*a*) AT1, and (*b*) AT2 phase field models. The solid grey lines denote the fracture predictions according to the material strength and to Griffith's criterion (4.10). (Online version in colour.)

In terms of constitutive choices for the crack density function, both AT1 and AT2 models appear to provide a good agreement with the limiting cases of $\sigma_f = \sigma_c$ and $G = G_c$. The agreement appears to be slightly better for the AT2 case, in that the material strength is only attained when using the AT1 model for very short cracks (much smaller than the transition flaw size). Or, in other words, the transition between pure strength and pure toughness-driven criteria appears to span a wider range of crack sizes in the case of the AT1 formulation.

5. Discussion

Our results show that phase field fracture models provide a good approximation to classical fracture mechanics predictions. Three research questions have been answered, the first one being: can phase field fracture methods capture crack growth initiation at the appropriate energy release rate? By modelling crack growth from an existing (long) crack upon the application of a remote G (or K), we have seen that cracking takes place at $G \approx G_c$ but only for certain modelling choices. Specifically, using the phase field variable to induce the initial crack provides a result closer to Griffith's criterion, while introducing the crack geometrically leads to crack initiation values of G that are slightly larger than G_c. It is important to emphasize that this finding relates to a long, infinitesimally sharp crack. Similar conclusions were attained by Klinsmann *et al.* [55]

Downloaded from https://royalsocietypublishing.org/ on 21 June 2021

for a finite crack using the AT2 model and a pure bending boundary value problem. We also find that the specific constitutive choice for the crack density function (AT1 versus AT2) does not play a significant role, with the AT2 model predicting the initiation of crack growth at a slightly larger G. We have also shown that these conclusions hold for $\ell \to 0$, independently of whether or not the irreversibility condition is employed. In fact, enforcing damage irreversibility appears to have a negligible effect on the efficacy of phase field models for accurately predicting crack initiation, under the conditions considered here (a long sharp crack). Our analysis suggests that the delay in initiating fracture when the initial crack is geometrically prescribed is related to the natural boundary condition (2.8)b, constraining ϕ to be constant near the crack surface, and the additional energy expenditure required to build-up a highly constrained phase field region around the crack tip (even behind the crack). There are other sources that can potentially contribute to discrepancies in crack initiation predictions, which have not been quantified as we have judged them *a priori* to be of secondary importance. For example, in elastic-plastic solids, plasticity introduces non-proportional straining but, while this effect can be significant during continued crack growth [56,57], a very minor influence is expected for crack initiation under small-scale yielding conditions. Also, the extent to which a Griffith-like energy balance can be used for ductile solids is questionable [53,58–61]; the thermodynamics picture will change, as local plastic flow provides a localized source of heat. Along the same lines, different constitutive choices for the crack density function can also provide different degrees of approximation, in the same way that this is observed with different traction-separation laws in cohesive zone models, where larger unloading regimes in the traction-separation law lead to larger differences compared to a proportional loading scenario. Hence, for cohesive zone models, a trapezoidal law with a smaller unloading region, like the one by Tvergaard & Hutchinson [62], can provide a better approximation of crack initiation, relative to an exponential law, such as that by Xu & Needleman [63], with a large unloading regime. In any case, differences are expected to be small also for phase field models; our results show that both AT1 and AT2 models predict the initiation of crack growth at $G \approx G_c$ (for a phase field induced initial crack) despite their different unloading regimes—see figure 2. It must be emphasized that our findings are related to solids containing cracks; phase field fracture models can also predict the nucleation of cracks from pristine samples and non-sharp defects such as notches, where the conclusions reported here might not apply. In particular, the conclusions drawn in regard to the irreversibility condition might change [50,51] and it has been reported that prescribing $\phi = 1$ at the defect surface is not the most accurate way of capturing crack nucleation from blunted notches [10].

The second research question deals with the capabilities of phase field fracture models in predicting stable crack growth, in agreement with beam theory and the fracture energy balance. We gained new insight by modelling the progressive failure of a double cantilever beam with a known analytical solution, based on Timoshenko beam theory. The results revealed a satisfactory agreement but also noticeable quantitative differences depending on the approach employed to measure the crack extension and the constitutive model. The best result was attained by employing the AT1 model and, more importantly, measuring the degree of crack extension through the crack density function—equation (2.12). The lack of a similar study in the literature, to the best of our knowledge, hinders gaining further insight by comparing to previous studies.

Finally, we aimed at shedding light on the capabilities of phase field fracture models to capture, by attributing ℓ a physical meaning, well-known size effects that cannot be predicted with Griffith theory. Griffith's framework and linear elastic fracture mechanics can capture how the critical load for fracture scales as $1/\sqrt{L}$, where L is the reference size of the specimen, and how the strength of the specimen decreases with increasing crack size. However, this scaling size effect breaks down as the load required to fracture small samples ($L \to 0$) does not go to infinity—cracks do not propagate if they are smaller than a reference length (the transition flaw size), and failure by other mechanisms sets in. These inconsistencies can be addressed by incorporating a length scale or a critical strength. In the context of phase field models, the consideration of ℓ as a material constant naturally introduces a critical stress—see (2.4). We have shown that this approach can readily

Downloaded from https://royalsocietypublishing.org/ on 21 June 2021

capture the transition flaw size concept, gradually changing from toughness-driven to strength-driven failures. This is observed with the initial crack prescribed using the phase field and for both AT1 and AT2 models (with a slightly better performance using the latter). Similar conclusions were drawn by Tanné *et al.* [10] using a different boundary value problem (a plate with a central crack), the AT1 model and a geometrically induced initial crack. Thus, our findings demonstrate that phase field models without an elastic phase can also reconcile toughness and strength. The capabilities of variational phase field models in incorporating the concepts of material strength and toughness bring them in agreement with the coupled criterion of finite fracture mechanics [64,65], but with the additional modelling capabilities intrinsic to phase field models. Along these lines, several modelling strategies and constitutive prescriptions have been presented to enhance the crack nucleation capabilities of phase field models and decouple the strength and the phase field length scale [43,66,67].

6. Conclusion

We have reviewed the most widely used phase field fracture models and revisited their ability to deliver predictions in agreement with classical fracture mechanics theory. The energy balance of Griffith theory was cast in a variational form and approximated using a regularized phase field functional. Then, the nucleation and growth of cracks were predicted based on this global energy minimization problem. We focused our efforts on three boundary value problems of particular relevance, all of which involve solids containing sharp cracks.

First, we used a boundary layer model to impose an increasing G and assess whether phase field fracture can predict the initiation of growth at $G = G_c$. We found that this result is only attained with accuracy if the initial crack is introduced by prescribing the initial value of the phase field variable ϕ, while the models containing a geometrically induced crack overestimate the critical value of G. From our predictions of phase field distribution and crack surface evolution, we conclude that this is due to the natural boundary condition for the phase field $\nabla\phi \cdot \mathbf{n} = 0$ and the energy barrier associated with the build-up of a highly constrained phase field region around the crack tip. In addition, we have tested and discussed other hypotheses that can potentially rationalize the mismatch with Griffith's criterion; we conclude that, for the conditions considered here, the irreversibility condition and non-proportional straining play a secondary role. Secondly, we assessed for the first time the capabilities of phase field fracture in predicting sustained, stable crack growth in agreement with beam theory and Griffith's energy balance. While all predictions were deemed satisfactory, the degree of agreement improved notably if the crack extension was measured using the crack density functional and, for the AT1 model, if the crack was introduced using the phase field. Finally, we treated the phase field length scale as a material property and modelled the failure of a plate with different crack sizes, showing that the consideration of a constant $\ell > 0^+$ enables capturing the vanishing effect of small flaws on the fracture strength and reconciles toughness and strength failure criteria. This size effect, which cannot be captured by Griffith's theory, was appropriately predicted with both AT1 and AT2 models.

It is therefore concluded that phase field models can deliver accurate fracture predictions if suitable modelling choices are made. Specifically, we note that (for the conditions examined here) the constitutive choices for the crack density function (AT1 versus AT2) play a secondary role but accuracy can be improved noticeably if the initial crack is defined using the phase field and the crack extension is measured using the crack density function (2.12). These findings have been discussed in the context of the literature, emphasizing the new and complementary insight provided, which is hoped to be valuable in assessing the capabilities of phase field fracture models in delivering predictions in agreement with the energy balance that gave birth to fracture mechanics.

Data accessibility. This article has no additional data.

Competing interests. We declare we have no competing interests.

Downloaded from https://royalsocietypublishing.org/ on 21 June 2021

Funding. The authors gratefully acknowledge financial support from the Danish Hydrocarbon Research and Technology Centre (DHRTC). E. Martínez-Pañeda additionally acknowledges financial support from the EPSRC (grant nos EP/R010161/1 and EP/R017727/1) and from the Royal Commission for the 1851 Exhibition (RF496/2018).

References

1. Griffith AA. 1920 The phenomena of rupture and flow in solids. *Phil. Trans. A* **221**, 163–198. (doi:10.1098/rsta.1921.0006)
2. Irwin GR. 1956 Onset of fast crack propagation in high strength steel and aluminum alloys. In *Sagamore Research Conference Proceedings*, vol. 2, pp. 289–305. New York, NY: Springer.
3. Anderson TL 2005 *Fracture mechanics*. Fundamentals and applications, 3rd edn. Taylor & Francis, Boca Raton: CRC Press.
4. Kendall K. 2021 *Crack control: using fracture theory to create tough new materials*. Amsterdam, The Netherlands: Elsevier.
5. Bourdin B, Francfort GA, Marigo JJ. 2008 *The variational approach to fracture*. Amsterdam, The Netherlands: Springer.
6. Bourdin B, Francfort GA, Marigo J-J. 2000 Numerical experiments in revisited brittle fracture. *J. Mech. Phys. Solids* **48**, 797–826. (doi:10.1016/S0022-5096(99)00028-9)
7. Miehe C, Welshinger F, Hofacker M. 2010 Thermodynamically consistent phase field models of fracture: variational principles and multi-field FE implementations. *Int. J. Numer. Methods Eng.* **83**, 1273–1311. (doi:10.1002/nme.2861)
8. Pons AJ, Karma A. 2010 Helical crack-front instability in mixed-mode fracture. *Nature* **464**, 85–89. (doi:10.1038/nature08862)
9. Borden MJ, Verhoosel CV, Scott MA, Hughes TJR, Landis CM. 2012 A phase field description of dynamic brittle fracture. *Comput. Methods Appl. Mech. Eng.* **217–220**, 77–95. (doi:10.1016/j.cma.2012.01.008)
10. Tanné E, Li T, Bourdin B, Marigo J-J, Maurini C. 2018 Crack nucleation in variational phase field models of brittle fracture. *J. Mech. Phys. Solids* **110**, 80–99. (doi:10.1016/j.jmps.2017.09.006)
11. Bourdin B, Francfort GA. 2019 Past and present of variational fracture. *SIAM News* **52**, 1–5.
12. Borden MJ, Hughes TJR, Landis CM, Anvari A, Lee IJ. 2016 A phase field formulation for fracture in ductile materials: finite deformation balance law derivation, plastic degradation, and stress triaxiality effects. *Comput. Methods Appl. Mech. Eng.* **312**, 130–166. (doi:10.1016/j.cma.2016.09.005)
13. Miehe C, Mauthe S. 2016 Phase field modeling of fracture in multi-physics problems. Part III. Crack driving forces in hydro-poro-elasticity and hydraulic fracturing of fluid-saturated porous media. *Comput. Methods Appl. Mech. Eng.* **304**, 619–655. (doi:10.1016/j.cma.2015.09.021)
14. Kristensen PK, Niordson CF, Martínez-Pañeda E. 2020 Applications of phase field fracture in modelling hydrogen assisted failures. *Theor. Appl. Fract. Mech.* **110**, 102837. (doi:10.1016/j.tafmec.2020.102837)
15. Wu J-Y, Huang Y, Nguyen VP. 2021 Three-dimensional phase field modeling of mode I + II/III failure in solids. *Comput. Methods Appl. Mech. Eng.* **373**, 113537. (doi:10.1016/j.cma.2020.113537)
16. Quintanas-Corominas A, Reinoso J, Casoni E, Turon A, Mayugo JA. 2019 A phase field approach to simulate intralaminar and translaminar fracture in long fiber composite materials. *Compos. Struct.* **220**, 899–911. (doi:10.1016/j.compstruct.2019.02.007)
17. Tan W, Martínez-Pañeda E. 2021 Phase field predictions of microscopic fracture and R-curve behaviour of fibre-reinforced composites. *Compos. Sci. Technol.* **202**, 108539. (doi:10.1016/j.compscitech.2020.108539)
18. Simoes M, Martínez-Pañeda E. 2021 Phase field modelling of fracture and fatigue in shape memory alloys. *Comput. Methods Appl. Mech. Eng.* **373**, 113504. (doi:10.1016/j.cma.2020.113504)
19. Zhou S, Zhuang X, Zhu H, Rabczuk T. 2018 Phase field modelling of crack propagation, branching and coalescence in rocks. *Theor. Appl. Fract. Mech.* **96**, 174–192. (doi:10.1016/j.tafmec.2018.04.011)

Downloaded from https://royalsocietypublishing.org/ on 21 June 2021

20. Martínez-Pañeda E, Golahmar A, Niordson CF. 2018 A phase field formulation for hydrogen assisted cracking. *Comput. Methods Appl. Mech. Eng.* **342**, 742–761. (doi:10.1016/j.cma.2018.07.021)
21. Martínez-Pañeda E, Harris ZD, Fuentes-Alonso S, Scully JR, Burns JT. 2020 On the suitability of slow strain rate tensile testing for assessing hydrogen embrittlement susceptibility. *Corros. Sci.* **163**, 108291. (doi:10.1016/j.corsci.2019.108291)
22. Hirshikesh , Natarajan S, Annabattula RK, Martínez-Pañeda E. 2019 Phase field modelling of crack propagation in functionally graded materials. *Compos. Part B: Eng.* **169**, 239–248. (doi:10.1016/j.compositesb.2019.04.003)
23. V. Kumar PKA, Dean A, Reinoso J, Lenarda P, Paggi M. 2021 Phase field modeling of fracture in functionally graded materials : G -convergence and mechanical insight on the effect of grading. *Thin-Walled Struct.* **159**, 107234. (doi:10.1016/j.tws.2020.107234)
24. McAuliffe C, Waisman H. 2016 A coupled phase field shear band model for ductile-brittle transition in notched plate impacts. *Comput. Methods Appl. Mech. Eng.* **305**, 173–195. (doi:10.1016/j.cma.2016.02.018)
25. Lo YS, Borden MJ, Ravi-Chandar K, Landis CM. 2019 A phase field model for fatigue crack growth. *J. Mech. Phys. Solids* **132**, 103684. (doi:10.1016/j.jmps.2019.103684)
26. Carrara P, Ambati M, Alessi R, De Lorenzis L. 2020 A framework to model the fatigue behavior of brittle materials based on a variational phase field approach. *Comput. Methods Appl. Mech. Eng.* **361**, 112731. (doi:10.1016/j.cma.2019.112731)
27. Miehe C, Aldakheel F, Raina A. 2016 Phase field modeling of ductile fracture at finite strains: a variational gradient-extended plasticity-damage theory. *Int. J. Plast.* **84**, 1–32. (doi:10.1016/j.ijplas.2016.04.011)
28. Alessi R, Ambati M, Gerasimov T, Vidoli S, De Lorenzis L. 2018 Comparison of phase field models of fracture coupled with plasticity. In *Advances in Computational Plasticity* (eds MCE Oñate, D Peric, E de Souza- Neto), pp. 1–21. New York, NY: Springer Nature.
29. Miehe C, Dal H, Schanzel L-M, Raina A. 2016 A phase field model for chemo-mechanical induced fracture in lithium-ion battery electrode particles. *Int. J. Numer. Methods Eng.* **106**, 683–711. (doi:10.1002/nme.5133)
30. Klinsmann M, Rosato D, Kamlah M, McMeeking RM. 2016 Modeling crack growth during Li extraction in storage particles using a fracture phase field approach. *J. Electrochem. Soc.* **163**, A102–A118. (doi:10.1149/2.0281602jes)
31. Francfort GA, Marigo J-J. 1998 Revisiting brittle fracture as an energy minimization problem. *J. Mech. Phys. Solids* **46**, 1319–1342. (doi:10.1016/S0022-5096(98)00034-9)
32. Carolan D, Chong HM, Ivankovic A, Kinloch AJ, Taylor AC. 2015 Co-continuous polymer systems: a numerical investigation. *Comput. Mater. Sci.* **98**, 24–33. (doi:10.1016/j.commatsci.2014.10.039)
33. Xia L, Yvonnet J, Ghabezloo S. 2017 Phase field modeling of hydraulic fracturing with interfacial damage in highly heterogeneous fluid-saturated porous media. *Eng. Fract. Mech.* **186**, 158–180. (doi:10.1016/j.engfracmech.2017.10.005)
34. Provatas N, Elder K. 2011 *Phase-field methods in materials science and engineering*. Weinheim, Germany: John Wiley & Sons.
35. Cui C, Ma R, Martínez-Pañeda E. 2021 A phase field formulation for dissolution-driven stress corrosion cracking. *J. Mech. Phys. Solids* **147**, 104254. (doi:10.1016/j.jmps.2020.104254)
36. Ambrosio L, Tortorelli VM. 1991 Approximation of functionals depending on jumps by elliptic functionals via gamma-convergence. *Commun. Pure Appl. Math.* **43**, 999–1036. (doi:10.1002/cpa.3160430805)
37. Mumford D, Shah J. 1989 Optimal approximations by piecewise smooth functions and associated variational problems. *Commun. Pure Appl. Math.* **42**, 577–685. (doi:10.1002/cpa.3160420503)
38. Bellettini G, Coscia A. 1994 Discrete approximation of a free discontinuity problem. *Numer. Funct. Anal. Optim.* **15**, 201–224. (doi:10.1080/01630569408816562)
39. Chambolle A. 2004 An approximation result for special functions with bounded deformation. *J. des Mathematiques Pures et Appliquees* **83**, 929–954. (doi:10.1016/j.matpur.2004.02.004)
40. Pham K, Amor H, Marigo JJ, Maurini C. 2011 Gradient damage models and their use to approximate brittle fracture. *Int. J. Damage Mech.* **20**, 618–652. (doi:10.1177/1056789510386852)

Downloaded from https://royalsocietypublishing.org/ on 21 June 2021

41. Karma A, Kessler DA, Levine H. 2001 Phase-field model of mode III dynamic fracture. *Phys. Rev. Lett.* **87**, 45501–1–45501–4. (doi:10.1103/PhysRevLett.87.045501)
42. Freddi F, Iurlano F. 2017 Numerical insight of a variational smeared approach to cohesive fracture. *J. Mech. Phys. Solids* **98**, 156–171. (doi:10.1016/j.jmps.2016.09.003)
43. Wu J-Y. 2017 A unified phase field theory for the mechanics of damage and quasi-brittle failure. *J. Mech. Phys. Solids* **103**, 72–99. (doi:10.1016/j.jmps.2017.03.015)
44. Wu J-Y, Nguyen VP. 2018 A length scale insensitive phase field damage model for brittle fracture. *J. Mech. Phys. Solids* **119**, 20–42. (doi:10.1016/j.jmps.2018.06.006)
45. Papazafeiropoulos G, Muñiz-Calvente M, Martínez-Pañeda E. 2017 Abaqus2Matlab: a suitable tool for finite element post-processing. *Adv. Eng. Softw.* **105**, 9–16. (doi:10.1016/j.advengsoft.2017.01.006)
46. Wu J-Y, Huang Y, Nguyen VP. 2020 On the BFGS monolithic algorithm for the unified phase field damage theory. *Comput. Methods Appl. Mech. Eng.* **360**, 112704. (doi:10.1016/j.cma.2019.112704)
47. Kristensen PK, Martínez-Pañeda E. 2020 Phase field fracture modelling using quasi-Newton methods and a new adaptive step scheme. *Theor. Appl. Fract. Mech.* **107**, 102446. (doi:10.1016/j.tafmec.2019.102446)
48. Williams ML. 1957 On the stress distribution at the base of a stationary crack. *J. Appl. Mech.* **24**, 109–114.
49. Falk ML, Needleman A, Rice JR. 2001 A critical evaluation of cohesive zone models of dynamic fracture. *J. Phys. IV* **11**, 43–50. (doi:10.1051/jp4:2001506)
50. Linse T, Hennig P, Kästner M, de Borst R. 2017 A convergence study of phase field models for brittle fracture. *Eng. Fract. Mech.* **184**, 307–318. (doi:10.1016/j.engfracmech.2017.09.013)
51. Strobl M, Seelig T. 2020 Phase field modeling of Hertzian indentation fracture. *J. Mech. Phys. Solids* **143**, 104026. (doi:10.1016/j.jmps.2020.104026)
52. Amor H, Marigo JJ, Maurini C. 2009 Regularized formulation of the variational brittle fracture with unilateral contact: numerical experiments. *J. Mech. Phys. Solids* **57**, 1209–1229. (doi:10.1016/j.jmps.2009.04.011)
53. Duda FP, Ciarbonetti A, Sánchez PJ, Huespe AE. 2015 A phase field/gradient damage model for brittle fracture in elastic-plastic solids. *Int. J. Plast.* **65**, 269–296. (doi:10.1016/j.ijplas.2014.09.005)
54. Kristensen PK, Niordson CF, Martínez-Pañeda E. 2020 A phase field model for elastic-gradient-plastic solids undergoing hydrogen embrittlement. *J. Mech. Phys. Solids* **143**, 104093. (doi:10.1016/j.jmps.2020.104093)
55. Klinsmann M, Rosato D, Kamlah M, McMeeking RM. 2015 An assessment of the phase field formulation for crack growth. *Comput. Methods Appl. Mech. Eng.* **294**, 313–330. (doi:10.1016/j.cma.2015.06.009)
56. Martínez-Pañeda E, Fleck NA. 2018 Crack growth resistance in metallic alloys: the role of isotropic versus kinematic hardening. *J. Appl. Mech.* **85**, 11002. (6 pages). (doi:10.1115/1.4038285)
57. Juul KJ, Martínez-Pañeda E, Nielsen KL, Niordson CF. 2019 Steady-state fracture toughness of elastic-plastic solids: isotropic versus kinematic hardening. *Eng. Fract. Mech.* **207**, 254–268. (doi:10.1016/j.engfracmech.2018.12.016)
58. Orowan E. 1948 Fracture and strength of solids. *Rep. Prog. Phys.* **XII**, 185. (doi:10.1088/0034-4885/12/1/309)
59. Gurtin ME. 1979 Thermodynamics and the Griffith criterion for brittle fracture. *Int. J. Solids Struct.* **15**, 553–560. (doi:10.1016/0020-7683(79)90082-9)
60. Hutchinson JW. 1983 Fundamentals of the phenomenological theory of nonlinear fracture mechanics. *J. Appl. Mech. Trans. ASME* **50**, 1042–1051. (doi:10.1115/1.3167187)
61. Stevens RN, Guiu F. 1991 Energy balance concepts in the physics of fracture. *Proc. R. Soc. Lond. A* **435**, 169–184. (doi:10.1098/rspa.1991.0136)
62. Tvergaard V, Hutchinson JW. 1992 The relation between crack growth resistance and fracture process parameters in elastic-plastic solids. *J. Mech. Phys. Solids* **40**, 1377–1397. (doi:10.1016/0022-5096(92)90020-3)
63. Xu XP, Needleman A. 1994 Numerical simulations of fast crack growth in brittle solids. *J. Mech. Phys. Solids* **42**, 1397–1434. (doi:10.1016/0022-5096(94)90003-5)

64. Leguillon D. 2002 Strength or toughness? A criterion for crack onset at a notch. *Eur. J. Mech., A/Solids* **21**, 61–72. (doi:10.1016/S0997-7538(01)01184-6)
65. Molnár G, Doitrand A, Estevez R, Gravouil A. 2020 Toughness or strength? Regularization in phase field fracture explained by the coupled criterion. *Theor. Appl. Fract. Mech.* **109**, 102736. (doi:10.1016/j.tafmec.2020.102736)
66. Sargado JM, Keilegavlen E, Berre I, Nordbotten JM. 2018 High-accuracy phase field models for brittle fracture based on a new family of degradation functions. *J. Mech. Phys. Solids* **111**, 458–489. (doi:10.1016/j.jmps.2017.10.015)
67. Kumar A, Bourdin B, Francfort GA, Lopez-Pamies O. 2020 Revisiting nucleation in the phase field approach to brittle fracture. *J. Mech. Phys. Solids* **142**, 104027. (doi:10.1016/j.jmps.2020.104027)

Downloaded from https://royalsocietypublishing.org/ on 21 June 2021

[P3]

Golahmar, Alireza, Kristensen, Philip K., Niordson, Christian F., Martínez-Pañeda, Emilio. A phase field model for hydrogen-assisted fatigue. International Journal of Fatigue 2022. 154. 106521.

International Journal of Fatigue 154 (2022) 106521

Contents lists available at ScienceDirect

International Journal of Fatigue

journal homepage: www.elsevier.com/locate/ijfatigue

A phase field model for hydrogen-assisted fatigue

Alireza Golahmar [a], Philip K. Kristensen [a], Christian F. Niordson [a], Emilio Martínez-Pañeda [b,*]

[a] Department of Mechanical Engineering, Technical University of Denmark, DK-2800 Kgs. Lyngby, Denmark
[b] Department of Civil and Environmental Engineering, Imperial College London, London SW7 2AZ, UK

ARTICLE INFO

Keywords:
Phase field
Finite element method
Fatigue
Crack growth
Hydrogen embrittlement

ABSTRACT

We present a new theoretical and numerical phase field-based formulation for predicting hydrogen-assisted fatigue. The coupled deformation-diffusion-damage model presented enables predicting fatigue crack nucleation and growth for arbitrary loading patterns and specimen geometries. The role of hydrogen in increasing fatigue crack growth rates and decreasing the number of cycles to failure is investigated. Our numerical experiments enable mapping the three loading frequency regimes and naturally recover Paris law behaviour for various hydrogen concentrations. In addition, *Virtual* S–N curves are obtained for both notched and smooth samples, exhibiting a good agreement with experiments.

1. Introduction

There is a growing interest in understanding and optimising the fatigue behaviour of metals in the presence of hydrogen (see, e.g., [1–6] and Refs. therein). Two aspects have mainly motivated these endeavours. Firstly, hydrogen-assisted cracking is a well-known concern in the transport, construction, defence and energy sectors. Hydrogen is ubiquitous and significantly reduces the ductility, strength, toughness and fatigue crack growth resistance of metallic materials, with the problem being exacerbated by the higher susceptibility of modern, high-strength alloys [7]. Secondly, hydrogen is seen as the energy carrier of the future, fostering a notable interest in the design and prognosis of infrastructure for hydrogen transportation and storage [8,9]. In the majority of these applications, susceptible components are exposed to alternating mechanical loads and thus being able to predict the synergistic effects of hydrogen and fatigue damage is of utmost importance.

Significant progress has been achieved in the development of computational models for hydrogen-assisted fracture. Dislocation-based methods [10,11], weakest-link approaches [12,13], cohesive zone models [14–16], gradient damage theories [17] and phase field fracture formulations [18–21] have been presented to predict the nucleation and subsequent growth of hydrogen-assisted cracks. Multi-physics phase field fracture models have been particularly successful, demonstrating their ability to capture complex cracking conditions, such as nucleation from multiple sites or the coalescence of numerous defects, in arbitrary geometries and dimensions [22,23]. However, the surge in modelling efforts experienced in the context of monotonic, static fracture has not been observed in fatigue. Hydrogen can influence the cyclic constitutive behaviour [24,25], reduce the number of cycles required to initiate cracks [26,27] and, most notably, accelerate fatigue crack growth [28,29]. Predicting the significant reduction in fatigue life observed in the presence of hydrogen requires capturing how hydrogen elevates crack growth rates, which is dependent on the hydrogen content, the material susceptibility to embrittlement, the diffusivity of hydrogen and the loading amplitude and frequency, among other factors. Given the complexity and higher computational demands of fatigue damage, it is not surprising that the role of hydrogen in augmenting fatigue crack growth rates has been predominantly assessed from an experimental viewpoint, with a few exceptions [30,31]. Moreover, the success of phase field formulations in predicting hydrogen-assisted static fracture has not been extended to fatigue yet.

In this work, we present the first phase field model for hydrogen-assisted fatigue. The main elements of the coupled deformation-diffusion-fatigue formulation presented are: (i) a thermodynamically-consistent extension of Fick's law of mass diffusion, (ii) a fatigue history variable and associated degradation function, (iii) a phase field description of crack-solid interface evolution, (iv) a penalty-based formulation to update environmental boundary conditions, and (v) an atomistically-inspired relation between the hydrogen content and the fracture surface energy. This novel variational framework is numerically implemented in the context of the finite element method and used to model hydrogen-assisted fatigue in several boundary value problems of particular interest. Firstly, the paradigmatic benchmark of a cracked square plate is modelled to quantify the dependency of the number of cycles to failure on the hydrogen content. Secondly, a boundary layer approach is used to gain insight into the competing

* Corresponding author.
E-mail address: e.martinez-paneda@imperial.ac.uk (E. Martínez-Pañeda).

https://doi.org/10.1016/j.ijfatigue.2021.106521
Received 28 June 2021; Received in revised form 29 July 2021; Accepted 30 August 2021
Available online 6 September 2021
0142-1123/© 2021 Elsevier Ltd. All rights reserved.

role of loading frequency and hydrogen diffusivity. We show how the model captures the main experimental trends; namely, the sensitivity of fatigue crack growth rates to the loading frequency and the environment. The Paris law, and its sensitivity to hydrogen, are naturally recovered. Finally, *Virtual* S–N curves are computed for both smooth and notched samples, exhibiting a promising agreement with experimental data. The remainder of the paper is organised as follows. Section 2 presents the theoretical framework and provides details of the finite element implementation. In Section 3, the performance of the proposed modelling framework is benchmarked against several representative numerical examples as well as relevant experimental measurements. Finally, concluding remarks are given in Section 4.

2. A phase field theory for hydrogen-assisted fatigue

We present a theoretical and numerical framework for modelling hydrogen assisted fatigue. Our formulation is grounded on the phase field fracture method, which has gained notable traction in recent years. Applications include battery materials [32,33], composites [34,35], ceramics [36,37], shape memory alloys [38], functionally graded materials [39,40] and both ductile [41,42] and embrittled [43] metals. The success of phase field fracture methods is arguably twofold. First, phase field provides a robust computational framework to simulate complex cracking phenomena in arbitrary geometries and dimensions. Secondly, it provides a variational platform for Griffith's energy balance [44,45]. Thus, consider a cracked elastic solid with strain energy density $\psi(\boldsymbol{\varepsilon})$. Under prescribed displacements, the variation of the total potential energy of the solid $\mathcal{E}$ due to an incremental increase in crack area $\mathrm{d}A$ is given by

$$\frac{\mathrm{d}\mathcal{E}}{\mathrm{d}A} = \frac{\mathrm{d}\psi(\boldsymbol{\varepsilon})}{\mathrm{d}A} + \frac{\mathrm{d}W_c}{\mathrm{d}A} = 0, \tag{1}$$

where W_c is the work required to create new surfaces and $\boldsymbol{\varepsilon}$ is the strain tensor. The fracture resistance of the solid is given by the term $\mathrm{d}W_c/\mathrm{d}A$, also referred to as the material toughness or critical energy release rate G_c. A pre-existing crack will grow when the energy stored in the material is high enough to overcome G_c. Griffith's minimality principle can be formulated in a variational form as follows

$$\mathcal{E} = \int_\Omega \psi\,(\boldsymbol{\varepsilon})\,\mathrm{d}V + \int_\Gamma G_c\,\mathrm{d}\Gamma\,. \tag{2}$$

Arbitrary cracking phenomena can be predicted based on the thermodynamics of fracture, provided one can computationally track the crack surface Γ. The phase field paradigm is key to tackling the challenge of predicting the evolution of the crack surface topology. The crack-solid interface is described by means of an auxiliary variable, the phase field ϕ, which takes distinct values in each of the phases and varies smoothly in between. This implicit representation of an evolving interface has proven to be useful in modelling other complex interfacial phenomena, such as microstructural evolution [46] or corrosion [47]. In the context of fracture mechanics, the phase field ϕ resembles a damage variable, taking values of 0 in intact material points and of 1 inside the crack. Thus, upon a convenient constitutive choice for the crack surface density function γ, the Griffith functional (2) can be approximated by means of the following regularised functional:

$$\begin{aligned}\mathcal{E}_\ell &= \int_\Omega \left[g\,(\phi)\,\psi_0\,(\boldsymbol{\varepsilon}) + G_c\gamma\,(\phi,\ell)\right]\mathrm{d}V \\ &= \int_\Omega \left[(1-\phi)^2\,\psi_0\,(\boldsymbol{\varepsilon}) + G_c\left(\frac{\phi^2}{2\ell} + \frac{\ell}{2}|\nabla\phi|^2\right)\right]\mathrm{d}V\,.\end{aligned} \tag{3}$$

Here, ℓ is a length scale parameter that governs the size of the fracture process zone, ψ_0 denotes the strain energy density of the undamaged solid and $g(\phi)$ is a degradation function. It can be shown through Gamma-convergence that $\mathcal{E}_\ell$ converges to $\mathcal{E}$ when $\ell \to 0^+$ [48].

Now, let us extend this framework to incorporate fatigue damage and hydrogen embrittlement. Define a *degraded* fracture energy $\mathcal{G}_d$ that is a function of the hydrogen concentration C and a fatigue history variable $\bar{\alpha}$, such that

$$\mathcal{G}_d = f_C\,(C)\,f_{\bar{\alpha}}\,(\bar{\alpha})\,G_c \tag{4}$$

where f_C and $f_{\bar{\alpha}}$ are two suitably defined degradation functions to respectively incorporate hydrogen and fatigue damage, as described later. Replacing G_c by $\mathcal{G}_d$, taking the variation of the functional (3) with respect to $\delta\phi$, and applying Gauss' divergence theorem renders the following phase field equilibrium equation,

$$\mathcal{G}_d\left(\frac{\phi}{\ell} - \ell\nabla^2\phi\right) - 2\,(1-\phi)\,\psi_0 = 0 \tag{5}$$

Considering the homogeneous solution to (5) provides further insight into the role of the phase field length scale ℓ. Thus, in a 1D setting, consider a sample with Young's modulus E, subjected to a uniaxial stress $\sigma = g\,(\phi)\,E\varepsilon$; the homogeneous solution for the stress reaches a maximum at the following critical strength:

$$\sigma_c = \left(\frac{27E\mathcal{G}_d}{256\ell}\right)^{1/2}. \tag{6}$$

Hence, ℓ can be seen not only as a regularising parameter but also as a material property that defines the material strength. This enables phase field models to predict crack nucleation and naturally recover the transition flaw size effect [49,50].

2.1. Hydrogen degradation function

We proceed to provide constitutive definitions for the degradation functions. The dramatic drop in fracture resistance observed in metals exposed to hydrogen is captured by taking inspiration from atomistic insight. As discussed elsewhere [14,18], DFT calculations of surface energy degradation with hydrogen coverage θ exhibit a linear trend, with the slope being sensitive to the material system under consideration. Thus, a quantum mechanically informed degradation law can be defined as follows,

$$f_C = 1 - \chi\theta \qquad \text{with} \qquad \theta = \frac{C}{C + \exp\left(-\Delta g_b^0/(\mathcal{R}T)\right)} \tag{7}$$

where χ is the hydrogen damage coefficient, which is taken in this study to be $\chi = 0.89$, as this provides the best fit to the DFT calculations by Jiang and Carter in iron [18,51]. Also, the second part of (7) makes use of the Langmuir–McLean isotherm to estimate, as dictated by thermodynamic equilibrium, the hydrogen coverage θ at decohering interfaces as a function of the bulk concentration C, the universal gas constant $\mathcal{R}$, the temperature T, and the associated binding energy Δg_b^0. Here, we follow Serebrinsky et al. [14] and assume $\Delta g_b^0 = 30$ kJ/mol, as is commonly done for grain boundaries. These specific choices are based on the assumption of a hydrogen assisted fracture process governed by interface decohesion. However, we emphasise that the phase field framework for hydrogen assisted fatigue presented is general and can accommodate any mechanistic or phenomenological interpretation upon suitable choices of f_C.

2.2. Fatigue degradation function

Fatigue damage is captured by means of a degradation function $f_{\bar{\alpha}}(\bar{\alpha})$, a cumulative history variable $\bar{\alpha}$ and a fatigue threshold parameter α_T. Following the work by Carrara et al. [52], two forms of $f_{\bar{\alpha}}(\bar{\alpha})$ are considered:

$$f_{\bar{\alpha}}(\bar{\alpha}) = \begin{cases} 1 & \text{if} \quad \bar{\alpha} \le \alpha_T \\ \left(\dfrac{2\alpha_T}{\bar{\alpha} + \alpha_T}\right)^2 & \text{if} \quad \bar{\alpha} > \alpha_T \end{cases} \qquad \text{(Asymptotic)} \tag{8}$$

$$f_{\bar{\alpha}}(\bar{\alpha}) = \begin{cases} 1 & \text{if} \quad \bar{\alpha} \le \alpha_T \\ \left[1 - \kappa \log\left(\dfrac{\bar{\alpha}}{\alpha_T}\right)\right]^2 & \text{if} \quad \alpha_T \le \bar{\alpha} \le \alpha_T 10^{1/\kappa} \quad \text{(Logarithmic)} \\ 0 & \text{if} \quad \bar{\alpha} \ge \alpha_T 10^{1/\kappa} \end{cases} \tag{9}$$

where κ is a material parameter that governs the slope of the logarithmic function. For simplicity, the asymptotic function will be generally used in our numerical experiments unless otherwise stated. The fatigue history variable $\bar{\alpha}$ evolves in time t as follows,

$$\bar{\alpha}(t) = \int_0^t \mathrm{H}(\alpha\dot{\alpha})|\dot{\alpha}|\,\mathrm{d}t\,, \tag{10}$$

where $\mathrm{H}(\alpha\dot{\alpha})$ is the Heaviside function, such that $\bar{\alpha}$ only grows during loading. Finally, consistent with our energy balance, the cumulative fatigue variable is defined as $\bar{\alpha} = g(\phi)\psi_0$.

2.3. Coupled deformation-diffusion-fracture problem

The hydrogen and fatigue damage framework presented is coupled to the solution of the displacement field, as given by the balance of linear momentum:

$$\nabla \cdot \boldsymbol{\sigma} + \mathbf{b} = \mathbf{0}\,, \tag{11}$$

and mass transport,

$$\dot{C} + \nabla \cdot \mathbf{J} = 0\,. \tag{12}$$

Here, $\boldsymbol{\sigma}$ is the Cauchy stress tensor, $\mathbf{b}$ is the body force vector, and $\mathbf{J}$ is the hydrogen flux. In relation to the mechanical problem, linear elastic material behaviour is assumed, with the strain energy density given as $\psi_0 = \frac{1}{2}\boldsymbol{\varepsilon} : \boldsymbol{C} : \boldsymbol{\varepsilon}$, where $\boldsymbol{C}$ is the fourth order elasticity tensor. The hydrogen transport problem is characterised by the following definition of the chemical potential,

$$\mu = \mu_0 + \mathcal{R}T \ln\frac{\theta}{1-\theta} - \bar{V}_H \sigma_H \tag{13}$$

where μ_0 denotes the chemical potential in the standard state and $\bar{V}_H$ is the partial molar volume of hydrogen in solid solution. Our numerical examples are focused on iron-based materials and consequently $\bar{V}_H = 2000$ mm^3/mol. It must be emphasised that the hydrostatic stress σ_H lowers the chemical potential, increasing the hydrogen solubility as a result of lattice dilatation and thus attracting hydrogen to areas of high volumetric strains, such as crack tips. Finally, the hydrogen flux is related to $\nabla\mu$ through the following linear Onsager relation,

$$\mathbf{J} = -\frac{DC}{\mathcal{R}T}\nabla\mu\,, \tag{14}$$

where D is the hydrogen diffusion coefficient. The role of microstructural trapping sites in slowing diffusion can be accounted for by considering D to be the effective diffusion coefficient (as opposed to the lattice one). Also, as shown in Ref. [43] in the context of static fracture, the framework can readily be extended to capture the influence of dislocation traps, which evolve with mechanical load.

2.4. Numerical implementation

The weak forms of Eqs. (5), (11) and (12) are discretised and solved using the finite element method. In addition, the following features enrich our numerical implementation. Firstly, damage irreversibility is enforced by means of a history field that satisfies the Kuhn–Tucker conditions [53]. Secondly, damage under compressive fields is prevented by adopting a tension-compression split of the strain energy density, together with a hybrid implementation [54]. Two approaches are considered, the volumetric-deviatoric split by Amor et al. [55] and the spectral decomposition by Miehe et al. [53]; the former is generally used unless otherwise stated. Thirdly, the system of equations is solved with a staggered approach that converges to the monolithic result upon controlling the residual norm [56]. Finally, a penalty approach is adopted to implement *moving* chemical boundary conditions, by which the diffusion-environment interface evolves as dictated by the phase field crack [21,23,57].

3. Results

The predictive capabilities of the model are demonstrated through the following numerical experiments. Firstly, in Section 3.1, we validate our numerical implementation in the absence of hydrogen and extend it to demonstrate how the model can capture the role of hydrogen in accelerating crack growth rates. Secondly, in Section 3.2, we use a boundary layer formulation to gain insight into hydrogen-assisted fatigue crack growth under small scale yielding conditions. Stationary and propagating cracks are modelled to shed light on the sensitivity of the crack tip hydrogen concentration to the fatigue frequency and compute Paris law coefficients for various hydrogen contents. Also, crack growth rates versus loading frequency regimes are mapped. Thirdly, we examine the fracture and fatigue behaviour of notched components in Section 3.3, computing *Virtual* S–N curves for various hydrogenous environments. Finally, in Section 3.4 we compare model predictions with fatigue experiments on smooth samples, observing a very good agreement. Two materials are considered, with samples being exposed either to air or to high pressure hydrogen gas.

3.1. Cracked square plate subjected to fatigue in a hydrogenous environment

The case of a square plate with an initial crack subjected to uniaxial tension has become a paradigmatic benchmark in the phase field fracture community. Loading conditions and sample dimensions (in mm) are illustrated in Fig. 1a. As in Refs. [52,58], material properties read $E = 210$ GPa, $\nu = 0.3$, $G_c = 2.7$ kJ/m^2, $\ell = 0.004$ mm and $\alpha_T = 56.25$ MPa. The sample is discretised using 27,410 eight-node plane strain quadrilateral elements with reduced integration. The mesh is refined in the crack propagation region to ensure that the characteristic element length h is sufficiently small to resolve the fracture process zone ($h < \ell/5.4$ [18]). The plate is subjected to a piece-wise linear cyclic remote displacement with a load frequency of $f = 400$ Hz, a zero mean value (i.e. a load ratio of $R = -1$) and a constant range of $\Delta u = 4 \times 10^{-3}$ mm.

We proceed first to validate the model in the absence of hydrogen. The results obtained are shown in Fig. 2 in terms of crack extension Δa (in mm) versus the number of cycles N. The computations have been conducted for three choices of the strain energy density decomposition: no split, volumetric/deviatoric [55] and spectral [53]. A very good agreement is observed with the predictions of Carrara et al. [52] and Kristensen and Martínez-Pañeda [58]. The agreement is particularly good with the latter work, which uses a quasi-Newton monolithic implementation, while the work by Carrara et al. [52] employs an energy-based criterion to ensure that the staggered solution scheme iterates until reaching the monolithic solution [54]. As discussed in the literature, higher fatigue crack growth rates are predicted if no tension-compression split is considered as both tension and compression loading cycles contribute to damage.

Subsequently, the cracked square plate is exposed to a hydrogenous environment at room temperature. We assume that the plate is made of an iron-based material with diffusion coefficient $D = 0.0127$ mm^2/s. Furthermore, it is assumed that the sample has been pre-charged and is exposed to a hydrogenous environment throughout the experiment. Accordingly, a uniform hydrogen distribution is assigned as an initial condition $C(t=0) = C_0 = C_{\text{env}}\ \forall\, x$ and a constant hydrogen concentration $C(t) = C_{\text{env}}$ is prescribed at all the outer boundaries of the plate,

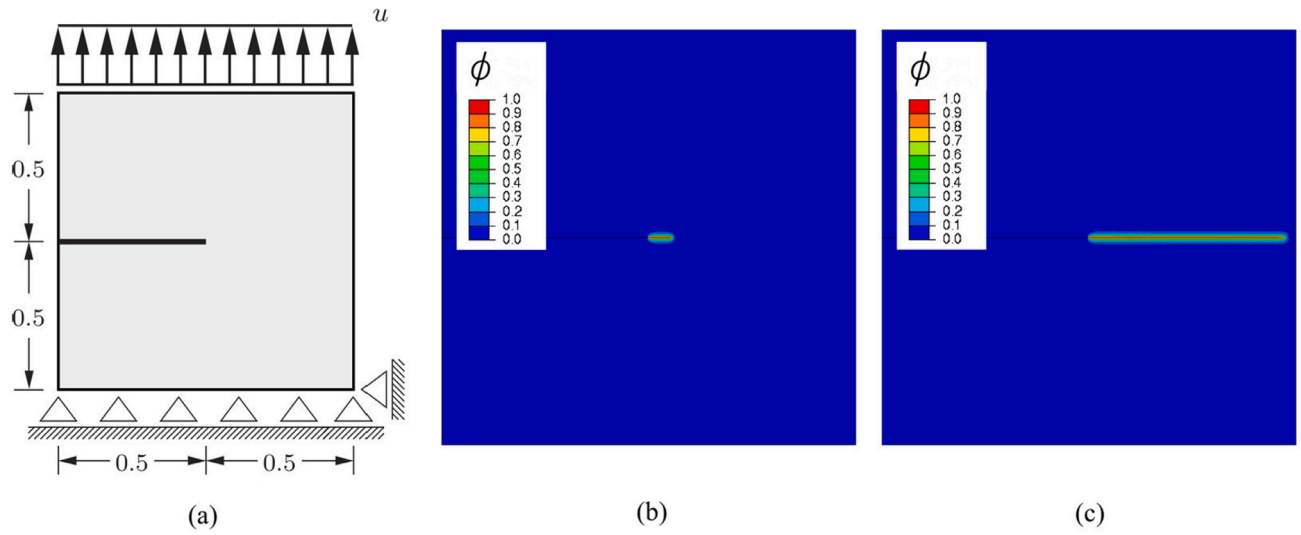

Fig. 1. Cracked square plate: (a) Loading configuration (with dimensions in mm) and phase field contours after (b) 80 and (c) 280 loading cycles.

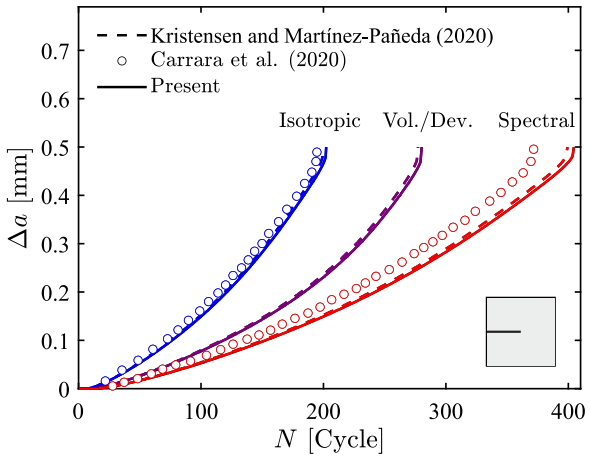

Fig. 2. Cracked square plate, validation in an inert environment: crack extension versus number of cycles and comparison with the results of Kristensen and Martínez-Pañeda [58] and Carrara et al. [52].

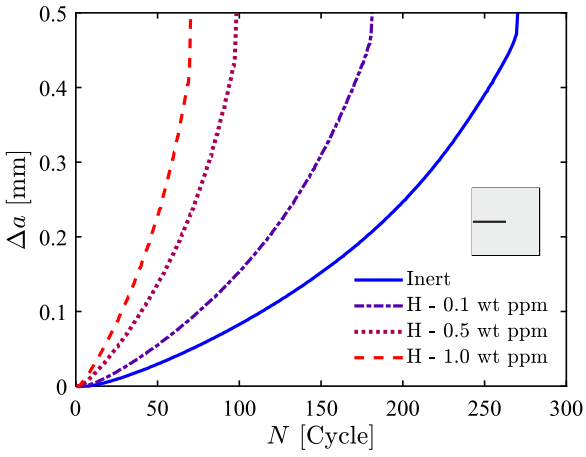

Fig. 3. Cracked square plate, influence of hydrogen: crack extension versus number of cycles for various hydrogen concentration levels.

including the crack faces.[1] The results obtained are shown in Fig. 3 for three selected values of the environmental hydrogen concentration: 0.1, 0.5 and 1 wt ppm. The results reveal that the model correctly captures the trend expected: fatigue crack growth rates increase with increasing hydrogen content (see, e.g., [9,64]).

3.2. Boundary layer model

Next, we gain insight into hydrogen-assisted fatigue under small scale yielding conditions. A boundary layer model is used to prescribe a remote K_{I} field in a circular region of a body containing a sharp crack. As shown in Fig. 4, only the upper half of the domain is considered due to its symmetry. The remote, elastic K_{I} field is applied by prescribing the displacements of the nodes in the outer region following the Williams [65] expansion. Thus, for a polar coordinate system (r,θ) centred at the crack tip, the horizontal and vertical displacements respectively read

$$\begin{aligned} u_x(r,\theta) &= K_{\mathrm{I}}\frac{1+\nu}{E}\sqrt{\frac{r}{2\pi}}\cos\left(\frac{\theta}{2}\right)\left[3-4\nu-\cos(\theta)\right] \\ u_y(r,\theta) &= K_{\mathrm{I}}\frac{1+\nu}{E}\sqrt{\frac{r}{2\pi}}\sin\left(\frac{\theta}{2}\right)\left[3-4\nu-\cos(\theta)\right] \end{aligned} \tag{15}$$

Cyclic loading conditions are attained by defining the applied stress intensity factor as the following sinusoidal function,

$$K_{\mathrm{I}} = K_{\mathrm{m}} + \frac{\Delta K}{2}\sin(2\pi f\, t)\,, \qquad \text{with} \qquad K_{\mathrm{m}} = \frac{\Delta K}{2} + \frac{R\,\Delta K}{1-R} \tag{16}$$

where f denotes the load frequency, t the test time, K_{m} the load mean value, $\Delta K = K_{\max} - K_{\min}$ the load range, and $R = K_{\min}/K_{\max}$ the load ratio. To capture the loading history with fidelity, each cycle is divided into at least 20 computational time increments. The circular domain is discretised using 4,572 quadratic plane strain quadrilateral elements with reduced integration and, as shown in Fig. 4b, the mesh is refined along the crack propagation region.

Consider first the case of a stationary crack in a solid with Young's modulus $E = 210$ GPa, Poisson's ratio $\nu = 0.3$ and diffusion coefficient $D = 0.0127\ \mathrm{mm}^2/\mathrm{s}$. The sample is assumed to be pre-charged with a uniform concentration of $C(t=0) = C_0 = 0.5$ wt ppm. The load range is chosen to be $\Delta K = 1\ \mathrm{MPa}\sqrt{\mathrm{m}}$, the load frequency equals $f = 1$ Hz,

[1] We note that, while a constant hydrogen concentration has been prescribed at the crack faces for simplicity, the use of generalised Neumann-type boundary conditions [59,60] or σ_H-dependent Dirichlet boundary conditions [61–63] is more appropriate.

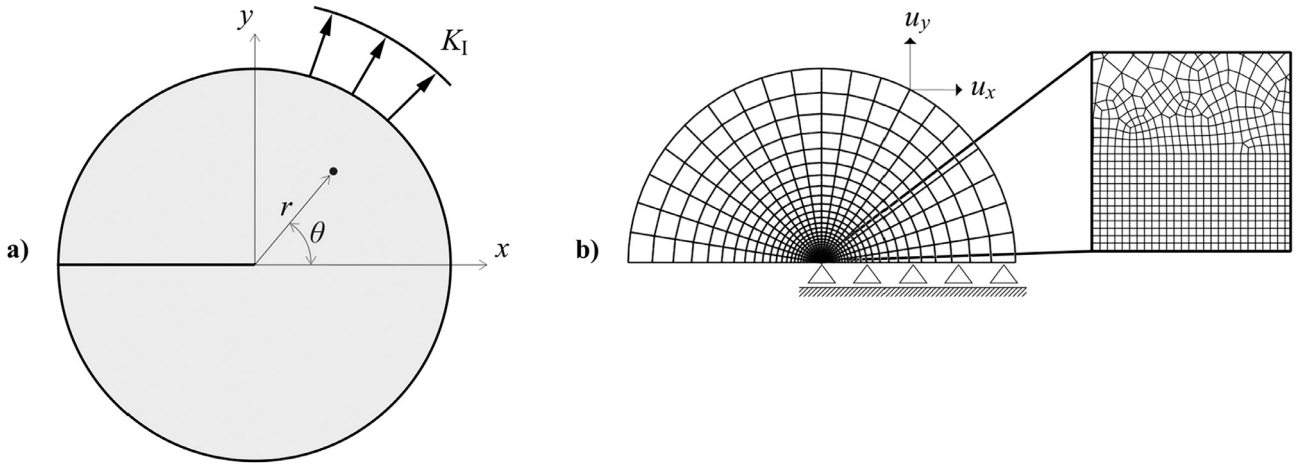

Fig. 4. Boundary layer model: (a) Geometry and boundary conditions, and (b) finite element mesh, including details of the mesh refinement ahead of the crack tip.

and the load ratio is $R = 0$. The evolution of the crack tip hydrogen distribution as a function of time t can be quantified by the following dimensionless groups, as dictated by the Buckingham Π theorem,

$$\frac{C}{C_0} = \mathcal{F}\left(\frac{f L_0^2}{D}, \quad \frac{tD}{L_0^2}, \quad \frac{E\bar{V}_H}{\mathcal{R}T}\right) \tag{17}$$

where $L_0 = (K_m/E)^2$ is a length parameter that results from the dimensional analysis and provides a measure of the gradients close to the crack tip. The first two dimensionless groups quantify the competing influence of test and diffusion times, which are denoted as the normalised frequency $\bar{f} = f L_0^2/D$ and the normalised time $\bar{t} = tD/L_0^2$, respectively.

Hydrogen diffusion is (partially) driven by gradients of hydrostatic stress, see Eq. (13), such that hydrogen atoms will accumulate in areas with high volumetric strains. Under steady state conditions, the hydrogen concentration is given as,

$$C = C_0 \exp\left(\frac{\bar{V}_H \sigma_H}{\mathcal{R}T}\right). \tag{18}$$

Accordingly, the hydrogen distribution ahead of the crack will vary during the loading cycle. Fig. 5 shows the results obtained at the maximum K_{max}, mean K_m and minimum $K_{min} = 0$ stages of the first load cycle, for a sufficiently low frequency such that conditions resemble those of steady state. In agreement with expectations, the hydrogen concentration increases with the applied load, reaching its maximum value in the vicinity of the crack tip (where σ_H is highest), and remains constant for a zero value of the hydrostatic stress at $K_{min} = 0$ ($R = 0$).

Let us now consider the more common case of transient conditions and investigate the competing role of the loading frequency and diffusion time. Fig. 6 illustrates the variation in time of the hydrogen concentration near the crack tip, at a point located at $r/L_0 \approx 0.2 \times 10^7$, as denoted by a star in Fig. 5. The results reveal that, irrespectively of the test duration, the maximum hydrogen content that can be attained ahead of the crack tip is sensitive to the loading frequency. If the diffusivity of hydrogen is sufficiently large relative to the time required to complete one cycle (low f), the amplitude of the hydrogen concentration follows that of the hydrostatic stress, as in the steady state case — see Eq. (18). Contrarily, for high loading frequencies, unloading begins before the hydrogen distribution reaches the steady state solution (18) and consequently the maximum value of C reached during the experiment is smaller than that of lower frequencies. It can be seen that, for the highest frequency ($f = 10^3$ Hz) the hydrogen concentration does not oscillate and flattens out towards a constant value that is roughly 5% lower than the maximum concentration attained at low loading frequencies (for the material properties and distance ahead of the crack

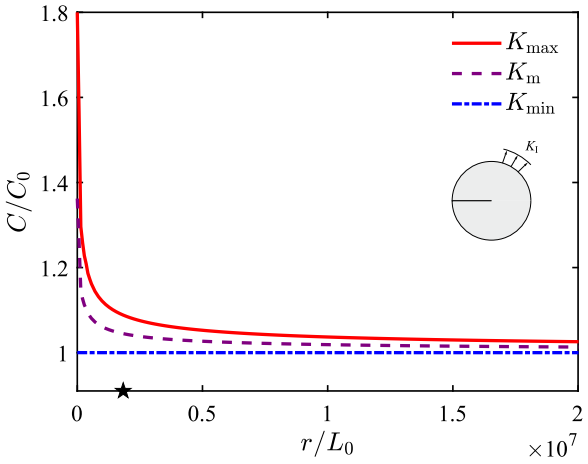

Fig. 5. Boundary layer model: Hydrogen concentration ahead of a stationary crack tip for three stages of the first load cycle. The results have been obtained under steady state conditions and with load ratio $R = 0$.

here considered). Recall that the relevant non-dimensional group $\bar{f} = f L_0^2/D$ involves the material diffusion coefficient. It follows that the present results could support the use of *beneficial* traps, which lower the material diffusivity but are not involved in the fracture process, as a viable strategy for designing materials resistant to hydrogen-assisted fatigue.

We proceed to investigate the influence of the diffusion time–frequency interplay on fatigue crack growth rates. The phase field fatigue model outlined in Section 2 is used, with material properties $G_c = 2.7\,\text{kJ/m}^2$ and $\ell = 0.0048$ mm. A reference stress intensity factor, in the absence of hydrogen, is defined as,

$$K_0 = \sqrt{\frac{G_c E}{(1-\nu^2)}} \tag{19}$$

and a fracture process zone length L_f, can be defined as [49,50]:

$$L_f = \frac{G_c\,(1-\nu^2)}{E} \tag{20}$$

Fig. 7 shows the results obtained in terms of (normalised) crack extension versus number of cycles, as a function of the environmental hydrogen concentration C_{env}. These computations have been conducted for a pre-charged solid ($C(t=0) = C_{env}$) that is exposed to a hydrogenous environment during the test ($C(t) = C_{env}$ at the boundaries). The load range equals $\Delta K/K_0 = 0.08$, while the load frequency and ratio

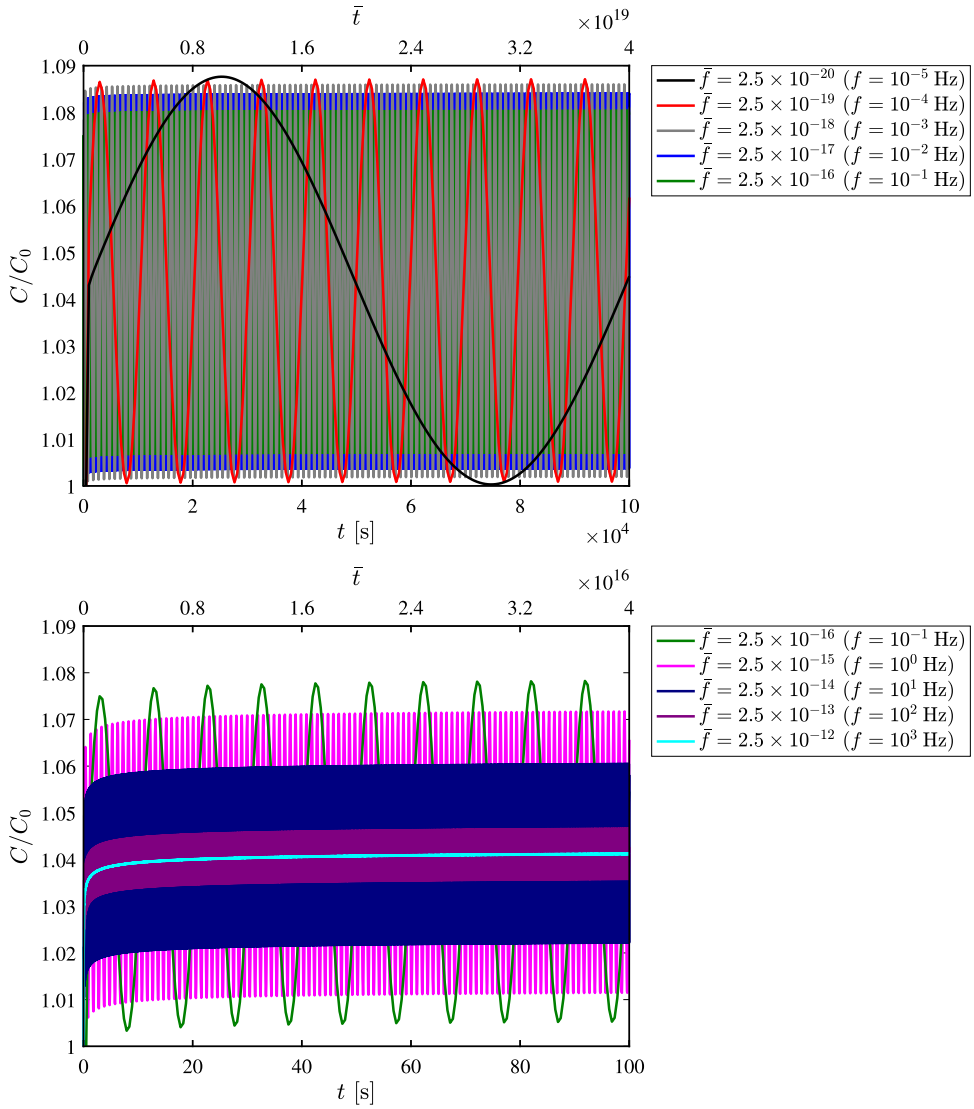

Fig. 6. Boundary layer model: Variation in time of the hydrogen concentration at a point ahead of a stationary crack tip for various loading frequencies and load ratio $R = 0$.

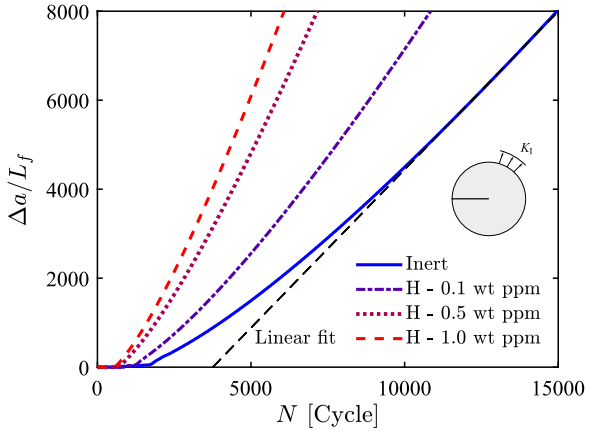

Fig. 7. Boundary layer model: Crack extension versus the number of cycles for different hydrogen concentrations. Results have been obtained for $\Delta K/K_0 = 0.08$, under a load ratio of $R = 0.1$ and load frequency $f = 1$ Hz.

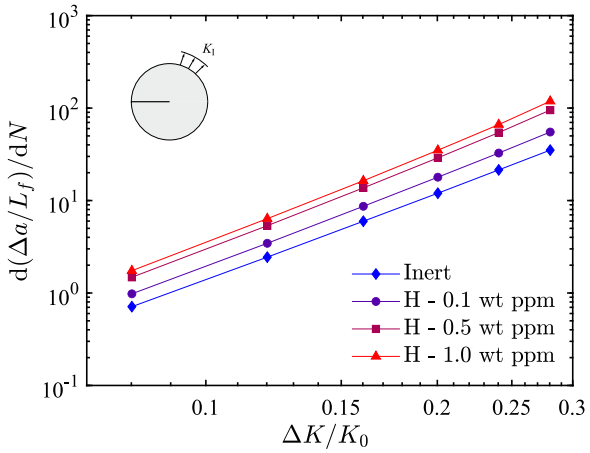

Fig. 8. Boundary layer model, Paris law behaviour: Fatigue crack growth rate versus load range for different hydrogen concentrations. Results have been obtained for a load ratio of $R = 0.1$ and load frequency $f = 1$ Hz.

equal $f = 1$ Hz and $R = 0.1$, respectively. The results shown in Fig. 7 reveal that the model is able to capture the expected trends — for a

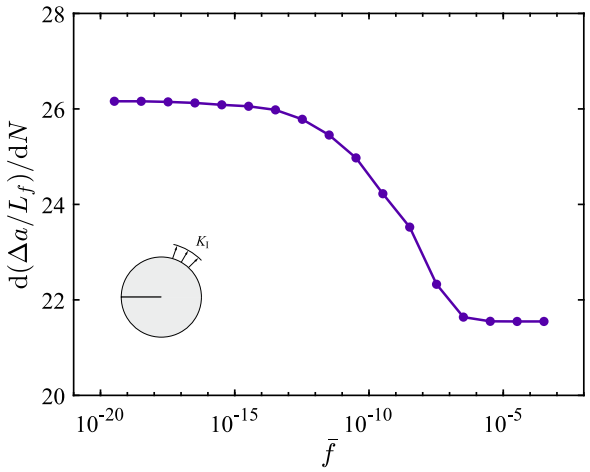

Fig. 9. Boundary layer model, mapping frequency regimes: fatigue crack growth rate versus normalised frequency $\bar{f} = fL_0^2/D$. Results have been obtained for $\Delta K/K_0 = 0.24$, under a load ratio of $R = 0$ and a hydrogen concentration of $C_0 = C_{env} = 0.1$ wt ppm.

given number of cycles, the higher the hydrogen concentration, the larger the crack extension. As depicted in Fig. 7, a linear fit can be applied to the linear part of the curve to derive the slope (crack growth rates).

The fatigue crack growth rates obtained for different ΔK and hydrogen concentrations are shown in Fig. 8, using a log–log plot. The computed curves behave linearly in the so-called Paris regime, where cracks propagate stably, as expected. By applying the well-known Paris equation $da/dN = C\Delta K^m$, one can readily observe that C increases with the hydrogen content, in agreement with the experimental trends. On the other hand, results yield a Paris exponent that appears to be less sensitive to the environment, with a magnitude ($m \approx 3.2$) that is within the range reported for metals in inert environments [66]. The present framework is capable of providing as an output (not input) the Paris law behaviour, enabling the prediction of the role of hydrogen in accelerating sub-critical crack growth rates.

Finally, Fig. 9 illustrates the sensitivity of fatigue crack growth rates to the loading frequency. Here, we consider a pre-charged sample with $C_0 = 0.1$ wt ppm exposed to a load amplitude of $\Delta K/K_0 = 0.24$ and a load ratio of $R = 0$. It is shown that the model captures another widely observed experimental trend; the fatigue behaviour of metals in the presence of hydrogen varies between two limiting cases: (i) fast tests (high f), where hydrogen does not have enough time to diffuse to the fracture process zone and the susceptibility to embrittlement diminishes, and (ii) slow tests (low f), where hydrogen atoms have sufficient time to accumulate in areas of high σ_H, magnifying embrittlement. The model readily captures the transition between these two limiting regimes.

3.3. Notched cylindrical bar

Fatigue crack growth in samples containing non-sharp defects is subsequently investigated. Consider a cylindrical bar with a notch on its surface, as sketched in Fig. 10a. Axisymmetric conditions are exploited to model one planar section of the sample only. The finite element model contains 17,003 quadratic axisymmetric quadrilateral elements with reduced integration, with the mesh being refined ahead of the notch tip, where the characteristic element size is 6 times smaller than the phase field length scale ℓ (see Fig. 10b). The assumed material properties read $E = 210$ GPa, $\nu = 0.3$, $G_c = 64$ kJ/m^2, $\ell = 0.015$ mm, $D = 0.0127$ mm^2/s, and $\alpha_T = 355.56$ MPa. The bar is pre-charged and subsequently loaded in the same environment such that all the outer boundaries of the bar, including the notch faces, are in contact with the environment during the entire numerical experiment. Three environments are considered, corresponding to hydrogen concentrations of 0.1, 0.5 and 1 wt ppm. Cyclic loading is prescribed by subjecting the bar to a piece-wise linear remote displacement with a load frequency of $f = 1$ Hz and a load ratio of $R = 0$.

The results obtained are shown in Fig. 11, in terms of the remote stress amplitude versus the number of cycles to failure, also known as S–N curves. The stress amplitude is normalised by the material strength, as given by (6). For a given stress amplitude, shorter fatigue lives are observed as the hydrogen content is increased. In all cases, the number of cycles to failure increases with decreasing stress amplitude, and the slope of the S–N curve appears to be rather insensitive to the hydrogen content.

Accurate fatigue crack growth predictions in harmful environments require suitable boundary conditions. As mentioned in Section 2, we adopt a penalty approach to implicitly enforce *moving* chemical boundary conditions, so as to capture how the newly created crack surfaces

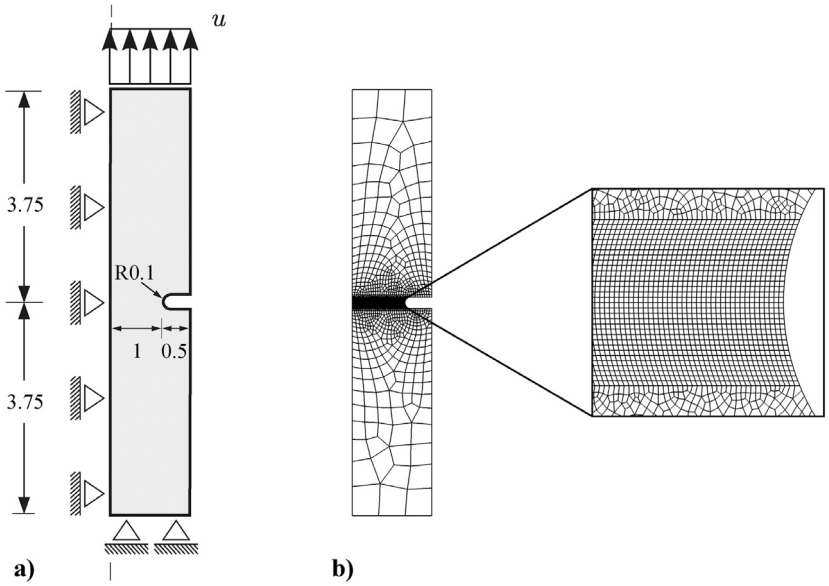

Fig. 10. Notched cylindrical bar: (a) geometry (with dimensions in mm) and boundary conditions, and (b) finite element mesh, including a detailed view of the mesh ahead of the notch tip.

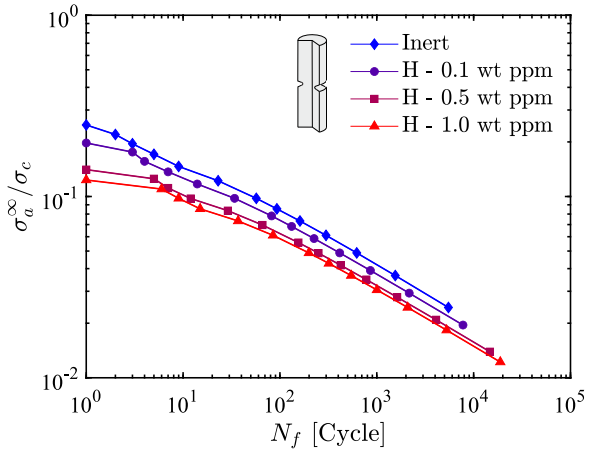

Fig. 11. Notched cylindrical bar, *Virtual* S–N curves: alternating remote stress versus number of cycles to failure for different hydrogen concentrations. The stress concentration factor equals $K_t = 3.354$.

are promptly exposed to the environment. This is illustrated in Fig. 12 by means of phase field and hydrogen concentration contours; as the crack grows, the concentration in the damaged regions equals C_{env}. Note that the contours correspond to $\sigma^\infty = \sigma_{\min} = 0$, and as a result there is no effect of σ_H on the hydrogen concentration.

3.4. Comparison with experimental S-N curves

We conclude the results section by comparing model predictions with S–N curves obtained from uniaxial tension-compression fatigue experiments on smooth samples. The tests were carried out by Matsunaga et al. [67] on two types of steels, a Cr-Mo steel (JIS-SCM435) with tensile strength of 840 MPa and a carbon steel (JIS-SM490B) with tensile strength of 530 MPa. The experiments were carried out in laboratory air and in 115 MPa hydrogen gas under constant stress amplitudes at a stress ratio of $R = -1$ and a test frequency of $f = 1$ Hz. As it is common with steels, both materials are assumed to have a Young's modulus of $E = 210$ GPa and a Poisson's ratio of $\nu = 0.3$. The toughness is assumed to be equal to $G_c = 60$ kJ/m^2 and $G_c = 27$ kJ/m^2 for JIS-SCM435 and JIS-SM490B, respectively, based on fracture toughness measurements reported in Refs. [68,69]. The boundary value problem can be solved in a semi-analytical fashion, by considering the homogeneous solution to (5). A piece-wise cyclic linear variation of the remote stress is assumed. Under 1D conditions, the length scale and the strength are related via (6), and this relation renders magnitudes of $\ell = 1.88$ mm and $\ell = 2.13$ mm for JIS-SCM435 and JIS-SM490B, respectively. The logarithmic fatigue degradation function (9) is used, together with the spectral tension-compression split [53]. The fatigue parameters α_T and κ are chosen so as to provide the best fit to the experiments in air; the magnitudes of $\alpha_T = 24$ MPa and $\kappa = 0.15$ provided the best fit to both JIS-SCM435 and JIS-SM490B data. Then, the fatigue response of samples exposed to hydrogen can be estimated by relating the H_2 pressure with the hydrogen concentration. The latter can be given as a function of the solubility S and the fugacity f_{H_2} by means of Sievert's law:

$$C = S\sqrt{f_{H_2}} \qquad \text{with} \qquad S = S_0 \exp\left(\frac{-E_s}{RT}\right), \tag{21}$$

where E_s is an activation energy. For JIS-SCM435 and JIS-SM490B, the magnitudes of S_0 and E_s are taken from Ref. [70] by considering the data reported for similar steels (AISI 4130 and AISI 1020, respectively); namely: $E_s = 27.2$ kJ/mol, $S_0 = 102$ mol/m$^3\sqrt{\text{MPa}}$ (JIS-SCM435) and $E_s = 23.54$ kJ/mol, $S_0 = 159$ mol/m$^3\sqrt{\text{MPa}}$ (JIS-SM490B). Assuming that the Abel–Noble equation is appropriate, the fugacity can be related to the hydrogen pressure p as follows,

$$f_{H_2} = p \exp\left(\frac{pb}{RT}\right) \tag{22}$$

where the Abel-Noble parameter is taken to be $b = 15.84$ cm^3/mol, rendering $f_{H_2} = 242.9$ MPa, and hydrogen concentrations of 0.00577 wt ppm (JIS-SCM435) and 0.04042 wt ppm (JIS-SM490B). The solubility dependence on the hydrostatic stress should also be accounted for; thus, we scale the hydrogen concentration according to (18) to determine the final magnitude of hydrogen uptake.

The experimental and numerical results obtained are shown in Fig. 13. Despite the scatter typically associated with these experiments, the *Virtual* S–N curves predicted are in good agreement with the measured data. In both experiments and simulations, a higher susceptibility to hydrogen-assisted fatigue is observed in the case of JIS-SM490B, a steel with a higher solubility, where hydrogen reduces the number of

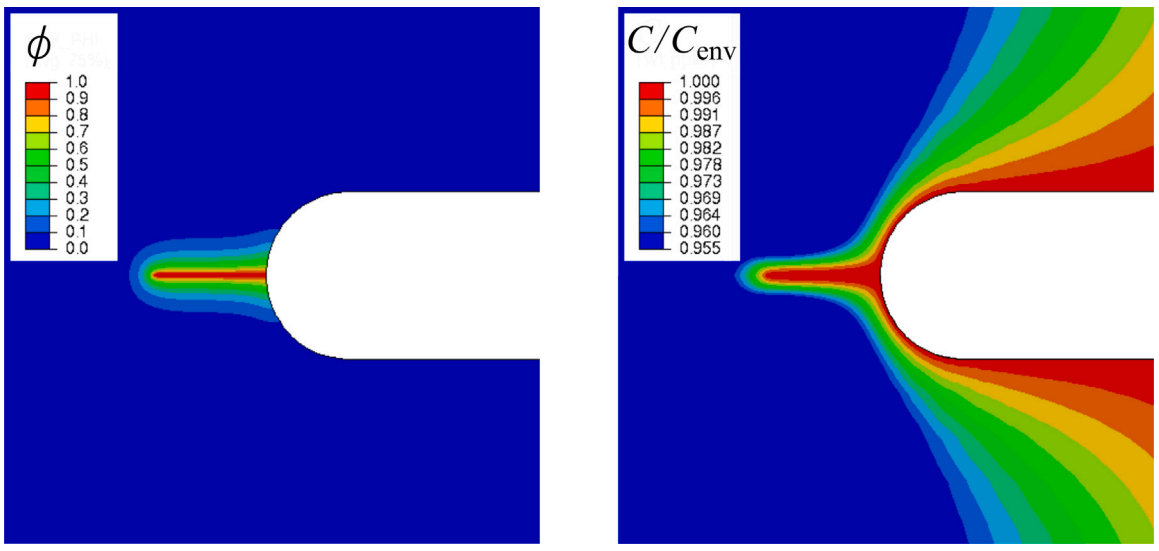

Fig. 12. Notched cylindrical bar, influence of the *moving* chemical boundary conditions: contours of the phase field ϕ (a) and hydrogen concentration (b). Results have been obtained for $C_{\text{env}} = 1$ wt ppm after 700 cycles and are plotted at $u = u_{\min} = 0$.

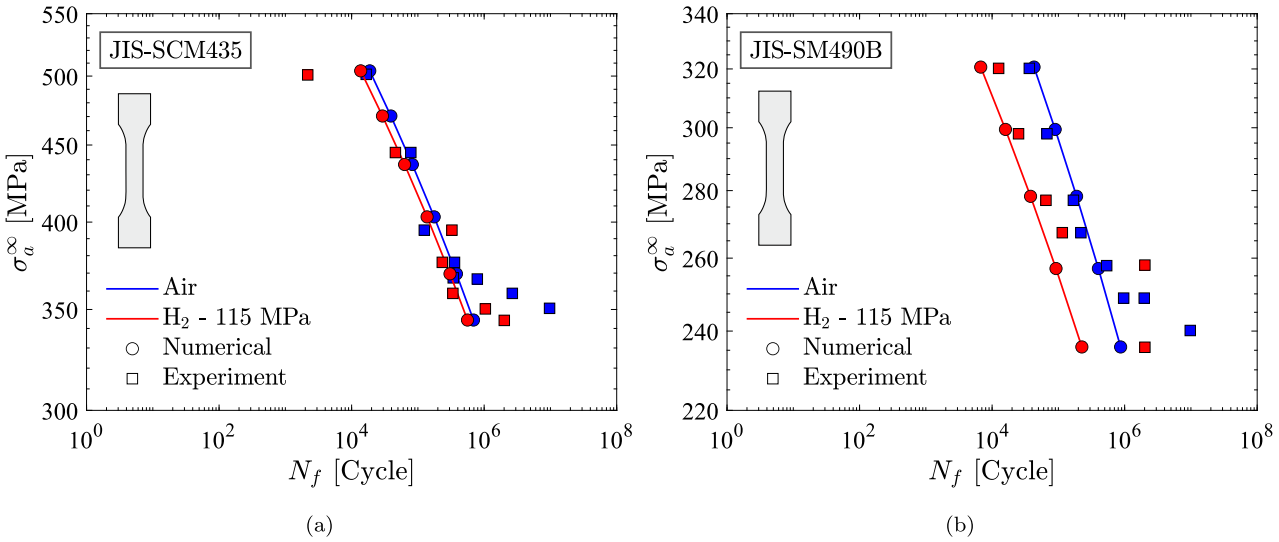

Fig. 13. S–N curves from smooth samples: numerical (present) and experimental [67] in air and at hydrogen pressure of 115 MPa. Two materials are considered: (a) JIS-SCM435, a Cr-Mo steel, and (b) JIS-SM490B, a carbon steel.

cycles to failure by almost an order of magnitude. It is also worth noting that the agreement with experiments becomes less satisfactory at low stress amplitudes, particularly in the absence of hydrogen. This is likely to be improved if a fatigue endurance limit is incorporated into the modelling. Future work will be targeted towards this extension and the investigation of the role of hydrogen in the fatigue endurance of metals.

4. Conclusions

We have presented a multi-physics phase field-based model for hydrogen-assisted fatigue. Cracking is predicted with an energy based criterion grounded on the thermodynamics of crack growth, and the role of hydrogen is incorporated through a first-principles degradation of the fracture energy. Deformation, diffusion and fatigue crack growth are coupled, with the model capturing the solubility dependence on the hydrostatic stress and the evolving environment-diffusion interface. Several findings shall be emphasised:

- The crack tip hydrogen distribution is very sensitive to the loading frequency f and the material diffusivity D. Sufficiently high f values lead to a hydrogen concentration that does not exhibit cyclic oscillations and increases in time up to a saturation value (even for a load ratio of $R = 0$).
- The model adequately captures the sensitivity of fatigue crack growth rates to hydrogen content.
- The model naturally recovers the Paris law behaviour and thus can quantify the influence of hydrogen on the Paris law parameters.
- The sensitivity of crack growth rates to loading frequency is mapped, revealing two limit states, as observed experimentally, and predicting a smooth transition in-between.
- *Virtual* S–N curves are obtained for various environments and both notched and smooth samples. Parameter-free predictions of the impact of hydrogen on the S–N curves reveal a promising agreement with experiments.

The theoretical and numerical framework presented provides a platform for addressing the long-standing challenge of predicting hydrogen-assisted fatigue failures.

Declaration of competing interest

The authors declare that they have no known competing financial interests or personal relationships that could have appeared to influence the work reported in this paper.

Acknowledgements

A. Golahmar acknowledges financial support from Vattenfall Vindkraft A/S and Innovation Fund Denmark (grant 0153-00018B). E. Martínez-Pañeda acknowledges financial support from the EPSRC, United Kingdom (grant EP/V009680/1) and from the Royal Commission for the 1851 Exhibition, United Kingdom (RF496/2018).

References

[1] Martin ML, Sofronis P, Robertson IM, Awane T, Murakami Y. A microstructural based understanding of hydrogen-enhanced fatigue of stainless steels. Int J Fatigue 2013;57:28–36.
[2] Colombo C, Fumagalli G, Bolzoni F, Gobbi G, Vergani L. Fatigue behavior of hydrogen pre-charged low alloy Cr-Mo steel. Int J Fatigue 2015;83:2–9.
[3] Yamabe J, Yoshikawa M, Matsunaga H, Matsuoka S. Hydrogen trapping and fatigue crack growth property of low-carbon steel in hydrogen-gas environment. Int J Fatigue 2017;102:202–13.
[4] Peral LB, Zafra A, Blasón S, Rodríguez C, Belzunce J. Effect of hydrogen on the fatigue crack growth rate of quenched and tempered CrMo and CrMoV steels. Int J Fatigue 2019;120:201–14.
[5] Shinko T, Hénaff G, Halm D, Benoit G, Bilotta G, Arzaghi M. Hydrogen-affected fatigue crack propagation at various loading frequencies and gaseous hydrogen pressures in commercially pure iron. Int J Fatigue 2019;121:197–207.
[6] Ogawa Y, Umakoshi K, Nakamura M, Takakuwa O, Matsunaga H. Hydrogen-assisted, intergranular, fatigue crack-growth in ferritic iron: Influences of hydrogen-gas pressure and temperature variation. Int J Fatigue 2020;140:105806.
[7] Gangloff RP. Hydrogen-assisted cracking. In: Milne I, Ritchie R, Karihaloo B, editors. Comprehensive structural integrity. vol. 6, New York, NY: Elsevier Science; 2003, p. 31–101.
[8] Murakami Y, Matsunaga H. The effect of hydrogen on fatigue properties of steels used for fuel cell system. Int J Fatigue 2006;28(11):1509–20.
[9] Gangloff RP, Somerday BP. Gaseous hydrogen embrittlement of materials in energy technologies. Cambridge: Woodhead Publishing Limited; 2012, p. 520.
[10] Martínez-Pañeda E, Niordson CF, Gangloff RP. Strain gradient plasticity-based modeling of hydrogen environment assisted cracking. Acta Mater 2016;117:321–32.
[11] Burns JT, Harris ZD, Dolph JD, Gangloff RP. Measurement and modeling of hydrogen environment-assisted cracking in a Ni-Cu-Al-Ti superalloy. Metall Mater Trans 2016;47(3):990–7.
[12] Novak P, Yuan R, Somerday BP, Sofronis P, Ritchie R. A statistical, physical-based, micro-mechanical model of hydrogen-induced intergranular fracture in steel. J Mech Phys Solids 2010;58(2):206–26.
[13] Ayas C, Deshpande VS, Fleck N. A fracture criterion for the notch strength of high strength steels in the presence of hydrogen. J Mech Phys Solids 2014;63(1):80–93.
[14] Serebrinsky S, Carter EA, Ortiz M. A quantum-mechanically informed continuum model of hydrogen embrittlement. J Mech Phys Solids 2004;52(10):2403–30.

[15] Yu H, Olsen JS, Olden V, Alvaro A, He J, Zhang Z. Continuum level simulation of the grain size and misorientation effects on hydrogen embrittlement in nickel. Eng Fail Anal 2017;81:79–93.
[16] Elmukashfi E, Tarleton E, Cocks ACF. A modelling framework for coupled hydrogen diffusion and mechanical behaviour of engineering components. Comput Mech 2020;66:189–220.
[17] Anand L, Mao Y, Talamini B. On modeling fracture of ferritic steels due to hydrogen embrittlement. J Mech Phys Solids 2019;122:280–314.
[18] Martínez-Pañeda E, Golahmar A, Niordson CF. A phase field formulation for hydrogen assisted cracking. Comput Methods Appl Mech Engrg 2018;342:742–61.
[19] Duda FP, Ciarbonetti A, Toro S, Huespe AE. A phase-field model for solute-assisted brittle fracture in elastic-plastic solids. Int J Plast 2018;102:16–40.
[20] Wu J-Y, Mandal T, Nguyen VP. A phase-field regularized cohesive zone model for hydrogen assisted cracking. Comput Methods Appl Mech Engrg 2020;358:112614.
[21] Kristensen PK, Niordson CF, Martínez-Pañeda E. A phase field model for elastic-gradient-plastic solids undergoing hydrogen embrittlement. J Mech Phys Solids 2020;143:104093.
[22] Kristensen PK, Niordson CF, Martínez-Pañeda E. Applications of phase field fracture in modelling hydrogen assisted failures. Theor Appl Fract Mech 2020;110:102837.
[23] Martínez-Pañeda E, Harris ZD, Fuentes-Alonso S, Scully JR, Burns JT. On the suitability of slow strain rate tensile testing for assessing hydrogen embrittlement susceptibility. Corros Sci 2020;163:108291.
[24] Castelluccio GM, Geller CB, McDowell DL. A rationale for modeling hydrogen effects on plastic deformation across scales in FCC metals. Int J Plast 2018;111:72–84.
[25] Hosseini ZS, Dadfarnia M, Nagao A, Kubota M, Somerday BP, Ritchie RO, et al. Modeling the hydrogen effect on the constitutive response of a low carbon steel in cyclic loading. J Appl Mech Trans ASME 2021;88(3):1–14.
[26] Esaklul KA, Wright AG, Gerberich WW. The effect of hydrogen induced surface asperities on fatigue crack closure in ultrahigh strength steel. Scr Metall 1983;17(9):1073–8.
[27] Esaklul KA, Gerberich WW. On the influence of internal hydrogen on fatigue thresholds of HSLA steel. Scr Metall 1983;17:1079–82.
[28] Fernández-Sousa R, Betegón C, Martínez-Pañeda E. Analysis of the influence of microstructural traps on hydrogen assisted fatigue. Acta Mater 2020;199:253–63.
[29] Shinko T, Halm D, Benoit G, Hénaff G. Controlling factors and mechanisms of fatigue crack growth influenced by high pressure of gaseous hydrogen in a commercially pure iron. Theor Appl Fract Mech 2021;112:102885.
[30] Moriconi C, Hénaff G, Halm D. Cohesive zone modeling of fatigue crack propagation assisted by gaseous hydrogen in metals. Int J Fatigue 2014;68:56–66.
[31] del Busto S, Betegón C, Martínez-Pañeda E. A cohesive zone framework for environmentally assisted fatigue. Eng Fract Mech 2017;185:210–26.
[32] Zhao Y, Xu BX, Stein P, Gross D. Phase-field study of electrochemical reactions at exterior and interior interfaces in Li-ion battery electrode particles. Comput Methods Appl Mech Engrg 2016;312:428–46.
[33] Mesgarnejad A, Karma A. Phase field modeling of chemomechanical fracture of intercalation electrodes: Role of charging rate and dimensionality. J Mech Phys Solids 2019;132.
[34] Quintanas-Corominas A, Turon A, Reinoso J, Casoni E, Paggi M, Mayugo J. A phase field approach enhanced with a cohesive zone model for modeling delamination induced by matrix cracking. Comput Methods Appl Mech Engrg 2020;358:112618.
[35] Tan W, Martínez-Pañeda E. Phase field predictions of microscopic fracture and R-curve behaviour of fibre-reinforced composites. Compos Sci Technol 2021;202:108539.
[36] Carollo V, Reinoso J, Paggi M. Modeling complex crack paths in ceramic laminates: A novel variational framework combining the phase field method of fracture and the cohesive zone model. J Eur Ceram Soc 2018;38(8):2994–3003.
[37] Li W, Shirvan K. Multiphysics phase-field modeling of quasi-static cracking in urania ceramic nuclear fuel. Ceram Int 2021;47:793–810.
[38] Simoes M, Martínez-Pañeda E. Phase field modelling of fracture and fatigue in Shape Memory Alloys. Comput Methods Appl Mech Engrg 2021;373:113504.
[39] Hirshikesh S, Annabattula RK, Martínez-Pañeda E. Phase field modelling of crack propagation in functionally graded materials. Composites B 2019;169:239–48.
[40] Kumar PKAV, Dean A, Reinoso J, Lenarda P, Paggi M. Phase field modeling of fracture in Functionally Graded Materials: G -convergence and mechanical insight on the effect of grading. Thin-Walled Struct 2021;159:107234.
[41] McAuliffe C, Waisman H. A unified model for metal failure capturing shear banding and fracture. Int J Plast 2015;65:131–51.
[42] Borden MJ, Hughes TJR, Landis CM, Anvari A, Lee IJ. A phase-field formulation for fracture in ductile materials: Finite deformation balance law derivation, plastic degradation, and stress triaxiality effects. Comput Methods Appl Mech Engrg 2016;312:130–66.
[43] Isfandbod M, Martínez-Pañeda E. A mechanism-based multi-trap phase field model for hydrogen assisted fracture. Int J Plast 2021;144:103044.
[44] Francfort GA, Marigo J-J. Revisiting brittle fracture as an energy minimization problem. J Mech Phys Solids 1998;46(8):1319–42.
[45] Bourdin B, Francfort GA, Marigo J-J. Numerical experiments in revisited brittle fracture. J Mech Phys Solids 2000;48(4):797–826.
[46] Provatas N, Elder K. Phase-field methods in materials science and engineering. Weinheim, Germany: John Wiley & Sons; 2011.
[47] Cui C, Ma R, Martínez-Pañeda E. A phase field formulation for dissolution-driven stress corrosion cracking. J Mech Phys Solids 2021;147:104254.
[48] Chambolle A. An approximation result for special functions with bounded deformation. J Des Math Pures Et Appl 2004;83(7):929–54.
[49] Tanné E, Li T, Bourdin B, Marigo J-J, Maurini C. Crack nucleation in variational phase-field models of brittle fracture. J Mech Phys Solids 2018;110:80–99.
[50] Kristensen PK, Niordson CF, Martínez-Pañeda E. An assessment of phase field fracture: crack initiation and growth. Phil Trans R Soc A 2021;379:20210021.
[51] Jiang DE, Carter EA. First principles assessment of ideal fracture energies of materials with mobile impurities: Implications for hydrogen embrittlement of metals. Acta Mater 2004;52(16):4801–7.
[52] Carrara P, Ambati M, Alessi R, De Lorenzis L. A framework to model the fatigue behavior of brittle materials based on a variational phase-field approach. Comput Methods Appl Mech Engrg 2020;361:112731.
[53] Miehe C, Hofacker M, Welschinger F. A phase field model for rate-independent crack propagation: Robust algorithmic implementation based on operator splits. Comput Methods Appl Mech Engrg 2010;199(45–48):2765–78.
[54] Ambati M, Gerasimov T, De Lorenzis L. A review on phase-field models of brittle fracture and a new fast hybrid formulation. Comput Mech 2015;55:383–405.
[55] Amor H, Marigo JJ, Maurini C. Regularized formulation of the variational brittle fracture with unilateral contact: Numerical experiments. J Mech Phys Solids 2009;57(8):1209–29.
[56] Seleš K, Lesičar T, Tonković Z, Sorić J. A residual control staggered solution scheme for the phase-field modeling of brittle fracture. Eng Fract Mech 2019;205:370–86.
[57] Renard Y, Poulios K. GetFEM: Automated FE modeling of multiphysics problems based on a generic weak form language. ACM Trans Math Softw 2020;47(1):1–31.
[58] Kristensen PK, Martínez-Pañeda E. Phase field fracture modelling using quasi-Newton methods and a new adaptive step scheme. Theor Appl Fract Mech 2020;107:102446.
[59] Turnbull A, Ferriss DH, Anzai H. Modelling of the hydrogen distribution at a crack tip. Mater Sci Eng A 1996;206(1):1–13.
[60] Martínez-Pañeda E, Díaz A, Wright L, Turnbull A. Generalised boundary conditions for hydrogen transport at crack tips. Corros Sci 2020;173:108698.
[61] Di Leo CV, Anand L. Hydrogen in metals: A coupled theory for species diffusion and large elastic-plastic deformations. Int J Plast 2013;43:42–69.
[62] Martínez-Pañeda E, del Busto S, Niordson CF, Betegón C. Strain gradient plasticity modeling of hydrogen diffusion to the crack tip. Int J Hydrogen Energy 2016;41(24):10265–74.
[63] Díaz A, Alegre JM, Cuesta II. Coupled hydrogen diffusion simulation using a heat transfer analogy. Int J Mech Sci 2016;115–116:360–9.
[64] Gangloff RP. Corrosion fatigue crack propagation in metals. In: NASA contractor report 4301. Tech. rep., NASA; 1990, p. 1–194, 19900015089.
[65] Williams ML. On the stress distribution at the base of a stationary crack. J Appl Mech 1957;24:109–14.
[66] Anderson TL. Fracture mechanics. Fundamentals and applications. third ed. Boca Raton: CRC Press, Taylor & Francis; 2005.
[67] Matsunaga H, Yoshikawa M, Kondo R, Yamabe J, Matsuoka S. Slow strain rate tensile and fatigue properties of Cr-Mo and carbon steels in a 115 MPa hydrogen gas atmosphere. Int J Hydrogen Energy 2015;40(16):5739–48.
[68] Matsumoto T, Kubota M, Matsuoka S, Ginet P, Furtado J, Barbier F. Threshold stress intensity factor for hydrogen-assisted cracking of CR-MO steel used as stationary storage buffer of a hydrogen refueling station. Int J Hydrogen Energy 2017;42(11):7422–8.
[69] Ogawa Y, Matsunaga H, Yamabe J, Yoshikawa M, Matsuoka S. Unified evaluation of hydrogen-induced crack growth in fatigue tests and fracture toughness tests of a carbon steel. Int J Fatigue 2017;103:223–33.
[70] San Marchi C, Somerday BP. Technical reference for hydrogen compatibility of materials. In: SANDIA report SAND2012-7321. Tech. rep., SANDIA National Labs; 2012.

[P4]

Kristensen, Philip K., Niordson, Christian F., Martínez-Pañeda, Emilio. Applications of phase field fracture in modelling hydrogen assisted failures. Theoretical and Applied Fracture Mechanics 2020. 110, 102837.

Theoretical and Applied Fracture Mechanics 110 (2020) 102837

Contents lists available at ScienceDirect

Theoretical and Applied Fracture Mechanics

journal homepage: www.elsevier.com/locate/tafmec

Applications of phase field fracture in modelling hydrogen assisted failures

Philip K. Kristensen [a], Christian F. Niordson [a], Emilio Martínez-Pañeda [b,*]

[a] Department of Mechanical Engineering, Technical University of Denmark, DK-2800 Kgs. Lyngby, Denmark
[b] Department of Civil and Environmental Engineering, Imperial College London, London SW7 2AZ, UK

ARTICLE INFO

Keywords:
Phase field fracture
Hydrogen embrittlement
Fracture
Virtual testing
Finite element analysis

ABSTRACT

The phase field fracture method has emerged as a promising computational tool for modelling a variety of problems including, since recently, hydrogen embrittlement and stress corrosion cracking. In this work, we demonstrate the potential of phase field-based multi-physics models in transforming the engineering assessment and design of structural components in hydrogen-containing environments. First, we present a theoretical and numerical framework coupling deformation, diffusion and fracture, which accounts for inertia effects. Several constitutive choices are considered for the crack density function, including choices with and without an elastic phase in the damage response. The material toughness is defined as a function of the hydrogen content using an atomistically-informed hydrogen degradation law. The model is numerically implemented in 2D and 3D using the finite element method. The resulting computational framework is used to address a number of case studies of particular engineering interest. These are intended to showcase the model capabilities in: (i) capturing complex fracture phenomena, such as dynamic crack branching or void-crack interactions, (ii) simulating standardised tests for critical components, such as bolts, and (iii) enabling simulation-based paradigms such as *Virtual Testing* or *Digital Twins* by coupling model predictions with inspection data of large-scale engineering components. The evolution of defects under in-service conditions can be predicted, up to the ultimate failure. By reproducing the precise geometry of the defects, as opposed to re-characterising them as sharp cracks, phase field modelling enables more realistic and effective structural integrity assessments.

1. Introduction

Hydrogen has been known for decades to notably reduce the toughness, ductility and fatigue life of engineering components [1–3]. Hydrogen ingress into a metallic sample can happen during its initial forming, during the coating or plating of a protective layer, through exposure to hydrogen or hydrogen-containing molecules in the air, soil or water, or through corrosion processes. Hydrogen absorbed from gaseous or aqueous environments diffuses within the metal and is attracted to areas of high hydrostatic stress, where damage takes place by means of mechanisms that are still being debated [4–7]. This so-called hydrogen embrittlement phenomenon is now pervasive across applications in the construction, defence, transport and energy sectors, due to the ubiquity of hydrogen and the higher susceptibility of modern, high-strength alloys [8,9].

The use of fracture mechanics-based models for hydrogen-sensitive applications could be a game-changer in preventing catastrophic failures and optimising material performance. For example, reliable modelling of hydrogen assisted fracture could enable a controlled use of high strength alloys, accelerate material certification, and govern inspection planning and fitness-for-service assessment. Yet, the development of models capable of predicting crack initiation and growth as a function of material, loading and environmental variables has not been an easy task. Two main challenges hold back the use of predictive models in engineering assessment. The first one is the physical complexity of the problem at hand. Hydrogen embrittlement is a complicated chemical and micro-mechanical phenomenon that involves multiple hydrogen-metal interactions at several scales. However, several mechanistic models have been proposed that show good agreement with experiments with little or no calibration [10–12]. Predictions based on nominal material properties and parameters that can be independently determined are now possible. The second challenge lies in developing a computational framework capable of capturing, in arbitrary geometries and dimensions, the multi-physics elements of the problem and their interaction with the complex cracking phenomena occurring in engineering applications. The phase field fracture method [13] appears to

* Corresponding author.
E-mail address: e.martinez-paneda@imperial.ac.uk (E. Martínez-Pañeda).

https://doi.org/10.1016/j.tafmec.2020.102837
Received in revised form 10 November 2020; Accepted 14 November 2020
Available online 19 November 2020
0167-8442/© 2020 Elsevier Ltd. All rights reserved.

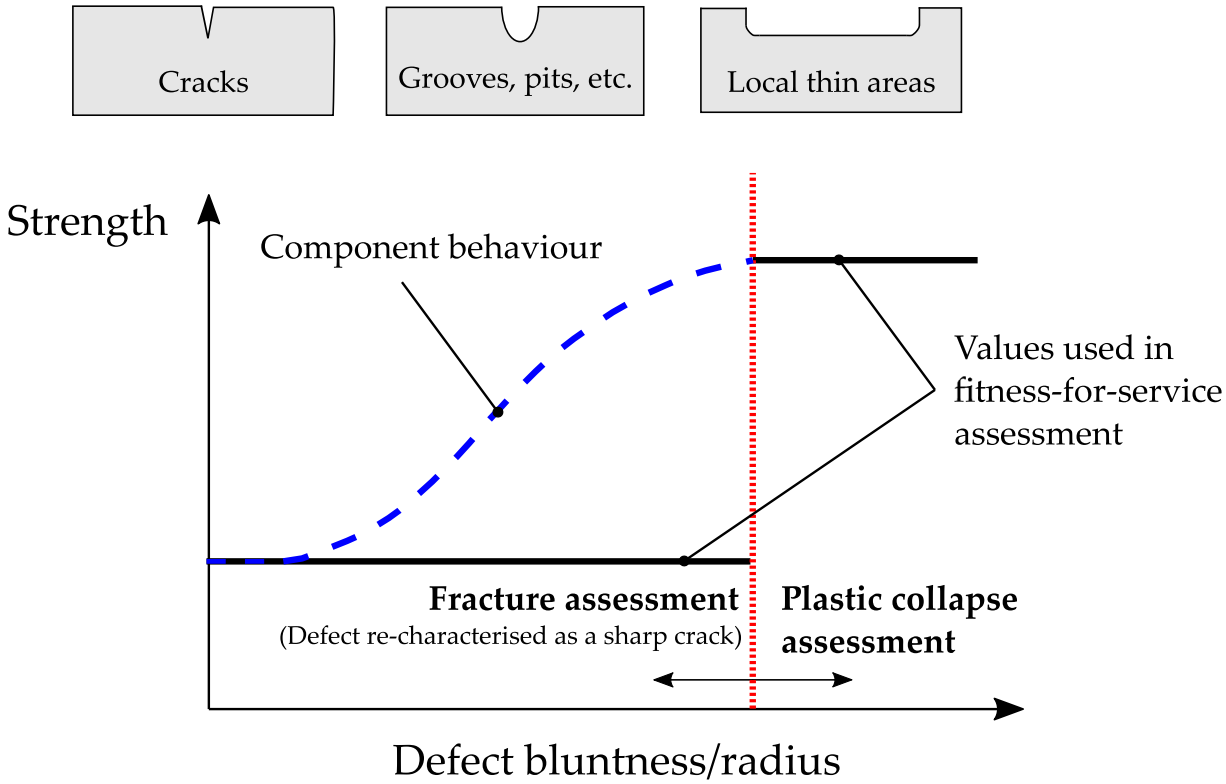

Fig. 1. Using phase field to enable defect mechanics-based assessments that can reduce overly conservative fitness-for-service assessment. Schematic of current assessment procedures for a defect of length larger than the transition flaw size; adapted from standardised engineering assessment of burst pressure, see Ref. [26].

provide a suitable framework for overcoming this obstacle.

Martínez-Pañeda *et al.* [14] have recently extended the phase field fracture method to predict hydrogen assisted failures and the approach has quickly gained popularity as a framework for incorporating various hydrogen embrittlement models [15–20]. The main experimental trends have been captured and advanced fracture features such as crack merging, nucleation from arbitrary sites and branching are predicted without convergence problems or the need for remeshing. However, the vast majority of the analyses are restricted to 2D boundary value problems of mostly academic relevance. In this work, we demonstrate the potential of the phase field fracture method in predicting large scale hydrogen assisted failures of practical engineering interest. This includes, for the first time, (i) the modelling of hydrogen assisted fractures resulting from dynamic loading, where inertia is relevant, and (ii) the consideration of both AT1 [21] and AT2 [13,22] constitutive choices for the dissipation function of the phase field fracture method. Overall, the goal is to showcase the capabilities of phase field-based hydrogen assisted cracking formulations in enabling *Virtual Testing* in hydrogen-sensitive applications. To this end, case studies will be addressed involving (i) crack branching in a hydrogen embrittled plate subjected to dynamic loading, (ii) crack-void interactions in a hydrogen-containing 3D bar, (iii) failure of a screw anchor exposed to an aggressive solution, simulating a standardised experiment, and (iv) cracking evolution in a pipeline with internal defects, as measured by in-line inspection. The last example showcases the possibility of combining phase field modelling with inspection data to create (so-called) *Digital Twins* of critical infrastructure, minimising expensive testing and monitoring. In this regard, there is a further motivation for the use of phase field for engineering assessment. Unlike other computational approaches, such as discrete fracture methods [23–25], predictions are not restricted to the evolution of sharp cracks but the growth of defects of any arbitrary shape can be simulated, and without any prior knowledge regarding the extent of growth or the growth direction. This opens the possibility of conducting *defect mechanics*-based assessments of notch-like defects, significantly reducing the conservatism associated with re-characterising all detected defects into sharp cracks. The concept is illustrated in Fig. 1 for a given defect length (larger than the transition flaw size); simulating the real defect geometry, as opposed to an equivalent crack, can provide more realistic and sustainable criteria for engineering assessment.

The remainder of this paper is organised as follows. A generalised phase field framework for chemo-mechanical fracture is given in Section 2, including inertia effects. Details of the finite element implementation are given in Section 3. The four case studies described above are presented in Section 4. Finally, the manuscript ends with concluding remarks in Section 5.

2. A phase field fracture formulation for hydrogen embrittlement

2.1. Potential energy of the solid

Consider a domain $\Omega \in \mathbb{R}^n$ $(n \in [1, 2, 3])$, with outer boundary $\delta\Omega \in \mathbb{R}^{n-1}$. The domain contains a deformable solid with displacement field $\boldsymbol{u}$ and internal crack surface $\Gamma \in \mathbb{R}^{n-1}$. An absorbed species of concentration c might diffuse through the solid and interact with the mechanical behaviour. The variational energy functional for the solid can be postulated as [27,28]:

$$\Pi = \int_\Omega \left\{ \frac{1}{2}\rho \dot{\boldsymbol{u}}\cdot\dot{\boldsymbol{u}} + \psi_s(\boldsymbol{u}, c) + \psi_{chem}(\boldsymbol{u}, c) \right\} \mathrm{dV} + \int_\Gamma \mathrm{G_c}\, \mathrm{dS}. \tag{1}$$

Here, the first term of the volume integral represents the kinetic energy density of the solid, with $\dot{\boldsymbol{u}}$ denoting the velocity field and ρ the mass density. Also within the volume integral, the second and third terms respectively denote the strain energy density and the chemical energy density related to the transport of solute species. The surface integral represents the fracture energy as proposed by Griffith [29], with G_c

being the material toughness. The crack geometry Γ is unknown, hindering minimisation of (1). This can be overcome by introducing a continuous phase field variable $\phi \in [0,1]$. The phase field resembles a damage variable, representing the intact state of the material when $\phi = 0$ and the completely fractured state when $\phi = 1$. A regularised potential energy can be defined considering this auxiliary phase field and a regularisation length scale ℓ, such that (1) can be approximated as [13,28]:

$$\Pi_\ell = \int_\Omega \left\{ \frac{1}{2}\rho \dot{\boldsymbol{u}}\cdot\dot{\boldsymbol{u}} + \psi_s(\boldsymbol{u}, c, \phi) + \psi_{chem}(\boldsymbol{u}, c) + G_c\gamma(\phi) \right\} \mathrm{dV}. \tag{2}$$

In the regularized formulation, γ represents a crack surface density function. In the following, we introduce a number of specific choices for the above formulation, specialising it for brittle fracture of hydrogen-containing metals. As discussed (e.g.) in Refs. [30,31], the phase field length scale can have different interpretations. As rigorously proven using Γ-convergence, the regularised functional Π_ℓ, Eq. (2), converges to that of Π, Eq. (1), for a fixed $\ell \to 0^+$ and thus minimising (2) provides the solution for the Griffith variational problem. Accordingly, ℓ can be interpreted as a regularising parameter in its vanishing limit. However, a finite material strength is introduced for $\ell > 0^+$ and the phase field length scale becomes a material property governing the material strength, σ_c. For example, under plane stress conditions,

$$\sigma_c \propto \sqrt{\frac{G_c E}{\ell}} = \frac{K_{Ic}}{\sqrt{\ell}} \tag{3}$$

Thus, the fracture behaviour of the solid is governed by the material toughness G_c and strength σ_c, as defined by the choice of G_c and ℓ. Therefore, phase field models provide a suitable framework to link fracture (in a Griffith sense) and damage. The phase field length scale also regularises the numerical solution; results are mesh-independent if the finite element mesh is sufficiently fine to resolve the fracture process zone, whose size is governed by ℓ.

2.2. Constitutive prescriptions

2.2.1. Linear elasticity

We start by introducing the assumption of linear elastic behaviour. Even within the realm of brittle fracture, this is an appreciable simplification as plasticity will develop locally at the tip of sharp defects. However, the crack tip stresses predicted by conventional plasticity are insufficient to accurately predict crack tip hydrogen concentrations [32,33] and the use of strain gradient plasticity models reveals: (i) the existence of an elastic core surrounding the crack tip [34,35], and (ii) a crack tip stress distribution over the fracture process zone that is closer to that of linear elasticity [36,37]. Thus, linear elasticity provides a conservative, less computationally demanding alternative to multi-scale plasticity models. In addition, the formulation is made under the assumptions of small strains such that the strain tensor is given by,

$$\boldsymbol{\varepsilon} = \frac{1}{2}\left(\nabla \boldsymbol{u} + \nabla \boldsymbol{u}^T\right). \tag{4}$$

For an (undamaged) linear elastic stiffness tensor, $\mathbf{C}_0$, the strain energy density of the intact material is defined as

$$\psi_0 = \frac{1}{2}\boldsymbol{\varepsilon} : \mathbf{C}_0 : \boldsymbol{\varepsilon}. \tag{5}$$

Thus, it is assumed that the diffusive species has no influence on the strain energy, which is a common assumption for hydrogen in metals [38].

2.2.2. Phase field fracture

We proceed to make constitutive choices for the phase field fracture formulation. Two models will be considered, which are known to provide accurate descriptions of fracture phenomena in a regularized setting. The strain energy density and the crack surface density function are given by:

$$\psi_s = g(\phi)\psi_0, \tag{6}$$

$$\gamma = \frac{1}{4c_w\ell}\left(w(\phi) + \ell^2|\nabla\phi|^2\right). \tag{7}$$

Where the degradation function $g(\phi)$ is continuous and monotonic and takes the values $g(0) = 1$ and $g(1) = 0$. The function $w(\phi)$ must fulfill $w(0) = 0$ and $w(1) = 1$. Finally,

$$c_w = \int_0^1 \sqrt{w(\varphi)}\,\mathrm{d}\varphi. \tag{8}$$

This choice of phase field formulation has been shown to Γ-converge to the Griffith solution [39]. Common choices for $g(\phi)$ and $w(\phi)$ include $g(\phi) = (1-\phi)^2$ and $w(\phi) = \phi^2$, which produces the so-called *standard* or AT2 phase field model [22]. Another common choice is the same quadratic degradation function and $w(\phi) = \phi$, which is often referred to as the AT1 phase field model [21]. The latter formulation introduces an elastic regime prior to any damage in the solid.

2.2.3. Modified Fickian diffusion

Finally, for the absorbed diffusive species, we adopt a modified version of Fickian diffusion. In addition to concentration gradients, diffusion is assumed to be driven by gradients of hydrostatic stress, such that atomic hydrogen accumulates in areas where the lattice is being expanded. Mass conservation requirements relate the rate of change of the hydrogen concentration c with the hydrogen flux $\boldsymbol{J}$ through the external surface,

$$\int_\Omega \frac{\mathrm{d}c}{\mathrm{d}t}\,\mathrm{d}V + \int_{\partial\Omega} \boldsymbol{J}\cdot\boldsymbol{n}\,\mathrm{d}S = 0. \tag{9}$$

Diffusion is driven by the gradient of the chemical potential $\nabla\mu$. Thus, for a diffusion coefficient D, the flux is related to $\nabla\mu$ through a linear Onsager relationship,

$$\boldsymbol{J} = -\frac{Dc}{RT}\nabla\mu. \tag{10}$$

The chemical potential includes a hydrostatic stress σ_H-dependent term to account for the role of volumetric strains in driving diffusion. For an occupancy of lattice sites θ_L and partial molar volume of hydrogen $\overline{V}_H$, the chemical potential of hydrogen in lattice sites is given by,

$$\mu = \mu^0 + RT\ln\frac{\theta_L}{1-\theta_L} - \overline{V}_H\sigma_H \tag{11}$$

Here, μ^0 denotes the chemical potential in the reference case, R is the gas constant and T is the absolute temperature. Consider now the relation between the occupancy and the number of sites $\theta_L = c/N$, and make the common assumptions of low occupancy ($\theta_L \ll 1$) and constant interstitial sites concentration ($\nabla N = 0$); inserting (11) into (10) then renders,

$$\boldsymbol{J} = -D\nabla c + \frac{Dc}{RT}\overline{V}_H\nabla\sigma_H \tag{12}$$

2.2.4. Hydrogen degradation of the toughness

The material toughness is defined to be sensitive to the hydrogen content, $G_c(c)$, as consistently observed experimentally. First, the Langmuir–McLean isotherm is used to estimate, from the bulk concentration, the hydrogen coverage θ at decohering interfaces,

$$\theta = \frac{c}{c + \exp\left(\frac{-\Delta g_b^0}{RT}\right)}. \tag{13}$$

Here, g_b^0 is the binding energy for the impurity at the site of interest. A value of 30 kJ/mol is assumed throughout this study, which is representative of hydrogen trapped at grain boundaries [40]. Following

atomistic studies of surface energy sensitivity to hydrogen coverage [41], a linear degradation of the fracture energy with θ is assumed,

$$G_c(\theta) = (1 - \chi\theta)G_c(0) \tag{14}$$

where χ is a hydrogen damage coefficient, a material parameter that can be estimated by calibrating with experiments [18] or inferred from atomistic calculations [14]. We adopt the latter approach and assume a value of $\chi = 0.89$ throughout our calculations; this magnitude provides the best fit to atomistic calculations on iron [14,42]. A failure model based on grain boundary decohesion is implicitly assumed for the above choices: a degradation law based on atomistic calculations of surface energy sensitivity to hydrogen content, and the consideration of a grain boundary binding energy in (13). However, we emphasise that the framework is universal; the degradation law can be adapted to accommodate any other mechanistic interpretation (e.g., including a dependence on parameters such as the dislocation density or the void volume fraction) or chosen to be phenomenological, relating G_c to c and to a hydrogen damage coefficient χ to be calibrated.

2.3. Coupled force balances

We proceed to present the weak and strong form of the problem considering the constitutive choices above. First, following Refs. [15,43], a scalar field η is defined to determine the kinematics of composition changes, such that

$$\dot{\eta} = \mu \quad \text{and} \quad \eta(\boldsymbol{x}, t) = \int_0^t \mu(\boldsymbol{x}, t)\,\mathrm{d}t \tag{15}$$

Thus, from a kinematic viewpoint, the domain Ω can be described by the displacement $\boldsymbol{u}$, phase field parameter ϕ, and chemical displacement η. Taking the first derivative of (2) and incorporating the constitutive prescriptions adopted, the coupled weak form reads, in the absence of body forces and external tractions and fluxes, as follows:

$$\int_\Omega \Big\{ \rho\ddot{\boldsymbol{u}}\delta\boldsymbol{u} + (1-\phi)^2\boldsymbol{\sigma} : \mathrm{sym}\nabla\delta\boldsymbol{u} - 2(1-\phi)\delta\phi\psi_0(\boldsymbol{u}) - \frac{\mathrm{d}c}{\mathrm{d}t}\delta\eta \tag{16}$$

$$+ \left(\frac{Dc}{RT}\overline{V}_H\nabla\sigma_H - D\nabla c\right)\cdot\nabla\delta\eta + G_c(c)\left(\frac{\phi}{\ell}\delta\phi + \ell\nabla\phi\cdot\nabla\delta\phi\right)\Big\}\,\mathrm{d}V = 0.$$

Here, $\boldsymbol{\sigma}$ is the undamaged Cauchy stress tensor. The local force balances can then be readily derived by applying Gauss' divergence theorem and noting that (16) must hold for any kinematically admissible variations of the virtual quantities. Accordingly,

$$\begin{aligned} \nabla\left[(1-\phi)^2\boldsymbol{\sigma}\right] &= 0 \\ G_c(c)\left(\frac{\phi}{\ell} - \ell\nabla^2\phi\right) - 2(1-\phi)\psi_0(\boldsymbol{u}) &= 0 \\ \frac{\mathrm{d}c}{\mathrm{d}t} - D\nabla^2 c + \nabla\cdot\left(\frac{D\overline{V}_H}{RT}c\nabla\sigma_H\right) &= 0 \end{aligned} \tag{17}$$

The coupling between the different physical elements of the problem is evident in (17). First, as damage increases, the phase field reduces the stiffness of the solid in the linear momentum balance, Eq. (17a). As observed in (17b), the phase field evolves driven by the competition between strain energy density ψ_0 and toughness G_c, the latter diminishing with increasing hydrogen concentration. Finally, (17c), diffusion of atomic hydrogen is governed by concentration gradients and the lattice dilation, as characterised by the hydrostatic stress.

3. Finite element implementation

We shall now describe the details of the numerical implementation in the context of the finite element method. First, some numerical considerations are presented for the phase field problem in Section 3.1, to guarantee damage irreversibility and prevent crack growth from compressive stresses. Secondly, a threshold is defined in Section 3.2 to address the implementation peculiarities inherent to the AT1 model. Thirdly, the discretisation of the problem and the formulation of residuals and stiffness matrices is described in Section 3.3. The implementation is carried out in the commercial finite element package Abaqus by means of a user element (UEL) subroutine. The UEL subroutine developed includes multiple choices of elements; in 2D, linear and quadratic quadrilateral elements for both plane stress and plane strain; in 3D, linear and quadratic hexahedral elements, as well as quadratic tetrahedral elements. Abaqus2Matlab is employed to preprocess the input files [44].

3.1. Addressing irreversibility and crack growth in compression

First, a history variable field H is introduced to ensure damage irreversibility. Thus, for a time t,

$$H = \max_{\tau\in[0,t]}\psi_0(\tau). \tag{18}$$

Secondly, we introduce a strain energy decomposition to prevent cracking in compression. The volumetric-deviatoric split by Amor *et al.* [45] is adopted, by which the compressive volumetric strain energy does not contribute to damage. Thus, the strain energy density is decomposed into the following terms:

$$\psi_0^+ = \frac{1}{2}K\langle tr(\boldsymbol{\varepsilon})\rangle_+^2 + \mu(\boldsymbol{\varepsilon}' : \boldsymbol{\varepsilon}'), \tag{19}$$

$$\psi_0^- = \frac{1}{2}K\langle tr(\boldsymbol{\varepsilon})\rangle_-^2, \tag{20}$$

where K is the bulk modulus, $\langle a\rangle_\pm = (a \pm |a|)/2$ and $\boldsymbol{\varepsilon}' = \boldsymbol{\varepsilon} - tr(\boldsymbol{\varepsilon})\boldsymbol{I}/3$. In addition, we follow the hybrid implementation of Ambati *et al.* [46] in considering only ψ_0^+ in the evaluation of the history variable field H, therefore referring to it as H^+ henceforth, while considering ψ_0 in the displacement problem.

3.2. Implementing the AT1 phase field formulation

Unlike the AT2 phase field model, the AT1 formulation does not inherently ensure that the lower bound on the phase field is enforced. If no measures are taken, the phase field can become negative for all strains below the critical strain, which is given by

$$\varepsilon_{c,AT1} = \sqrt{\frac{3G_c}{8\ell E}}. \tag{21}$$

To overcome this, we introduce a lower bound by re-defining the history field as:

$$H = \max\left[\max_{\tau\in[0,t]}\psi_0(\tau),\ \frac{1}{2}\mathrm{E}\varepsilon_{\mathrm{c,AT1}}^2\right], \tag{22}$$

The minimum threshold employed for the history field corresponds to the strain energy density magnitude that yields a vanishing phase field in the homogeneous 1D case [47]. Other methods exist for implementing the AT1 formulation, such as using constrained optimization solvers.

3.3. Finite element discretisation of variational principles

We proceed to discretise the linearised problem and present the associated residuals and stiffness matrices. First, making use of Voigt notation, the displacement field $\boldsymbol{u}$, phase field ϕ and hydrogen concentration c can be discretised as

$$\boldsymbol{u} = \sum_{i=1}^{m}\boldsymbol{N}_i^u\boldsymbol{u}_i, \quad \phi = \sum_{i=1}^{m}N_i\phi_i, \quad c = \sum_{i=1}^{m}N_ic_i, \tag{23}$$

where N_i denotes the shape function associated with node i, for a total number of nodes m. Here, $N_i^{\boldsymbol{u}}$ is a diagonal interpolation matrix with the nodal shape functions N_i as components. Similarly, using the standard strain–displacement $\boldsymbol{B}$ matrices, the associated derivatives are discretised as,

$$\boldsymbol{\varepsilon} = \mathrm{sym}\nabla\boldsymbol{u} = \sum_{i=1}^{m} \boldsymbol{B}_i^{\boldsymbol{u}} \boldsymbol{u}_i\,, \quad \nabla\phi = \sum_{i=1}^{m} \boldsymbol{B}_i \phi_i\,, \quad \nabla c = \sum_{i=1}^{m} \boldsymbol{B}_i c_i\,. \tag{24}$$

Considering this finite element discretisation and the weak form balances (16), the resulting discrete equations of the balances for the displacement, phase field and concentration can be expressed as the following residuals:

$$\mathbf{r}_i^{\mathbf{u}} = \int_\Omega \left\{ \left[(1-\phi)^2 + k\right] \left(\mathbf{B}_i^{\mathbf{u}}\right)^T \boldsymbol{\sigma} + \rho \left(\mathbf{N}_i^{\mathbf{u}}\right)^T \ddot{\boldsymbol{u}} \right\} \mathrm{d}V \tag{25}$$

$$r_i^{\phi} = \int_\Omega \left\{ -2(1-\phi) N_i H^+ + G_c(c) \left[\frac{\phi}{\ell} N_i + \ell \left(\mathbf{B}_i^{\phi}\right)^T \nabla\phi \right] \right\} \mathrm{d}V \tag{26}$$

$$r_i^{c} = \int_\Omega \left[N_i \left(\frac{1}{D} \frac{\mathrm{d}c}{\mathrm{d}t} \right) + \mathbf{B}_i^T \nabla c - \mathbf{B}_i^T \left(\frac{\overline{V}_H}{RT} c \nabla\sigma_H \right) \right] \mathrm{d}V \tag{27}$$

where k is a numerical parameter introduced to keep the system of equations well-conditioned; a value of $k = 1 \times 10^{-7}$ is adopted throughout this work. This choice is grounded on previous studies [48,49]; the use of smaller values has no influence in the results. Subsequently, the tangent stiffness matrices are calculated as:

$$\boldsymbol{K}_{ij}^{\boldsymbol{u},\boldsymbol{u}} = \frac{\partial \boldsymbol{r}_i^{\boldsymbol{u}}}{\partial \boldsymbol{u}_j} = \int_\Omega \left\{ \left[(1-\phi)^2 + k\right] \left(\boldsymbol{B}_i^{\boldsymbol{u}}\right)^T \boldsymbol{C}_0 \boldsymbol{B}_j^{\boldsymbol{u}} + \frac{\rho}{(\mathrm{d}t)^2} \left(\boldsymbol{N}_i^{\boldsymbol{u}}\right)^T \boldsymbol{N}_j^{\boldsymbol{u}} \right\} \mathrm{d}V \tag{28}$$

$$\boldsymbol{K}_{ij}^{\phi,\phi} = \frac{\partial r_i^{\phi}}{\partial \phi_j} = \int_\Omega \left\{ \left[2H^+ + \frac{G_c(c)}{\ell} \right] N_i N_j + G_c(c) \ell \boldsymbol{B}_i^T \boldsymbol{B}_j \right\} \mathrm{d}V \tag{29}$$

$$\boldsymbol{K}_{\mathrm{ij}}^{c,c} = \frac{\partial r_i^{c}}{\partial c_j} = \int_\Omega \left(N_i^T \frac{1}{D\mathrm{d}t} N_j + \boldsymbol{B}_i^T \boldsymbol{B}_j - \boldsymbol{B}_i^T \frac{\overline{V}_H}{RT} \nabla\sigma_H N_j \right) \mathrm{d}V \tag{30}$$

Unless otherwise stated, the global system of equations for the linearised problem will be solved using a staggered, alternative minimisation scheme [14,50].

4. Results

The potential of the formulation in simulating complex fracture phenomena and transforming engineering assessment is demonstrated by addressing four case studies of particular interest. First, we model for the first time dynamic failure of a hydrogen pre-charged steel plate, using the AT1 model; see Section 4.1. Next, in Section 4.2, we address the failure of a tensile bar due to the interaction between a tilted crack and a neighboring void. Thirdly, in Section 4.3, we model the brittle fracture of an anchor in a concrete element subjected to a corrosive environment, following the ASTM E488 standard [51]. Finally, the progressive failure of a pipeline is simulated; coupling modelling with in-line inspection data, the model incorporates the numerous defects that typically arise due to pitting corrosion and captures their growth and coalescence under in-service conditions.

4.1. Crack branching in an embrittled steel plate due to dynamic loading

For the first case study, we consider the paradigmatic boundary value problem of dynamic crack branching in a rectangular plate [28,52,53]. The geometry and boundary conditions are given in Fig. 2. This well-known case study is based on dynamic experiments on brittle materials such as glassy polymers [54]. Here, we aim to illustrate the influence of hydrogen on the dynamic fracture pattern of a martensitic steel of type 440C, which is known to exhibit very brittle fracture in the presence of hydrogen [55].

The elastic parameters for the martensitic steel considered are $E = 194$ GPa, $\nu = 0.3$ and $\rho = 7850$ kg/m^3, yielding a Rayleigh wave speed of $v_n = 5768$ m/s. The plane strain fracture toughness of martensitic steel of type 440C is $K_{IC} \approx 22$ MPa$\cdot m^{1/2}$ [56], which corresponds to a Griffith energy of $G_c = 2.33$ J/mm^2; recall that $K_{Ic} = \sqrt{G_c E/(1-\nu^2)}$. The material is assumed to be pre-charged with either 5 or 0.1 wppm of hydrogen. As a reference case, a specimen without hydrogen has also been included. The fracture length scale has been chosen as two times the characteristic element length $\ell = 2h_e = 0.4$ mm and the specimen is subjected to a tensile impact load of 60 MPa. The domain is meshed with quadratic rectangular (square) elements and the initial crack has been introduced through the phase field rather than as a discontinuity in the mesh. A total of 50,000 elements are used, taking advantage of symmetry. In this dynamic case, crack propagation is expected to be faster than hydrogen diffusion by at least an order of magnitude, allowing us to neglect the influence of hydrogen transport. Without the diffusion equations the global stiffness matrix is symmetric, which allows us to make use of a monolithic scheme in conjunction with the quasi-Newton method [57,58] to solve the problem more efficiently. For this specific problem, the AT1 phase field model is used. Thus, this case study also constitutes the first example involving AT1 and quasi-Newton solution methods, confirming the successful performance observed with other phase field models [57,58]. The increment size has been chosen as $\Delta t < h_e/v_n$ to completely resolve the stress waves in the material.

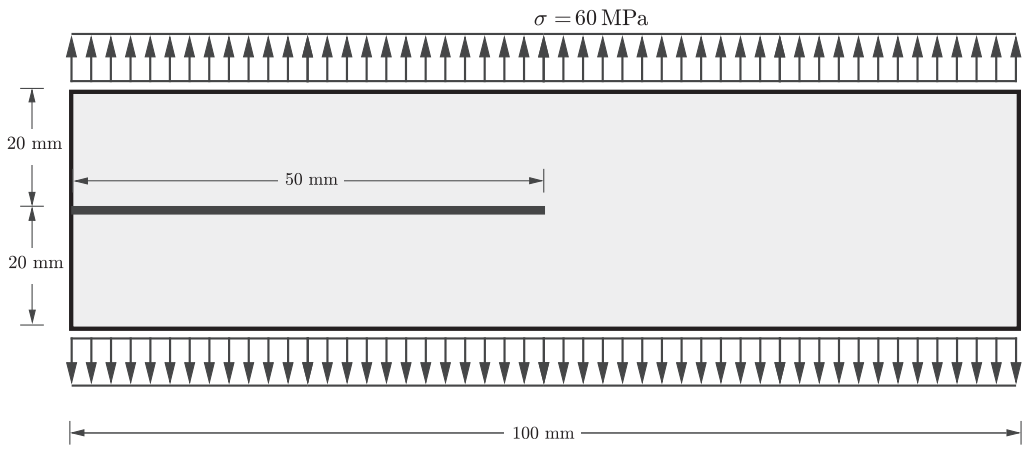

Fig. 2. Dimensions and loading conditions for the dynamic branching problem.

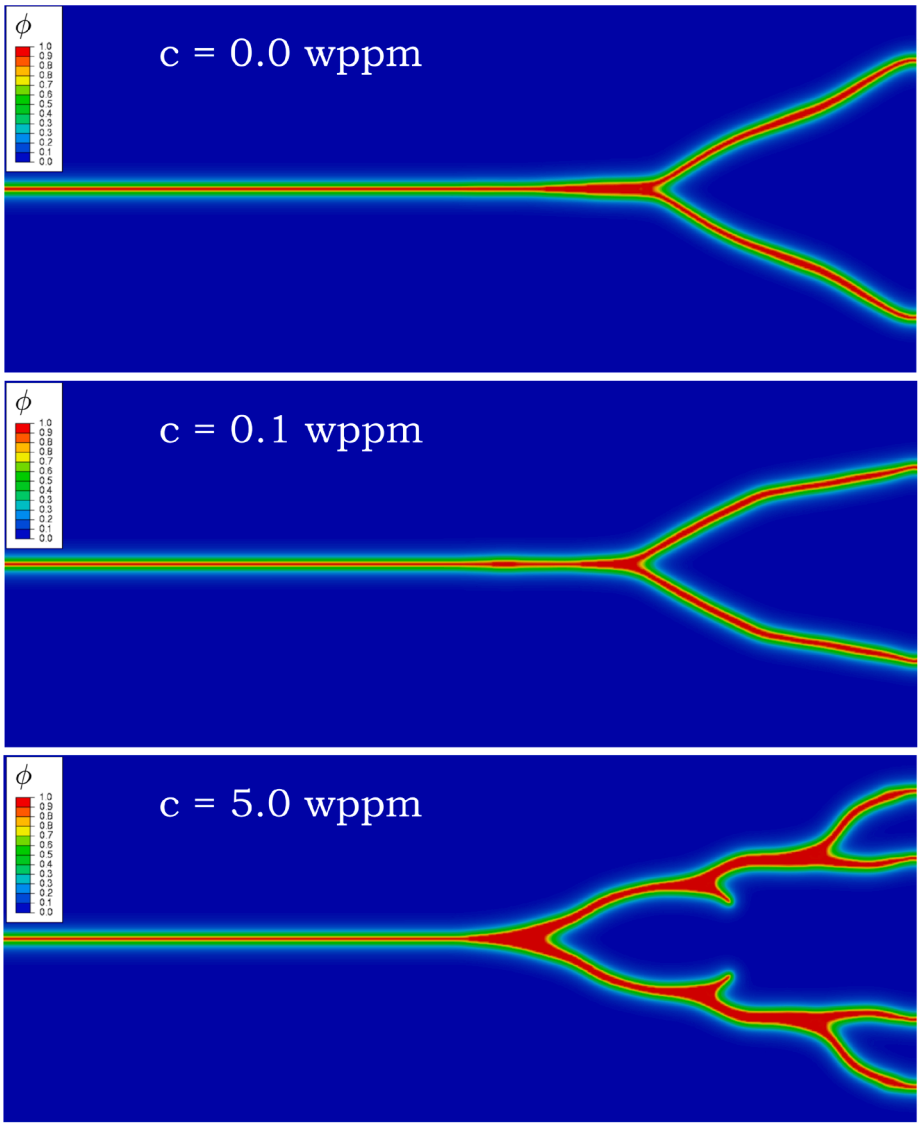

Fig. 3. Increasing degree of crack branching with increasing hydrogen pre-charged content in a martensitic steel plate subjected to dynamic loading. Phase field contours, with blue representing intact material ($\phi \approx 0$) and red denoting the crack ($\phi \approx 1$).

The finite element results obtained are reported in Fig. 3 in terms of the phase field contours; blue colour represents intact material ($\phi \approx 0$) while red colour is used to denote the crack ($\phi \approx 1$). The results reveal that the crack pattern is very sensitive to the hydrogen content. A noticeable influence is observed for the case of a $c_0 = 0.1$ wppm hydrogen concentration and extensive branching is seen for the case of $c_0 = 5$ wppm, which might be interpreted as mild shattering. We emphasise that branching is intrinsically related to inertia effects, which are significant in this boundary value problem, and the material brittleness, which is sensitive to the hydrogen content. The results showcase the capability of the proposed framework for capturing inertia effects and the complex crack patterns that might occur in hydrogen-assisted fractures. The remaining case studies will deal with quasi-static loading conditions and accordingly the kinetic energy terms will be dropped from the model.

4.2. Void-crack interaction in a 3D tensile bar

The second case study deals with the prediction of crack initiation, growth and unstable failure in a rectangular prismatic bar containing a circular void and a tilted circular edge crack. The bar is shown in Fig. 4, with length $L_0 = 800$ mm and cross-sectional dimensions $W_0 = D_0 = 80$ mm. The bar contains an edge crack of radius $a_0 = 15$ mm, which is tilted $\varphi_0 = 20^\circ$. In addition, a spherical void of diameter $d_s = 8$ mm exists in the plane of the crack. The void has been pre-charged with a hydrogen content of 1 wppm. Neumann-type boundary conditions $\boldsymbol{J} = \boldsymbol{0}$ are considered in all the outer boundaries. The in-plane position of the void is illustrated in Fig. 4, with $x_s = 10$ mm and $y_s = 20$ mm. The bar is simply supported at one end and subjected to tension at the other end by means of a prescribed displacement $\overline{u}$.

The void and crack are introduced as initial conditions in the phase field. The domain is meshed with quadratic tetrahedrons with a characteristic element size of $h_e = 1$ mm. We consider a high strength steel

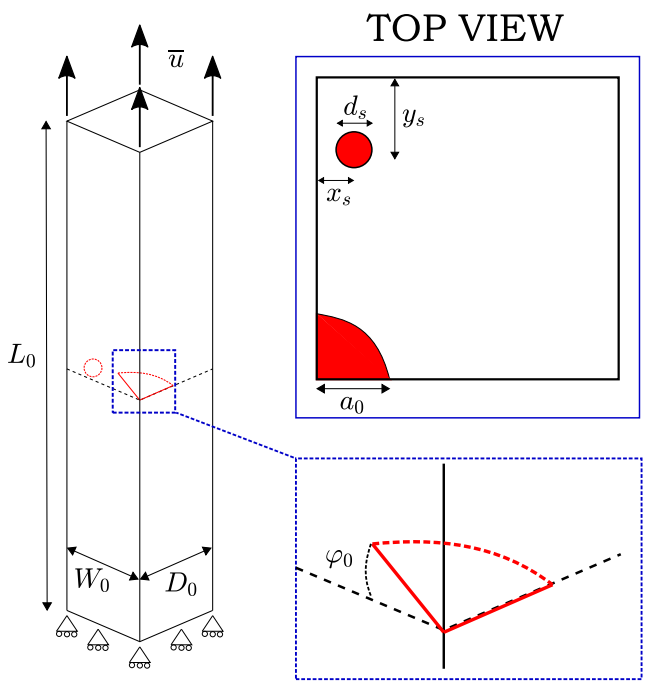

Fig. 4. Void-crack interaction in a 3D tensile bar: geometry and loading configuration.

with $E = 210$ GPa, $\nu = 0.3, G_c = 4.54$ kJ/m^2 and $\ell = 8$ mm. The phase field AT2 model is considered and the material is assumed to have a diffusion coefficient of $D = 0.0127$ mm^2/s. A small loading rate is applied, allowing for the hydrogen to re-distribute through the sample.

The results obtained are shown in Figs. 5 (side view) and 6 (top view). Cracking contours ($\phi > 0.95$) are shown for different levels of remote loading. Initially, the crack kinks towards a plane perpendicular to the applied load, but it preserves its bluntness - see Fig. 5(a)-(b). After the reorientation of the tilted crack, the interaction with the stress concentration of the void is sufficient for the crack to propagate in an unstable manner, as shown in Fig. 5(c) and 6(c)-(d). The stages of unstable crack growth, occurring almost instantaneously, can be captured with a staggered scheme and small time increments. As shown in Fig. 6 (c)-(d), the crack first interacts with the void and propagates up to the failure of the entire cross-section. The hydrogen in the void diffuses to embrittle, mainly, three regions: (i) the entire crack front, (ii) the region surrounding the void, due to the associated stress concentration, and (iii) the diffusion path between the void and crack tip. The accumulation of hydrogen in these regions facilitates the crack-void interaction, resulting in the cracking pattern observed.

4.3. Virtual experiments: design of screw anchors against brittle fracture

Our third case study models the failure of screw anchors in aggressive environments, mimicking the testing conditions of the ASTM E488/E488M standard [51]. The aim is to showcase the capabilities of the model in optimising experimental campaigns and certification, while addressing the phenomenon of bolt failure due to hydrogen ingress, a significant concern in offshore engineering [59].

Screw anchors for use in concrete are often made out of high-strength galvanized steel. The zinc coating provides excellent corrosion protection but it can potentially increase the risk of hydrogen embrittlement. If the coating is damaged, the corrosion potential can be lowered sufficiently for hydrogen evolution to occur even in the highly alkaline conditions observed in concrete. To simulate the brittle failure of screws exposed to hydrogen-containing environments, we choose to replicate the test provided in the ASTM E488/E488M standard [51] for assessing the susceptibility of screw anchors to hydrogen embrittlement. The setup for the test is illustrated in Fig. 7. The general approach for the standardised test is to pre-charge the anchor with hydrogen and then carry out a tensile test up to ultimate failure. The pre-charging occurs by exposing the sample, for an extended period of time, to a solution representative of the one found in concrete pores. The pre-charging is carried out with the anchor in tension and potentiostatic control of the potential. The applied potential is kept sufficiently low for hydrogen evolution to occur. To estimate the hydrogen content of the bolt we

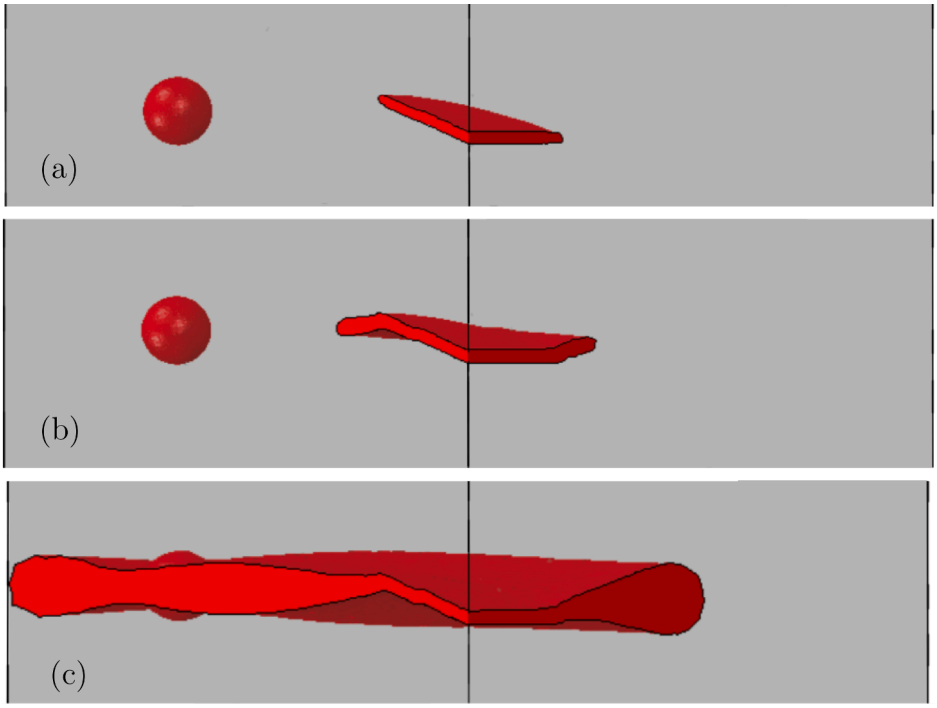

Fig. 5. Crack initiation and growth in a rectangular prismatic bar with multiple defects, side view. The bar is subjected to tension using a prescribed displacement of: (a) $\overline{u} = 0$ mm, (b) $\overline{u} = 6.53$ mm, (c) $\overline{u} = 6.57$ mm.

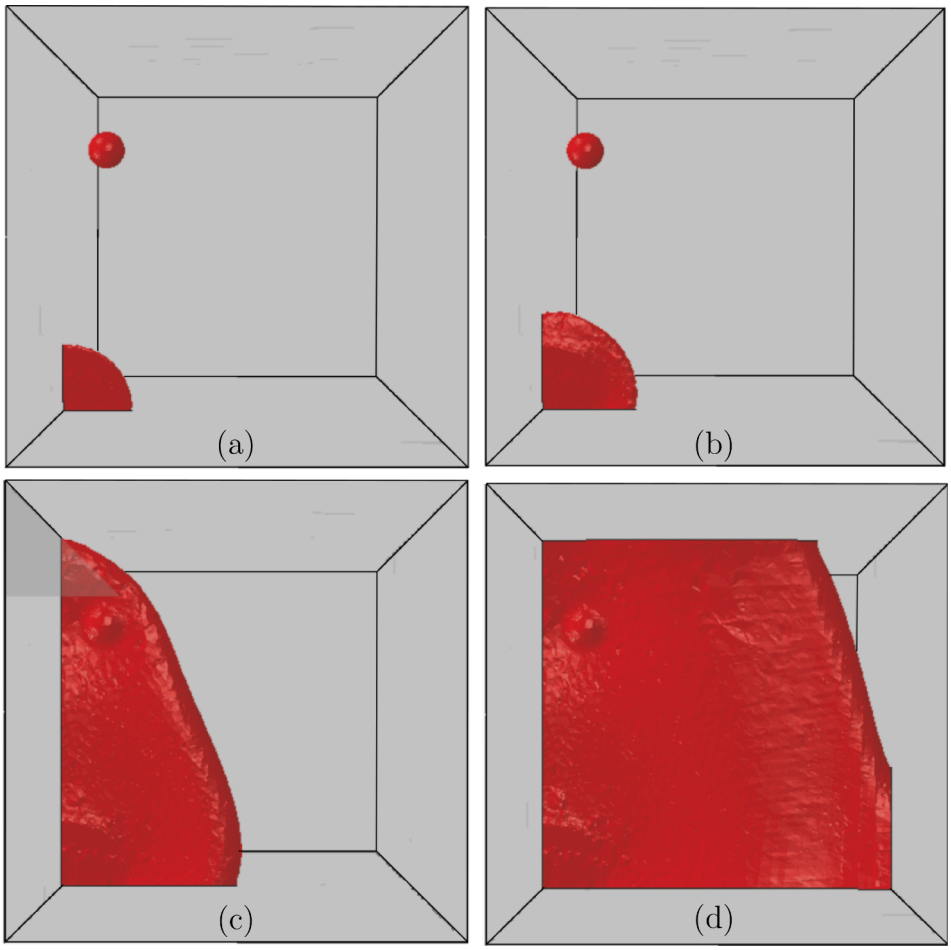

Fig. 6. Crack initiation and growth in a rectangular prismatic bar with multiple defects, top view. (a) Initial configuration, (b) initial crack kinking, and (c)-(d) stages of unstable crack propagation.

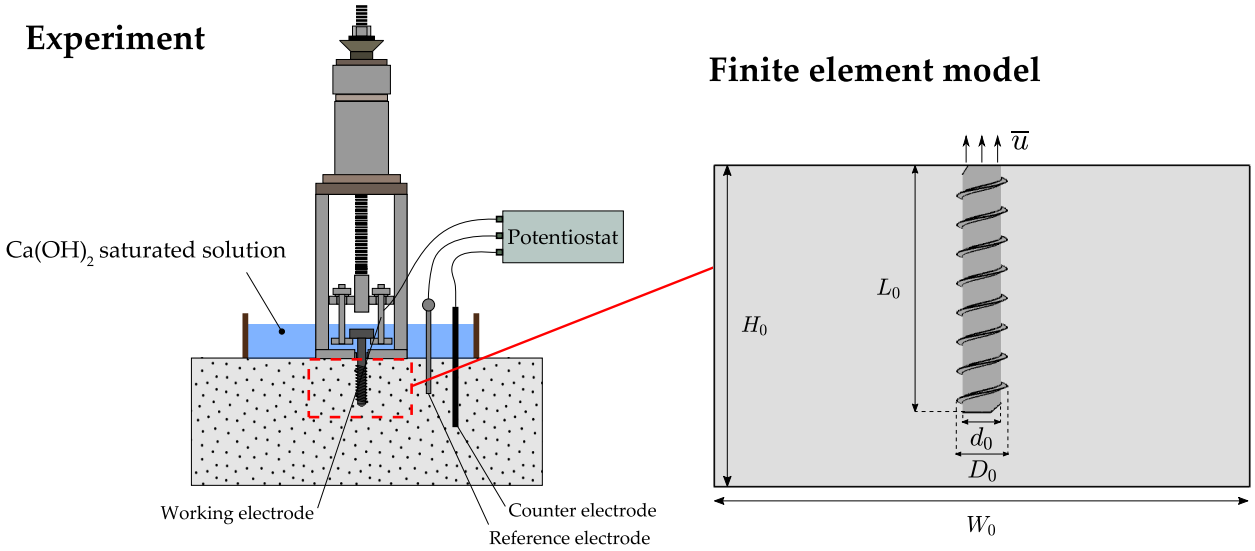

Fig. 7. Virtual Testing of screw anchors. Confined test setup and sketch of the finite element model.

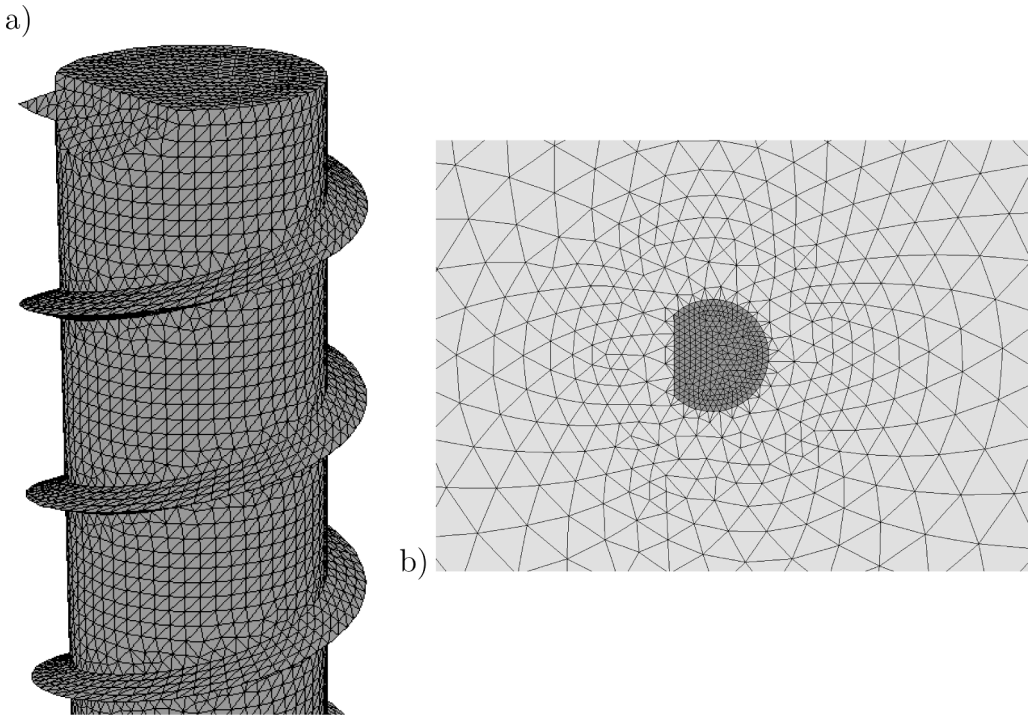

Fig. 8. Finite element mesh for the screw anchor test setup: a) mesh of the screw anchor; and, b) mesh of the concrete (light grey) around the screw anchor (dark grey), as seen from above.

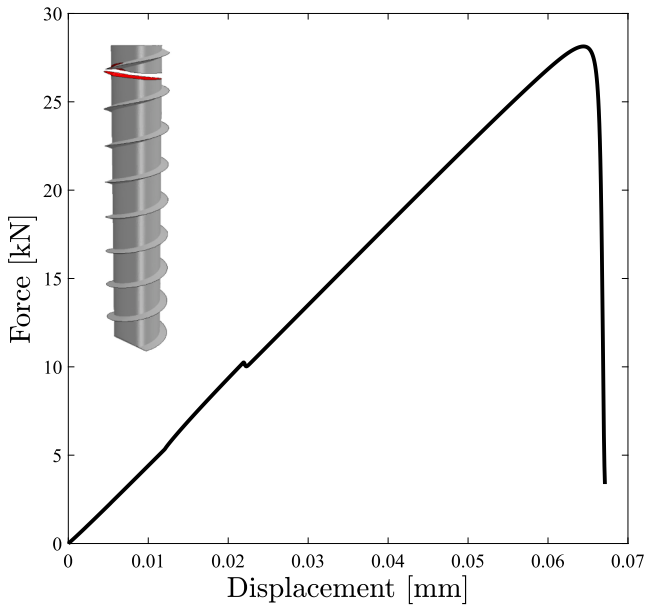

Fig. 9. Virtual Testing of screw anchors. Force versus displacement curve for the screw test.

consider the work by Recio *et al.* [60], where a similar pre-charging protocol was employed. Based on the results therein and the differences between protocols, the initial hydrogen concentration is expected to be equal to 2 wppm or higher. A magnitude of 2 wppm is assumed.

The modelling domain consists of a rectangular concrete slab and a steel screw anchor, as illustrated in Fig. 7. The concrete slab has height $H_0 = 76.2$ mm and the width in both directions is $W_0 = 127$ mm. The screw anchor has a length $L_0 = 58.4$ mm and a core diameter of $d_0 = 9.1$ mm. The outer diameter of the thread is $D_0 = 11.9$ mm. Only mechanical deformation is considered in the concrete slab, which is modelled as a linear elastic material, while the steel anchor uses the deformation-diffusion-damage formulation presented above. Contact between the thread surface of the screw anchor and the concrete is modelled including friction, with a coefficient of friction $\mu = 0.35$. Material constants for the concrete slab are $E_c = 23.6$ GPa and $\nu_c = 0.2$. For the steel screw, the material properties read: $E_s = 210$ GPa, $\nu_s = 0.3$ and $G_c = 64$ N/mm^2, corresponding to a plane strain fracture toughness of 121.5 MPa $\cdot$ m$^{1/2}$. The diffusion coefficient is assumed to be $D_s = 0.0127$ mm^2/s. The phase field length scale has been set to $\ell = 3.05$ mm, approximately five times the characteristic element length $h_e = 0.6$ mm. Both parts of the modeling domain are meshed using tetrahedral elements with quadratic shape functions. The mesh is illustrated in Fig. 8. The concrete domain is discretised with 117,456 elements while a total of 155,278 elements are used for the screw. As the problem considers crack initiation from a stress concentration, it is deemed suitable to adopt the AT1 phase field model [30]. The standard test method contains no specifications about the load rate, although it can be expected to have an influence on the result. In the model presented here, the screw anchor fractures after a loading period of 0.53 s. The load is applied under displacement control conditions.

Representative finite element results are shown in Figs. 9 and 10. The force versus displacement response is shown in Fig. 9; the force increases until it reaches a peak value of 27.88 kN, after which a significant drop is observed, indicative of unstable brittle fracture. The peak force corresponds to a nominal core stress of 429 MPa, which is less than the typical yield stress of the materials used in these applications. The broken state of the screw is shown in Fig. 10, where it can be seen that fracture occurs close to the head of the screw. A stress concentration is observed along the root of the thread, where crack initiation is observed - see Fig. 10a. The location of crack initiation agrees with expectations as the first

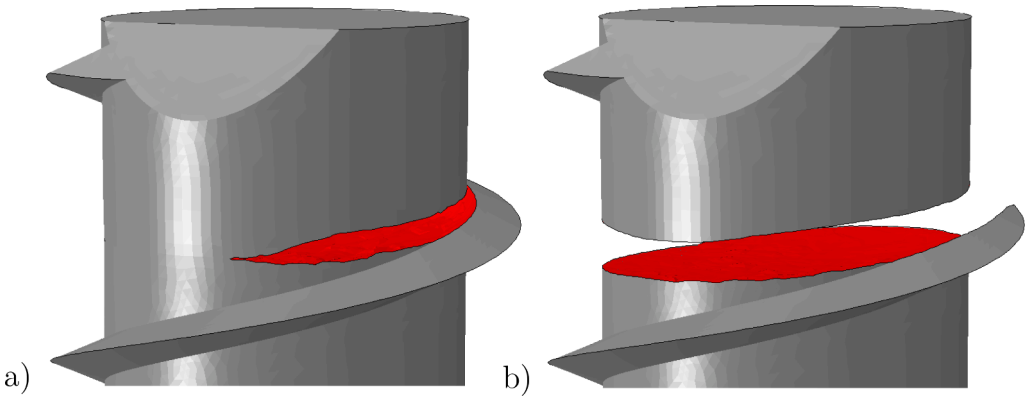

Fig. 10. Virtual Testing of screw anchors. Broken state of the screw anchor: a) areas with $\phi > 0.98$ removed, $\phi = 0.98$ shown in red, and b) $\phi > 0.96$ removed, $\phi = 0.96$ shown in red.

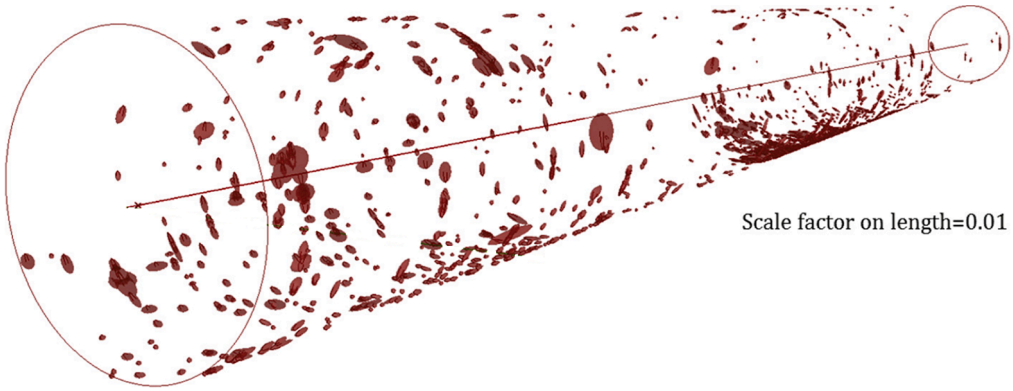

Fig. 11. Initial distribution of defects in a corroded pipeline, as measured by in-line inspection (ILI). Adapted from [26].

winding of the thread carries the highest load. The predictions of the proposed model indicate that a galvanized screw anchor of this type is susceptible to brittle fracture under hydrogen embrittlement if the steel is exposed to a concrete pore solution.

4.4. Coupling with NDE: Failure of a pipeline with internal defects

The final case study showcases how phase field methods can be coupled to non-destructive evaluation (NDE) to develop high-fidelity models for real-time assessment of critical infrastructure. This is exemplified with the modelling of the progressive failure of a pipeline with numerous internal defects. The structural integrity of pipelines subjected to aggressive environments is a major concern in the energy industry [61]. Corrosion damage nucleates pits that act as stress concentrators, attracting hydrogen that triggers early cracking. Thus, we consider the structural failure of a pipeline as a paradigmatic case study and show how our multi-physics model can predict cracking in large scale components as a function of the material properties, the environmental hydrogen concentration and the loading conditions. In addition, we aim at enabling a *Virtual Testing* paradigm by coupling the present phase field predictions with defect characterisation from NDE inspections. The distribution of defects in a pipeline is shown in Fig. 11, as measured from in-line inspection (ILI) and reported by Larrosa *et al.* [26]. A three-dimensional finite element model is developed based on this data.

A total of 1,750 defects were characterised by Larrosa *et al.* [26] in the pipeline shown in Fig. 11, of length 11 km, outer radius 162 mm, and thickness 40 mm. We mimic the outer radius and thickness of the pipeline but we restrict our attention to a critical span of 2 meters length, containing a total of 112 defects. Taking advantage of symmetry, only a quarter of the pipe cross-section is modelled. A uniform mesh of 129,600 20-node brick elements is employed, with the characteristic element length being equal to $h = 4$ mm. The internal pit defects are introduced by prescribing $\phi = 1$ as an initial condition. The defects are approximated as ellipsoids and a script is created to identify nodal sets based on the defect location, dimensions and rotations. The depths, lengths and widths of the defects are taken from a normal distribution that follows the mean and standard deviation reported from the in-line inspection (ILI) rendering. The defects are also subjected to a random rotation. Material properties are given by $E = 210$ GPa, $\nu = 0.3, \ell = 8$ mm, $D = 0.0127$ mm^2/s, and $G_c = 140$ kJ/m^2 (as estimated from a fracture toughness of $K_{Ic} = 180$ MPa$\sqrt{m}$). The phase field AT2 model is considered. We assume that the pipeline has been pre-charged with an initial hydrogen concentration of $c_0 = 1$ wppm and is continuously exposed to the same environment, which corresponds to a 3% NaCl aqueous solution. We note that a fixed concentration is prescribed for simplicity but a constant chemical potential should instead be used as boundary condition when aiming at quantitative results [62,32,63]. Mimicking in-service loading conditions in a riser, we subject the pipeline to an internal pressure of 152 MPa and to axial tension, with a remote stress of 105 MPa. The internal pressure is increased linearly in time while the remote stress is held constant throughout the analysis. The evolution of defects and cracks predicted is shown in Fig. 12 by plotting the completely cracked regions ($\phi > 0.8$).

As shown in Figs. 12 and 13, finite element predictions reveal that damage initiates at a few critical defects where the local stress concentrations increase the local concentration of hydrogen, causing the defects to eventually grow and merge. The coalescence of defects rapidly propagates the damage, leading to a complete failure of the cross-section and the appearance of axial cracks.

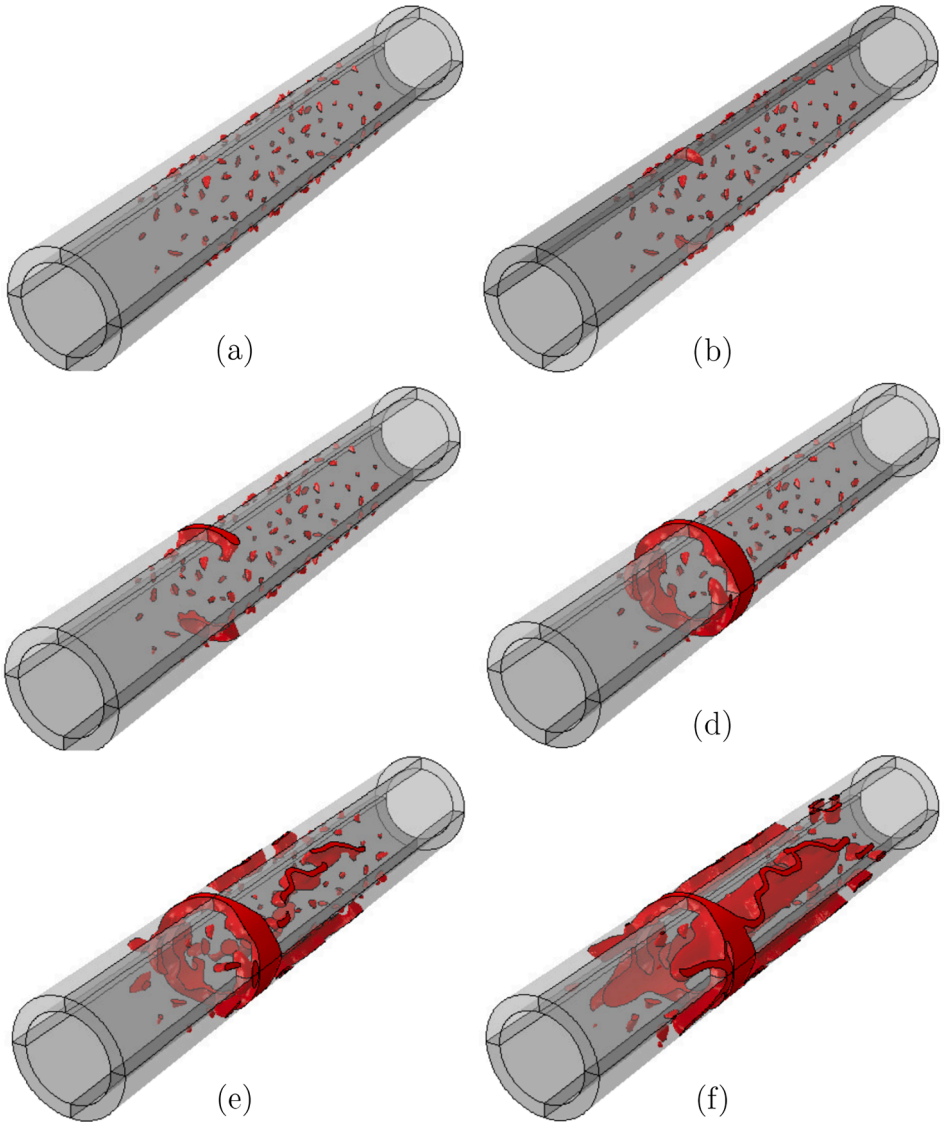

Fig. 12. Crack initiation and growth predicted in a pipeline with an initial distribution of defects. The figure shows a transparent cross-section of the pipeline with $\phi = 0.8$ contours. The pipe is subjected to constant tension of 105 MPa, although this load is no longer carried when the crack severs the pipe in (d). The internal pressure in the pipe is (a) 0 MPa, (b) 19.6 MPa, (c) 22.1 MPa, (d) 23.8 MPa, (e) 75.7 MPa, and (f) 85 MPa.

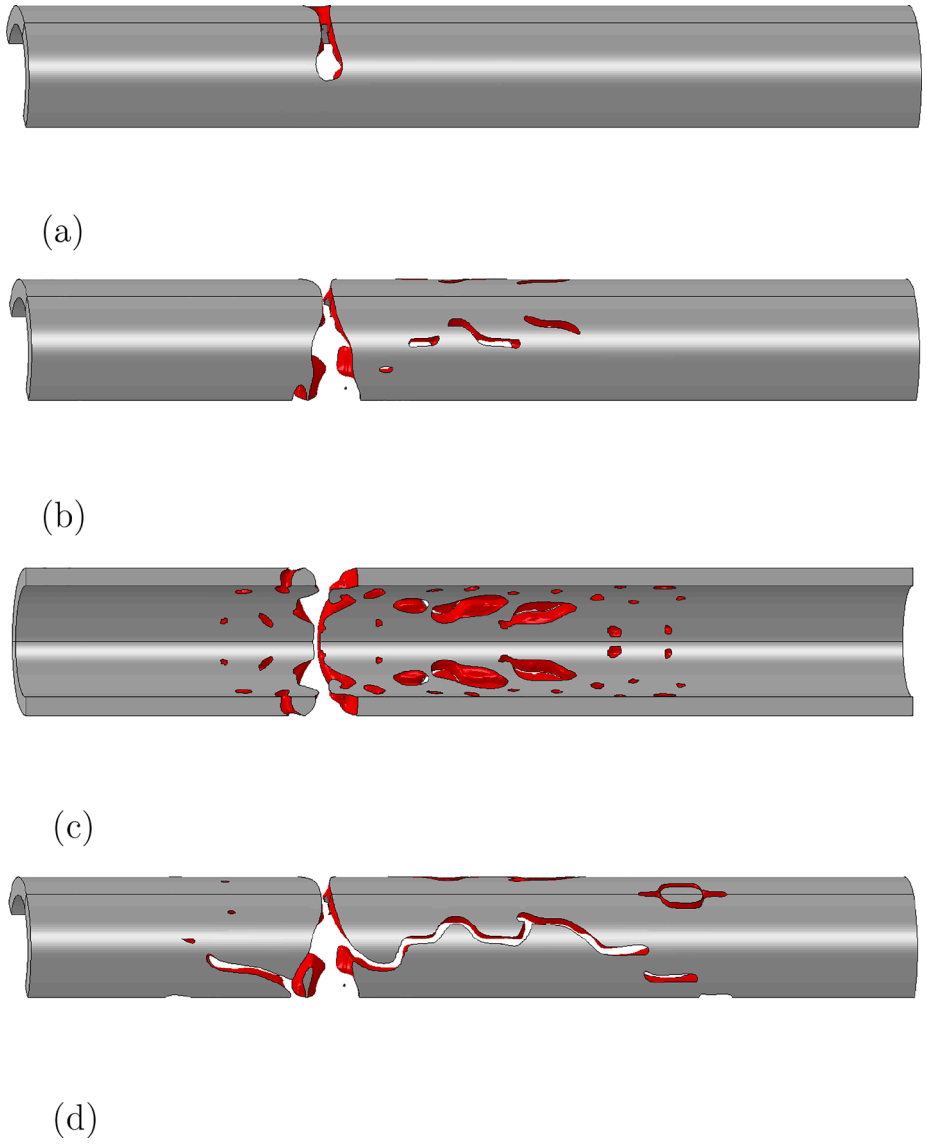

Fig. 13. Crack initiation and growth predicted in a pipeline with an initial distribution of defects. Cracks are visualized by removing areas with $\phi > 0.8$. Each of the subfigures corresponds to an internal pressure of: (a) 22.95 MPa, (b) 72.25 MPa, (c) 74.8 MPa, and (d) 85 MPa.

5. Conclusions

We have presented a generalised phase field formulation for predicting hydrogen assisted fracture. The coupled deformation-diffusion-damage framework developed considers, for the first time, both AT1 and AT2 phase field models, the role of inertia, and a 3D finite element implementation. By addressing four case studies of particular interest, the capabilities of phase field-based models in opening new horizons in structural integrity assessment are showcased. Specifically, we demonstrate that the model can: (i) capture the complex cracking patterns resulting from dynamic loading of an embrittled material, (ii) predict advanced fracture phenomena such as crack kinking, the interaction between neighboring defects and unstable fracture, (iii) conduct virtual experiments involving contact, friction and multiple components, and (iv) simulate in-service conditions, including the current damage state of large scale engineering components. One notable strength of the framework is the possibility of introducing existing defects by assigning an initial value to the phase field variable, without the need of *ad hoc* and complicated finite element geometries/meshing. This enables a smooth coupling with inspection data and the development of so-called *Digital Twins* of critical structural elements. The results suggest that multi-physics phase field-based simulations can be key in preventing catastrophic failures, enabling virtual fitness-for-service assessment and optimising material selection, structural design and inspection planning.

CRediT authorship contribution statement

Philip K. Kristensen: Conceptualization, Data curation, Formal analysis, Investigation, Methodology, Validation, Visualization, Writing - review & editing. **Christian F. Niordson:** Conceptualization, Writing - review & editing. **Emilio Martínez-Pañeda:** Conceptualization, Investigation, Methodology, Validation, Visualization, Writing - original draft, Writing - review & editing.

Declaration of Competing Interest

The authors declare that they have no known competing financial interests or personal relationships that could have appeared to influence the work reported in this paper.

Acknowledgments

The authors gratefully acknowledge financial support from the Danish Hydrocarbon Research and Technology Centre (DHRTC). E. Martínez-Pañeda additionally acknowledges financial support from the EPSRC (grants EP/R010161/1 and EP/R017727/1) and from the Royal Commission for the 1851 Exhibition (RF496/2018).

References

[1] W.H. Johnson, On some remarkable changes produced in iron and steel by the action of hydrogen and acids, Proce. Roy. Soc. London 23 (1875) 168–179.
[2] R.P. Gangloff, Hydrogen-assisted Cracking, in: I. Milne, R. Ritchie, B. Karihaloo (Eds.), Comprehensive Structural Integrity, vol. 6, Elsevier Science, New York, NY, 2003, pp. 31–101.
[3] R. Fernández-Sousa, C. Betegón, E. Martínez-Pañeda, Analysis of the influence of microstructural traps on hydrogen assisted fatigue, Acta Mater. 199 (2020) 253–263.
[4] H.K. Birnbaum, P. Sofronis, Hydrogen-enhanced localized plasticity - a mechanism for hydrogen related fracture, Mater. Sci. Eng., A 176 (1994) 191–202.
[5] Z.D. Harris, S.K. Lawrence, D.L. Medlin, G. Guetard, J.T. Burns, B.P. Somerday, Elucidating the contribution of mobile hydrogen-deformation interactions to hydrogen-induced intergranular cracking in polycrystalline nickel, Acta Mater. 158 (2018) 180–192.
[6] E. Martínez-Pañeda, V.S. Deshpande, C.F. Niordson, N.A. Fleck, The role of plastic strain gradients in the crack growth resistance of metals, J. Mech. Phys. Solids 126 (2019) 136–150.
[7] S.S. Shishvan, G. Csányi, V.S. Deshpande, Hydrogen induced fast-fracture, J. Mech. Phys. Solids 134 (2020) 103740.
[8] R.P. Gangloff, B.P. Somerday, Gaseous Hydrogen Embrittlement of Materials in Energy Technologies, Woodhead Publishing Limited, Cambridge, 2012.
[9] M.B. Djukic, G.M. Bakic, V. Sijacki Zeravcic, A. Sedmak, B. Rajicic, The synergistic action and interplay of hydrogen embrittlement mechanisms in steels and iron: Localized plasticity and decohesion, Eng. Fract. Mech. 216 (2019) 106528.
[10] S. Serebrinsky, E.A. Carter, M. Ortiz, A quantum-mechanically informed continuum model of hydrogen embrittlement, J. Mech. Phys. Solids 52 (10) (2004) 2403–2430.
[11] P. Novak, R. Yuan, B.P. Somerday, P. Sofronis, R.O. Ritchie, A statistical, physical-based, micro-mechanical model of hydrogen-induced intergranular fracture in steel, J. Mech. Phys. Solids 58 (2) (2010) 206–226.
[12] E. Martínez-Pañeda, C.F. Niordson, R.P. Gangloff, Strain gradient plasticity-based modeling of hydrogen environment assisted cracking, Acta Mater. 117 (2016) 321–332.
[13] B. Bourdin, G.A. Francfort, J.-J. Marigo, Numerical experiments in revisited brittle fracture, J. Mech. Phys. Solids 48 (4) (2000) 797–826.
[14] E. Martínez-Pañeda, A. Golahmar, C.F. Niordson, A phase field formulation for hydrogen assisted cracking, Comput. Methods Appl. Mech. Eng. 342 (2018) 742–761.
[15] F.P. Duda, A. Ciarbonetti, S. Toro, A.E. Huespe, A phase-field model for solute-assisted brittle fracture in elastic-plastic solids, Int. J. Plast 102 (2018) 16–40.
[16] L. Anand, Y. Mao, B. Talamini, On modeling fracture of ferritic steels due to hydrogen embrittlement, J. Mech. Phys. Solids 122 (2019) 280–314.
[17] J.-Y. Wu, T.K. Mandal, V.P. Nguyen, A phase-field regularized cohesive zone model for hydrogen assisted cracking, Comput. Methods Appl. Mech. Eng. 358 (2020) 112614.
[18] E. Martínez-Pañeda, Z.D. Harris, S. Fuentes-Alonso, J.R. Scully, J.T. Burns, On the suitability of slow strain rate tensile testing for assessing hydrogen embrittlement susceptibility, Corros. Sci. 163 (2020) 108291.
[19] C. Huang, X. Gao, Phase field modeling of hydrogen embrittlement, Int. J. Hydrogen Energy 45 (38) (2020) 20053–20068.
[20] P.K. Kristensen, C.F. Niordson, E. Martínez-Pañeda, A phase field model for elastic-gradient-plastic solids undergoing hydrogen embrittlement, J. Mech. Phys. Solids 143 (2020) 104093.
[21] K. Pham, H. Amor, J.J. Marigo, C. Maurini, Gradient damage models and their use to approximate brittle fracture, Int. J. Damage Mech 20 (4) (2011) 618–652.
[22] L. Ambrosio, V.M. Tortorelli, Approximation of functionals depending on jumps by elliptic functionals via gamma-convergence, Commun. Pure Appl. Math. 43 (1990) (1991) 999–1036.
[23] H. Yu, J.S. Olsen, A. Alvaro, V. Olden, J. He, Z. Zhang, A uniform hydrogen degradation law for high strength steels, Eng. Fract. Mech. 157 (2016) 56–71.
[24] A. Díaz, J.M. Alegre, I.I. Cuesta, Numerical simulation of hydrogen embrittlement and local triaxiality effects in notched specimens, Theoret. Appl. Fract. Mech. 90 (2017) 294–302.
[25] S. del Busto, C. Betegón, E. Martínez-Pañeda, A cohesive zone framework for environmentally assisted fatigue, Eng. Fract. Mech. 185 (2017) 210–226.
[26] N.O. Larrosa, P. Lopez-Crespo, R.A. Ainsworth, An efficient procedure for reducing in-line-inspection datasets for structural integrity assessments, Theoret. Appl. Fract. Mech. 93 (2018) 79–87.
[27] G. Francfort, J.-J. Marigo, Revisiting brittle fracture as an energy minimization problem, J. Mech. Phys. Solids 46 (8) (1998) 1319–1342.
[28] M.J. Borden, C.V. Verhoosel, M.A. Scott, T.J.R. Hughes, C.M. Landis, A phase-field description of dynamic brittle fracture, Comput. Methods Appl. Mech. Eng. 217–220 (2012) 77–95.
[29] A. Griffith, The phenomena of rupture and flow in solids, Philosoph. Trans. A 221 (1920) 163–198.
[30] E. Tanné, T. Li, B. Bourdin, J.-J. Marigo, C. Maurini, Crack nucleation in variational phase-field models of brittle fracture, J. Mech. Phys. Solids 110 (2018) 80–99.
[31] W. Tan, E. Martínez-Pañeda, Phase field predictions of microscopic fracture and R-curve behaviour of fibre-reinforced composites, Compos. Sci. Technol. (2021) 108539.
[32] E. Martínez-Pañeda, S. del Busto, C.F. Niordson, C. Betegón, Strain gradient plasticity modeling of hydrogen diffusion to the crack tip, Int. J. Hydrogen Energy 41 (24) (2016) 10265–10274.
[33] E. Martínez-Pañeda, A. Díaz, L. Wright, A. Turnbull, Generalised boundary conditions for hydrogen transport at crack tips, Corros. Sci. 173 (2020) 108698.
[34] E. Martínez-Pañeda, N.A. Fleck, Mode I crack tip fields: Strain gradient plasticity theory versus J2 flow theory, Eur. J. Mech. A. Solids 75 (2019) 381–388.
[35] S. Fuentes-Alonso, E. Martínez-Pañeda, Fracture in distortion gradient plasticity, Int. J. Eng. Sci. 156 (2020) 103369.
[36] E. Martínez-Pañeda, C. Betegón, Modeling damage and fracture within strain-gradient plasticity, Int. J. Solids Struct. 59 (2015) 208–215.
[37] E. Martínez-Pañeda, S. Natarajan, S. Bordas, Gradient plasticity crack tip characterization by means of the extended finite element method, Comput. Mech. 59 (2017) 831–842.
[38] J.P. Hirth, Effects of hydrogen on the properties of iron and steel, Metall. Trans. A 11 (6) (1980) 861–890.
[39] A. Braides, Approximation of Free-discontinuity Problems, lecture no ed., Springer Science & Business Media, 1998.
[40] H.K.D.H. Bhadeshia, Prevention of Hydrogen Embrittlement in Steels, ISIJ Int. 56 (1) (2016) 24–36.
[41] A. Alvaro, I. Thue Jensen, N. Kheradmand, O.M. Løvvik, V. Olden, Hydrogen embrittlement in nickel, visited by first principles modeling, cohesive zone simulation and nanomechanical testing, Int. J. Hydrogen Energy 40 (47) (2015) 16892–16900.
[42] D.E. Jiang, E.A. Carter, Diffusion of interstitial hydrogen into and through bcc Fe from first principles, Phys. Rev. B - Condensed Matter Mater. Phys. 70 (6) (2004) 1–9.
[43] C. Cui, R. Ma, E. Martínez-Pañeda, A phase field formulation for dissolution-driven stress corrosion cracking, J. Mech. Phys. Solids (2021), https://doi.org/10.1016/j.jmps.2020.104254 (in press).
[44] G. Papazafeiropoulos, M. Muñiz-Calvente, E. Martínez-Pañeda, Abaqus2Matlab: A suitable tool for finite element post-processing, Adv. Eng. Softw. 105 (2017) 9–16.
[45] H. Amor, J.J. Marigo, C. Maurini, Regularized formulation of the variational brittle fracture with unilateral contact: Numerical experiments, J. Mech. Phys. Solids 57 (8) (2009) 1209–1229.
[46] M. Ambati, T. Gerasimov, L. De Lorenzis, Phase-field modeling of ductile fracture, Comput. Mech. 55 (5) (2015) 1017–1040.
[47] J.Y. Wu, Y. Huang, Comprehensive implementations of phase-field damage models in Abaqus, Theoret. Appl. Fract. Mech. 106 (2020) 102440.
[48] S. Hirshikesh, R.K. Natarajan, E. Annabattula, Martínez-Pañeda, Phase field modelling of crack propagation in functionally graded materials, Compos. Part B: Eng. 169 (2019) 239–248.
[49] M. Simoes, E. Martínez-Pañeda, Phase field modelling of fracture and fatigue in Shape Memory Alloys, Comput. Methods Appl. Mech. Eng. 373 (2021) 113504.
[50] C. Miehe, F. Welshinger, M. Hofacker, Thermodynamically consistent phase-field models of fracture: Variational principles and multi-field FE implementations, Int. J. Numer. Meth. Eng. 83 (2010) 1273–1311.
[51] ASTM E488/E488M Standard Test Methods for Strength of Anchors in Concrete Elements, ASTM International, West Conshohocken, PA.
[52] J.H. Song, H. Wang, T. Belytschko, A comparative study on finite element methods for dynamic fracture, Comput. Mech. 42 (2) (2008) 239–250.
[53] S. Zhou, T. Rabczuk, X. Zhuang, Phase field modeling of quasi-static and dynamic crack propagation: COMSOL implementation and case studies, Adv. Eng. Softw. 122 (2018) 31–49.
[54] M. Ramulu, A.S. Kobayashi, Mechanics of crack curving and branching – a dynamic fracture analysis, Int. J. Fract. 27 (3–4) (1985) 187–201.
[55] R.P. Jewett, R.J. Walter, W.T. Chandler, R.P. Frohmberg, Hydrogen environment embrittlement of metals, Tech. Rep., NASA CR-2163, 1973.
[56] B. Lou, B.L. Averbach, Effects of heat treatment on fracture toughness and fatigue crack growth rates in 440C and Bg42 steels, Metall. Trans. A, Phys. Metall. Mater. Sci. 14 A (9) (1983) 1899–1906.
[57] J.-Y. Wu, Y. Huang, V.P. Nguyen, On the BFGS monolithic algorithm for the unified phase field damage theory, Comput. Methods Appl. Mech. Eng. 360 (2020) 112704.
[58] P.K. Kristensen, E. Martínez-Pañeda, Phase field fracture modelling using quasi-Newton methods and a new adaptive step scheme, Theoret. Appl. Fract. Mech. 107 (2020) 102446.
[59] L.H. Wolfe, C.C. Burnette, M.W. Joosten, Hydrogen Embrittlement of Cathodically Protected Subsea Bolting Alloys, Tech. Rep., Society of Petroleum Engineers, 1990.
[60] F.J. Recio, M.C. Alonso, L. Gaillet, M. Sánchez, Hydrogen embrittlement risk of high strength galvanized steel in contact with alkaline media, Corros. Sci. 53 (9) (2011) 2853–2860.
[61] R. Heidersbach, Metallurgy and Corrosion Control in Oil and Gas Production, second ed., John Wiley & Sons, 2018.
[62] C.V. Di Leo, L. Anand, Hydrogen in metals: A coupled theory for species diffusion and large elastic-plastic deformations, Int. J. Plast 43 (2013) 42–69.
[63] A. Díaz, J.M. Alegre, I.I. Cuesta, Coupled hydrogen diffusion simulation using a heat transfer analogy, Int. J. Mech. Sci. 115–116 (2016) 360–369.

[P5]

Kristensen, Philip K., Niordson, Christian F., Martínez-Pañeda, Emilio. A phase field model for elastic-gradient-plastic solids undergoing hydrogen embrittlement. Journal of the Mechanics and Physics of Solids 2020. 143. 104093.

Journal of the Mechanics and Physics of Solids 143 (2020) 104093

Contents lists available at ScienceDirect

Journal of the Mechanics and Physics of Solids

journal homepage: www.elsevier.com/locate/jmps

A phase field model for elastic-gradient-plastic solids undergoing hydrogen embrittlement

Philip K. Kristensen[a], Christian F. Niordson[a], Emilio Martínez-Pañeda[b,*]

[a] Department of Mechanical Engineering, Technical University of Denmark, DK-2800 Kgs. Lyngby, Denmark
[b] Department of Civil and Environmental Engineering, Imperial College London, London SW7 2AZ, UK

ARTICLE INFO

Article history:
Received 20 May 2020
Revised 25 June 2020
Accepted 12 July 2020
Available online 13 July 2020

Keywords:
Phase field fracture
Strain gradient plasticity
Hydrogen embrittlement
Fracture
Stress-assisted diffusion

ABSTRACT

We present a gradient-based theoretical framework for predicting hydrogen assisted fracture in elastic-plastic solids. The novelty of the model lies in the combination of: (i) stress-assisted diffusion of solute species, (ii) strain gradient plasticity, and (iii) a hydrogen-sensitive phase field fracture formulation, inspired by first principles calculations. The theoretical model is numerically implemented using a mixed finite element formulation and several boundary value problems are addressed to gain physical insight and showcase model predictions. The results reveal the critical role of plastic strain gradients in rationalising decohesion-based arguments and capturing the transition to brittle fracture observed in hydrogen-rich environments. Large crack tip stresses are predicted, which in turn raise the hydrogen concentration and reduce the fracture energy. The computation of the steady state fracture toughness as a function of the cohesive strength shows that cleavage fracture can be predicted in otherwise ductile metals using sensible values for the material parameters and the hydrogen concentration. In addition, we compute crack growth resistance curves in a wide variety of scenarios and demonstrate that the model can appropriately capture the sensitivity to: the plastic length scales, the fracture length scale, the loading rate and the hydrogen concentration. Model predictions are also compared with fracture experiments on a modern ultra-high strength steel, AerMet100. A promising agreement is observed with experimental measurements of threshold stress intensity factor K_{th} over a wide range of applied potentials.

© 2020 Elsevier Ltd. All rights reserved.

1. Introduction

Variational phase field models for fracture are receiving much attention due to their modeling capabilities (see Wu et al., 2020b for a review). The phase field framework enables predicting advanced fracture features without remeshing, such as crack nucleation at arbitrary sites, crack growth along complex trajectories, and branching and coalescence of multiple cracks (Borden et al., 2012; McAuliffe and Waisman, 2016; Kristensen and Martínez-Pañeda, 2020). These predictions are based on the energy balance first proposed by Griffith (1920), with fracture occurring when the energy release rate of system reaches a critical value, G_c. In addition, both the discrete crack phenomenon and damage, in a continuum sense, can be captured in the phase field framework (Francfort and Marigo, 1998; Pham et al., 2011). Since the pioneering numerical experiments by Bourdin et al. (2000), phase field fracture models have gained increased interest. Recent applications include hydraulic

* Corresponding author.
E-mail address: e.martinez-paneda@imperial.ac.uk (E. Martínez-Pañeda).

https://doi.org/10.1016/j.jmps.2020.104093
0022-5096/© 2020 Elsevier Ltd. All rights reserved.

fracturing (Mikelic et al., 2015; Cajuhi et al., 2018), ductile damage (Borden et al., 2016; Alessi et al., 2018), lithium-ion batteries (Miehe et al., 2016b; Zhao et al., 2016), composites delamination (Carollo et al., 2017; Quintanas-Corominas et al., 2019), rock fracture (Zhou et al., 2018) and functionally graded materials (Hirshikesh et al., 2019), *inter alia*.

Recently, the success of phase field fracture methods has also been extended to model the phenomenon of hydrogen embrittlement (Duda et al., 2018; Martínez-Pañeda et al., 2018; Anand et al., 2019; Wu et al., 2020a). Hydrogen severely degrades the ductility and the fracture resistance of metals, with the fracture toughness of modern steels decreasing by up to 90% (Gangloff, 2003b). The problem is now pervasive in the transport, energy, construction and defence sectors due to the ubiquity of hydrogen and the higher susceptibility of high strength alloys (Gangloff and Somerday, 2012). Hydrogen atoms enter the material, diffuse through the crystal lattice and are attracted to regions of high hydrostatic stress, where damage occurs through mechanisms that are still being debated (Robertson et al., 2015; Harris et al., 2018; Lynch, 2019; Tehranchi and Curtin, 2019; Yu et al., 2019; Shishvan et al., 2020). By accounting for the degradation of the fracture energy with hydrogen content, multi-physics phase field fracture models capture the trends shown in the experiments (see, e.g., Martínez-Pañeda et al., 2020), while establishing a computational framework capable of dealing with the complex scenarios relevant to engineering practice. Phase field models are bringing a paradigm change to the hydrogen assisted cracking community, where modeling efforts were focused on discrete methods. Cohesive zone models have particularly enjoyed great popularity and have proven capable of capturing the strength degradation with increasing hydrogen content (Serebrinsky et al., 2004; Scheider et al., 2008; Moriconi et al., 2014; del Busto et al., 2017; Yu et al., 2017). However, discrete methods are limited when dealing with complex fracture conditions. Moreover, independently of the numerical methodology employed, conventional continuum models fail to resolve the critical length scale of hydrogen assisted fracture. Cracking occurs very close to the crack tip, at 1 μm or less (Gangloff, 2003a), where dislocation-based hardening governs material behavior. Large gradients of plastic strain are present within microns ahead of the crack tip, requiring a significant storage of *geometrically necessary* dislocations (GNDs) to accommodate lattice curvature (Ashby, 1970; Martínez-Pañeda and Betegón, 2015). The increased dislocation density associated with large gradients of plastic deformation promotes strain hardening and leads to crack tip stresses that are much larger than those predicted by conventional plasticity. The flow strength elevation associated with plastic strain gradients has been quantified in a wide range of experiments, from wire torsion (Fleck et al., 1994) to indentation (Nix and Gao, 1998); see (Voyiadjis and Song, 2019) for a review. Continuum models can be enriched to capture the local strengthening observed when the macroscopic strain field varies over microns. In this regard, the development of phenomenological strain gradient plasticity (SGP) theories has received particular attention (Dillon and Kratochvil, 1970; Gao et al., 1999; Fleck and Hutchinson, 2001; Anand et al., 2005;). SGP models have been used to investigate the influence of plastic strain gradients ahead of stationary and propagating cracks (Wei and Hutchinson, 1997; Komaragiri et al., 2008; Martínez-Pañeda and Niordson, 2016; Seiler et al., 2016). Predictions show notable strain gradient hardening, with crack tip stresses being substantially higher that those predicted by conventional plasticity. A similar level of local crack tip strengthening to that predicted by SGP is also found in discrete dislocation dynamics simulations (Balint et al., 2005; Chakravarthy and Curtin, 2010). The impact of this stress elevation on the understanding and modeling of hydrogen embrittlement is twofold. First, given the dependence of the hydrogen content on the hydrostatic stress, a high hydrogen concentration is attained close to the crack tip surface, in agreement with neutron activation and SIMS measurements (Mao and Li, 1998; Gerberich, 2012). Secondly, large crack tip tensile stresses and hydrogen concentrations rationalise decohesion-based mechanisms on high strength alloys (Martínez-Pañeda et al., 2016b). However, a continuum modeling framework capable of explicitly predicting cracking while accounting for the dislocation hardening mechanisms governing crack tip deformation has not been presented yet.

In this work, we aim at presenting a computationally compelling framework for modeling fracture in embrittled alloys, which is informed by atomistic and micromechanical considerations. The model builds upon: (i) higher order strain gradient plasticity (Gudmundson, 2004; Fleck and Willis, 2009), to accurately characterise crack tip stresses; (ii) a coupled mechanical and hydrogen diffusion response, driven by chemical potential gradients (Sofronis and McMeeking, 1989; Díaz et al., 2016); (iii) a phase field description of fracture (Miehe et al., 2010); and (iv) a hydrogen-dependent fracture energy degradation law, grounded on first principles calculations (Jiang and Carter, 2004). We demonstrate the potential of the proposed modeling framework in (1) providing relevant physical insight, by predicting the ductile-to-brittle transition observed when incorporating hydrogen, and (2) quantitatively capturing experimental measurements across a wide range of potentials. The remainder of this manuscript is organized as follows. The theoretical framework is presented in Section 2. The finite element implementation is briefly described in Section 3, with further details provided in Appendix A. Representative results are shown in Section 4. First, we aim at gaining physical insight into model predictions by computing crack tip stresses and crack growth resistance curves for a wide range of scenarios. Secondly, stress intensity factor thresholds are predicted as a function of the applied potential for AerMet100, so as to benchmark the capabilities of the model in quantitatively reproducing experiments. Finally, concluding remarks are given in Section 5.

Notation. We use lightface italic letters for scalars, e.g. ϕ, upright bold letters for vectors, e.g. $\mathbf{u}$, and bold italic letters, such as $\boldsymbol{\sigma}$, for second and higher order tensors. Inner products are denoted by a number of vertically stacked dots, corresponding to the number of indices over which summation takes place, such that $\boldsymbol{\sigma} : \boldsymbol{\varepsilon} = \sigma_{ij}\varepsilon_{ij}$, with indices referring to a Cartesian coordinate system. The full inner product of a tensor with itself is denoted $|\boldsymbol{\tau}|^2 = \boldsymbol{\tau} \vdots \boldsymbol{\tau} = \tau_{ijk}\tau_{ijk}$. The gradient and the Laplacian are respectively denoted by $\nabla \mathbf{u} = u_{i,j}$ and $\Delta\phi = \phi_{,ii}$. Finally, divergence is denoted by $\nabla \cdot \boldsymbol{\sigma} = \sigma_{ij,j}$, the

trace of a second order tensor is written as $\mathrm{tr}\,\boldsymbol{\varepsilon} = \varepsilon_{ii}$, and the deviatoric part of a tensor is written as $\boldsymbol{\sigma}' = \sigma_{ij} - \delta_{ij}\sigma_{kk}$, with δ_{ij} denoting the Kronecker delta.

2. Theory

In this section, we formulate our theory, which couples deformation, damage and hydrogen transport in elastic-plastic bodies. The theory refers to the response of a solid occupying an arbitrary domain $\Omega \subset \mathbb{R}^n$ ($n \in [1, 2, 3]$), with external boundary $\partial\Omega \subset \mathbb{R}^{n-1}$, on which the outwards unit normal is denoted as $\mathbf{n}$.

2.1. Kinematics

The primal kinematic variables of the model are the displacement field $\mathbf{u}$, the plastic strain tensor $\boldsymbol{\varepsilon}^p$, the damage phase field ϕ, and the hydrogen concentration C. We restrict our attention to small strains and isothermal conditions. Accordingly, the strain tensor $\boldsymbol{\varepsilon}$ is given by

$$\boldsymbol{\varepsilon} = \frac{1}{2}\left(\nabla\mathbf{u}^T + \nabla\mathbf{u}\right), \tag{1}$$

and we adopt the standard partition of strains into elastic and plastic components: $\boldsymbol{\varepsilon} = \boldsymbol{\varepsilon}^e + \boldsymbol{\varepsilon}^p$.

Regarding fracture, a smooth continuous scalar function, $\phi \in [0; 1]$, is introduced, which describes the degree of damage in a given material point in Ω. This function will be referred to as the *phase field*. The phase field takes the value 0 when the material is intact and 1 when the material is fully broken. Since ϕ is smooth and continuous, discrete cracks are represented in a diffuse fashion. The smearing of cracks is controlled by a phase field length scale ℓ. The purpose of this diffuse representation is to introduce the following approximation of the fracture energy over a discontinuous surface Γ:

$$\Psi^s = \int_\Gamma G_c \,\mathrm{d}S \approx \int_\Omega G_c \gamma(\phi, \nabla\phi)\,\mathrm{d}V, \qquad \text{for } \ell \to 0, \tag{2}$$

where γ is the crack surface density functional and G_c is the critical energy release rate (Griffith, 1920; Irwin, 1956). This approximation circumvents the need to track discrete crack surfaces, which is a major complication in numerical fracture models.

Regarding the diffusion of solute species. The concentration of hydrogen in a material point in Ω is given by the continuous smooth scalar function C. Due to conservation of mass, the rate of change in time of the hydrogen concentration $\dot{C} = dC/dt$ is equal to the concentration flux $\mathbf{J}\cdot\mathbf{n} = -\rho$ through the boundary $\partial\Omega$:

$$\int_\Omega \dot{C}\,\mathrm{d}V + \int_{\partial\Omega} \mathbf{J}\cdot\mathbf{n}\,\mathrm{d}S = 0, \tag{3}$$

with ρ denoting the inwards boundary flux. Alternatively, since the above must hold for any volume and by use of Gauss' divergence theorem, Eq. (3) can be formulated in a point-wise manner as:

$$\dot{C} + \nabla\cdot\mathbf{J} = 0. \tag{4}$$

The diffusion of solute species is driven by the chemical potential μ, which is also a smooth scalar function in Ω. The flux $\mathbf{J}$ is related to the chemical potential μ through a linear Onsager relation (Kirchheim, 2004)

$$\mathbf{J} = -\frac{DC}{RT}\nabla\mu, \tag{5}$$

where D is the diffusion coefficient of the material, R is the gas constant and T is the absolute temperature.

2.2. Principle of virtual work. Balance of forces

The balance equations for the coupled system are now derived using the principle of virtual work. Consider the four-field boundary value problem outlined in Fig. 1. The Cauchy stress $\boldsymbol{\sigma}$ is introduced, which is work conjugate to the elastic strains $\boldsymbol{\varepsilon}^e$. Correspondingly, for an outwards unit normal $\mathbf{n}$ on the boundary $\partial\Omega$ of the solid, a traction $\mathbf{T}$ is defined, which is work conjugate to the displacements $\mathbf{u}$. The plastic response is given by the so-called micro-stress tensor $\boldsymbol{q}$, work conjugate to the plastic strain $\boldsymbol{\varepsilon}^p$, and the higher order stress tensor $\boldsymbol{\tau}$, work conjugate to the plastic strain gradient $\nabla\boldsymbol{\varepsilon}^p$. A higher order traction $\boldsymbol{t}$ is also introduced on the boundary of the solid as work conjugate to the plastic strains. Regarding damage, we introduce a scalar stress-like quantity ω, which is work conjugate to the phase field ϕ, and a phase field micro-stress vector $\boldsymbol{\xi}$ that is work conjugate to the gradient of the phase field $\nabla\phi$. The phase field is assumed to be driven by the displacement problem alone. As a result, no external traction is associated with ϕ. Lastly, a boundary flux of hydrogen ρ is defined as work conjugate of the chemical potential in the diffusion problem. Accordingly, in the absence of body forces, the external virtual work is given by:

$$\delta W_{ext} = \int_{\partial\Omega} \left\{\mathbf{T}\cdot\delta\mathbf{u} + \boldsymbol{t} : \delta\boldsymbol{\varepsilon}^p + \rho\,\delta\mu\right\}\mathrm{d}S, \tag{6}$$

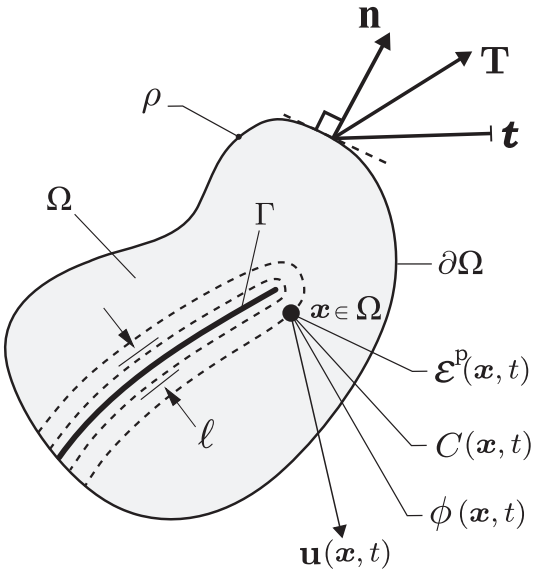

Fig. 1. Schematic representation of a solid body Ω, with a sharp crack Γ represented diffusively through the phase field.

where δ denotes a virtual quantity. The corresponding internal work reads:

$$\delta W_{int} = \int_{\Omega} \left\{ \boldsymbol{\sigma} : \delta\boldsymbol{\varepsilon} + \left(\boldsymbol{q} - \boldsymbol{\sigma}'\right) : \delta\boldsymbol{\varepsilon}^{p} + \boldsymbol{\tau} \vdots \delta\nabla\boldsymbol{\varepsilon}^{p} + \omega\delta\phi + \boldsymbol{\xi} \cdot \delta\nabla\phi + \dot{C}\delta\mu - \mathbf{J} \cdot \delta\nabla\mu \right\} \mathrm{d}V, \tag{7}$$

where $\boldsymbol{\sigma}'$ denotes the deviatoric part of $\boldsymbol{\sigma}$. For simplicity, the prime symbol is omitted from $\boldsymbol{q}$ and $\boldsymbol{\tau}$, as they can be inherently defined to be deviatoric. Eqs. (6) and (7) must hold for an arbitrary domain Ω and for any kinematically admissible variations of the virtual quantities. Thus, by making use of the fundamental lemma of calculus of variations, the local force balances are given by:

$$\begin{aligned} &\nabla \cdot \boldsymbol{\sigma} = 0 \\ &\nabla \cdot \boldsymbol{\tau} + \boldsymbol{\sigma}' - \boldsymbol{q} = 0 \\ &\nabla \cdot \boldsymbol{\xi} - \omega = 0 \\ &\dot{C} + \nabla \cdot \mathbf{J} = 0 \end{aligned} \quad \text{in } \Omega, \tag{8}$$

with natural boundary conditions:

$$\begin{aligned} &\boldsymbol{\sigma} \cdot \mathbf{n} = \mathbf{T} \\ &\boldsymbol{\tau} \cdot \mathbf{n} = \boldsymbol{t} \\ &\boldsymbol{\xi} \cdot \mathbf{n} = 0 \\ &-\mathbf{J} \cdot \mathbf{n} = \rho \end{aligned} \quad \text{on } \partial\Omega. \tag{9}$$

2.3. Energy imbalance

The first and second law of thermodynamics can be expressed through the Helmholtz free energy per unit volume $\Psi(\boldsymbol{\varepsilon}, \nabla\boldsymbol{\varepsilon}^{p}, \phi, \nabla\phi, C)$ and the external work W_{ext} in the Clausius-Duhem inequality:

$$\int_{\Omega} \dot{\Psi}\, \mathrm{d}V - \int_{\partial\Omega} \dot{W}_{ext}\, \mathrm{d}S \leq 0. \tag{10}$$

Inserting Eqs. (8)-(9) and applying the divergence theorem, the inequality may be restated as:

$$\int_{\Omega} \dot{\Psi}\, \mathrm{d}V - \int_{\Omega} \left\{ \boldsymbol{\sigma} : \nabla\dot{\mathbf{u}} + \left(\boldsymbol{q} - \boldsymbol{\sigma}'\right) : \dot{\boldsymbol{\varepsilon}}^{p} + \boldsymbol{\tau} \vdots \nabla\dot{\boldsymbol{\varepsilon}}^{p} + \omega\dot{\phi} + \boldsymbol{\xi} \cdot \nabla\dot{\phi} + \dot{C}\,\dot{\mu} - \mathbf{J} \cdot \nabla\dot{\mu} \right\} \mathrm{d}V \leq 0. \tag{11}$$

Since the above must hold for any volume Ω, it follows that it must also hold in a local fashion, such that:

$$\begin{aligned} &\left(\boldsymbol{\sigma} - \frac{\partial\Psi}{\partial\boldsymbol{\varepsilon}^{e}}\right) : \dot{\boldsymbol{\varepsilon}}^{e} + \left(\boldsymbol{q} - \frac{\partial\Psi}{\partial\boldsymbol{\varepsilon}^{p}}\right) : \dot{\boldsymbol{\varepsilon}}^{p} + \left(\boldsymbol{\tau} - \frac{\partial\Psi}{\partial\nabla\boldsymbol{\varepsilon}^{p}}\right) \vdots \nabla\dot{\boldsymbol{\varepsilon}}^{p} + \left(\omega - \frac{\partial\Psi}{\partial\phi}\right)\dot{\phi} \\ &\qquad + \left(\boldsymbol{\xi} - \frac{\partial\Psi}{\partial\nabla\phi}\right) \cdot \nabla\dot{\phi} + \left[\left(\mu - \frac{\partial\Psi}{\partial C}\right)\dot{C} - \mathbf{J} \cdot \nabla\mu\right] \geq 0. \end{aligned} \tag{12}$$

To satisfy this inequality, a free energy function Ψ is proposed, which is composed by the chemo-elastic energy stored in the bulk $\Psi^{e}(\boldsymbol{\varepsilon}^{e}, C, \phi)$, the plastic defect energy $\Psi^{p}(\nabla\boldsymbol{\varepsilon}^{p})$, the crack surface energy $\Psi^{s}(\phi, \nabla\phi, C)$, and the chemical free energy

$\Psi^c(C)$. Thus, consider a solid with bulk modulus K, shear modulus Q, number of lattice sites N (with a lattice site occupancy $\theta_L = C/N$), and partial molar volume of hydrogen $\overline{V}_H$. Denoting the reference chemical potential and hydrogen concentration as, respectively, μ^0 and C^0, the free energy is defined as:

$$\Psi = \underbrace{(1-\phi)^2\psi^e - K\overline{V}_H\left(C-C^0\right)\mathrm{tr}\boldsymbol{\varepsilon}^e}_{\Psi^e} + \underbrace{QL_E^2\nabla\boldsymbol{\varepsilon}^p}_{\Psi^p} + \underbrace{\frac{1}{2}G_c(C)\left(\frac{1}{\ell}\phi^2 + \ell|\nabla\phi|^2\right)}_{\Psi^s} + \underbrace{\mu^0 C + RTN[\theta_L\ln\theta_L + (1-\theta_L)\ln(1-\theta_L)]}_{\Psi^c}. \tag{13}$$

Here, ψ^e is the elastic strain energy density, which constitutes the driving force for fracture. The length scale L_E quantifies the degree to which the material exhibits energetic gradient hardening; for example, due to long range back-stresses associated with the stored elastic energy of GNDs. Also, we emphasize that the fracture resistance of the material, in terms of the critical energy release rate, is defined as a function of the hydrogen concentration $G_c(C)$.

2.4. Constitutive relations

Consistent with the free energy (13), we proceed now to develop a constitutive theory that couples the four primary kinematic variables of the problem.

2.4.1. Chemo-elasticity

Following a continuum damage mechanics approach, the phase field damage variable ϕ degrades the elastic stiffness of the solid. The degradation function is assumed to be of quadratic form:

$$g(\phi) = (1-\phi)^2, \tag{14}$$

and the elastic strain energy density ψ^e is defined as a function of the elastic strains $\boldsymbol{\varepsilon}^e$ and the isotropic elastic stiffness tensor $\boldsymbol{\mathcal{L}}_0$ in the usual manner:

$$\psi^e = \frac{1}{2}\boldsymbol{\varepsilon}^e : \boldsymbol{\mathcal{L}}_0 : \boldsymbol{\varepsilon}^e. \tag{15}$$

The Cauchy stress tensor $\boldsymbol{\sigma}$ follows immediately from the free energy definition (13) as:

$$\boldsymbol{\sigma} = \frac{\partial\Psi}{\partial\boldsymbol{\varepsilon}^e} = (1-\phi)^2\boldsymbol{\mathcal{L}}_0 : \boldsymbol{\varepsilon}^e - K\overline{V}_H(C-C_0)\boldsymbol{I} \tag{16}$$

where $\boldsymbol{I}$ denotes the identity matrix. The second term in Eq. (16), corresponding to the lattice dilation, is generally omitted in hydrogen embrittlement analyses due to its negligible influence (Hirth, 1980).

2.4.2. Strain gradient plasticity

We consider higher order strain gradient plasticity, incorporating both dissipative and energetic strain gradient contributions (Gudmundson, 2004; Martínez-Pañeda et al., 2019a). Thus, both the micro-stress tensor $\boldsymbol{q}$ and the higher order stress tensor $\boldsymbol{\tau}$ can be additively decomposed into their energetic and dissipative parts:

$$\boldsymbol{q} = \boldsymbol{q}^D + \boldsymbol{q}^E, \qquad \boldsymbol{\tau} = \boldsymbol{\tau}^D + \boldsymbol{\tau}^E. \tag{17}$$

Consistent with our free energy definition (13), plastic deformation is assumed to be a purely dissipative process: $\boldsymbol{q}^E = \partial\Psi/\partial\boldsymbol{\varepsilon}^p = 0$. Conversely, both energetic and dissipative terms are considered in relation to the plastic strain gradients. Accordingly, the plastic dissipation rate reads:

$$\dot{w}^p = \boldsymbol{q} : \dot{\boldsymbol{\varepsilon}}^p + \boldsymbol{\tau}^D \vdots \nabla\dot{\boldsymbol{\varepsilon}}^p, \tag{18}$$

where $\dot{w}^p(\dot{E}^p)$ is given in terms of a combined effective plastic rate:

$$\dot{E}^p = \left(\frac{2}{3}|\dot{\boldsymbol{\varepsilon}}^p|^2 + L_D^2|\nabla\dot{\boldsymbol{\varepsilon}}^p|^2\right)^{1/2}. \tag{19}$$

Here, L_D is the dissipative length scale, which quantifies the degree to which the material exhibits dissipative strengthening; for example, via mechanisms such as forest hardening. A thermodynamically consistent framework is obtained by defining an effective stress $\Sigma = \partial\dot{w}^p/\partial\dot{E}^p$, work conjugate to $\dot{E}^p$. The constitutive definitions of the dissipative stresses readily follow:

$$\boldsymbol{q} = \frac{\partial\dot{w}^p}{\partial\dot{\boldsymbol{\varepsilon}}^p} = \frac{2}{3}\frac{\Sigma}{\dot{E}^p}\dot{\boldsymbol{\varepsilon}}^p, \qquad \boldsymbol{\tau}^D = \frac{\partial\dot{w}^p}{\partial\nabla\dot{\boldsymbol{\varepsilon}}^p} = L_D^2\frac{\Sigma}{\dot{E}^p}\nabla\dot{\boldsymbol{\varepsilon}}^p. \tag{20}$$

On the other hand, the energetic part of the higher order stress is derived from the free energy definition (13) as

$$\boldsymbol{\tau}^E = \frac{\partial\Psi}{\partial\nabla\boldsymbol{\varepsilon}^p} = QL_E^2\nabla\boldsymbol{\varepsilon}^p. \tag{21}$$

For simplicity, we choose to define a single reference plastic length scale $L_p = L_E = L_D$, although the individual contributions from energetic and dissipative higher order gradients will also be explored.

The displacement $\mathbf{u}$ and plastic strain $\boldsymbol{\varepsilon}^p$ solutions are coupled by the deviatoric Cauchy stress, as evident from (8)b, and by the total strain decomposition. Given that the tensile response prior to fracture is typically unaffected by hydrogen, no explicit coupling between the hydrogen content and plasticity is defined. Lastly, as discussed below, fracture is assumed to be driven by the elastic strain energy density.

2.4.3. Phase field fracture

The constitutive relations for the micro-stress variables work conjugate to the phase field and the phase field gradient are obtained from the free energy (13). Thus, the scalar microstress ω is given by:

$$\omega = \frac{\partial \Psi}{\partial \phi} = -2(1-\phi)\psi^e + G_c(C)\frac{\phi}{\ell}. \tag{22}$$

Similarly, the phase field microstress vector $\boldsymbol{\xi}$ reads:

$$\boldsymbol{\xi} = \frac{\partial \Psi}{\partial \nabla \phi} = G_c(C)\,\ell\,\nabla\phi. \tag{23}$$

Now, insert (22) and (23) into the phase field local balance (8c). Neglecting the concentration gradient along the small region where $\nabla\phi \neq 0$, the local force balance can be reformulated as:

$$G_c(C)\left(\frac{\phi}{\ell} - \ell\Delta\phi\right) - 2(1-\phi)\psi^e = 0 \tag{24}$$

As evident from (24), fracture in the elastic-plastic solid is driven solely by the elastic component of the material strain energy density. The same assumption was adopted by Duda et al. (2015). The plastic contribution may also be weighted differently, through an *ad hoc* degradation function. These and other possibilities, including defining an explicit relation between the plastic yield condition and the damage variable, have been explored in the realm of phase field modeling of ductile fracture, see (Alessi et al., 2018). In addition, note that the coupling with the diffusion problem takes place through the fracture energy dependency to the hydrogen content. The specific choice of the function $G_c(C)$ is inspired by first principles, as discussed below.

2.4.4. Hydrogen transport

The gradient of the chemical potential $\nabla\mu$ is the driving force for hydrogen diffusion. The constitutive relation for μ can be determined from the free energy definition (13) as:

$$\mu = \frac{\partial \Psi}{\partial C} = \mu_0 + RT\ln\frac{\theta_L}{1-\theta_L} - \overline{V}_H\sigma_H + \frac{1}{2}\frac{dG_c(C)}{dC}\left(\frac{\phi^2}{\ell} + \ell|\nabla\phi|^2\right). \tag{25}$$

As evident from (25) and (5), hydrogen atoms diffuse from regions of high chemical potential to regions of low chemical potential. Hydrogen transport is enhanced by lattice dilatation, as characterised by hydrostatic tensile stresses σ_H. Note that, as opposed to the choice made in Martínez-Pañeda et al. (2018), the stress-dependent part of μ is chosen to be subjected to the degradation function $g(\phi)$. In addition, the last term in (25) enhances hydrogen transport from damaged regions to pristine regions. However, as discussed in Martínez-Pañeda et al. (2018), the definition of sound chemical boundary conditions in the presence of a propagating crack requires careful consideration. As elaborated in Section 3.4, we choose to neglect the last term in (25) and implement a penalty-based *moving* chemical boundary condition to capture how the environment promptly occupies the space created with crack advance. Accordingly, the constitutive equation for the hydrogen flux can be readily obtained by considering (5). Thus, after adopting the common assumptions of low occupancy ($\theta_L \ll 1$) and constant interestitial sites concentration ($\nabla N = 0$), the flux reads:

$$\mathbf{J} = -D\nabla C + \frac{DC}{RT}\overline{V}_H\nabla\sigma_H. \tag{26}$$

The relation between the fracture energy and the hydrogen content remains to be defined. In an implicit multi-scale approach, we define G_c according to the surface energy degradation with hydrogen coverage obtained from quantum mechanical calculations. The aim is to predict the sensitivity of the macroscopic fracture energy to hydrogen by quantifying the reduction in the atomic bond energy, without resorting to empirical parameters. The choice is inspired by the work of Serebrinsky et al. (2004) in the context of cohesive zone models. Density Functional Theory (DFT) calculations show that the atomic decohesion strength depends sensitively on the hydrogen surface coverage along atomic planes (Van der Ven and Ceder, 2003; Jiang and Carter, 2004; Kirchheim et al., 2015). Based on the recent first principles calculations by Alvaro et al. (2015), a linear degradation of G_c (and the surface energy) with hydrogen content θ is assumed:

$$G_c(\theta) = (1-\chi\theta)G_c(0). \tag{27}$$

Here, $G_c(0)$ is the critical energy release rate in an inert environment and χ is the hydrogen damage coefficient, to be calibrated with DFT calculations. For example, based on Jiang and Carter (2004), χ equals 0.89 in iron and 0.67 in aluminum.

Finally, we make use of the Langmuir-McLean isotherm to compute the hydrogen surface coverage θ from the bulk hydrogen concentration C as:

$$\theta = \frac{C}{C + \exp\left(-\Delta g_b^0 / RT\right)}, \tag{28}$$

with Δg_b^0 denoting the difference in Gibbs free energy between the decohering surface and the surrounding material. Assuming that fracture in the presence of hydrogen is intergranular, a value of 30 kJ/mol is assigned to Δg_b^0 based on the spectrum of experimental data available for the trapping energy at grain boundaries (Serebrinsky et al., 2004).

3. Numerical implementation

The main features of the finite element framework are introduced in this Section, with further details being provided in Appendix A. First, a history field and a strain energy split are defined to prevent damage reversibility and damage under compressive loading (Section 3.1). Secondly, in Section 3.2 we address the discretisation of the mixed finite element problem and formulate the residuals. In Section 3.3 we introduce the *ad hoc* viscoplastic law adopted. Finally, the new penalty-based chemical boundary conditions are presented in Section 3.4. The implementation is conducted within an Abaqus user-element (UEL) subroutine, with the pre-processing of the input files carried out using Abaqus2Matlab (Papazafeiropoulos et al., 2017).

3.1. Addressing damage in compression, irreversibility and crack interpenetration

First, a decomposition of the elastic strain energy density is adopted to prevent damage due to compressive stresses. We choose to follow the spherical/deviatoric split first introduced by Amor et al. (2009). Thus, in a solid with Lame's first parameter λ, the elastic strain energy density can be decomposed as $\psi^e = \psi_+^e + \psi_-^e$, with

$$\begin{aligned} \psi_+^e &= \frac{1}{2}\left(\lambda + \frac{2}{3}\mathrm{Q}\right)\langle \mathrm{tr}\ \boldsymbol{\varepsilon}^e\rangle_+^2 + \mathrm{Q}\,|\boldsymbol{\varepsilon}^{e'}|^2 \\ \psi_-^e &= \frac{1}{2}\left(\lambda + \frac{2}{3}\mathrm{Q}\right)\langle \mathrm{tr}\ \boldsymbol{\varepsilon}^e\rangle_-^2, \end{aligned} \tag{29}$$

and only ψ_+^e contributing to damage. Here, $\langle\rangle$ denote the Macaulay brackets. The strain energy decomposition is implemented by means of a hybrid approach, following Ambati et al. (2015). Damage irreversibility, $\phi_{t+\Delta t} \geq \phi_t$, is ensured by introducing a history variable field H (Miehe et al., 2010). Thus, for pseudo-time τ, the history variable at time t corresponds to the maximum value of ψ_+^e, i.e.:

$$H(t) = \max_{\tau \in [0,t]} \psi_+^e(\tau). \tag{30}$$

In addition, crack interpenetration is precluded by adding the following constraint (Ambati et al., 2015)

$$\phi = 0 \quad \text{if } \psi_+^e < \psi_-^e. \tag{31}$$

3.2. Finite element discretisation

Making use of Voigt notation, the nodal variables for the displacement field, $\hat{\mathbf{u}}$, the plastic strains $\hat{\boldsymbol{\varepsilon}}^p$, the phase field, $\hat{\phi}$, and the hydrogen concentration, $\hat{C}$ are interpolated as:

$$\mathbf{u} = \sum_{i=1}^{m} \boldsymbol{N}_i^{\boldsymbol{u}} \hat{\mathbf{u}}_i, \qquad \boldsymbol{\varepsilon}^p = \sum_{i=1}^{m} \boldsymbol{N}_i^{\boldsymbol{\varepsilon}^p} \hat{\boldsymbol{\varepsilon}}_i^p, \qquad \phi = \sum_{i=1}^{m} N_i \hat{\phi}_i, \qquad C = \sum_{i=1}^{m} N_i \hat{C}_i. \tag{32}$$

Here, N_i denotes the shape function associated with node i, for a total number of nodes m. The shape function matrices $\boldsymbol{N}_i^{\boldsymbol{u}}$ and $\boldsymbol{N}_i^{\boldsymbol{\varepsilon}^p}$ are given in Appendix A. Similarly, the associated gradient quantities can be discretised as:

$$\boldsymbol{\varepsilon} = \sum_{i=1}^{m} \boldsymbol{B}_i^{\boldsymbol{u}} \hat{\mathbf{u}}_i, \qquad \nabla \boldsymbol{\varepsilon}^p = \sum_{i=1}^{m} \boldsymbol{B}_i^{\boldsymbol{\varepsilon}^p} \hat{\boldsymbol{\varepsilon}}_i^p, \qquad \nabla \phi = \sum_{i=1}^{m} \mathbf{B}_i \hat{\phi}_i, \qquad \nabla C = \sum_{i=1}^{m} \mathbf{B}_i \hat{C}_i, \tag{33}$$

with the **B**-matrices explicitly given in Appendix A.

Considering the discretisation (32)-(33), we derive the residuals for each primal kinematic variable from (6) and (7) as:

- Linear momentum

$$\mathbf{R}_i^{\mathbf{u}} = \int_\Omega \left\{ \left[(1-\phi)^2 + k \right] \left(\boldsymbol{B}_i^{\mathbf{u}} \right)^T \boldsymbol{\sigma}_0 \right\} \mathrm{d}V - \int_{\partial\Omega} \left[\left(\boldsymbol{N}_i^{\mathbf{u}} \right)^T \mathbf{T} \right] \mathrm{d}S, \tag{34}$$

where $\boldsymbol{\sigma}_0$ is the undamaged stress tensor and k is a small positive parameter introduced to circumvent the complete degradation of the energy. We choose $k = 1 \times 10^{-7}$ to ensure that the algebraic conditioning number remains well-posed for fully-broken states.

- Microplasticity

$$\mathbf{R}_i^{\boldsymbol{\varepsilon}^p} = \int_\Omega \left[\left(\boldsymbol{N}_i^{\boldsymbol{\varepsilon}^p}\right)^T (\boldsymbol{q} - \boldsymbol{\sigma}) + \left(\boldsymbol{B}_i^{\boldsymbol{\varepsilon}^p}\right)^T \boldsymbol{\tau} \right] \mathrm{d}V - \int_{\partial\Omega} \left[\left(\boldsymbol{N}_i^{\boldsymbol{\varepsilon}^p}\right)^T \boldsymbol{t} \right] \mathrm{d}S. \tag{35}$$

- Phase field

$$R_i^{\phi} = \int_\Omega \left\{ -2(1-\phi) N_i H + G_c(C) \left[\frac{\phi}{\ell} N_i + \ell \left(\mathbf{B}_i\right)^T \nabla \phi \right] \right\} dV. \tag{36}$$

where H is the history field variable introduced in Section 3.1.

- Hydrogen transport

$$R_i^C = \int_\Omega \left[N_i \left(\frac{1}{D} \frac{dC}{dt} \right) + \mathbf{B}_i^T \nabla C - \mathbf{B}_i^T \left(\frac{\overline{V}_H C}{RT} \nabla \sigma_H \right) \right] \mathrm{d}V + \frac{1}{D} \int_{\partial\Omega_\rho} N_i \rho \, \mathrm{d}S. \tag{37}$$

The consistent tangent stiffness matrices $\boldsymbol{K}$, required to complete the finite element implementation, are obtained by considering the constitutive relations and differentiating the residuals with respect to the incremental nodal variables; details are given in Appendix A. For each element, the linearised weakly-coupled system reads:

$$\begin{bmatrix} \boldsymbol{K}^{\mathbf{u},\mathbf{u}} & \boldsymbol{K}^{\mathbf{u},\boldsymbol{\varepsilon}^p} & 0 & 0 \\ \boldsymbol{K}^{\boldsymbol{\varepsilon}^p,\mathbf{u}} & \boldsymbol{K}^{\boldsymbol{\varepsilon}^p,\boldsymbol{\varepsilon}^p} & 0 & 0 \\ 0 & 0 & \boldsymbol{K}^{\phi,\phi} & 0 \\ 0 & 0 & 0 & \boldsymbol{K}^{C,C} \end{bmatrix} \begin{bmatrix} \mathbf{u} \\ \boldsymbol{\varepsilon}^p \\ \phi \\ C \end{bmatrix} + \begin{bmatrix} 0 & 0 & 0 & 0 \\ 0 & 0 & 0 & 0 \\ 0 & 0 & 0 & 0 \\ 0 & 0 & 0 & \boldsymbol{M} \end{bmatrix} \begin{bmatrix} 0 \\ 0 \\ 0 \\ \dot{C} \end{bmatrix} = \begin{bmatrix} \mathbf{R}^{\mathbf{u}} \\ \mathbf{R}^{\boldsymbol{\varepsilon}^p} \\ R^{\phi} \\ R^C \end{bmatrix}, \tag{38}$$

where $\boldsymbol{M} = \partial R_i^C / \partial \dot{C}$ is the concentration capacity matrix. The global finite element system is solved, in an implicit time integration framework, by means of a staggered approach, following the work by Miehe et al. (2010). A time sensitivity study is conducted in all computations.

3.3. Viscoplastic law

We circumvent the need to track active plastic regions (see, Nielsen and Niordson, 2013) by employing a viscoplastic function that is particularized to the rate-independent limit. Thereby, the effective stress Σ is defined as:

$$\Sigma = \sigma_F(E^p) V\left(\dot{E}^p\right), \tag{39}$$

where σ_F is the current flow stress and $V(\dot{E}^p)$ is the viscoplastic function. We assume isotropic power-law hardening such that, for a strain hardening coefficient N, the flow rule reads

$$\sigma_F = \sigma_y \left(1 + \frac{E^p}{\varepsilon_y} \right)^N. \tag{40}$$

Here, σ_y denotes the initial yield stress, and accordingly the yield strain is given by $\varepsilon_y = E/\sigma_y$. For a reference strain rate $\dot{\varepsilon}_0$ and strain rate sensitivity exponent m, the viscoplastic function reads:

$$V\left(\dot{E}^p\right) = \left(\frac{\dot{E}^p}{\dot{\varepsilon}_0} \right)^m. \tag{41}$$

As discussed in Section 4.1, the values of $\dot{\varepsilon}_0$ and m are appropriately chosen so as to reproduce rate-independent behavior.

The widely used viscoplastic hardening rule (41) is implemented by adopting the viscoplastic split recently proposed by Fuentes-Alonso and Martínez-Pañeda (2020), which builds on the previous work by Panteghini and Bardella (2016). The aim is to bound the magnitude of $\partial\Sigma/\partial\Delta E^p$ when $\dot{E}^p \to 0$, preventing ill-conditioning. The definition in (41) is approximated by:

$$V\left(\dot{E}^p\right) = \begin{cases} \frac{\dot{E}^p}{\varpi \dot{\varepsilon}_0} & \text{if } \dot{E}^p m / \dot{E}^p_* \leq 1 \\ \left(\frac{\dot{E}^p - \frac{1-m}{m} \dot{E}^p_*}{\dot{\varepsilon}_0} \right)^m & \text{if } \dot{E}^p m / \dot{E}^p_* > 1 \end{cases} \tag{42}$$

.

Here, ϖ is a small positive constant ($\varpi \ll 1$) and $\dot{E}^p_*$ is a threshold quantity that is defined to ensure a smooth transition between states:

$$\dot{E}^p_* = \dot{\varepsilon}_0 \left(\frac{1}{\varpi m} \right)^{1/(m-1)}. \tag{43}$$

More details are given in Fuentes-Alonso and Martínez-Pañeda (2020).

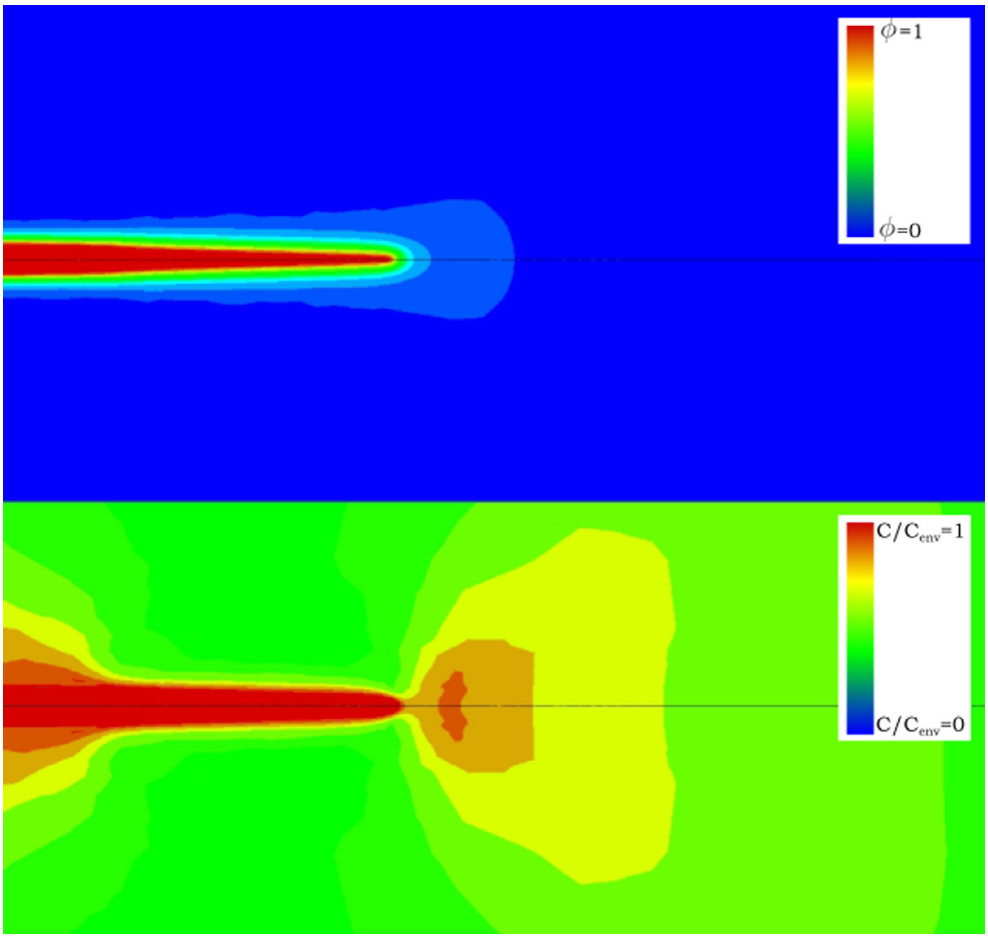

Fig. 2. *Moving* chemical boundary conditions with a propagating crack, contours of phase field damage (top) and hydrogen concentration (bottom). Details of the boundary value problem are given in Section 4.1.2.

3.4. Chemical conditions on a moving boundary

Consider a solid that is continuously exposed to a hydrogenous environment. Fracture modeling requires capturing how the environment-solid boundary advances with crack growth. The newly formed crack surface is promptly exposed to the environment, hydrogen gas or an aqueous electrolyte. The use of a phase field framework facilitates tracking crack advance and, accordingly, prescribing suitable chemical conditions on the moving boundary. Specifically, we make use of a penalty-based approach (Renard and Poulios, 2020), and include a penalty term P multiplying the first term of the hydrogen concentration residual (37), with the associated stiffness matrix being modified accordingly. The penalty term is defined in terms of a large positive penalty coefficient $k_p \approx 1 \times 10^5$ as:

$$P = k_p (C - C_{env}) \langle \phi - 0.5 \rangle_+, \tag{44}$$

such that the hydrogen concentration at the crack surface approaches the environmental hydrogen concentration C_{env} as $\phi \to 1$. Representative contours of crack advance, as defined by $\phi = 1$, and hydrogen concentration are given in Fig. 2. The role of the environment in providing a continuous source of hydrogen is captured.

4. Results

The capabilities of the model will be demonstrated by addressing representative case studies. First, in Section 4.1.1 the role of the plastic length scales on stationary crack tip fields is investigated. Secondly, physical insight will be gained by exploring the relation between crack growth resistance and fracture process parameters in a wide variety of scenarios. Crack growth resistance curves are computed to explore the sensitivity of the model to (i) the plastic length scale parameters, (ii) the fracture length scale parameter, (iii) the hydrogen concentration, and (iv) the rate of loading, see Section 4.1.2. In addition, the steady state fracture toughness is estimated as a function of the strength, showing that the model can naturally capture the ductile-to-brittle transition experienced in the presence of hydrogen. Finally, the capabilities of the model in quantitatively capturing experimental results are showcased in Section 4.2 by comparing with crack initiation measurements, K_{th}, under a wide range of environments (applied potentials, E_p).

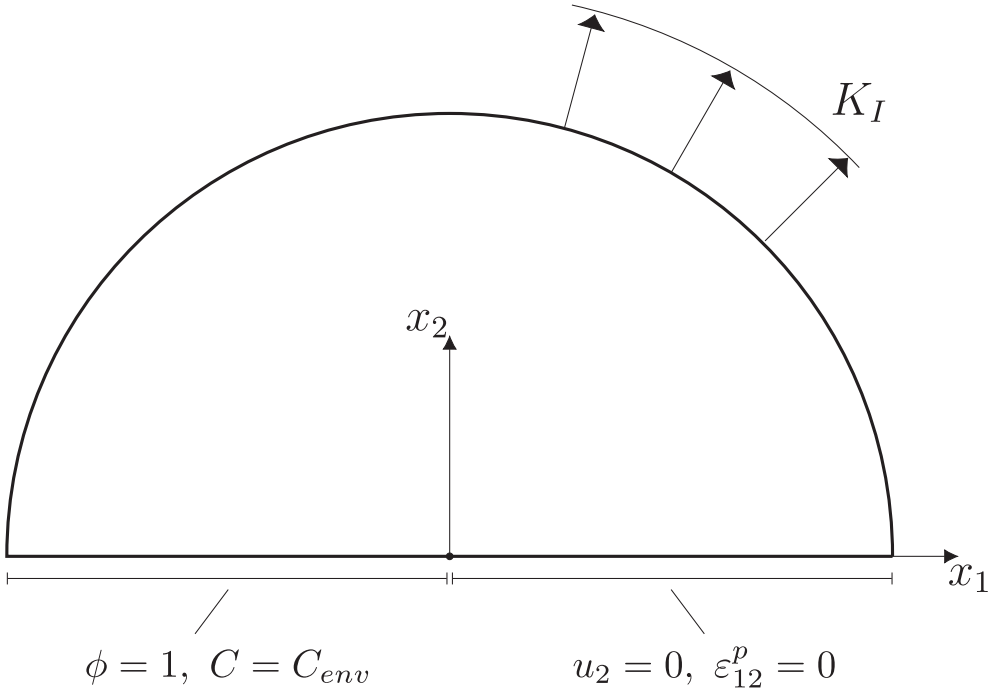

Fig. 3. Sketch of the boundary layer formulation and the associated mechanical, chemical and damage boundary conditions.

4.1. Mode I fracture of an elastic-plastic solid in the presence of hydrogen

We assume that small scale yielding conditions prevail and make use of a boundary layer formulation to prescribe a remote K_I field, see Fig. 3. Consider a crack with its tip at the origin of the coordinate system and with the crack plane along the negative axis of the Cartesian reference frame (x_1, x_2). The elastic response of the solid is characterised by the Young's modulus E and Poisson's ratio ν. Then, an outer K_I field is imposed by prescribing nodal displacements on the outer periphery of the mesh as

$$u_i = \frac{K_I}{E} r^{1/2} f_i(\theta, \nu), \tag{45}$$

where the subscript index i equals x_1 or x_2, and the functions $f_i(\theta, \nu)$ are given, in terms of polar coordinates (r, θ) centred at the crack tip, by

$$f_1 = \frac{1+\nu}{\sqrt{2\pi}} (3 - 4\nu - \cos\theta) \cos\left(\frac{\theta}{2}\right) \tag{46}$$

and

$$f_2 = \frac{1+\nu}{\sqrt{2\pi}} (3 - 4\nu - \cos\theta) \sin\left(\frac{\theta}{2}\right). \tag{47}$$

Upon exploiting reflective symmetry about the crack plane, only half of the finite element model is analysed. We note in passing that satisfying reflective symmetry requires careful consideration of the higher order boundary conditions. Consider (9)b; for a crack lying on the x_2 axis, micro-free boundary conditions $\boldsymbol{t} = \boldsymbol{0}$ imply, along the $x_2 = 0$ plane:

$$\tau_{222} = \tau_{112} = \tau_{122} = 0. \tag{48}$$

Symmetry dictates that $\varepsilon^p_{22,2} = \varepsilon^p_{11,2} = 0$ along the extended crack path, such that the Neumann boundary conditions $t_{11} = t_{22} = 0$ are appropriate. However, ε^p_{12} is an odd function in x_2 which requires prescribing instead $\varepsilon^p_{12} = 0$ at the symmetry plane, as the conventional Neumann boundary condition $\sigma_{12} = 0$ at $x_2 = 0$ does not imply $\varepsilon^p_{12} = 0$ for non-zero values of L_D and L_E.

The boundary layer formulation will be employed to shed light into the role of plastic strain gradients on stationary crack tip fields, and it is subsequently used to characterise crack growth resistance in embrittled elastic-plastic solids.

4.1.1. Stationary crack tip fields

Consider a semi-infinite, stationary crack in an elastic-plastic solid subjected to a remote elastic K_I and in the absence of hydrogen. A representative value for the plastic zone size R_p can be estimated from Irwin's approximation as:

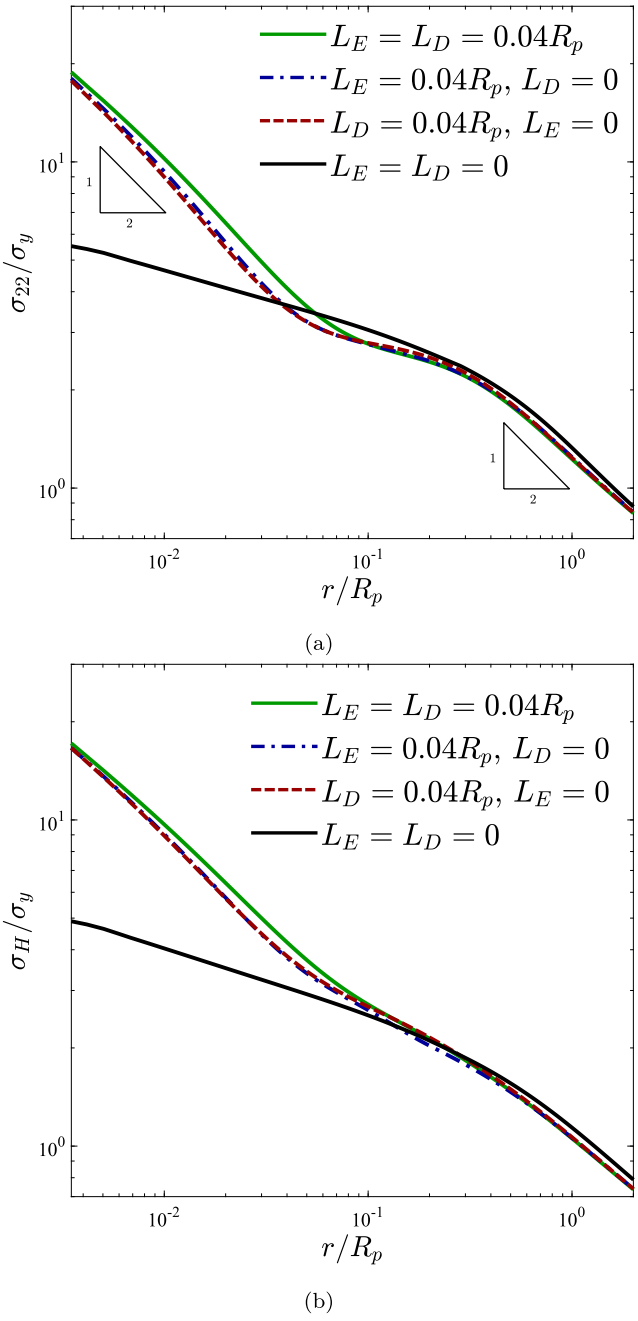

Fig. 4. Crack tip fields ahead of a stationary crack in the absence of hydrogen: (a) opening tensile stress distribution, and (b) hydrostatic stress distribution. Material properties: $\sigma_y/E = 0.003$, $\nu = 0.3$ and $N = 0.2$.

$$R_p = \frac{1}{3\pi}\left(\frac{K_I}{\sigma_y}\right)^2 \tag{49}$$

The viscoplastic parameters $\dot{\varepsilon}_0$ and m are chosen to ensure that we are close the rate-independent limit, as confirmed by comparison with conventional rate-independent plasticity predictions for $L_E = L_D = 0$.

Of interest here is the behavior of the opening tensile stresses, σ_{22}, and the hydrostatic stress, σ_H, relevant to both fracture and hydrogen transport. In the rate independent limit, any stress quantity ahead of the crack is a function of the following non-dimensional parameters:

$$\frac{\sigma}{\sigma_y} = F\left(\frac{x_1}{R_p},\ \frac{L_E}{R_p},\ \frac{L_D}{R_p},\ N,\ \nu,\ \frac{E}{\sigma_y}\right). \tag{50}$$

The numerical results obtained for σ_{22}/σ_y and σ_H/σ_y ahead of the crack tip are shown in a log-log scale in Figs. 4a and 4b, respectively. Results are obtained for a solid with $\sigma_y/E = 0.003$, $\nu = 0.3$ and strain hardening exponent $N = 0.2$. Regarding the plastic length scales, different combinations are considered: (i) conventional plasticity, $L_E = L_D = 0$; (ii) purely

energetic hardening $L_E = 0.04R_p$ (with $L_D = 0$); (iii) purely dissipative strengthening $L_D = 0.04R_p$ (with $L_E = 0$); and (iv) combined dissipative and energetic strengthening, $L_E = L_D = 0.04R_p$. Consider first the case of the opening tensile stress distribution, Fig. 4a. Away from the crack tip, predictions agree, independently of the value of L_D and L_E. However, strain gradient plasticity predictions lead to much higher stresses than those obtained with conventional plasticity as we approach the crack tip. In fact, for all cases when L_D or L_E are non-zero, the finite element results reveal the existence of an inner K_I-field, where the stress field recovers the linear elastic $r^{-1/2}$ singularity. The existence of this *elastic core* has been recently justified analytically by Martínez-Pañeda and Fleck (2019) and it is reminiscent of a dislocation free crack tip zone, as introduced by Suo et al. (1993). Note that the inner K_I-field is present for any non-zero choice of L_E and L_D, with the purely energetic result predicting slightly higher stresses than the purely dissipative case but with differences being minimal. For the nearly-proportional loading conditions of the stationary crack tip problem, differences are due to the different weighting of energetic and dissipative higher order contributions, see (20b) and (21).

The hydrostatic stress σ_H distribution is shown in 4b and reveals the same qualitative trends. First, the stress distribution predicted by strain gradient plasticity agrees with the conventional plasticity result far from the crack tip, but predictions start to differ when r is on the order of the relevant plastic length scale. Also, similar results are obtained when strain gradient contributions are purely energetic ($L_E > 0$, $L_D = 0$) and purely dissipative ($L_D > 0$, $L_E = 0$). In both cases, a substantial stress elevation is attained close to the crack tip, where the hydrostatic stress level is roughly four times larger than the conventional plasticity prediction. This could have important implications for modeling hydrogen transport, given the exponential dependence of the hydrogen concentration on the hydrostatic stress. For example, for a given hydrogen concentration at the boundary C_{env}, the hydrogen concentration C at steady state reads (Liu, 1970):

$$C = C_{env} \exp\left(\frac{\bar{V}_H \sigma_H}{RT}\right) \tag{51}$$

The prediction of large hydrogen concentrations within a few microns of the crack tip surface is consistent with experimental measurements, see Martínez-Pañeda et al. (2016a) and Gerberich (2012).

4.1.2. Crack growth resistance

Consider now the case of a growing crack, as dictated by the phase field. Insight will be first gained on the role of the plastic length scales, and the effect of hydrogen will be subsequently taken into consideration. A fracture process zone length R_0 can be defined, as done by Tvergaard and Hutchinson (1992) in the context of cohesive zone models, as

$$R_0 = \frac{1}{3\pi\left(1-\nu^2\right)}\frac{EG_c}{\sigma_y^2}, \tag{52}$$

In addition, a cohesive bonding strength can be defined to frame the ductile versus brittle dichotomy. In the context of phase field models, a critical stress $\hat{\sigma}$ can be defined from the homogeneous solution to (24) in a one dimensional setting. As shown by, for example, Borden et al. (2012) and Martínez-Pañeda et al. (2018), this cohesive strength can be expressed as a function of Young's modulus E, the fracture energy G_c and the phase field length scale ℓ as:

$$\hat{\sigma} = \frac{9}{16}\sqrt{\frac{EG_c}{3\ell}}. \tag{53}$$

Thus, ℓ is a material parameter that determines the magnitude of the critical stress. Crack initiation is based on a purely energetic criterion, $G = G_c$, but crack growth resistance will be affected by the material strength, as determined through ℓ. Also, given (53), the material strength $\hat{\sigma}$ will decrease with increasing hydrogen content *via* its relation with $G_c(C)$. Using (53) one can establish an analogy with cohesive zone models, where the traction-separation law is characterised by its shape, the value of the fracture energy G_c and the cohesive strength $\hat{\sigma}$. However, we emphasize that, in general, Eq. (53) constitutes an approximation. Accordingly, we choose to favour using ℓ/R_0 as a relevant non-dimensional group, which is inversely related to $\hat{\sigma}/\sigma_y$, the common choice in cohesive zone analyses, as:

$$\frac{R_0}{\ell} = \frac{256}{81\pi\left(1-\nu^2\right)}\left(\frac{\hat{\sigma}}{\sigma_y}\right)^2 \tag{54}$$

Thus, in the absence of hydrogen and in the rate-independent limit, dimensional analysis implies that the crack growth resistance depends on the following non-dimensional groups:

$$\frac{K_I}{K_0} = F\left(\frac{\Delta a}{R_0},\ \frac{\ell}{R_0},\ N,\ \frac{E}{\sigma_y},\ \frac{L_p}{R_0},\ \nu\right), \tag{55}$$

where L_p is the reference plastic length scale: $L_E = L_D = L_p$, Δa is the crack extension, and K_0 is the reference stress intensity factor at which cracking initiates. Under plane strain conditions, the remote load at which cracking initiates is given by:

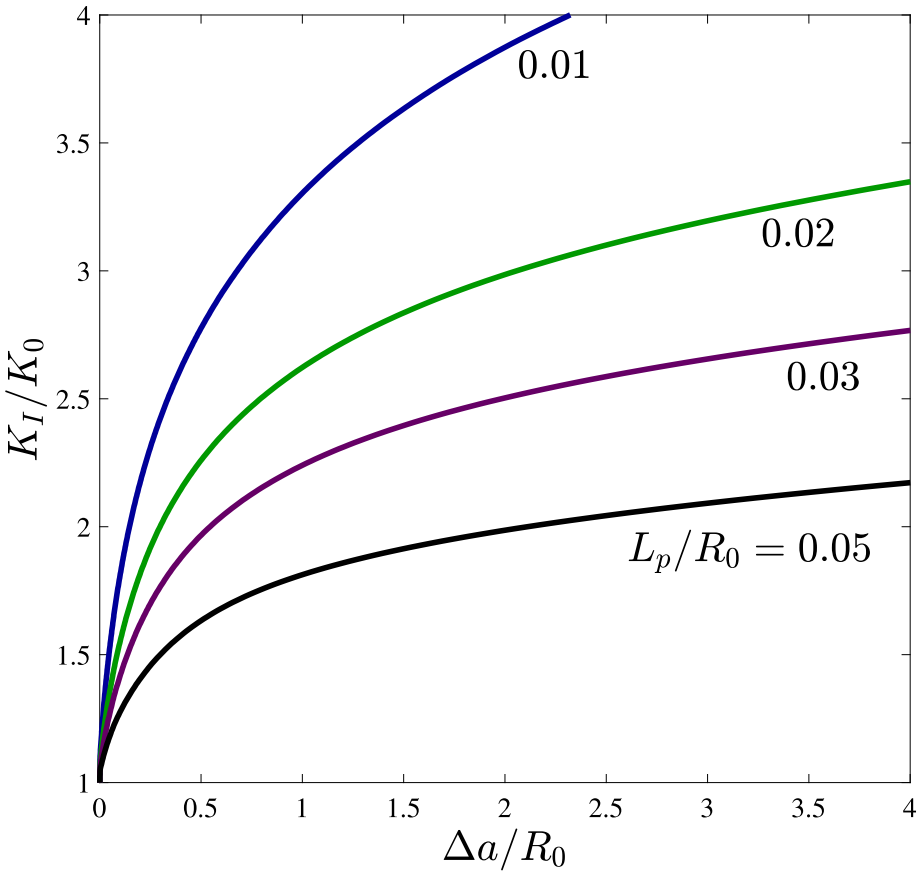

Fig. 5. Influence of the plastic length scale on crack growth resistance. Material properties: $\sigma_y/E = 0.003$, $\nu = 0.3$, $N = 0.2$, and $\ell/R_0 = 1/35$ $\left(\hat{\sigma}/\sigma_y \approx 5.6\right)$.

$$K_0 = \left(\frac{EG_c}{1-\nu^2}\right)^{1/2} \tag{56}$$

Results are computed using the boundary layer formulation shown in Fig. 3. The crack is introduced by prescribing the phase field parameter, $\phi = 1$. We assume plane strain conditions and the domain is discretised using a total of approximately 36,000 quadratic quadrilateral elements with reduced integration. The characteristic element length along the crack propagation path is at least 6 times smaller than the phase field length scale ℓ, so as to resolve the fracture process zone and ensure mesh insensitive results (Martínez-Pañeda et al., 2018). Material properties are given by $\sigma_y/E = 0.003$, $\nu = 0.3$ and $N = 0.2$, unless otherwise stated. The viscoplastic parameters are chosen to model the rate-independent limit. Specifically, we define the following dimensionless constant:

$$c_r = \frac{\dot{K}_I \varepsilon_y}{K_0 \dot{\varepsilon}_0},$$

and make suitable choices for c_r and m. The combination $c_r = 0.24$ and $m = 0.025$ reproduces the rate-independent limit, as confirmed by comparing with the results obtained with rate-independent J2 plasticity (for $L_p = 0$) and with the viscoplastic function by Panteghini and Bardella (2016).

First, the influence of the plastic length scale on the fracture resistance is assessed. As shown in Fig. 5, crack growth resistance curves (R-curves) are computed for selected values of L_p/R_0. In agreement with expectations, larger values of L_p/R_0 magnify gradient effects, elevating crack tip stresses and reducing the fracture resistance. The precise magnitude of L_p/R_0 depends mainly on the potential of the material to strengthen or harden in the presence of plastic strain gradients, as given by L_p, and on the work of fracture, as given by G_c - see (52). The fracture energy G_c can vary from a few J/m^2, as in fracture processes governed by atomic decohesion, to hundreds of kJ/m^2, as in ductile damage. Consequently, dislocation hardening effects have a higher influence in brittle cracking, where the work of separation and the fracture process zone are small.

We aim at elucidating the contributions of the individual energetic and dissipative plastic length scales to the reduction in fracture resistance with increasing L_p/R_0 shown in Fig. 5. As non-proportional straining becomes relevant with crack advance, the expectation is to observe larger differences than those reported in Fig. 4 for the stationary crack. Crack growth resistance curves are shown in Fig. 6 for three cases: (i) $L_E = 10L_D = 0.03R_0$, (ii) $L_D = 10L_E = 0.03R_0$, and (iii) $L_D = L_E = 0.03R_0$ (the reference case). Results are given for two choices of the strain hardening exponent: $N = 0.2$ and $N = 0$ (perfectly plastic

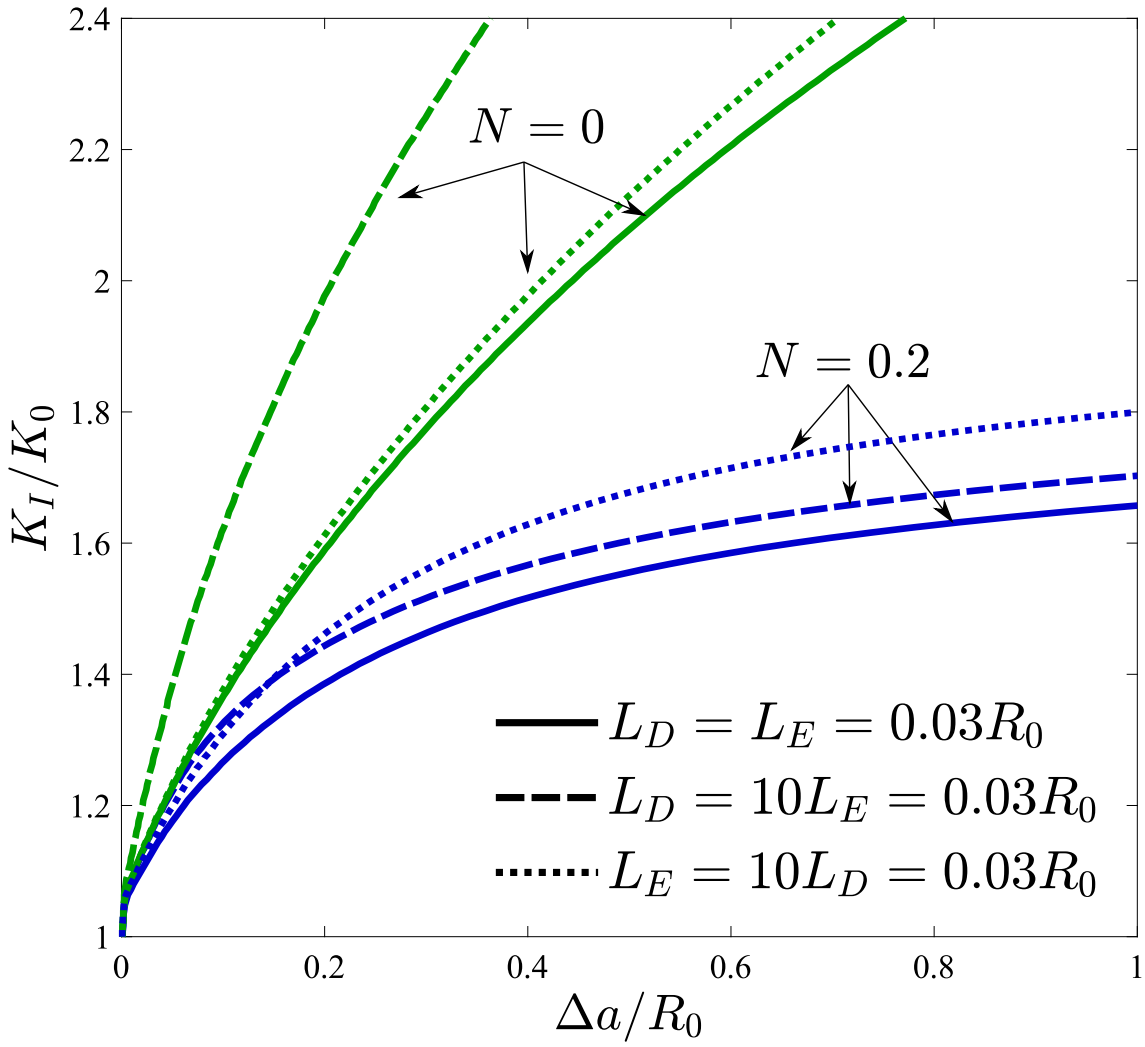

Fig. 6. Individual influence of the energetic and dissipative plastic length scales on crack growth resistance. Material properties: $\sigma_y/E = 0.003$, $\nu = 0.3$, and $\ell/R_0 = 1/15$ $\left(\hat{\sigma}/\sigma_y \approx 3.7\right)$. Green curves correspond to $N = 0$ while blue curves denote the $N = 0.2$ case.

behavior). As it would be expected, the less steep R-curves for both $N = 0$ and $N = 0.2$ cases are given by the combined energetic and dissipative strengthening results, $L_D = L_E = 0.03R_0$. Interestingly, dissipative effects appear to dominate the response for $N = 0.2$, while energetic contributions are more significant in the $N = 0$ case. Differences between energetic-dominated ($L_E \gg L_D$) and dissipative-dominated ($L_D \gg L_E$) predictions are due to the constitutive definitions of their associated higher order stresses, $\boldsymbol{\tau}^E$ and $\boldsymbol{\tau}^D$, see (20b) and (21). While $\boldsymbol{\tau}^D$ is related to the plastic strain gradients through a power-law expression, $\boldsymbol{\tau}^E$ is related to $\nabla\boldsymbol{\varepsilon}^p$ by a linear relation. As evident from Fig. 6, fracture takes place at smaller loads and thereby at smaller plastic strains for $N = 0.2$, a domain where $\boldsymbol{\tau}^D$ will dominate. Conversely, for a fixed ℓ/R_0 ($\hat{\sigma}/\sigma_y$), much larger strains and plastic dissipation take place in the case where $N = 0$. In addition, one should note that differences may also arise due to the kinematic nature of the energetic contribution, which resembles a back-stress (Legarth and Niordson, 2010). As shown recently by Martínez-Pañeda and Fleck (2018) and Juul et al. (2019) in the context of conventional plasticity, kinematic hardening increases plastic dissipation and fracture resistance, relative to isotropic hardening.

We proceed to vary the ℓ/R_0 ratio to explore the sensitivity of the fracture resistance to the critical stress (see (53)). As shown in Fig. 7, augmenting ℓ/R_0 (or $\hat{\sigma}/\sigma_y$) increases the steepness of the R-curve. This qualitative trend agrees with the results obtained by Tvergaard and Hutchinson (1992) using cohesive zone models. Since atomic decohesion requires attaining $\hat{\sigma}/\sigma_y$ values on the order of 10 or larger (as opposed to ductile fracture, $\hat{\sigma}/\sigma_y \approx 4$), the magnitude of the phase field length scale can be tailored to capture a specific cracking mechanism. The results shown in Fig. 7 span a wide range of scenarios, with $\ell < L_p$ and $L_p < \ell$. Miehe et al. (2016a) have chosen the phase field length scale to be smaller than the plastic length scale, on the grounds of a regularised crack zone lying inside the plastic zone. However, we emphasize that the magnitude of ℓ does not correspond to the width of the crack smearing function, and that L_p is a (constant) material property that does not correspond to the size of the plastic zone. More importantly, Fig. 7 shows that, if L_p/R_0 is sufficiently large, fracture can be attained at critical stresses on the order of the theoretical lattice strength $\hat{\sigma} = 10\sigma_y$. Thus, atomic decohesion in the presence of plasticity, as observed in numerous material systems (Elssner et al., 1994; Bagchi and Evans, 1996; Korn et al.,

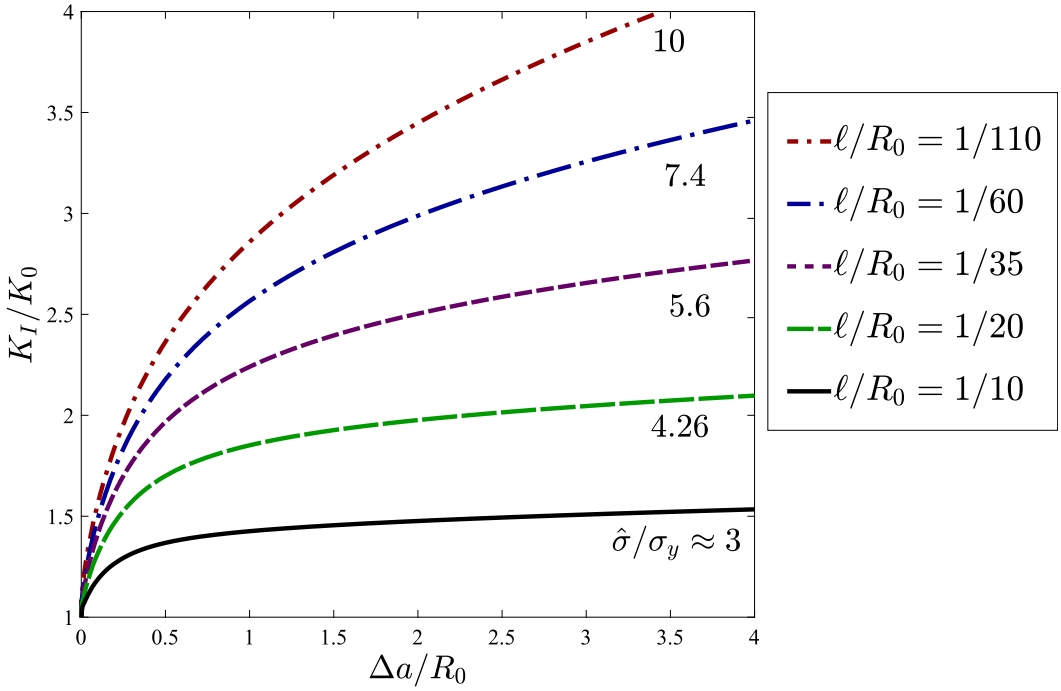

Fig. 7. Influence of the strength $\hat{\sigma}/\sigma_y$ (ℓ/R_0) on the crack growth resistance. Material properties: $\sigma_y/E = 0.003$, $\nu = 0.3$, $N = 0.2$ and $L_p/R_0 = 0.03$.

2002), can be rationalised in the context of strain gradient plasticity. This is unlike conventional plasticity, where crack tip stresses are only 3–5 larger than the initial yield stress and, consequently, fracture does not occur if the cohesive strength $\hat{\sigma}$ is on the order of the theoretical lattice strength ($\approx 10\sigma_y$) or the grain boundary strength ($\approx 9\sigma_y$), see (Tvergaard and Hutchinson, 1992; Duda et al., 2015). In the absence of hydrogen, the magnitude of L_p/R_0 has to be increased up to 0.03 to predict quasi-cleavage, i.e. fracture with $\hat{\sigma} = 10\sigma_y$. Note that L_p/R_0 values in the 0.001-0.01 range are expected for ductile steels; L_p is a material property that can be measured from micro-scale experiments, with $L_p \approx 1 - 10$ μm for most metals, and R_0 is on the order of 1 mm or more for void controlled fracture processes, where a work of fracture of tens of kJ/m^2 is at least required (Wei and Hutchinson, 1997). Such values of L_p/R_0 will be insufficient to trigger cleavage fracture in the absence of hydrogen, as crack growth is governed by other mechanisms, like void nucleation, growth and coalescence. However, hydrogen significantly reduces the work of fracture G_c, entailing an increase in the magnitude of L_p/R_0 that can trigger the ductile to brittle transition observed in the experiments.

Consider now the influence of hydrogen. Can we predict cleavage failure ($\hat{\sigma} = 10\sigma_y$) for L_p/R_0 values that are realistic for ductile steels? We proceed to compute crack growth resistance curves with $\ell/R_0 = 1/110$, $L_p/R_0 = 0.001$ and selected values of the environmental hydrogen concentration $C_{env} = 0.1$, 0.5, 1, and 2 wppm. C_{env} is prescribed at the crack surfaces and the specimen is not initially pre-charged, such that hydrogen charging and mechanical loading start at the same time. A value for the diffusion coefficient typical of iron-based materials is assumed, $D = 0.0127$ mm^2/s, following Sofronis and McMeeking (1989). The remote loading is prescribed at a rate of $\dot{K}_I/K_0 = 4 \times 10^{-7}$ s^{-1} and the hydrogen damage coefficient is chosen to be $\chi = 0.89$, based on the atomistic calculations by Jiang and Carter (2004) for hydrogen in Fe. The predictions obtained are shown in Fig. 8; the model appropriately captures the observed trend of a decreasing fracture resistance with increasing hydrogen concentration. We emphasize that no hydrogen pre-charging is considered and the results are reported relative to the initial (inert) values of K_0 and R_0. Thus, cracking initiates below $K_I/K_0 = 1$ in all cases, with the magnitude of K_I/K_0 at crack initiation decreasing with increasing C_{env}. By incorporating the role of hydrogen, fracture is predicted assuming cleavage cracking, $\hat{\sigma} = 10\sigma_y$, in an otherwise ductile material, $L_p/R_0 = 0.001$. The implications of this finding will be discussed below by computing the relation between the steady state fracture toughness K_{SS} and the critical cohesive strength $\hat{\sigma}$.

Steady state curves are shown in Fig. 9 for both an inert and a hydrogenous environment ($C_{env} = 1$ wppm). The steady state fracture toughness is estimated from the R-curves, with K_{SS} being the limiting value attained by K_I as the crack approaches steady state. The magnitude of K_{SS}/K_0 is computed for a wide range of strengths (ℓ/R_0) and selected values of L_p/R_0. Consider first the results in the absence of hydrogen, Fig. 9a. The model predicts ductile fracture for values of L_p/R_0 below 0.03 ($\hat{\sigma}/\sigma_y < 10$). As discussed above, this is consistent with the magnitude of R_0 in ductile metals, as given by the work of fracture. On the other hand, brittle fracture is predicted for high values of L_p/R_0, as it is the case in metal-ceramic interfaces (O'dowd et al., 1992), ferritic steels at low temperatures (Qian et al., 2011; Martínez-Pañeda et al., 2019b) and other material systems (see, e.g., Wang and Anderson, 1991) where the fracture energy is on the order of 1 kJ/m^2 or lower. However, the response changes drastically when hydrogen is taken into consideration, see Fig. 9b. Even for the case of ductile metals,

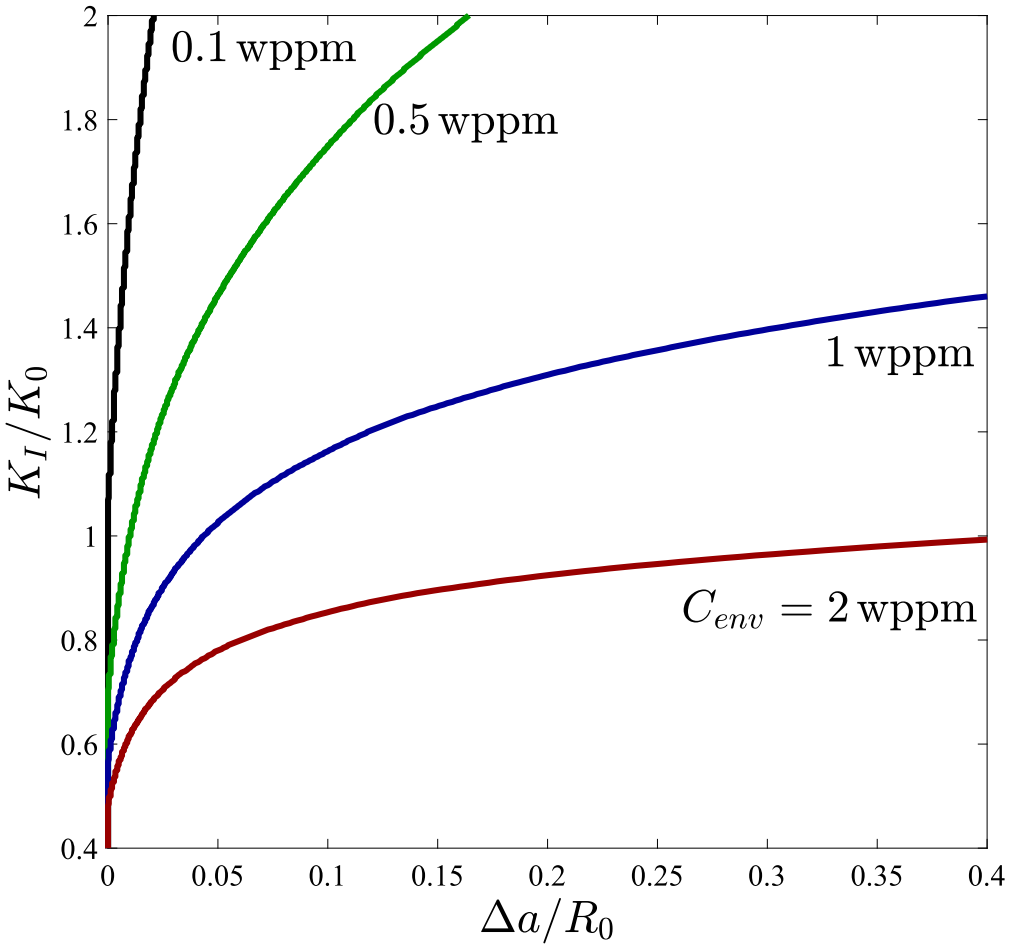

Fig. 8. Influence of the environmental hydrogen concentration on the fracture resistance. Material properties: $\sigma_y/E = 0.003$, $\nu = 0.3$, $N = 0.2$, $\ell/R_0 = 1/110$ ($\hat{\sigma}/\sigma_y = 10$), $L_p/R_0 = 0.001$, $D = 0.0127$ mm^2/s and $\chi = 0.89$. Loading rate $\dot{K}_I/K_0 = 4 \times 10^{-7}$ s^{-1}.

$L_p/R_0 \approx 0.01$, the steady state curve intersects the brittle fracture threshold, $\hat{\sigma}/\sigma_y = 10$. Thus, the transition from ductile to brittle fracture observed in the experiments is captured.

In addition, we show that the model is also capable of predicting internal hydrogen assisted cracking and the sensitivity of the R-curve to the loading rate. Thus, a uniform hydrogen pre-charging of 1 wppm is assumed, and crack growth resistance curves are computed for selected values of the loading rate $\dot{K}_I/K_0$. The results, shown in Fig. 10, exhibit the expected trends: slower loading rates emphasize embrittlement and lead to less steep R-curves. As we increase the loading rate there is less time for the hydrogen to diffuse to the fracture process zone, where σ_H is large, and the hydrogen-induced degradation of the local fracture energy is less severe (relative to slower loading rates).

The crack growth resistance results presented show that the model can rationalise and capture the transition to brittle fracture due to hydrogen, as well as reproducing the main experimental trends (sensitivity to loading rate and hydrogen concentration).

4.2. Comparison with experiments: Predicting the onset of cracking in ultra-high strength steel (AerMet100)

We proceed to compare model predictions with experimental measurements of stress intensity thresholds K_{th} for crack initiation. This analysis is inspired by the encouraging agreement with experiments on ultra-high alloys obtained by Martínez-Pañeda et al. (2016b). In their work, strain gradient plasticity analyses of crack tip fields and electrochemical assessment of hydrogen solubility were integrated into Gerberich (2012) dislocation-based model. Cracking thresholds K_{th} and stage II crack growth rates da/dt_{II} predictions showed a very good agreement with experiments conducted over a wide range of applied potentials on a nickel superalloy, Monel K-500, and on an ultra-high strength steel, AerMet100. Here, we seek to demonstrate the same capability for our proposed model which explicitly models both cracking and hydrogen transport. Attention is limited to the case of the modern ultra-high strength steel AerMet100 and the estimation of the threshold stress intensity factor K_{th}.

As detailed in (Lee and Gangloff, 2007; Pioszak and Gangloff, 2017), pre-cracked fracture mechanics specimens were subjected to slowly increasing mode I loading, while submerged in an aqueous solution of 0.6 M NaCl. Loading is feedback

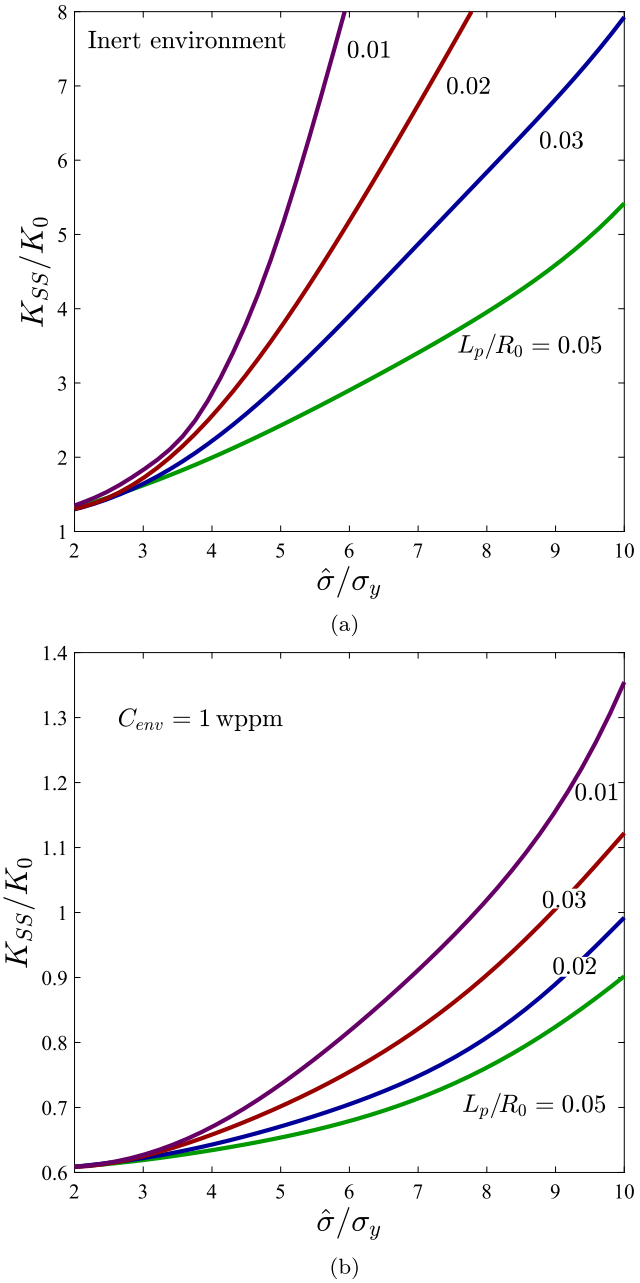

Fig. 9. Steady state fracture toughness K_{SS}/K_0 as a function of the cohesive strength $\hat{\sigma}/\sigma_y$ for selected values of L_p/R_0: (a) inert environment, and (b) hydrogenous environment, with $C_{env} = 1$ wppm. Material properties: $\sigma_y/E = 0.003$, $\nu = 0.3$, $N = 0.2$, $D = 0.0127$ mm^2/s and $\chi = 0.89$. Loading rate $\dot{K}_I/K_0 = 4 \times 10^{-7}$ s^{-1}.

Table 1
Material parameters for AerMet100.

E [GPa]	ν [-]	σ_y [MPa]	N [-]	D [cm^2/s]
194	0.3	1725	0.077	1×10^{-9}

controlled such that after an initial loading to 6 MPa$\sqrt{\text{m}}$, the loading rate is held constant at $\dot{K} = 6.8 \cdot 10^{-4}$ MPa$\sqrt{\text{m}}$/s. A wide range of environments are considered, with the applied potential ranging from -1.1 to -0.5 V_{SCE}. The measured material properties of AerMet100 are given in Table 1 (Lee and Gangloff, 2007).

The reference plastic length scale is chosen to be equal to $L_p = 5$ μm, an intermediate value within the range of experimentally measured length scales reported in the literature (Fuentes-Alonso and Martínez-Pañeda, 2020). The phase field length scale ℓ is chosen appropriately such that the material strength corresponds to the cleavage strength $\hat{\sigma}/\sigma_y = 10$. Regarding the fracture and hydrogen damage properties, the choice of G_c (or K_0) will establish the maximum value of K_{th}

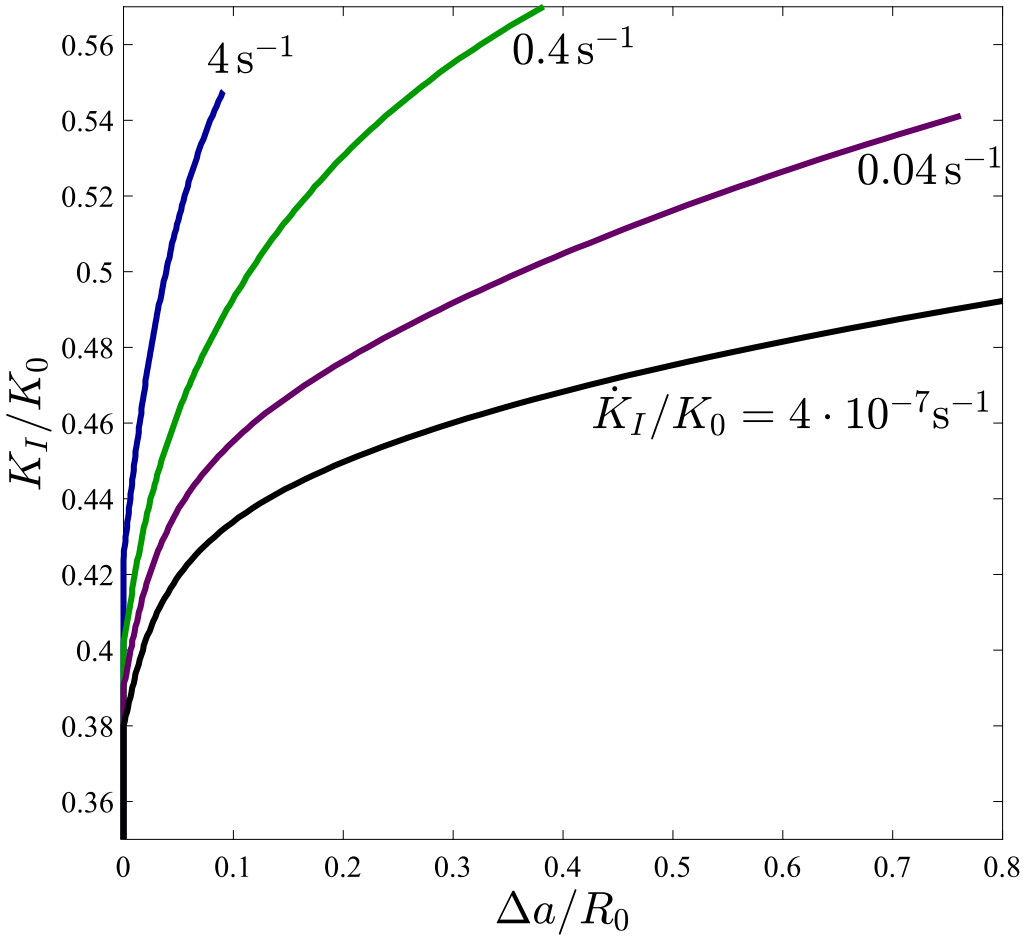

Fig. 10. Influence of the loading rate $\dot{K}_I/K_0$ on the fracture resistance in a sample pre-charged uniformly with a hydrogen concentration of 1 wppm. Material properties: $\sigma_y/E = 0.003$, $\nu = 0.3$, $N = 0.2$, $\ell/R_0 = 1/60$, $L_p/R_0 = 0.01$, $D = 0.0127$ mm^2/s and $\chi = 0.89$.

that can be reached. Since our model and choice of material strength aim at reproducing quasi-cleavage, we choose K_0 to approximately match the maximum value of K_{th} that is attained in the experiments without observing ductile fracture features. According to Pioszak and Gangloff (2017), when soluble hydrogen is below 0.8 wppm, corresponding to the potential range $E_p = -0.770$ V_{SCE} to -0.667 V_{SCE}, part of the fracture process is controlled by void coalescence. Hence, we assume $K_0 = 30$ MPa$\sqrt{m}$. The hydrogen damage coefficient χ is calibrated to provide a best fit to the experiments and our choice is subsequently discussed.

Small scale yielding conditions are assumed, and a boundary layer formulation is employed, as illustrated in Fig. 3. The remote K-field is applied at a constant rate of $\dot{K} = 7.0 \cdot 10^{-4}$ MPa$\sqrt{m}$/s. The rate-independent limit for the viscoplastic law is attained using the measures described in Section 4.1.2. The diffusible hydrogen concentration associated with each value of the applied potential is obtained from the analysis by Kehler and Scully (2008). For an applied potential E_p below -0.75 V_{SCE}, both the upper and lower bounds of the crack tip soluble hydrogen are given by:

$$C_{env}(\text{wppm}) = 19.125E_p^3 + 78.568E_p^2 + 80.026E_p + 24.560\ (\text{V}_{\text{SCE}}) \tag{57}$$

For potentials above -0.75V_{SCE}, the upper bound solution is applied, which is given by:

$$C_{env}(\text{wppm}) = -739.24E_p^5 - 3121.1E_p^4 - 5147.1E_p^3 - 4099.2E_p^2 - 1563.8E_p - 225.77\ (\text{V}_{\text{SCE}}) \tag{58}$$

The crack initiation threshold K_{th} predictions of the present model are shown in Fig. 11, along with experimental results for AerMet100 and Ferrium M54, a similar alloy (Martínez-Pañeda et al., 2016b; Pioszak and Gangloff, 2017). A very good agreement with experiments is observed over the range of potentials where fracture is reported as quasi-brittle. The best fit is given for a choice of the hydrogen damage coefficient equal to $\chi = 0.97$. This value is above the first principles estimate for iron, $\chi = 0.89$, see (Jiang and Carter, 2004; Martínez-Pañeda et al., 2018). However, the choice of the hydrogen damage coefficient that best fits the experimental results is sensitive to the choice of trap binding energy; $\Delta g_b^0 = 30$ kJ/mol in Eq. (28). Traps with higher binding energies than 30 kJ/mol are likely to be present in AerMet100 and participate in the fracture process (Li et al., 2004).

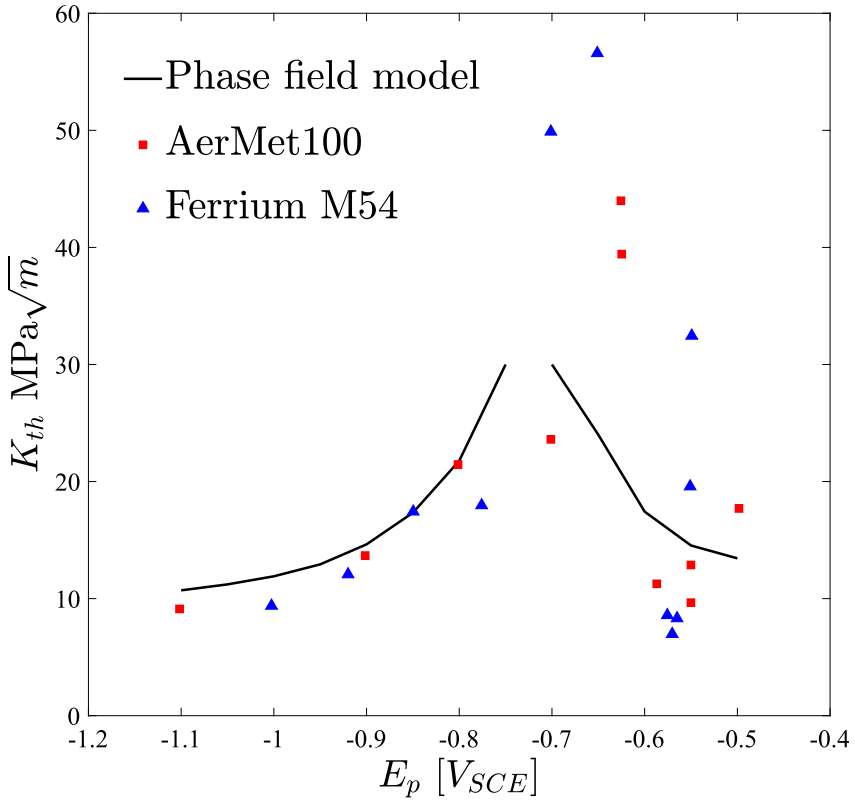

Fig. 11. Stress intensity threshold K_{th} predictions as a function of the applied potential. The experimental results obtained in AerMet100 and Ferrium M54 by Gangloff and co-workers (Lee and Gangloff, 2007; Martínez-Pañeda et al., 2016b; Pioszak and Gangloff, 2017) are shown for comparison. Ductile fracture features are observed in the range $E_p = -0.770$ V_{SCE} to -0.667 V_{SCE}.

5. Conclusions

We have presented a new coupled deformation-diffusion-fracture theory for modeling hydrogen embrittlement in elastic-plastic solids. The model builds upon a stress-assisted diffusion formulation, driven by chemical potential gradients, and a chemo-mechanical phase field description of fracture. A fracture energy degradation law is defined that establishes a direct and quantitative connection with atomistic calculations of surface energy reduction with hydrogen coverage. More importantly, the model takes into consideration the role of plastic strain gradients and the associated dislocation hardening mechanisms. The aim is to capture the flow strength elevation observed in mechanical tests involving non-homogeneous plastic deformation and in crack tip discrete dislocation dynamics simulations. Both energetic hardening and dissipative strengthening dislocations mechanisms are considered through their associated plastic length scales: L_E and L_D, respectively. In addition, the model is also non-local with respect to the damage variable, with a phase field length scale entering the constitutive relations due to dimensional consistency. Starting from the principle of virtual work, chemical-, micro- and macro-force balances are derived, together with a standard free-energy imbalance. The formulation is completed with a set of thermodynamically-consistent constitutive equations for the deformation, diffusion and fracture problems.

The coupled model is implemented in a four-field finite element framework, with displacements, plastic strains, hydrogen concentration and phase field parameter being the primary kinematic variables. Suitable *moving* chemical boundary conditions, viscoplastic function and energy split are introduced, and the coupled problem is solved in an implicit time integration scheme. Numerical calculations are conducted to gain fundamental physical insight and showcase the capabilities of the model. First, the role of plastic strain gradients in elevating crack tip stresses and hydrogen concentrations is assessed in the context of stationary cracks. Much higher crack tip stresses and hydrogen concentrations are predicted, relative to conventional plasticity, providing a suitable physical ground for atomic-scale decohesion. Crack growth resistance curves (R-curves) are computed to elucidate the interplay between the different plastic and fracture length scales involved in the formulation. Increasing L_E or L_D relative to the plastic zone size reduces the steepness of the R-curve, as gradient hardening is exacerbated. On the other side, decreasing the magnitude of the phase field length scale is equivalent to augmenting the strength $\hat{\sigma}$, leading to an increased fracture resistance. The steady state fracture toughness is computed as a function of $\hat{\sigma}/\sigma_y$ to gain insight into the underlying fracture mechanism; brittle fracture occurs when the strength is on the order of $10\sigma_y$ or larger, following lattice and grain boundary strength arguments. Results reveal a high sensitivity to the ratio of the reference plastic length scale, $L_p = L_D = L_E$, to the fracture process zone R_0, whose magnitude is mainly governed by the work of fracture G_c. In the absence of hydrogen, brittle fracture is only predicted for large values of L_p/R_0, characteristic of

low fracture energy material systems, such as metal-ceramic interfaces or ferritic steels at low temperatures. However, when hydrogen is taken into consideration, the fracture energy is substantially reduced and brittle fracture is predicted also for ductile metals, where L_p/R_0 is initially small. Therefore, a framework is proposed that can rationalise quasi-cleavage in the presence of plasticity and the change from microvoid cracking to brittle fracture observed in ductile steels in the presence of hydrogen. Lastly, the quantitative predictive capabilities of the model have been benchmarked by reproducing mode I fracture experiments on an ultra-high strength steel, AerMet100. The results obtained under a wide range of applied potentials reveal a promising agreement with experiments.

Credit Author Statement

Philip K. Kristensen: Investigation, Methodology, Software, Writing – original draft, Writing – review & editing. **Christian F. Niordson**: Conceptualization, Funding acquisition, Investigation, Supervision, Writing – review & editing. **Emilio Martínez Pañeda**: Conceptualization, Funding acquisition, Investigation, Methodology, Software, Supervision, Writing – original draft, Writing – review & editing.

Declaration of Competing Interest

The authors declare no conflict of interest.

Acknowledgments

The authors gratefully acknowledge financial support from the Danish Hydrocarbon Research and Technology Centre (DHRTC) under the "Reliable in-service assessment in aggressive environments" project, publication number DHRTC-PRP-101. E. Martínez-Pañeda also acknowledges financial support from ExxonMobil, Wolfson College Cambridge (Junior Research Fellowship) and from the Royal Commission for the 1851 Exhibition through their Research Fellowship programme (RF496/2018). C.F. Niordson additionally acknowledges support from the Danish Council for Independent Research through the research project "Advanced Damage Models with InTrinsic Size Effects" (Grant no: DFF-7017-00121).

Appendix A. Details of numerical implementation

Here, we provide explicit expressions for the matrix operators and the stiffness matrix components used in Section 3.2.

A1. Matrix operators

Assuming plane strain conditions, for a node i, the nodal solutions to the deformation problem read:

$$\hat{\mathbf{u}}_i = [\hat{u}_1^i,\ \hat{u}_2^i]\ , \qquad \hat{\boldsymbol{\varepsilon}}_i^p = [\varepsilon_{11}^{p\,i},\ \varepsilon_{22}^{p\,i},\ \varepsilon_{12}^{p\,i},\ \varepsilon_{13}^{p\,i},\ \varepsilon_{23}^{p\,i}]. \tag{A.1}$$

Accordingly, the shape function matrices are given as follows:

$$\boldsymbol{N}_i^{\mathbf{u}} = \begin{bmatrix} N_i & 0 \\ 0 & N_i \end{bmatrix}, \quad \boldsymbol{N}_i^{\boldsymbol{\varepsilon}^p} = \begin{bmatrix} N_i & 0 & 0 \\ 0 & N_i & 0 \\ -N_i & -N_i & 0 \\ 0 & 0 & N_i \end{bmatrix}, \tag{A.2}$$

while the gradient quantities are discretised using:

$$\mathbf{B}_i = \begin{bmatrix} \frac{\partial N_i}{\partial x} \\ \frac{\partial N_i}{\partial y} \end{bmatrix}, \qquad \boldsymbol{B}_i^{\mathbf{u}} = \begin{bmatrix} \frac{\partial N_i}{\partial x} & 0 \\ 0 & \frac{\partial N_i}{\partial y} \\ 0 & 0 \\ \frac{\partial N_i}{\partial y} & \frac{\partial N_i}{\partial x} \end{bmatrix}, \qquad \boldsymbol{B}_i^{\boldsymbol{\varepsilon}^p} = \begin{bmatrix} \frac{\partial N_i}{\partial x} & 0 & 0 \\ \frac{\partial N_i}{\partial y} & 0 & 0 \\ 0 & \frac{\partial N_i}{\partial x} & 0 \\ 0 & \frac{\partial N_i}{\partial y} & 0 \\ -\frac{\partial N_i}{\partial x} & -\frac{\partial N_i}{\partial x} & 0 \\ -\frac{\partial N_i}{\partial y} & -\frac{\partial N_i}{\partial y} & 0 \\ 0 & 0 & \frac{\partial N_i}{\partial x} \\ 0 & 0 & \frac{\partial N_i}{\partial y} \end{bmatrix}. \tag{A.3}$$

A2. Stiffness matrix components

The stiffness matrix is constructed by differentiating the residuals with respect to the nodal variables. The entries related purely to the displacement field may thus be found as:

$$\boldsymbol{K}_{ij}^{\mathbf{u},\mathbf{u}} = \frac{\partial \mathbf{R}_i^{\mathbf{u}}}{\partial \mathbf{u}_j} = \int_\Omega \left[(1-\phi)^2 + k\right] \left(\boldsymbol{B}_i^{\mathbf{u}}\right)^T \boldsymbol{\mathcal{L}}_0 \boldsymbol{B}_i^{\mathbf{u}} \, \mathrm{d}V. \tag{A.4}$$

In a similar manner, the plastic strain field stiffness is given by:

$$\begin{aligned}\boldsymbol{K}_{ij}^{\boldsymbol{\varepsilon}^p,\boldsymbol{\varepsilon}^p} = \frac{\partial \mathbf{R}_i^{\boldsymbol{\varepsilon}^p}}{\partial \boldsymbol{\varepsilon}_j^p} = \int_\Omega \Bigg\{ \left(\boldsymbol{N}_i^{\boldsymbol{\varepsilon}^p}\right)^T \Bigg[\left(\frac{\partial \boldsymbol{q}^D}{\partial \boldsymbol{\varepsilon}_j^p} - \left[(1-\phi)^2 + k\right] \boldsymbol{\mathcal{L}}_0 \right) \boldsymbol{N}_j^{\boldsymbol{\varepsilon}^p} + \frac{\partial \boldsymbol{q}^D}{\partial \nabla \boldsymbol{\varepsilon}_j^p} \boldsymbol{B}_j^{\boldsymbol{\varepsilon}^p} \Bigg] \\ + \left(\boldsymbol{B}_i^{\boldsymbol{\varepsilon}^p}\right)^T \left(\frac{\partial \boldsymbol{\tau}^D}{\partial \boldsymbol{\varepsilon}_j^p} \boldsymbol{N}_j^{\boldsymbol{\varepsilon}^p} + \frac{\partial \boldsymbol{\tau}^D}{\partial \nabla \boldsymbol{\varepsilon}_j^p} \boldsymbol{B}_j^{\boldsymbol{\varepsilon}^p} + \frac{\partial \boldsymbol{\tau}^E}{\partial \nabla \boldsymbol{\varepsilon}_j^p} \boldsymbol{B}_j^{\boldsymbol{\varepsilon}^p} \right) \Bigg\} \, \mathrm{d}V.\end{aligned} \tag{A.5}$$

The coupling terms are found as:

$$\boldsymbol{K}_{ij}^{\mathbf{u},\boldsymbol{\varepsilon}^p} = \frac{\partial \mathbf{R}_i^{\mathbf{u}}}{\partial \boldsymbol{\varepsilon}_j^p} = -\int_\Omega \left[(1-\phi)^2 + k\right] \left(\boldsymbol{B}_i^{\mathbf{u}}\right)^T \boldsymbol{\mathcal{L}}_0 \boldsymbol{N}_j^{\boldsymbol{\varepsilon}^p} \, \mathrm{d}V, \tag{A.6}$$

$$\boldsymbol{K}_{ij}^{\boldsymbol{\varepsilon}^p,\mathbf{u}} = \frac{\partial \mathbf{R}_i^{\boldsymbol{\varepsilon}^p}}{\partial \mathbf{u}_j} = -\int_\Omega \left[(1-\phi)^2 + k\right] \left(\boldsymbol{N}^{\boldsymbol{\varepsilon}^p}\right)^T \boldsymbol{\mathcal{L}}_0 \boldsymbol{B}_j^{u} \, \mathrm{d}V. \tag{A.7}$$

The stiffness related to the crack phase field is determined in an equivalent manner:

$$\boldsymbol{K}_{ij}^{\phi,\phi} = \frac{\partial R_i^{\phi}}{\partial \phi_j} = \int_\Omega \left[\left(2H + \frac{G_c}{\ell}\right) N_i N_j + G_c \ell \mathbf{B}_i^T \mathbf{B}_j \right] \mathrm{d}V. \tag{A.8}$$

Finally, the contributions from the mass transport of hydrogen in the metal lattice include a diffusivity matrix:

$$\boldsymbol{K}_{ij}^{C,C} = \int_\Omega \left(\mathbf{B}_i^T \mathbf{B}_j - \mathbf{B}_i^T \frac{\overline{V}_H}{RT} \nabla \sigma_H N_j \right) \mathrm{d}V, \tag{A.9}$$

and a concentration capacity matrix:

$$\boldsymbol{M}_{ij} = \int_\Omega N_i^T \frac{1}{D} N_j \, \mathrm{d}V. \tag{A.10}$$

The complete element assemble is given by (38), where the time derivative of the hydrogen concentration $\dot{C}$ is discretised in an analogous manner to C.

References

Alessi, R., Ambati, M., Gerasimov, T., Vidoli, S., De Lorenzis, L., 2018. Comparison of Phase-Field Models of Fracture Coupled with Plasticity. In: E. Oñate, D. Peric, E. de Souza-Neto, M.C. (Ed.), Advances in Computational Plasticity. Springer Nature, pp. 1–21.

Alvaro, A., Thue Jensen, I., Kheradmand, N., Løvvik, O.M., Olden, V., 2015. Hydrogen embrittlement in nickel, visited by first principles modeling, cohesive zone simulation and nanomechanical testing. Int. J. Hydrogen Energy 40 (47), 16892–16900.

Ambati, M., Gerasimov, T., De Lorenzis, L., 2015. A review on phase-field models of brittle fracture and a new fast hybrid formulation. Comput. Mech. 55, 383–405.

Amor, H., Marigo, J.J., Maurini, C., 2009. Regularized formulation of the variational brittle fracture with unilateral contact: numerical experiments. J. Mech. Phys. Solids 57 (8), 1209–1229.

Anand, L., Gurtin, M.E., Lele, S.P., Gething, C., 2005. A one-dimensional theory of strain-gradient plasticity: formulation, analysis, numerical results. J. Mech. Phys. Solids 53 (8), 1789–1826.

Anand, L., Mao, Y., Talamini, B., 2019. On modeling fracture of ferritic steels due to hydrogen embrittlement. J. Mech. Phys. Solids 122, 280–314.

Ashby, M.F., 1970. The deformation of plastically non-homogeneous materials. Philos. Mag. 21 (170), 399–424.

Bagchi, A., Evans, A.G., 1996. The mechanics and physics of thin-film decohesion and its measurement. Interface Sci. 3, 169–193.

Balint, D.S., Deshpande, V.S., Needleman, A., Van Der Giessen, E., 2005. Discrete dislocation plasticity analysis of crack-tip fields in polycrystalline materials. Philos. Mag. 85, 3047–3071.

Borden, M.J., Hughes, T.J.R., Landis, C.M., Anvari, A., Lee, I.J., 2016. A phase-field formulation for fracture in ductile materials: finite deformation balance law derivation, plastic degradation, and stress triaxiality effects. Comput. Methods Appl. Mech. Eng. 312, 130–166.

Borden, M.J., Verhoosel, C.V., Scott, M.A., Hughes, T.J.R., Landis, C.M., 2012. A phase-field description of dynamic brittle fracture. Comput. Methods Appl. Mech. Eng. 217–220, 77–95.

Bourdin, B., Francfort, G.A., Marigo, J.J., 2000. Numerical experiments in revisited brittle fracture. J. Mech. Phys. Solids 48 (4), 797–826.

del Busto, S., Betegón, C., Martínez-Pañeda, E., 2017. A cohesive zone framework for environmentally assisted fatigue. Eng. Fract. Mech. 185, 210–226.

Cajuhi, T., Sanavia, L., De Lorenzis, L., 2018. Phase-field modeling of fracture in variably saturated porous media. Comput. Mech. 61 (3), 299–318.

Carollo, V., Reinoso, J., Paggi, M., 2017. A 3D finite strain model for intralayer and interlayer crack simulation coupling the phase field approach and cohesive zone model. Compos. Struct. 182, 636–651.

Chakravarthy, S.S., Curtin, W.A., 2010. Origin of plasticity length-scale effects in fracture. Phys. Rev. Lett. 105 (11), 1–4.

Díaz, A., Alegre, J.M., Cuesta, I.I., 2016. Coupled hydrogen diffusion simulation using a heat transfer analogy. Int. J. Mech. Sci. 115–116, 360–369.

Dillon, O.W., Kratochvil, J., 1970. A strain gradient theory of plasticity. Int. J. Solids Struct. 6 (12), 1513–1533.

Duda, F.P., Ciarbonetti, A., Sánchez, P.J., Huespe, A.E., 2015. A phase-field/gradient damage model for brittle fracture in elastic-plastic solids. Int. J. Plast. 65, 269–296.

Duda, F.P., Ciarbonetti, A., Toro, S., Huespe, A.E., 2018. A phase-field model for solute-assisted brittle fracture in elastic-plastic solids. Int. J. Plast. 102, 16–40.
Elssner, G., Korn, D., Rühle, M., 1994. The influence of interface impurities on fracture energy of UHV diffusion bonded metal-ceramic bicrystals. Scr. Metall. Mater. 31 (8), 1037–1042.
Fleck, N.A., Hutchinson, J.W., 2001. A reformulation of strain gradient plasticity. J. Mech. Phys. Solids 49 (10), 2245–2271.
Fleck, N.A., Muller, G.M., Ashby, M.F., Hutchinson, J.W., 1994. Strain gradient plasticity: theory and experiment. Acta Metall. Mater. 42 (2), 475–487.
Fleck, N.A., Willis, J.R., 2009. A mathematical basis for strain-gradient plasticity theory. part II: tensorial plastic multiplier. J. Mech. Phys. Solids 57 (7), 1045–1057.
Francfort, G., Marigo, J.-J., 1998. Revisiting brittle fracture as an energy minimization problem. J. Mech. Phys. Solids 46 (8), 1319–1342.
Fuentes-Alonso, S., Martínez-Pañeda, E., 2020. Fracture in distortion gradient plasticity. (submitted).
Gangloff, R.P., 2003. Diffusion control of hydrogen environment embrittlement in high strength alloys. In: Moody, N.R., Thompson, A.W., Ricker, R.E., Was, G.S., Jones, R.H. (Eds.), Hydrogen Effects on Material Behavior and Corrosion Deformation Interactions. The Minerals, Metals & Materials Society, Warrendale, pp. 477–497.
Gangloff, R.P., 2003. Hydrogen-assisted Cracking. In: Milne, I., Ritchie, R., Karihaloo, B. (Eds.), Comprehensive Structural Integrity Vol. 6. Elsevier Science, New York, NY, pp. 31–101.
Gangloff, R.P., Somerday, B.P., 2012. Gaseous Hydrogen Embrittlement of Materials in Energy Technologies. Woodhead Publishing Limited, Cambridge.
Gao, H., Hang, Y., Nix, W.D., Hutchinson, J.W., 1999. Mechanism-based strain gradient plasticity - I. theory. J. Mech. Phys. Solids 47 (6), 1239–1263.
Gerberich, W.W., 2012. Modeling hydrogen induced damage mechanisms in metals. In: Gangloff, R.P., Somerday, B.P. (Eds.), Gaseous Hydrogen Embrittlement of Materials in Energy Technologies Vol. II. Woodhead Publishing, pp. 209–246.
Griffith, A., 1920. The phenomena of rupture and flow in solids. Philos. Trans. A, 221, 163–198.
Gudmundson, P., 2004. A unified treatment of strain gradient plasticity. J. Mech. Phys. Solids 52 (6), 1379–1406.
Harris, Z.D., Lawrence, S.K., Medlin, D.L., Guetard, G., Burns, J.T., Somerday, B.P., 2018. Elucidating the contribution of mobile hydrogen-deformation interactions to hydrogen-induced intergranular cracking in polycrystalline nickel. Acta Mater. 158, 180–192.
Hirshikesh, Natarajan, S., Annabattula, R.K., Martínez-Pañeda, E., 2019. Phase field modelling of crack propagation in functionally graded materials. Compos. Part B 169, 239–248.
Hirth, J.P., 1980. Effects of hydrogen on the properties of iron and steel. Metall. Trans. A 11 (6), 861–890.
Irwin, G.R., 1956. Onset of Fast Crack Propagation in High Strength Steel and Aluminum Alloys. In: Sagamore Research Conference Proceedings Vol. 2, pp. 289–305.
Jiang, D.E., Carter, E.A., 2004. First principles assessment of ideal fracture energies of materials with mobile impurities: implications for hydrogen embrittlement of metals. Acta Mater. 52 (16), 4801–4807.
Juul, K.J., Martínez-Pañeda, E., Nielsen, K.L., Niordson, C.F., 2019. Steady-state fracture toughness of elastic-plastic solids: isotropic versus kinematic hardening. Eng. Fract. Mech. 207, 254–268.
Kehler, B.A., Scully, J.R., 2008. Predicting the effect of applied potential on crack tip hydrogen concentration in low-alloy martensitic steels. Corrosion 64 (5), 465–477.
Kirchheim, R., 2004. Solid solutions of hydrogen in complex materials. In: Ehrenreich, H., Spaepen, F. (Eds.), Solid State Physics, 59. Elsevier Inc., pp. 203–291.
Kirchheim, R., Somerday, B.P., Sofronis, P., 2015. Chemomechanical effects on the separation of interfaces occurring during fracture with emphasis on the hydrogen-iron and hydrogen-nickel system. Acta Mater. 99, 87–98.
Komaragiri, U., Agnew, S.R., Gangloff, R.P., Begley, M.R., 2008. The role of macroscopic hardening and individual length-scales on crack tip stress elevation from phenomenological strain gradient plasticity. J. Mech. Phys. Solids 56 (12), 3527–3540.
Korn, D., Elssner, G., Cannon, R.M., Ruhle, M., 2002. Fracture properties of interfacially doped Nb-A12O3 bicrystals: i, fracture characteristics. Acta Mater. 50 (15), 3881–3901.
Kristensen, P.K., Martínez-Pañeda, E., 2020. Phase field fracture modelling using quasi-Newton methods and a new adaptive step scheme. Theor. Appl. Fract. Mech. 107, 102446.
Lee, Y., Gangloff, R.P., 2007. Measurement and modeling of hydrogen environment-assisted cracking of ultra-high-strength steel. Metall. Mater. Trans. A 38 A (13), 2174–2190.
Legarth, B.N., Niordson, C.F., 2010. Debonding failure and size effects in micro-reinforced composites. Int. J. Plast. 26 (1), 149–165.
Li, D., Gangloff, R.P., Scully, J.R., 2004. Hydrogen trap states in ultrahigh-Strength AERMET 100 steel. Metall. Mater. Trans. A 35 A (3), 849–864.
Liu, H.W., 1970. Stress-corrosion cracking and the interaction between crack-tip stress field and solute atoms. J. Basic Eng. Trans. ASME 92 (3), 633–638.
Lynch, S., 2019. Discussion of some recent literature on hydrogen-embrittlement mechanisms: addressing common misunderstandings. Corros. Rev. 37 (5), 377–395.
Mao, S.X., Li, M., 1998. Mechanics and thermodynamics on the stress and hydrogen interaction in crack tip stress corrosion : experiment and theory. J. Mech. Phys. Solids 46 (6), 1125–1137.
Martínez-Pañeda, E., Betegón, C., 2015. Modeling damage and fracture within strain-gradient plasticity. Int. J. Solids Struct. 59, 208–215.
Martínez-Pañeda, E., del Busto, S., Niordson, C.F., Betegón, C., 2016. Strain gradient plasticity modeling of hydrogen diffusion to the crack tip. Int. J. Hydrogen Energy 41 (24), 10265–10274.
Martínez-Pañeda, E., Deshpande, V.S., Niordson, C.F., Fleck, N.A., 2019. The role of plastic strain gradients in the crack growth resistance of metals. J. Mech. Phys. Solids 126, 136–150.
Martínez-Pañeda, E., Fleck, N.A., 2018. Crack growth resistance in metallic alloys: the role of isotropic versus kinematic hardening. Journal of Applied Mechanics 85. 11002 (6 pages)
Martínez-Pañeda, E., Fleck, N.A., 2019. Mode I crack tip fields: strain gradient plasticity theory versus J2 flow theory. Eur. J. Mech. A. Solids 75, 381–388.
Martínez-Pañeda, E., Fuentes-Alonso, S., Betegón, C., 2019. Gradient-enhanced statistical analysis of cleavage fracture. Eur. J. Mech. A. Solids 77, 103785.
Martínez-Pañeda, E., Golahmar, A., Niordson, C.F., 2018. A phase field formulation for hydrogen assisted cracking. Comput. Methods Appl. Mech. Eng. 342, 742–761.
Martínez-Pañeda, E., Harris, Z.D., Fuentes-Alonso, S., Scully, J.R., Burns, J.T., 2020. On the suitability of slow strain rate tensile testing for assessing hydrogen embrittlement susceptibility. Corros. Sci. 163, 108291.
Martínez-Pañeda, E., Niordson, C.F., 2016. On fracture in finite strain gradient plasticity. Int. J. Plast. 80, 154–167.
Martínez-Pañeda, E., Niordson, C.F., Gangloff, R.P., 2016. Strain gradient plasticity-based modeling of hydrogen environment assisted cracking. Acta Mater. 117, 321–332.
McAuliffe, C., Waisman, H., 2016. A coupled phase field shear band model for ductile-brittle transition in notched plate impacts. Comput. Methods Appl. Mech. Eng. 305, 173–195.
Miehe, C., Aldakheel, F., Raina, A., 2016. Phase field modeling of ductile fracture at finite strains: a variational gradient-extended plasticity-damage theory. Int. J. Plast. 84, 1–32.
Miehe, C., Dal, H., Schanzel, L.-M., Raina, A., 2016. A phase-field model for chemo-mechanical induced fracture in lithium-ion battery electrode particles. Int. J. Numer. Methods Eng. 106, 683–711.
Miehe, C., Hofacker, M., Welschinger, F., 2010. A phase field model for rate-independent crack propagation: robust algorithmic implementation based on operator splits. Comput. Methods Appl. Mech. Eng. 199 (45–48), 2765–2778.
Mikelic, A., Wheeler, M., Wick, T., 2015. A phase-field method for propagating fluid-filled fractures coupled to a surrounding porous medium. Multiscale Model. Simullat. 13, 367–398.
Moriconi, C., Hénaff, G., Halm, D., 2014. Cohesive zone modeling of fatigue crack propagation assisted by gaseous hydrogen in metals. Int. J. Fatigue 68, 56–66.

Nielsen, K.L., Niordson, C.F., 2013. A 2D finite element implementation of the Fleck-Willis strain-gradient flow theory. Eur. J. Mech. A/Solids 41, 134–142.
Nix, W.D., Gao, H.J., 1998. Indentation size effects in crystalline materials: alaw for strain gradient plasticity. J. Mech. Phys. Solids 46 (3), 411–425.
O'dowd, N.P., Stout, M.G., Shih, C.F., 1992. Fracture toughness of alumina-niobium interfaces: experiments and analyses. Philos. Mag. A 66 (6), 1037–1064.
Panteghini, A., Bardella, L., 2016. On the finite element implementation of higher-order gradient plasticity, with focus on theories based on plastic distortion incompatibility. Comput. Methods Appl. Mech. Eng. 310, 840–865.
Papazafeiropoulos, G., Muñiz-Calvente, M., Martínez-Pañeda, E., 2017. Abaqus2Matlab: a suitable tool for finite element post-processing. Adv. Eng. Softw. 105, 9–16.
Pham, K., Amor, H., Marigo, J.J., Maurini, C., 2011. Gradient damage models and their use to approximate brittle fracture. Int. J. Damage Mech. 20 (4), 618–652.
Pioszak, G.L., Gangloff, R.P., 2017. Hydrogen environment assisted cracking of modern ultra-High strength martensitic steels. Metall. Mater. Trans. A 48 (9), 4025–4045.
Qian, X., Zhang, S., Swaddiwudhipong, S., 2011. Calibration of weibull parameters using the conventional mechanism-based strain gradient plasticity. Eng. Fract. Mech. 78 (9), 1928–1944.
Quintanas-Corominas, A., Reinoso, J., Casoni, E., Turon, A., Mayugo, J.A., 2019. A phase field approach to simulate intralaminar and translaminar fracture in long fiber composite materials. Compos. Struct. 220, 899–911.
Renard, Y., Poulios, K., 2020. Getfem: automated FE modeling of multiphysics problems based on a generic weak form language. (submitted).
Robertson, I.M., Sofronis, P., Nagao, A., Martin, M.L., Wang, S., Gross, D.W., Nygren, K.E., 2015. Hydrogen embrittlement understood. Metallurg. Mater. Trans. B 46 (3), 1085–1103.
Scheider, I., Pfuff, M., Dietzel, W., 2008. Simulation of hydrogen assisted stress corrosion cracking using the cohesive model. Eng. Fract. Mech. 75 (15), 4283–4291.
Seiler, P.E., Siegmund, T., Zhang, Y., Tomar, V., Kruzic, J.J., 2016. Stationary and propagating cracks in a strain gradient visco-plastic solid. Int. J. Fract. 202 (1), 111–125.
Serebrinsky, S., Carter, E.A., Ortiz, M., 2004. A quantum-mechanically informed continuum model of hydrogen embrittlement. J. Mech. Phys. Solids 52 (10), 2403–2430.
Shishvan, S.S., Csányi, G., Deshpande, V.S., 2020. Hydrogen induced fast-fracture. J. Mech. Phys. Solids 134, 103740.
Sofronis, P., McMeeking, R.M., 1989. Numerical analysis of hydrogen transport near a blunting crack tip. J. Mech. Phys. Solids 37 (3), 317–350.
Suo, Z., Shih, C.F., Varias, A.G., 1993. A theory for cleavage cracking in the presence of plastic flow. Acta Metall. Mater. 41 (5), 1551–1557.
Tehranchi, A., Curtin, W.A., 2019. The role of atomistic simulations in probing hydrogen effects on plasticity and embrittlement in metals. Eng. Fract. Mech. 216, 106502.
Tvergaard, V., Hutchinson, J.W., 1992. The relation between crack growth resistance and fracture process parameters in elastic-plastic solids. J. Mech. Phys. Solids 40 (6), 1377–1397.
Van der Ven, A., Ceder, G., 2003. Impurity-induced van der waals transition during decohesion. Phys. Rev. B 67 (6), 1–4.
Voyiadjis, G.Z., Song, Y., 2019. Strain gradient continuum plasticity theories: theoretical, numerical and experimental investigations. Int. J. Plast. 121, 21–75.
Wang, J.S., Anderson, P.M., 1991. Fracture behavior of embrittled F.C.C. metal bicrystals. Acta Metall. Mater. 39 (5), 779–792.
Wei, Y., Hutchinson, J.W., 1997. Steady-state crack growth and work of fracture for solids characterized by strain gradient plasticity. J. Mech. Phys. Solids 45 (8), 1253–1273.
Wu, J.-Y., Mandal, T.K., Nguyen, V.P., 2020. A phase-field regularized cohesive zone model for hydrogen assisted cracking. Comput. Methods Appl. Mech. Eng. 358, 112614.
Wu, J.-Y., Nguyen, V.P., Nguyen, C.T., Sutula, D., Sinaie, S., Bordas, S., 2020. Phase-field modelling of fracture. Adv. Appl. Mech. 53.
Yu, H., Cocks, A., Tarleton, E., 2019. Discrete dislocation plasticity HELPs understand hydrogen effects in bcc materials. J. Mech. Phys. Solids 123, 41–60.
Yu, H., Olsen, J.S., Olden, V., Alvaro, A., He, J., Zhang, Z., 2017. Continuum level simulation of the grain size and misorientation effects on hydrogen embrittlement in nickel. Eng. Fail. Anal. 81, 79–93.
Zhao, Y., Xu, B.X., Stein, P., Gross, D., 2016. Phase-field study of electrochemical reactions at exterior and interior interfaces in Li-ion battery electrode particles. Comput. Methods Appl. Mech. Eng. 312, 428–446.
Zhou, S., Zhuang, X., Zhu, H., Rabczuk, T., 2018. Phase field modelling of crack propagation, branching and coalescence in rocks. Theor. Appl. Fract. Mech. 96, 174–192.

DTU Construct
Section of Solid Mechanics
Technical University of Denmark

Koppels Allé, Bld. 404
DK-2800 Kgs. Lyngby
Denmark
Tlf.: +45 4525 4250
Fax: +45 4525 1961

www.mek.dtu.dk

November 2022

ISBN: 978-87-7475-711-5

DCAMM
Danish Center for Applied Mathematics and Mechanics

Koppels Allé, Bld. 404
DK-2800 Kgs. Lyngby
Denmark
Phone (+45) 4525 4250
Fax (+45) 4525 1961

www.dcamm.dk

DCAMM Special Report No. S322

ISSN: 0903-1685